



TECHNISCHE  
UNIVERSITÄT  
WIEN

DISSERTATION

# A Masing Diamond: Triggered and Self-Induced Superradiance

ausgeführt zum Zwecke der Erlangung des akademischen Grades eines  
Doktors der technischen Wissenschaften

unter der Leitung von

**Univ.Prof. Dipl.-Ing. Dr.techn. Hannes-Jörg Schmiedmayer**

eingereicht an der Technische Universität Wien  
Fakultät für Physik

von

**Dipl.-Ing. Wenzel Nikolaus Kersten**

Fendigasse 9/28

1050 Wien

Wien, January 2025

---

W. Kersten

Gutachter:

---

H.-J. Schmiedmayer

---

G. Kirchmair

---

P. Rabl



*“Remember when you were young  
You shone like the sun  
Shine on you crazy diamond”*

Pink Floyd, 1975



# Abstract

In this work, I present experimental studies of cavity quantum electrodynamics (cQED) with a focus on superradiant emission from a hybrid system of nitrogen-vacancy (NV) centers in diamond strongly coupled to a microwave cavity. The research centers on two key experiments that investigate superradiance, a collective phenomenon where synchronized emitters generate a coherent burst of radiation with nonlinear intensity scaling, facilitated by their common coupling to the cavity mode.

First, I demonstrate a protocol for generating and storing a uniformly inverted spin ensemble, enabling the controlled release of a superradiant burst. By extending the inversion storage time for up to tens of milliseconds, I achieve a fully upright, metastable spin state with vanishing transverse spin components. I explore the onset of superradiance, revealing that weak microwave trigger pulses on the order of  $10^{-11}$  photons per spin are sufficient to influence the superradiant decay in both timing and phase.

Second, following the initial decay, I observe unexpected self-induced superradiant dynamics that evolve from a periodic pulsing regime into quasi-continuous masing, lasting up to a millisecond. This behavior, which cannot be explained by known cQED effects, is driven by direct spin-spin interactions that redistribute the spectral spin inversion within the inhomogeneously broadened NV ensemble. These findings reveal a new role for spin-spin interactions as an active drive of superradiant emission, rather than merely a source of decoherence.

The experimental results are prefaced by a theoretical framework and numerical simulations. Additionally, I present microwave cavity designs aimed at achieving strong and uniform spin coupling with reduced mode volumes. These designs, realized through finite-element simulations and experiments, explore a range of resonator types — from bulk copper and superconducting niobium to on-chip, nano-fabricated structures — paving the way for future cQED experiments and quantum technology applications.



# Zusammenfassung

In dieser Arbeit präsentiere ich experimentelle Studien zu Effekten der Resonator-Quantenelektrodynamik (cQED), mit einem Fokus auf superradiante Strahlung eines stark gekoppelten hybriden Systems bestehend aus Stickstoff-Fehlstellen-Zentren (NV-Zentren) in Diamant und einem Mikrowellenresonator. Im Mittelpunkt stehen zwei Schlüsselversuche zur Superradianz – einem kollektiven Prozess, bei dem synchronisierte Emittoren einen kohärenten Lichtpuls von nichtlinearer Intensität erzeugen, vermittelt durch ihre gemeinsame Kopplung an die Resonatormode.

Zunächst erarbeite ich ein Verfahren zur Erzeugung und Speicherung eines gleichmäßig invertierten NV-Ensembles sowie zur späteren kontrollierten Auslösung des superradianten Zerfalls. Eine Verlängerung der Inversionsspeicherzeit auf bis zu mehrere zehn Millisekunden führt zum Verschwinden der transversalen Spin-Komponenten und zur Erzeugung eines vollständig aufrechten, metastabilen Zustands. Ausgehend von diesem Zustand untersuche ich den Initialmoment der Superradianz und zeige, dass schwache Mikrowellenpulse von etwa  $10^{-11}$  Photonen pro Spin ausreichen, um sowohl den Zeitpunkt als auch die Phasenlage des superradianten Zerfalls zu beeinflussen.

Anschließend beobachte ich nach dem anfänglichen Zerfall eine unerwartete, selbstinduzierte superradiante Dynamik, die sich von einem periodischen Pulsregime zu einer quasi-kontinuierlichen Emission weiterentwickelt und bis zu einer Millisekunde andauert. Diese Dynamik, die durch keine bekannten cQED-Effekte erklärt werden kann, wird durch direkte Spin-Spin-Wechselwirkungen angetrieben, welche die spektrale Spin-Inversion im inhomogen verbreiterten NV-Ensemble umverteilen. Diese Ergebnisse weisen auf eine neue Rolle der Spin-Spin-Wechselwirkungen als aktive Triebkraft der superradianten Strahlung hin, anstatt lediglich als Quelle der Dekohärenz zu fungieren.

Die experimentellen Ergebnisse werden durch ein theoretisches Rahmenwerk eingeleitet und durch numerische Simulationen untermauert. Zusätzlich präsentiere ich neu entwickelte Mikrowellenresonatoren, die eine starke und gleichmäßige Photonen-Spin Kopplung bei reduziertem Modenvolumen ermöglichen. Diese Resonatoren, die mithilfe von Finite-Elemente-Simulationen und experimentellen Umsetzungen untersucht werden, umfassen eine Reihe von Archetypen – von Realisierungen aus Kupfer und supraleitendem Niob bis hin zu Chip-basierten und nanofabrierten Strukturen – und ebnet den Weg für zukünftige cQED-Experimente sowie Anwendungen in Quantentechnologien.



# Publications

Parts of this thesis are based on the following publications:

- **Self-Induced Superradiant Masing**

Wenzel Kersten, Nikolaus de Zordo, Elena S. Redchenko, Nikolaos Lagos, Andrew N. Kanagin, Andreas Angerer, William J. Munro, Kae Nemoto, Igor E. Mazets, Jörg Schmiedmayer  
arXiv:2402.08537

- **Triggered Superradiance and Spin Inversion Storage in a Hybrid Quantum System**

Wenzel Kersten, Nikolaus de Zordo, Oliver Diekmann, Tobias Reiter, Matthias Zens, Andrew N. Kanagin, Stefan Rotter, Jörg Schmiedmayer, and Andreas Angerer  
Phys. Rev. Lett., 131, 043601 (2023); arXiv:2301.04100

- **Enhanced Molecular Spin-Photon Coupling at Superconducting Nanoconstrictions**

Ignacio Gimeno\*, Wenzel Kersten\*, María C. Pallarés, Pablo Hermosilla, María José Martínez-Pérez, Mark D. Jenkins, Andreas Angerer, Carlos Sánchez-Azqueta, David Zueco, Johannes Majer, Anabel Lostao, and Fernando Luis  
ACS nano, 14(7), 8707-8715 (2020); arXiv:2006.03386

- **Additive-Manufactured and Topology-Optimized Permanent-Magnet Spin Rotator for Neutron Interferometry**

Wenzel Kersten, Laurids Brandl, Richard Wagner, Christian Huber, Florian Bruckner, Yuji Hasegawa, Dieter Suess, and Stephan Spönar  
Physical Review Applied, 12(1), 014023 (2019); arXiv:1810.13225

Other publications to which the author has contributed:

- **Direct Experimental Test of Commutation Relation via Imaginary Weak Value**

Richard Wagner, Wenzel Kersten, Armin Danner, Hartmut Lemmel, Alok Kumar Pan, and Stephan Sponar

Physical Review Research, 3(2), 023243 (2021); arXiv:2012.08171

- **Spin-Rotation Coupling Observed in Neutron Interferometry**

Armin Danner, Bülent Demirel, Wenzel Kersten, Hartmut Lemmel, Richard Wagner, Stephan Sponar and Yuji Hasegawa NPJ Quantum Information, 6(1), 23 (2020); arXiv:1904.07085

- **Quantum Causality Emerging in a Delayed-Choice Quantum Cheshire Cat Experiment with Neutrons**

Richard Wagner, Wenzel Kersten, Hartmut Lemmel, Stephan Sponar and Yuji Hasegawa

Scientific Reports, 13(1), 3865 (2023)

# Contents

<b>1</b>	<b>Introduction</b>	<b>1</b>
<b>2</b>	<b>Theory of Spins in Cavities</b>	<b>5</b>
2.1	A single spin in a static field . . . . .	5
2.2	A quantized spring . . . . .	9
2.3	Quantization of the electromagnetic field . . . . .	12
2.4	Coupling a spin to a cavity — the Jaynes-Cummings model . . . . .	14
2.5	Many spins in a cavity . . . . .	18
2.5.1	The Dicke ladder . . . . .	20
2.5.2	Dephasing of the collective spin states . . . . .	22
2.6	Loss mechanisms for spins and photons . . . . .	24
2.7	Cavity input and output theory . . . . .	25
2.8	Maxwell-Bloch equations . . . . .	27
2.9	Superradiance . . . . .	32
<b>3</b>	<b>Experimental Setup and Instrumentation</b>	<b>43</b>
3.1	Cryostats . . . . .	43
3.2	Microwave techniques . . . . .	46
3.2.1	IQ-mixing . . . . .	46
3.2.2	Time-resolved and spectroscopy measurement setup . . . . .	48
3.2.3	Pulse photon number calibration . . . . .	49
<b>4</b>	<b>Spin Systems</b>	<b>55</b>
4.1	Nitrogen-vacancy center in diamond . . . . .	55
4.1.1	Structure and ground state level scheme . . . . .	56
4.1.2	NV samples used in this work . . . . .	62
4.2	Molecular spins . . . . .	64

---

<b>5</b>	<b>Microwave Cavity Designs</b>	<b>67</b>
5.1	Design principles for microwave resonators . . . . .	68
5.2	Microwave resonators . . . . .	73
5.2.1	Enhancing the single spin coupling with nanoconstrictions . . . . .	73
5.2.2	Loop-Gap-Wedge cavity . . . . .	79
5.2.3	Double-Chip resonator . . . . .	84
5.2.4	3D-Cavity towards a superradiant diamond maser . . . . .	94
<b>6</b>	<b>Experiments</b>	<b>105</b>
6.0.1	Hybrid system characterization . . . . .	106
6.0.2	Inversion pulses . . . . .	110
6.0.3	Inversion storage using the rapid detuning loop . . . . .	118
6.1	Triggered superradiance . . . . .	123
6.2	Self-induced superradiant masing . . . . .	137
6.2.1	Spin-spin interactions . . . . .	155
6.2.2	Spin exchange between detuned sub-ensembles . . . . .	161
<b>7</b>	<b>Conclusion and future directions</b>	<b>171</b>
	<b>Appendix A Integral evaluation of the spectral hole filling rate <math>\mathcal{J}</math></b>	<b>175</b>
A.1	Frequency dependent spectral hole refilling . . . . .	177
	<b>References</b>	<b>181</b>
	<b>Curriculum Vitae</b>	<b>191</b>

# Chapter 1

## Introduction

One of the most fundamental interactions shaping the world around us is the interaction between light and matter. From the discovery of electromagnetism — which describes the behavior of “invisible” fields generated by static and dynamic charges — to Maxwell’s realization that these fields are equivalent to visible light [1], our understanding of light-matter interactions has profoundly deepened. This development was further advanced by the emergence of quantum mechanics in the early 20th century [2], which revealed the remarkable dual nature of both light and matter — exhibiting both wave-like, non-local behavior and the graininess associated with particles. These groundbreaking developments culminated in the field of quantum electrodynamics (QED) [3], which bridges classical electromagnetism and quantum mechanics, forming a comprehensive fundamental description of light-matter interactions at the quantum level.

Notably, the very existence of matter in its seemingly infinite possible shapes and configurations is a direct result of these light-matter interactions. Light acts as a mediator, while matter is the substrate, allowing for the formation of atomic orbitals, molecular bonds, and crystal structures that define the properties of organic and inorganic materials, encompassing everything that surrounds us from the microscopic to the macroscopic scale.

The study of light-matter interactions has led to revolutionary technological advancements, from electric motors and illumination to modern electronics and telecommunications. One key development in this area is the laser, a prototypical example of controlled light-matter interaction. The laser, originally realized as a maser in the microwave regime, is a product of the field known as cavity QED [4]. Cavity QED investigates the interaction between quantized fields of electromagnetic radiation and

atomic or spin-based systems confined within cavities, providing insights into both fundamental physics and practical applications.

In cavity QED, a key goal is to achieve strong coupling between light and matter. This regime allows for coherent energy exchange between the quantized field in the cavity and the system of quantum emitters on a faster timescale than energy dissipation. Achieving strong coupling opens the door to the manipulation and readout of quantum systems for computing, sensing, and communication. A central challenge in this area is designing cavity geometries that maximize this interaction, particularly when working with solid-state systems like nitrogen-vacancy (NV) centers in diamond [5] or molecular spin systems [6].

In my work, I developed new cavity geometries and chips to enhance the coupling between microwave fields and spin ensembles, with the goal of reaching the high cooperativity regime with ever-smaller spin ensembles. This is a crucial step towards realizing quantum computing architectures [7] with spin systems [8], enabling scalable qubit operation and quantum information processing with nature’s largest indistinguishable unit: single molecules.

The main focus of my thesis is based on explorations with a particularly promising microwave cavity design. When coupled to a small NV diamond, this cavity forms a highly cooperative hybrid system, enabling rapid and efficient excitation of the NV spin ensemble and offering unprecedented control over the resulting metastable inverted spin state. A fascinating phenomenon that arises from the strong light-matter coupling in this hybrid system is superradiance, a collective emission of radiation from an ensemble of excited emitters. First described by Dicke in 1954 [9], superradiance is a synchronized emission process that produces a highly coherent and intense burst of light, profoundly distinct from the sum of individual contributions of independent emitters [10].

In this thesis, I study superradiant dynamics with a diamond-cavity hybrid system. My initial focus lies on investigating the onset of superradiance — revealing a remarkable sensitivity of the inverted spin system to weak trigger pulses down to  $10^{-11}$  photons per spin. Moreover, using this experimental platform, I uncover an unexpected mechanism appearing as a driving force for said superradiant emission: direct spin-spin interactions of NV centers within the crystalline diamond lattice. This novel observation, where the spin-spin interactions facilitate energy transfer into a spectral window of “active” superradiant emitting spins, is underpinned by several experimental pieces of evidence. This constructive role of direct spin-spin interactions in driving the superradiant emission stands in contrast to their typical appearance as a detrimental

source of dissipative decoherence effects. Not only remarkable from a fundamental viewpoint, this observation holds implications that extend into a practical domain of applied physics, where superradiant lasing offers the potential for ultranarrow frequency generation.

These exciting results breach only the surface of how these spin-spin interactions work in detail, so far only understood with an effective description of self-induced superradiant dynamics. Further studies are needed to fully understand the mechanisms at play — complex spin-spin dynamics, possibly only accessible via a many-body description — and to explore their fundamental aspects and potential applications in quantum technologies.

## Outline

This thesis is structured as follows:

In Chapter 2, I present the theoretical framework for the relevant cavity QED physics, starting with the basic quantum aspects of electromagnetic fields and spin systems, advancing to their mutual (collective) interactions, and finally discussing the cooperative emission phenomenon of superradiance.

Chapter 3 gives a short description of the experimental setup and techniques, including the cryogenic systems and microwave equipment used in the experiments.

In Chapter 4, I cover the spin systems relevant to this work: NV centers in diamond. Additionally, I shortly touch on the topic of molecular spins, particularly a simple testbed molecular spin species used in a study on enhancing spin-photon coupling.

Chapter 5 is focused on cavity designs for reaching the strong coupling regime, offering my viewpoint and design approaches for chip-based and 3D lumped-element microwave resonators, based on several different cavity designs developed and characterized in the course of my studies.

In Chapter 6, I present the main experimental results with our<sup>1</sup> hybrid diamond-cavity platform: (i) triggered superradiance, realizing the controlled release of superradiant emission and investigating the sensitivity to weak trigger signals; and (ii)

---

<sup>1</sup>This introduction chapter is written in a first-person style, stressing that the presented contents are my original work. In the following chapters, I mostly adopt the commonly used scientific *we*. This has a twofold meaning: First, even though I am the main contributor, at least in the results based on my first-authored publications, scientific work nowadays is rarely a single-person job; it would be impossible without the environment of a research group and collaborators. Secondly, *we* is meant to include me and the reader of this thesis, attempting to make the involvement more engaging.

self-induced superradiance, uncovering a novel pumping mechanism driven by direct spin-spin interactions.

In the final Chapter 7, I offer a brief outlook on possible future explorations of our experimental platform and conclude the thesis with final remarks and open questions.

# Chapter 2

## Theory of Spins in Cavities

*From a single spin and the quantum harmonic oscillator to collective light-matter interaction*

In this chapter, we will start by introducing two fundamental concepts in quantum mechanics: the spin of a particle and the quantization of the electromagnetic field. These two systems are on opposite ends when considering linearity in the number of excitations. The simplest spin system is a two-level system with only two possible states: spin up  $|\uparrow\rangle$  and spin down  $|\downarrow\rangle$ , thus can only absorb or emit one excitation quantum. On the other hand, a single mode of the electromagnetic field has no limit in the number of photons it can carry, a property making it a bosonic system. Naturally, it follows to look at the interactions between these two quantum systems — photons and spins — opening up the vast field of cavity QED, for which the basic theoretical concepts will be laid out. Our goal will be to arrive at a description of the dynamics involving an ensemble of a large number of spins coupled to a single electromagnetic mode, and finally, to have a set of equations that will allow us to quantitatively model these dynamics.

### 2.1 A single spin in a static field

Spin is a quantum property of elementary particles such as electrons, protons, and neutrons that carry a magnetic dipole moment. Although the prominent spin system of this work, the negatively charged NV center, involves two electrons bound to a point defect in a diamond crystal, in this section, I will introduce the concept of spin with the example of a neutron spin. This is done to later support this theoretical description

with an instructive experiment carried out at the very beginning of my PhD journey — a neutron interferometry experiment that uses 3D printed permanent magnets to exemplify two important concepts: the superposition principle and the  $4\pi$ -symmetry of spin  $S = 1/2$  particles.

The neutron is a spin  $S = 1/2$  particle, which means that upon measurement, one would find that its spin is in either one of two possible states, either spin up  $|\uparrow\rangle$  or spin down  $|\downarrow\rangle$  with regards to the measurement direction, conventionally the  $+z$ -direction. The spin projection along this axis can only take discrete values in half-integer units of Planck's constant  $\pm\hbar/2$ . Prior to this measurement, the neutron's spin can be in an arbitrary superposition of these two states, and its wave function is written as

$$|\Psi\rangle = \cos(\theta/2) |\downarrow\rangle + \sin(\theta/2)e^{i\phi} |\uparrow\rangle . \quad (2.1)$$

This parametrization of the state  $|\Psi\rangle$  is very useful, as it allows us to understand the direction of the magnetic dipole  $\vec{\mu}$  associated with the arbitrary spin state  $|\Psi\rangle$ , represented by a point on the surface of the Bloch sphere, determined by the two angles  $\theta$  and  $\phi$ , see Fig. 2.1. The magnetic dipole moment is calculated using the spin operators as

$$\vec{\mu} = \frac{g_n\mu_n}{\hbar} \langle\Psi| \vec{S} |\Psi\rangle = \gamma_n \langle\Psi| (S_x, S_y, S_z)^T |\Psi\rangle , \quad (2.2)$$

which are given in terms of the Pauli matrices  $S_i = \frac{\hbar}{2}\sigma_i$ . Here,  $g_n$  is the neutron's  $g$ -factor and  $\mu_n$  is the nuclear magneton, resulting in the neutron's gyromagnetic ratio  $\gamma_n \approx -1.83 \times 10^8 \text{ s}^{-1} \text{ T}^{-1}$ .

The Hamiltonian of a (neutron) spin in a static magnetic field is written as

$$\mathcal{H} = -\vec{\mu} \cdot \vec{B} = -\gamma_n \vec{S} \cdot \vec{B} . \quad (2.3)$$

We can see how the static field causes rotations of the spin around an axis given by the field's direction. Suppose the spin is initially polarized in the  $+x$ -direction, where its wavefunction is given by  $|\psi_0\rangle = |+\rangle = \frac{1}{\sqrt{2}}(|\uparrow\rangle + |\downarrow\rangle)$ , and the magnetic field is oriented along the  $+z$  axis,  $\vec{B} = B_0\vec{e}_z$ . Then, we can use the Schrödinger equation to calculate the time evolution of  $|\psi(t)\rangle$

$$\mathcal{H} |\psi(t)\rangle = i\hbar \frac{\partial}{\partial t} |\psi(t)\rangle . \quad (2.4)$$

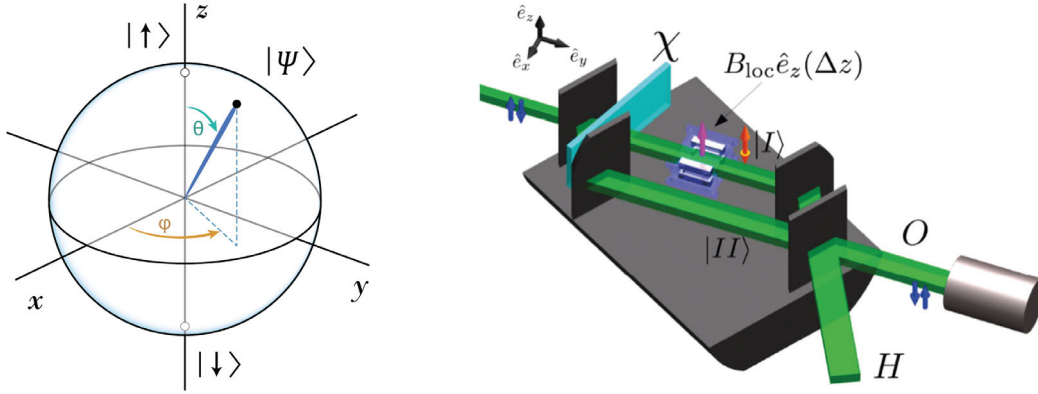


**Figure 2.1** (Left) Bloch sphere to visualize the two possible spin orientations,  $|\uparrow_z\rangle$  and  $|\downarrow_z\rangle$ , and their arbitrary superposition. (Right) Excursion into neutron interferometry: A neutron interferometer, where unpolarized neutrons pass through from left to right into a detector. Inside the interferometer, the neutron beam is split evenly into path  $|I\rangle$  and  $|II\rangle$ . Neutrons in path  $|I\rangle$  experience an additional spin rotation around the  $z$  axis through the 3D-printed permanent magnet spin rotators, controllable by the magnet distance  $\Delta z$ . Before entering the detector, the two paths are recombined. Rotating the phase plate introduces a path-dependent phase shift  $\chi$  to record an interferogram.

Since  $\mathcal{H} = -\hbar\frac{\gamma_n B_0}{2}\sigma_z$  is independent of time, we can simply apply the unitary time evolution operator  $U(t) = e^{-i\mathcal{H}t/\hbar}$  to calculate the state at a later time  $t$  from the initial state  $|\psi_0\rangle$  at  $t = 0$ .

$$\begin{aligned} |\psi(t)\rangle &= U(t) |\psi_0\rangle = \exp\left(i\frac{\gamma_n B_0}{2} t \sigma_z\right) \frac{1}{\sqrt{2}}(|\uparrow\rangle + |\downarrow\rangle) \\ &= \frac{1}{\sqrt{2}}\left(e^{+i\frac{\gamma_n B_0}{2} t} |\uparrow\rangle + e^{-i\frac{\gamma_n B_0}{2} t} |\downarrow\rangle\right). \end{aligned} \quad (2.5)$$

Comparing this result with Eq. (2.1) and Eq. (2.2), we see that the spin state and also its associated magnetic dipole moment undergoes a rotation in the  $xy$ -plane around the equator of the Bloch sphere. This rotation occurs at the Larmor frequency, denoted as  $\omega_L = \gamma_n B_0$ .

## An instructive excursion into neutron interferometry

In the experiment of Ref. [11], we see an instructive demonstration of spin rotations and the superposition principle. Here, I will only explain the basic result of this experiment without going into detail about the broad topic of neutron interferometry, as it is not the main focus of this thesis. A neutron interferometer, see Fig. 2.1 is a very useful

tool to study phenomena of a perfectly isolated quantum system: the neutron, as it moves through the interferometer. A neutron interferometer is cut from a single silicon crystal, such that all its crystal planes are perfectly aligned. This allows for the coherent diffraction of a neutron beam via Bragg reflection at the four plates of the interferometer, which act as mirrors and beam splitters. This way, the incident beam is split into two paths, which are later recombined to interfere. The spatial separation of neutrons in the two paths enables the possibility of independent manipulation. The low flux of neutrons and their rather high speed of  $2 \text{ km s}^{-1}$  makes sure that, on average, only maximally one neutron is passing through the interferometer, such that the observed quantum phenomena stem from self-interference of the neutrons. Assuming perfect interferometric contrast, the density matrix of an unpolarized (completely mixed spin state), and monochromatic (constant velocity) neutron inside the interferometer can be written as

$$\rho = |\psi_i\rangle\langle\psi_i| \otimes \frac{1}{2}(|\uparrow\rangle\langle\uparrow| + |\downarrow\rangle\langle\downarrow|), \quad (2.6)$$

where  $|\psi_i\rangle = \frac{1}{\sqrt{2}}(|I\rangle + e^{i\chi}|II\rangle)$  is the path state after the phase plate, which introduces a path-dependent phase shift  $\chi$ . Importantly, this phase shift can be varied by rotating a phase plate after the first beam splitter. In path  $|I\rangle$  there is a 3D-printed permanent magnet spin rotator, as shown in Fig. 2.1. Adjusting the distance  $\Delta z$  of the two permanent magnet pairs allows for a change in the rotation angle of the spins around the  $+z$ -axis in this path. The action of this spin rotator can be written by the unitary transformation

$$U_{\text{int}} = |I\rangle\langle I| \otimes e^{i(\alpha/2)\sigma_z} + |II\rangle\langle II| \otimes \mathbb{1}, \quad (2.7)$$

where the rotation angle  $\alpha(\Delta z) = (g_n \mu_n / \hbar) B_{\text{loc}} \Delta t$  depends on the local magnetic field  $B_{\text{loc}}(\Delta z)$  created by the spin rotator, which acts for a fixed duration  $\Delta t$  while the neutron passes through. The last interferometer plate recombines the two paths and projects on the final path state  $|\psi_f\rangle = \frac{1}{\sqrt{2}}(|I\rangle + |II\rangle)$  with the projection operator  $P_f = |\psi\rangle\langle\psi|_f \otimes \mathbb{1}$ .

The neutron beam intensity at the detector is then given by

$$I_O(\chi, \alpha(\Delta z)) \propto \frac{1}{C} \text{Tr}(P_f U_{\text{int}} \rho U_{\text{int}}^\dagger P_f^\dagger) + \frac{C-1}{C} \quad (2.8)$$

$$= \frac{1}{2} \left( 1 + C \cos\left(\frac{\alpha}{2}\right) \cos \chi \right), \quad (2.9)$$

where  $0 \leq C \leq 1$  takes the limited contrast of the neutron interferometer into account. The recorded interferograms, measured at the Atominstitut's TRIGA MARK-II reactor, are shown in Fig. 2.2. The effective interferometric contrast, represented by  $C \cos(\alpha/2)$ ,

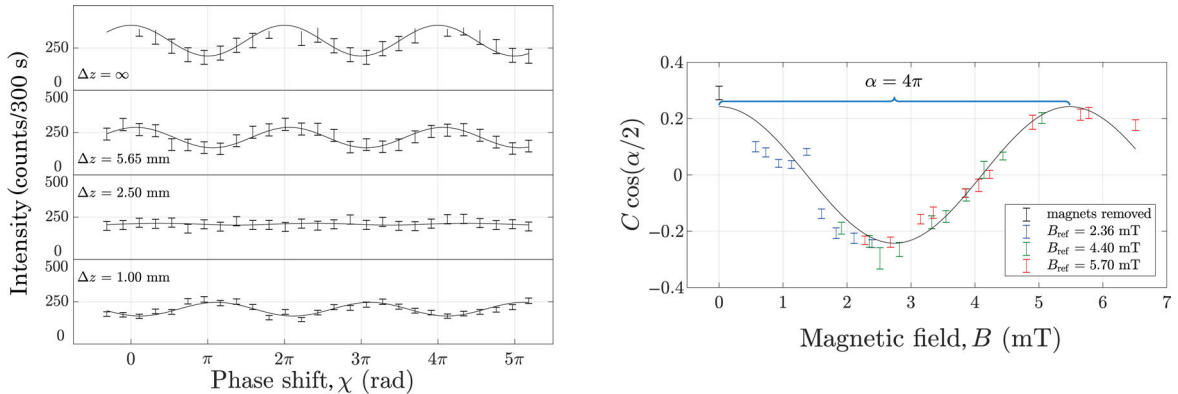


**Figure 2.2** Neutron interferometric measurements. (Left) Recorded interferograms with different  $\Delta z$  values, measured with a magnetization strength of the permanent magnets of  $B_{\text{ref}} = 4.4$  mT. (Right) A plot of the effective contrast  $C \cos(\alpha/2)$  derived from fits to the interferograms over the spin rotator’s magnetic field strength measured at the center. Datasets using different base magnetization strengths of the permanent magnet spin rotators are shown.

becomes zero for spin-rotation angles  $\alpha$  equal to odd multiples of  $\pi$ , which causes the spin states in the different paths to become orthogonal. When  $\alpha$  reaches  $2\pi$ , the interferogram displays a phase shift of  $\pi$  compared to the case  $\alpha = 0$  (magnets removed). Only at  $\alpha = 4\pi$  does the interferogram restore its initial contrast and phase, which occurs at twice the magnetic field strength needed to rotate an equivalent classical magnetic dipole of strength  $\mu_n$  to return to its original state.

We end this short excursion into neutron interferometry with a summary. This experiment, a replication of Helmuth Rauch’s seminal experiment from 1975 [12] (its novelty being the topology optimized 3D-printed permanent magnet spin rotators), illustrates two things: (i) the principle of superposition and interference, where the neutron beam is split into two paths and then recombined, and (ii) the  $4\pi$ -symmetry of the spin- $\frac{1}{2}$  property of neutrons, where the permanent magnet spin rotators cause a phase shift in the interferometer, even though the unpolarized spin state has no net magnetic dipole moment.

## 2.2 A quantized spring

The quantization of the electromagnetic field can be understood by starting from every physicist’s favorite pet model: the harmonic oscillator. Later, we can use a formal equivalence in their descriptions to gain a deeper understanding of these systems. The

derivations given here follow in parts Refs. [4, 13]. The Hamiltonian of the harmonic oscillator — the sum of kinetic and potential energy as a function of the position and momentum of, for example, a mass on a spring moving along the  $x$ -direction — is written in the standard form as

$$\mathcal{H} = \frac{\hat{p}^2}{2m} + \frac{1}{2}m\omega^2\hat{x}^2. \quad (2.10)$$

Here,  $m$  is the mass, and the angular frequency  $\omega = \sqrt{k/m}$  is calculated via the spring constant  $k$ . Quantum physics involves an operator description for position  $\hat{x} = x$  and momentum  $\hat{p} = -i\hbar\frac{\partial}{\partial x}$ . In the definitions given here, these are explicitly written in the position-basis. These operators obey the canonical commutation relations  $[\hat{x}, \hat{p}] = i\hbar$ . An elegant way of solving Eq. (2.10) is achieved by introducing the non-hermitian operator  $a$  and its conjugate  $a^\dagger$

$$a = X_0 + iP_0, \quad a^\dagger = X_0 - iP_0. \quad (2.11)$$

These definitions involve dimensionless position and momentum operators:

$$X_0 = \sqrt{\frac{m\omega}{2\hbar}}\hat{x} \quad \text{and} \quad P_0 = \sqrt{\frac{1}{2\hbar m\omega}}\hat{p}. \quad (2.12)$$

The operators  $a$  and  $a^\dagger$  then obey the commutation relation

$$[a, a^\dagger] = 1. \quad (2.13)$$

The above allows us to rewrite the equation of the quantum harmonic oscillator (2.10) as

$$\mathcal{H} = \hbar\omega(P_0^2 + X_0^2). \quad (2.14)$$

We substitute  $X_0 = (a + a^\dagger)/2$  and  $P_0 = i(a - a^\dagger)/2$ , which finally leads to the result

$$\mathcal{H} = \hbar\omega(a^\dagger a + 1/2). \quad (2.15)$$

The operators  $a^\dagger$  and  $a$  are called creation and annihilation operators, which either add or subtract one quantum of energy  $\hbar\omega$  when acting on an eigenstate  $|\psi(E)\rangle$  with

energy  $E$

$$\begin{aligned}\mathcal{H} a |\psi(E)\rangle &= (E - \hbar\omega) a |\psi(E)\rangle , \\ \mathcal{H} a^\dagger |\psi(E)\rangle &= (E + \hbar\omega) a^\dagger |\psi(E)\rangle .\end{aligned}\tag{2.16}$$

These energy quanta of a mechanical oscillator are called phonons. However, subtracting an infinite number of quantum excitations from an arbitrary state is not possible. Thus, there must exist a state of lowest energy, which is the vacuum state  $|0\rangle$  with energy  $\hbar\omega/2$ . Explicitly written in the  $x$  representation, the vacuum state is given by a Gaussian wavefunction

$$\psi_0(x) = \langle x|0\rangle = (2/\pi)^{1/4} e^{-x^2} .$$

This state has minimum uncertainty in both  $\hat{x}$  and  $\hat{p}$  quadratures, fulfilling the lower bound of the Heisenberg uncertainty relation  $\sigma_x \sigma_p \geq \hbar/2$  for the standard deviations of position and momentum. Applying the creation operator  $n$ -times to the vacuum state  $|0\rangle$  yields the Fock states (or number states)

$$|n\rangle = \frac{(a^\dagger)^n}{\sqrt{n!}} |0\rangle ,\tag{2.17}$$

a complete set of basis states of the quantum harmonic oscillator's Hilbert space. The operators  $a$  and  $a^\dagger$  acting on a Fock state  $|n\rangle$  and obeying the commutation relation (2.13) result in

$$a |n\rangle = \sqrt{n} |n-1\rangle \quad \text{and} \quad a^\dagger |n\rangle = \sqrt{n+1} |n+1\rangle ,\tag{2.18}$$

and allow us to define the number operator  $\hat{n} = a^\dagger a$ . The energy of a Fock state  $|n\rangle$  is then given by  $\mathcal{H} |n\rangle = E_n |n\rangle = \hbar\omega(n + 1/2)$ .

Using the displacement operator, defined as

$$D(\alpha) = e^{(\alpha a^\dagger - \alpha^* a)} ,\tag{2.19}$$

with complex  $\alpha$  we introduce the coherent states

$$|\alpha\rangle = D(\alpha) |0\rangle = e^{-|\alpha|^2/2} \sum_{n=0}^{\infty} \frac{\alpha^n}{\sqrt{n!}} |n\rangle ,\tag{2.20}$$

which are eigenstates of the annihilation operator  $a |\alpha\rangle = \alpha |\alpha\rangle$ , with a mean excitation number of  $\langle n \rangle = |\alpha|^2$ . The action of this operator in phase space corresponds to a displacement of the vacuum state from the origin while maintaining minimum

uncertainty in both quadratures. This latter property makes the coherent state the closest analog to a classical state. An important example of a coherent state is the light field of a laser. The probability of measuring  $n$  photons in a laser pulse using a photon counter is obtained by projecting the coherent state onto the Fock state  $|n\rangle$ , resulting in a Poissonian distribution  $P_n = |\langle n|\alpha\rangle|^2 = e^{-|\alpha|^2} |\alpha|^{2n}/n!$  with variance  $(\Delta n)^2 = |\alpha|^2$ . For large numbers of excitations, the relative error  $\Delta n/\langle n\rangle = 1/|\alpha|$  vanishes via the correspondence principle between quantum and classical physics.

## 2.3 Quantization of the electromagnetic field

In this section, I will motivate the formal equivalence of a single electromagnetic mode, such as the electric and magnetic fields that oscillate in a resonant cavity (e.g. a rectangular box cavity), to the quantum harmonic oscillator described in the previous chapter. In doing this, I will mostly follow the derivations of Ref. [14]. The dynamics of the electromagnetic field in vacuum are described by the Maxwell equations:

$$\begin{aligned}\nabla \cdot \vec{E} &= 0, \\ \nabla \cdot \vec{B} &= 0, \\ \nabla \times \vec{E} &= -\frac{\partial \vec{B}}{\partial t}, \\ \nabla \times \vec{B} &= \mu_0 \epsilon_0 \frac{\partial \vec{E}}{\partial t}.\end{aligned}\tag{2.21}$$

A solution for the electric field that exists inside a cavity of volume  $V$  and length  $L$ , confined between two perfectly conducting walls (see Fig. 2.3), is given by:

$$E_x(z, t) = \sqrt{\frac{2\omega^2}{\epsilon_0 V}} q(t) \sin(kz),\tag{2.22}$$

while the magnetic field can be calculated from this result with the last line in Eq. (2.21) as (using  $c = 1/\sqrt{\mu_0 \epsilon_0}$ )

$$B_y(z, t) = \frac{1}{c^2 k} \sqrt{\frac{2\omega^2}{\epsilon_0 V}} \dot{q}(t) \cos(kz).\tag{2.23}$$

Here,  $q(t)$  describes the time dependence of the fields. We assume the cavity is oriented along the  $z$ -direction, while the electric field is polarized along  $x$ . The wave number is an integer multiple of  $k = m\pi/L$ , and the angular frequency of the mode

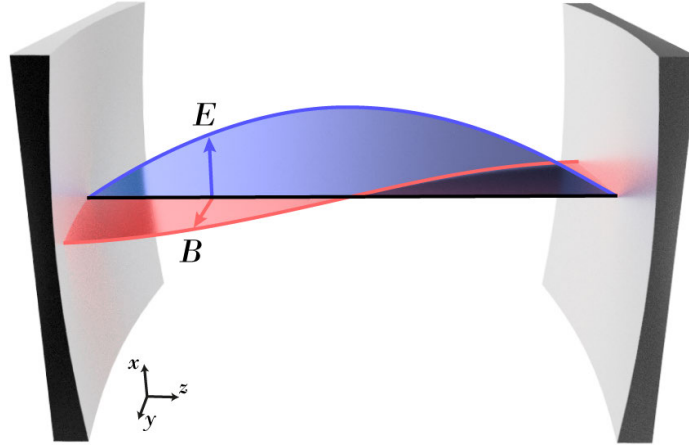


**Figure 2.3** The fundamental mode inside a resonant cavity: electric and magnetic fields are reflected between two perfectly conducting walls and form a standing wave, oscillating in time.

is given by  $\omega = ck$ . The total energy of the electromagnetic field can be recast in a familiar shape:

$$\mathcal{H} = \frac{1}{2} \int (\epsilon_0 \vec{E}^2 + \frac{1}{\mu_0} \vec{B}^2) dV = \frac{\omega^2 q^2}{2} + \frac{\dot{q}^2}{2}. \quad (2.24)$$

We recover the harmonic oscillator with unit mass  $m = 1$  by recognizing the formal equivalence of Eq. (2.24) and Eq. (2.10) when identifying  $\dot{q} = \hat{p}$  and  $q = \hat{x}$ . Using the same construction of the operators  $a$  and  $a^\dagger$  introduced in the previous chapter, this allows us to rewrite the oscillating electric and magnetic fields as

$$\begin{aligned} E_x(z, t) &= \mathcal{E}_0 (ae^{-i\omega t} + a^\dagger e^{+i\omega t}) \sin(kz), \\ B_y(z, t) &= -i\mathcal{B}_0 (ae^{-i\omega t} - a^\dagger e^{+i\omega t}) \cos(kz). \end{aligned} \quad (2.25)$$

We can see that a single mode of the electromagnetic field can carry excitation quanta  $\hbar\omega$  called photons and also has a state of minimum energy  $\hbar\omega/2$ , the vacuum state  $|0\rangle$ . Here, the time dependence of the fields is explicit but can be eliminated by moving into the rotating frame via the unitary transformation  $\tilde{a}(t) = e^{+i\mathcal{H}t/\hbar} a(0) e^{-i\mathcal{H}t/\hbar} = ae^{-i\omega t}$ . From now on we will refer to  $\tilde{a}$  as simply  $a$ . The amplitude of the magnetic field,

$$\mathcal{B}_0 = \sqrt{\frac{\mu_0 \hbar \omega}{2V}}, \quad (2.26)$$

is an important quantity for the experiments that will be discussed in the following chapters. It quantifies the root mean square magnetic field strength of the vacuum

fluctuations and depends on the volume and frequency of the mode. The electric field amplitude  $\mathcal{E}_0$  is analogously obtained by replacing  $\mu_0$  with  $1/\epsilon_0$ . The speed of spin rotations — and thus the ability to manipulate spin states within a given time — depends on the strength of the magnetic field. This principle applies to static fields, where it appears in the form of the Larmor frequency, but is also true for time-varying fields, such as those generated by driving the cavity with a microwave pulse. To anticipate a key point discussed later, this vacuum magnetic field strength can be effectively increased by shaping the environment of a mode with a specially designed cavity geometry, thereby deviating from a simple box mode, while decreasing the effective mode volume  $V$ . In the microwave (MW) regime, with frequencies in the gigahertz range, the concept of plane waves reflected off conducting walls often becomes too simplistic. Instead, it is more practical to consider the system as an LC resonant circuit — with spatially separate inductances  $L$  and capacitances  $C$ , or with  $L$  and  $C$  being distributed over the circuit. Nevertheless, a description using the total energy in the electromagnetic field, i.e. Eq. (2.24), will always be valid. Therefore the physics of any microwave resonator, cavity, or LC circuit is equivalent to the quantum harmonic oscillator.

## 2.4 Coupling a spin to a cavity — the Jaynes-Cummings model

Now, having introduced the most important concepts to describe the quantum excitations of spins and photonic modes, we are ready to take a look at the coupling of these two systems, and the basic phenomena resulting from their mutual interactions. We start by writing down a Hamiltonian as the sum of two contributions: the cavity mode and a single spin. The spin is assumed to experience the magnetic fields at a fixed position, allowing us to ignore the spatial dependencies.

$$\mathcal{H} = \mathcal{H}_{\text{cav}} + \mathcal{H}_{\text{spin+field}} = \hbar\omega_c(a^\dagger a + 1/2) - \vec{\mu} \cdot \vec{B}(t). \quad (2.27)$$

The cavity is described by the now familiar quantum harmonic oscillator, but looking at the Hamiltonian  $\mathcal{H}_{\text{spin+field}}$ , we can further expand it into two parts. We split the magnetic field into a static external field, which is purely classical, and a time-dependent cavity field necessitating a quantum description. The static field  $B_0\vec{e}_z$ , by convention assumed to be oriented along the  $z$ -direction, supplies the quantization axis which causes the spin- $\frac{1}{2}$  of an electron to have two well-defined energy levels for its two possible

states  $|\uparrow\rangle$  and  $|\downarrow\rangle$ . We recall the magnetic dipole moment is calculated with the formula  $\vec{\mu} = -\frac{g_e\mu_B}{\hbar}\vec{S} = -\gamma_e\frac{\hbar}{2}\vec{\sigma}$ , using the electron  $g$ -factor  $g_e \approx -2$ , the Bohr magneton  $\mu_B$ , and the electron gyromagnetic ratio of approximately  $\gamma_e/2\pi = 28 \text{ MHz mT}^{-1}$ . The oscillating cavity field, or radio-frequency (RF) field, oriented perpendicular to the quantization axis along the  $x$ -direction, is described in terms of the operators  $a$  and  $a^\dagger$ . These operators are defined in the rotating frame of the RF frequency, eliminating the explicit time dependence in the Hamiltonian. This leads to

$$\mathcal{H}_{\text{spin+field}} = \frac{\hbar}{2}\gamma_e B_0 \sigma_z + i\frac{\hbar}{2}\gamma_e B_{\text{cav}}(a - a^\dagger)\sigma_x. \quad (2.28)$$

We make use of the spin raising and lowering operators  $\sigma_+$  and  $\sigma_-$  with the definition  $\sigma_\pm = \frac{1}{2}(\sigma_x \pm i\sigma_y)$ . The action of these operators is to either excite a spin down  $\sigma_+ |\downarrow\rangle = |\uparrow\rangle$ , or de-excite an excited spin  $\sigma_- |\uparrow\rangle = |\downarrow\rangle$ , while the processes of exciting an already excited spin (or de-exciting a spin down)  $\sigma_+ |\uparrow\rangle = \sigma_- |\downarrow\rangle = 0$  are forbidden. With these operators to express  $\sigma_x = \sigma_+ + \sigma_-$  we finally write down the Jaynes-Cummings Hamiltonian

$$\mathcal{H}_{\text{JC}} = \hbar\omega_c \left( a^\dagger a + \frac{1}{2} \right) + \hbar\omega_s \frac{1}{2} \sigma_z + i\hbar g_0 (a\sigma_+ - a^\dagger\sigma_-), \quad (2.29)$$

using the spin transition frequency  $\omega_s = \gamma_e B_0$  and the coupling strength  $g_0 = \gamma_e B_{\text{cav}}/2$  of a single spin- $\frac{1}{2}$  to the cavity vacuum field. The vacuum energy offset  $\hbar\omega_c/2$  is here still included but will be dropped in subsequent calculations for simplicity. In this Hamiltonian, we have omitted terms such as  $a^\dagger\sigma_+$  and  $a\sigma_-$ , which either create or destroy two excitation quanta with total energy  $2\hbar\omega$ . These processes correspond to fast rotating terms: in the Schrödinger picture, the operator pairings of e.g.  $a_S e^{-i\omega_c t} \sigma_S^- e^{-i\omega_s t}$  rotate with double the frequency as compared to  $a_S^\dagger e^{+i\omega_c t} \sigma_S^- e^{-i\omega_s t}$ , where the frequencies cancel out on resonance. They are energy non-conserving and usually neglected under the rotating wave approximation, which is well justified in the limit of small couplings  $g_0 \ll \omega$  as compared to the transition frequencies.

Now, let us look at the solution space of the Jaynes-Cummings Hamiltonian, a universal description of a two-level system coupled to a bosonic mode. We can start by recognizing that under the action of this Hamiltonian, excitations can only be swapped from the cavity mode to the spin state, which will always conserve the total number of excitations. For a given subspace of  $n$  excitations, we can therefore write down two possible states with the two-level system (spin or atom) being either in the ground state  $|g\rangle$  or the excited state  $|e\rangle$ , and the cavity having an additional excitation  $|n+1\rangle$

or not  $|n\rangle$ , forming a basis

$$|g, n\rangle \equiv \begin{pmatrix} 1 \\ 0 \end{pmatrix} \quad \text{and} \quad |e, n-1\rangle \equiv \begin{pmatrix} 0 \\ 1 \end{pmatrix}. \quad (2.30)$$

Then, the Hamiltonian  $\mathcal{H}_{\text{JC}}$  can be written as a matrix

$$\mathcal{H}_{\text{JC}} = \hbar \begin{pmatrix} (n+1/2)\omega_c - \omega_s/2 & -ig_0\sqrt{n} \\ +ig_0\sqrt{n} & (n-1/2)\omega_c + \omega_s/2 \end{pmatrix}, \quad (2.31)$$

from which the eigenenergies

$$E_{n\pm} = \hbar n\omega_c \pm \hbar \frac{1}{2} \sqrt{4g_0^2 n + (\omega_c - \omega_s)^2}, \quad (2.32)$$

and the corresponding eigenstates

$$\begin{aligned} |n, +\rangle &= \cos(\theta/2) |g, n\rangle + i \sin(\theta/2) |e, n-1\rangle \quad \text{and} \\ |n, -\rangle &= \sin(\theta/2) |g, n\rangle - i \cos(\theta/2) |e, n-1\rangle, \end{aligned} \quad (2.33)$$

are obtained. These eigenstates, also called the polariton modes, are parametrized by the angle  $\theta = \arctan(2g_0\sqrt{n}/(\omega_c - \omega_s))$  and are plotted in Fig. 2.4. We can see that the eigenstates, initially degenerate on resonance for an uncoupled system with  $g_0 = 0$  and  $\Delta = \omega_c - \omega_s = 0$ , obtain a finite splitting  $\pm \hbar g_0$  in the one excitation manifold  $n = 1$ , called the vacuum Rabi splitting. The energy  $\hbar\omega$  is then equally shared between cavity and spin

$$|\pm\rangle = \frac{1}{\sqrt{2}}(|g, 1\rangle \pm i |e, 0\rangle), \quad (2.34)$$

and continually oscillates between the hybridized subsystems at a rate given by the coupling strength  $g_0$ . This can be seen by imagining the system to be in the state  $|\psi_0\rangle = |e, 0\rangle$  at  $t = 0$ . Then, its time evolution is given by (expanding in the eigenstate basis and using Eq. (2.32))

$$|\psi(t)\rangle = e^{-i\mathcal{H}t/\hbar} |e, 0\rangle = \frac{1}{\sqrt{2}i} (e^{-i(\omega_c+g_0)t} |+\rangle - e^{-i(\omega_c-g_0)t} |-\rangle). \quad (2.35)$$

Now, using the Born rule we calculate the probability of the system to be in the state  $|g, 1\rangle$  at time  $t$  as

$$P_g(t) = |\langle g, 1|\psi(t)\rangle|^2 = \left| \frac{1}{2i} e^{-i\omega_c t} (e^{-ig_0 t} - e^{+ig_0 t}) \right|^2 = \sin^2(g_0 t). \quad (2.36)$$

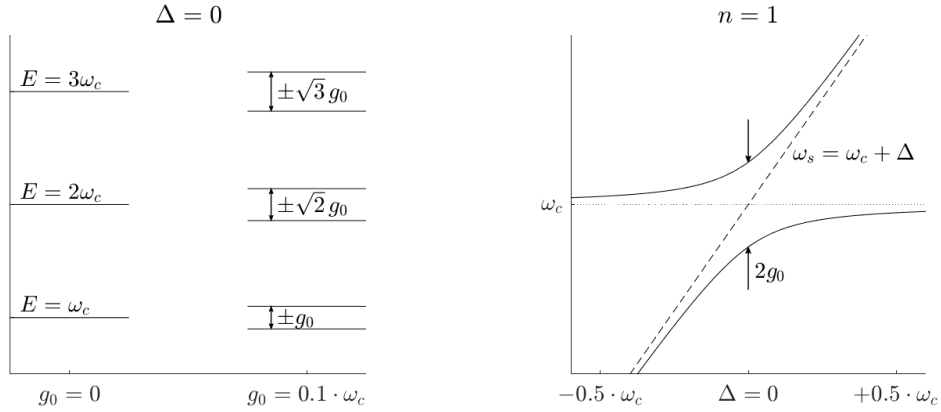


**Figure 2.4** Eigenstates of the Jaynes-Cummings Hamiltonian. We assume  $\hbar = 1$  and shift all energy levels by  $+(\omega_c - \omega_s)/2$ , such that the cavity level becomes a flat line. (Left) For the resonant case between spin and cavity ( $\Delta = \omega_c - \omega_s = 0$ ), the polariton modes are split symmetrically by  $\pm\sqrt{n}\hbar g_0$  relative to the originally degenerate states at zero coupling ( $g_0 = 0$ ). (Right) A scan of  $\Delta$  in the  $n = 1$  excitation subspace. At large detuning  $\Delta$  to either side, the eigenstates are very close to the uncoupled system and can be ascribed a rather definite spin or cavity character. On resonance  $\Delta = 0$  this is not the case, and the polariton modes carry equal contributions from both subsystems.

The probability of being in the state  $|e, 0\rangle$  is easily calculated by the counter probability  $P_e(t) = 1 - P_g(t) = \cos^2(g_0 t)$ . This continuous energy exchange between cavity mode and spin is called the vacuum Rabi oscillation.

For large detunings  $\Delta \gg g_0$ , known as the dispersive regime, it is instructive to look at the perturbation that the presence of the spin exerts onto the cavity eigenstate. For this, we write the Jaynes-Cummings Hamiltonian of Eq. (2.31) in the  $n = 1$  manifold in a slightly different way, corresponding to a shift  $+\omega_s/2$  of the diagonal entries, leaving the dynamics unchanged

$$\mathcal{H} = \hbar \begin{pmatrix} 0 & 0 \\ 0 & \Delta \end{pmatrix} + i\hbar g_0 \begin{pmatrix} 0 & -1 \\ +1 & 0 \end{pmatrix} = H_0 + V. \quad (2.37)$$

The second-order contribution of the perturbation term  $V$  using the basis states  $|g, 1\rangle \equiv (1, 0)^T$  and  $|e, 0\rangle \equiv (0, 1)^T$  (the first order gives zero contribution) is calculated using perturbation theory [15] as

$$E_g^{(2)} = \frac{|\langle g, 1 | V | e, 0 \rangle|^2}{E_e^{(0)} - E_g^{(0)}} = -\frac{g_0^2}{\Delta}, \quad (2.38)$$

similarly for  $E_e^{(2)} = +\frac{g_0^2}{\Delta}$ . We can therefore interpret the measured cavity frequency  $E_{g,e}^{\Delta \gg g_0} = E^{(0)} + E_{g,e}^{(2)} = \omega_c \pm \frac{g_0^2}{\Delta}$  in this regime to depend on the state of the spin, either shifted down for state  $|g\rangle$  or up for state  $|e\rangle$ . As the mutual influence of the spin on the cavity and vice versa the cavity on the spin is small, this allows us to infer the spin state with minimal disturbance by measuring the dispersive shift of the cavity peak, denoted as

$$\chi = \frac{g_0^2}{\Delta} \langle \sigma_z \rangle. \quad (2.39)$$

## 2.5 Many spins in a cavity

To arrive at a realistic description of the experiments presented in the next chapters, we extend the Jaynes-Cummings model to now include  $N$  spins, not just one. This extension, known as the Tavis-Cummings Hamiltonian, provides a framework to study collective phenomena and cooperative effects in systems with many spins coupled to a common cavity mode.

$$\mathcal{H}_{\text{TC}} = \hbar\omega_c a^\dagger a + \hbar \sum_{j=1}^N \frac{\omega_s^j}{2} \sigma_z^j + i\hbar \sum_{j=1}^N g_j (a\sigma_+^j - a^\dagger\sigma_-^j). \quad (2.40)$$

Here, we allow two generalizations for the  $N$  spins in the ensemble: each spin with index  $j$  can have its own transition frequency  $\omega_s^j$  and coupling constant  $g_j$ . Deviations in the spin energies  $\omega_s^j$  are due to inhomogeneities in the local environment of the spin. In the case of NV centers, this can be caused by the presence of crystal defects, different carbon isotopes, and other color centers. Together these effects lead to a broadening of the spin frequency distribution, referred to as inhomogeneous broadening. Similarly, inhomogeneities of the cavity's RF magnetic field over the spin sample volume cause deviations in the individual coupling strengths.

When we neglect these inhomogeneities, the system can be described using the collective spin operators

$$S_z = \frac{1}{2} \sum_{j=1}^N \sigma_z^j, \quad \text{and} \quad S_\pm = \sum_{j=1}^N \sigma_\pm^j. \quad (2.41)$$

The Hamiltonian (2.40) then reads

$$\mathcal{H} = \hbar\omega_c a^\dagger a + \hbar\omega_s S_z + i\hbar g_0 (aS_+ - a^\dagger S_-), \quad (2.42)$$

and describes the coupling of a mode to a collective spin  $S = N/2$ .

The Hilbert space of the spin system is spanned by the states  $|J, M\rangle$ , which are eigenstates of both operators  $S^2 = (S_x^2 + S_y^2 + S_z^2)$  and  $S_z$ . The quantum number  $J = 0, \dots, (\frac{N}{2} - 1), \frac{N}{2}$  of the total angular momentum operator  $S^2$  is given by  $S^2 |J, M\rangle = J(J + 1) |J, M\rangle$ , and  $M = -J, \dots, J$  is its projection on the  $z$ -axis given by  $S_z |J, M\rangle = M |J, M\rangle$ . These states couple to the cavity via the operators

$$S_{\pm} |J, M\rangle = \sqrt{(J \pm M + 1)(J \mp M)} |J, M \pm 1\rangle. \quad (2.43)$$

The lowest energy Dicke state has all spins in the ground state

$$|G\rangle = |J=\frac{N}{2}, M=-\frac{N}{2}\rangle = |g_1, \dots, g_N\rangle, \quad (2.44)$$

whereas the first excited Dicke state has one excitation shared equally among all spins, given by the symmetric superposition

$$|D_1\rangle = |J=\frac{N}{2}, M=-\frac{N}{2}+1\rangle = \frac{1}{\sqrt{N}} S_+ |G\rangle = \frac{1}{\sqrt{N}} \sum_{j=1}^N |g_1, \dots, e_j, \dots, g_N\rangle. \quad (2.45)$$

In the one excitation subspace, where either one photon is in the cavity  $|1_c\rangle$  and the spins are all in the ground state  $|G\rangle$ , or there is no cavity photon  $|0_c\rangle$  and the spin system is in the first Dicke state  $|D_1\rangle$ , the off-diagonal elements of the Hamiltonian are calculated as e.g.  $\langle 1_c, G | \mathcal{H} | 0_c, D_1 \rangle = i g_0 \sqrt{N}$ . We recover the result from above — the polariton modes — where the eigenstates are a symmetric or antisymmetric superposition between cavity and spins,

$$|\pm\rangle = \frac{1}{\sqrt{2}} (|1_c, G\rangle \pm i |0_c, D_1\rangle), \quad (2.46)$$

with energies  $E_{\pm} = \hbar\omega_c \pm \hbar g_0 \sqrt{N}$ . We can understand this energy-splitting as the vacuum Rabi splitting due to a collective coupling strength  $g_{\text{coll}} = \sqrt{\sum_{j=1}^N |g_0|^2} = g_0 \sqrt{N}$ , amplified by the factor  $\sqrt{N}$  as compared to a single spin.

For a large spin ensemble  $N$  (most experiments in this thesis have  $N \approx 5 \times 10^{13}$ ), when probing the system initialized in the ground state with low input power, we expect nearly all spins to remain in their ground state. At these low powers, the number of photons  $n \ll N$  compared to the number of spins is so low, that the probability for a photon to interact with a given spin twice is negligible. In this regime, the spin system

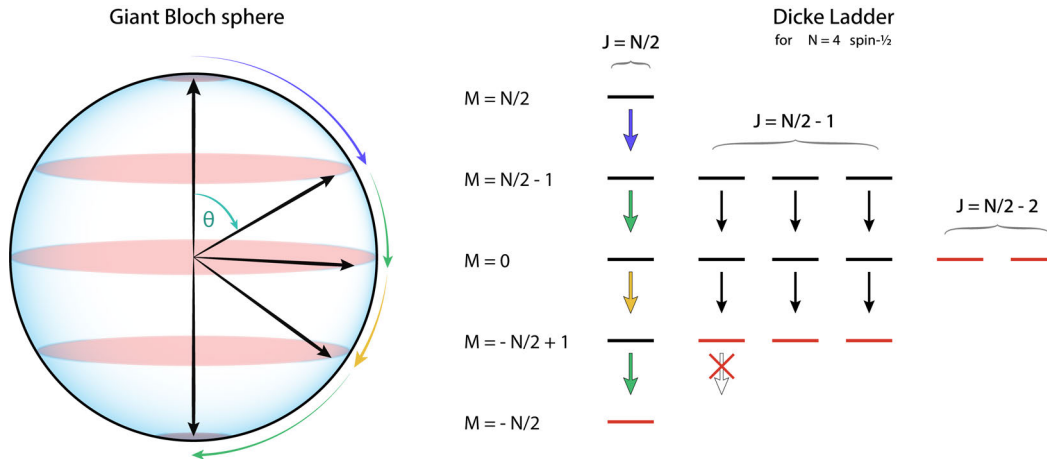


**Figure 2.5** Bloch sphere of the giant spin vector (left) and Dicke ladder diagram for four spin- $\frac{1}{2}$  (right). The most symmetric states are on the left side of the Dicke ladder with maximum  $J$  and are linked to each other via the operators  $S_{\pm}$ , which preserve the symmetry. This process is accompanied by the emission/absorption of a cavity photon  $a^{\dagger}S_{-}/aS_{+}$ , as symbolized by the arrows pointing down. States with lesser symmetry are located to the right. The red lines mark the lowest possible  $M$  states for a given  $J$ -manifold, which cannot couple to lower states via a cavity-mediated process. Different colors of the arrows mark the different transition rates associated with the spin decay, which is fastest at the equator of the Bloch sphere with tipping angle  $\theta = \pi/2$  and  $\Upsilon \propto N^2$ .

can be viewed as a bosonic mode able to accept equally spaced quanta of energy  $\hbar\omega_s$ , and the system response is that of two coupled harmonic oscillators.<sup>1</sup>

### 2.5.1 The Dicke ladder

Taking a closer look at the spin states, we can draw the Dicke ladder (see Fig. 2.5), a diagram that encompasses all possible basis states for quantum numbers  $J$  and  $M$ , not only the Dicke states which have the highest  $J = \frac{N}{2}$ . Starting from the ground state, we can apply the operator

$$B_k^{\dagger} |G\rangle = \frac{1}{\sqrt{N}} \sum_{j=1}^N \sigma_+^j e^{i(2\pi jk)/N} |G\rangle, \quad (2.47)$$

<sup>1</sup>This notion can be formulated in a mathematically exact way, which is known as the Holstein-Primakoff approximation, utilizing the bosonic operators  $b$  and  $b^{\dagger}$  [16]. They follow the commutation rule  $[b, b^{\dagger}] = 1$ , and lead to spin operators  $S_+ = (S_-)^{\dagger} = b^{\dagger} \sqrt{2S - b^{\dagger}b}$ , and  $S_z = (b^{\dagger}b - S)$ .

which raises the quantum number  $M$  by one, with  $k = 0, \dots, N - 1$ . The Dicke states correspond to  $k = 0$ , and are the result of applying  $m$ -times the operator  $S_+ \equiv B_0^+$

$$|D_m\rangle = \sqrt{\frac{m!(N-m)!}{N!}} (S^+)^m |G\rangle. \quad (2.48)$$

When  $k \neq 0$ , the states  $B_k^+ |G\rangle$  have phase differences between the terms in the sum that constitutes the total wave function, thus lesser permutation symmetry. The number of degenerate states that have in total  $m$  excited spins and  $z$ -projection  $M = -\frac{N}{2} + m$  is given by the possible pathways to combine  $B_{k_1}^+ B_{k_2}^+ \dots B_{k_m}^+$  to act on the ground state  $|G\rangle$  and create states with different permutation symmetries, calculated by the binomial coefficient  $\binom{N}{m}$ . Another way of seeing this is to count the number of possible replacements of (+) signs appearing in a sum with  $N$  terms to (−) signs, not counting arrangements that just introduce a global phase factor  $-1$ . This consideration also gives an intuition of how the symmetry is reduced by every additional (−) sign that is introduced in the wave function in this way: every (−) term decreases the number of possible permutations of spins (i.e. swapping two spins) that leave the total wave function unchanged.

From Eq. (2.43) we see that the operator  $S_-$  acting on a spin state with maximum  $J = \frac{N}{2}$  reduced by  $m$  gives zero:  $S_- |J=\frac{N}{2}-m, M=-\frac{N}{2}+m\rangle = 0$ . Therefore these states cannot be involved in a process  $a^\dagger S_-$  where a photon is emitted into the cavity. This characteristic assigns them the name *dark* or *subradiant states*. Other states that can be linked by possibly even a full cascade of multiple such processes are called *bright* or *superradiant states*.

Looking at the transition matrix elements that link two Dicke states by the process  $a^\dagger S_-$  for different projections  $M$ , we make an interesting observation that will become important later [only focusing on the spin part and using Eq. (2.43)]:

$$\Upsilon \propto |\langle J=\frac{N}{2}, M-1 | S_- | J=\frac{N}{2}, M \rangle|^2 \propto \begin{cases} N & \text{for } M = +\frac{N}{2} \\ N^2 & \text{for } M = 0 \end{cases} \quad (2.49)$$

We see that the squared amplitudes, corresponding to probabilities via the Born rule — and connected to the rates associated with the transitions — have different scaling with the number of spins  $N$  depending on their  $z$ -projection  $M$ . In other words, the decay rate  $\Upsilon$  depends on the tipping angle  $\theta = \arctan(|S_-|/S_z) = \arccos(M/J)$  of the collective spin vector  $\vec{S} = (S_x, S_y, S_z)^T$  on the giant Bloch sphere (see Fig. 2.5). At the

north pole of the Bloch sphere, the decay rate  $\Upsilon$  scales as  $N$ , whereas at the equator it scales as  $N^2$ .

### 2.5.2 Dephasing of the collective spin states

So far, we have talked about the possible spin states with different symmetries in the Dicke ladder, but we have not discussed how states of lesser symmetry can come about in the first place, especially when we keep in mind that cavity-mediated processes  $(a^\dagger S_-)^{(\dagger)}$  will only create Dicke states — the states with maximum symmetry — when starting from the ground state  $|G\rangle$ , thus corresponding to a vertical motion in the Dicke ladder. This is easily seen when we consider the inhomogeneous broadening of the spin frequencies  $\omega_s^j$  again. Now, when each spin has its own slightly different frequency  $\omega_s^j = \bar{\omega}_s + \Delta_s^j$ , over time this will lead to a phase difference  $e^{i\Delta_s^j t}$  between terms in the total spin wave function, for example as in

$$|\Psi_s(t)\rangle = \frac{1}{\sqrt{N}} \sum_{j=1}^N e^{i\Delta_s^j t} |g_1, \dots, e_j, \dots, g_N\rangle, \quad (2.50)$$

written in a frame rotating with the mean ensemble frequency  $\bar{\omega}_s$  and factoring out a physically insignificant global phase factor  $e^{-i\sum_j^N (\Delta_s^j t/2)}$ . As the frequency detunings  $\Delta_s^j$  are randomly sampled from the spin distribution  $\rho(\Delta_s)$  (assumed to be a smooth function for large  $N$ ), these phase differences quickly will cause the superradiant states to lose symmetry and become subradiant, corresponding to a lateral motion in the Dicke ladder.

Recalling the picture of a single spin in a static field and the spin- $\frac{1}{2}$  Bloch sphere, we remember that each spin rotates around the  $z$ -axis in the  $xy$ -plane with its individual frequency  $\omega_s^j$ . The detunings  $\Delta_s^j$  then will result in some spins rotating faster and others slower than the mean circular frequency  $\bar{\omega}_s$ . Considering the giant Bloch sphere of a collective spin again as a vectorial sum of all individual spins, we see that the inhomogeneous broadening leads to a decrease of the collective spin vector's transversal component  $|S_-|$  over time, as the individual spin constituents lose their mutual alignment and fan out. However, this situation is in principle reversible, as a  $\pi$ -rotation (achieved with a cavity pulse) around an axis in the  $xy$ -plane makes the fast and slow spins switch places, and over time, their phase evolution will be reversed. This effect, where the refocussing of spins generates an echo pulse, is known as a Hahn-echo [17], see Fig. 2.6.

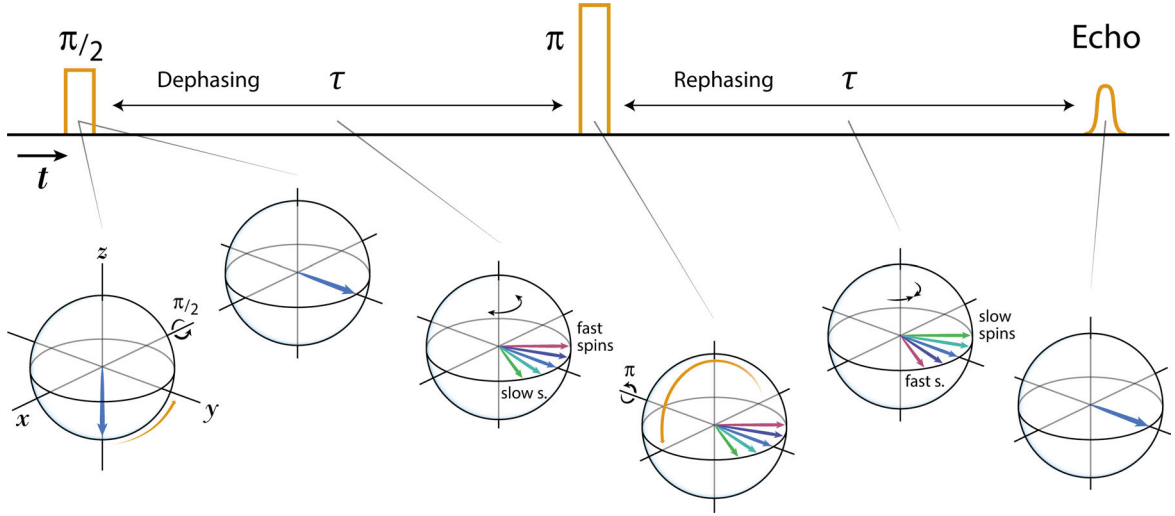


**Figure 2.6** Dephasing of the collective spin vector due to inhomogeneous broadening. A  $\pi$ -rotation, in this example around the  $y$ -axis, will reverse the dephasing and cause a refocusing of the collective spin vector.

At this point, it is also convenient to discuss the consequences of inhomogeneous single-spin couplings  $g_j$ , which occur when there is a gradient of the cavity's RF magnetic field  $B_{\text{cav}}(\vec{r})$  over the spin sample volume. Then, the state that is created via the spin-cavity interaction term acting on the state  $|1_c, G\rangle$  is written as

$$\begin{aligned} \mathcal{H}_{\text{int}} |1_c, G\rangle &= i\hbar \sum_{j=1}^N g_j (a\sigma_+^j - a^\dagger\sigma_-^j) |1_c, G\rangle \\ &\propto \sum_{j=1}^N g_j |0_c; g_1, \dots, e_j, \dots, g_N\rangle. \end{aligned} \quad (2.51)$$

This state exhibits asymmetry in the individual magnitudes of coefficients, compared to the symmetric Dicke state  $|D_1\rangle$ . The asymmetry is only amplified when considering multiple actions of the “inhomogeneous coupling” collective raising operator  $(\tilde{S}_+)^m \propto (\sum_j g_j \sigma_+^j)^m$ . For this reason, the simple picture of the Dicke ladder breaks down — linking states of sequential  $S_z$  projections via the collective cavity-spin interaction becomes impossible. Therefore, to observe the dynamics of superradiant Dicke states, it is important for all spins to couple to the cavity with a homogeneous coupling strength  $g_0$ .

## 2.6 Loss mechanisms for spins and photons

As we have seen above, inhomogeneous broadening decreases the transversal component of the collective spin vector over time. This process does not correspond to an actual loss of energy or coherence, as it is, in principle, reversible. However, other loss processes act on the level of individual spins and also on the cavity. Looking at a closed system, the law of energy conservation requires that energy is never lost. Similarly, information, such as the relative phase of a quantum superposition, cannot be destroyed but only transformed. This information can be distributed through interactions that entangle the state with other parts of the system, resulting in a total wave function of ever-increasing complexity. The apparent loss of energy and coherence comes about by making a distinction between the system of interest and its environment, which is usually too complex and has too many degrees of freedom to accurately model the dynamics of all its parts. The loss processes we want to describe here correspond to the dissipation of energy and coherence into this environment. The standard approach to calculating the dynamics of an open quantum system is given by the Lindblad master equation, which governs the dynamics of the density matrix  $\rho$ ,

$$\dot{\rho} = -\frac{i}{\hbar}[\mathcal{H}, \rho] + \underbrace{\sum_i \gamma_i \left( L_i \rho L_i^\dagger - \frac{1}{2} \{L_i^\dagger L_i, \rho\} \right)}_{\mathcal{L}(\rho)}. \quad (2.52)$$

Here,  $\{a, b\} = ab + ba$  denotes the anti-commutator, and the operators  $L_i$  and  $L_i^\dagger$  are called jump operators, influencing the time evolution of  $\rho$  at characteristic rates  $\gamma_i$ . This formalism is an extension of the van Neumann equation, which is given by Eq. (2.52) without the term  $\mathcal{L}(\rho)$  — it is a generalization of the Schrödinger equation that allows to model the time evolution of mixed states of an isolated quantum system. These states, described by the density matrix  $\rho$ , encompass coherent superpositions and incoherent additions within the system. The need to use incoherent additions, i.e. a statistical description, is a result of ignoring parts of the total wave function by tracing out the environmental degrees of freedom. Including the term  $\mathcal{L}(\rho)$  makes it possible to describe non-unitary dynamics that model dissipative processes and are associated with certain pathways of interaction with the environment.

For a spin system we can distinguish two processes:

- Loss of energy, where the excited state will eventually decay to the ground state with a characteristic timescale  $T_1$  and rate  $\gamma_{\parallel} = 1/T_1$ . This process affects the diagonal entries (or populations) of the density matrix  $\rho$  and is associated with

a decrease of the  $\rho_{ee}$  and a complementary increase of the  $\rho_{gg}$  components via the  $\sigma_-$  jump operator. It is caused by coupling to additional modes of the environment, such as phonons in the crystal host matrix of the spin, or coupling to modes of the electromagnetic field other than the cavity. In solid-state spin systems, this rate  $\gamma_{\parallel}$  is also called the spin-lattice relaxation rate.

- Loss of coherence, where the off-diagonal entries (or coherences) of the density matrix  $\rho_{eg}$  and  $\rho_{ge}$  decay with a timescale  $T_2$  and rate  $\gamma_{\perp} = 1/T_2$ . Over time this makes the relative phase in a coherent superposition of  $|e\rangle$  and  $|g\rangle$  vanish and turn it into an incoherent sum. This process is described with the  $\sigma_z$  jump operator and is associated with fluctuations of the external magnetic field  $B_z$ .

The cavity photons are also lost over time, leading to a decay of the cavity amplitude as  $|a| \propto e^{-\kappa t}$  with a dissipation rate  $\kappa$ . This process is caused by lossy channels, such as the surface resistance of metal walls in a box cavity, losses in a dielectric material, or lossy mirrors e.g. in a Fabry-Perot resonator. The associated jump operator is the annihilation operator  $a$ .

The full Lindblad operator for a system with  $N$  spins coupled to the cavity is given by

$$\begin{aligned} \mathcal{L}(\rho) = & \kappa (2a\rho a^\dagger - a^\dagger a\rho - \rho a^\dagger a) \\ & + \frac{\gamma_{\parallel}}{2} \sum_j^N (2\sigma_-^j \rho \sigma_+^j - \sigma_-^j \sigma_+^j \rho - \rho \sigma_+^j \sigma_-^j) \\ & + \frac{\gamma_{\perp}}{2} \sum_j^N (\sigma_z^j \rho \sigma_z^j - \rho), \end{aligned} \quad (2.53)$$

where we used the result  $\sigma_z^2 = 1$ . The choice of prefactors follows Ref. [18] and is determined by the equations of motion for the coupled system of cavity and spins — the Maxwell-Bloch equations — presented at the end of this chapter.

## 2.7 Cavity input and output theory

Having discussed an effective way of dealing with losses to the environment, we now want to describe how fields from outside couple to the photons in the cavity and simultaneously how these photons can escape the cavity to be measured, forming the basis for doing any experiment that probes the system. We consider a cavity with two ports, such as two lossy mirrors in a Fabry-Perot resonator as shown in Fig. 2.7.

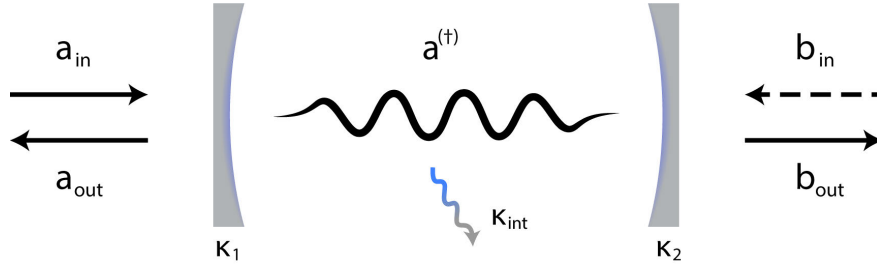


**Figure 2.7** Schematic representation of a cavity with two ports. The cavity field operator  $a^{(\dagger)}$  is coupled to the incident fields  $a_{\text{in}}$  and  $b_{\text{in}}$  and the outgoing fields  $a_{\text{out}}$  and  $b_{\text{out}}$ .

These mirrors allow external fields to enter the cavity and increase the number of photons inside. At the same time, photons within the cavity interact with the field amplitudes outside. The dynamics of the cavity annihilation operator  $a$  are governed by the quantum Langevin equation, following Ref. [19] as

$$\dot{a} = -\frac{i}{\hbar}[a, \mathcal{H}] - (\kappa_{\text{int}} + \kappa_1 + \kappa_2) a + \sqrt{2\kappa_1} a_{\text{in}} + \sqrt{2\kappa_2} b_{\text{in}}, \quad (2.54)$$

where the Hamiltonian of the cavity is just  $\mathcal{H} = \hbar\omega_c a^\dagger a$ , the cavity's internal loss rate is given by  $\kappa_{\text{int}}$  and we are using the coupling rates  $\kappa_1, \kappa_2$  to the impinging fields  $a_{\text{in}}, b_{\text{in}}$  at both ports. With the unitary transformation  $U = e^{i\omega_p a^\dagger a t}$  we can move into a frame rotating with the probe frequency  $\omega_p$ , where the transformed Hamiltonian is given by  $\tilde{\mathcal{H}} = U^\dagger \mathcal{H} U + i\hbar U^\dagger \frac{\partial U}{\partial t}$ . We then get the result

$$\dot{a} = -(i\Delta_c + \kappa_{\text{tot}}) a + \sqrt{2\kappa_1} a_{\text{in}}, \quad (2.55)$$

where  $\Delta_c = \omega_c - \omega_p$  is the detuning with respect to the probe frequency, the total loss rate is  $\kappa_{\text{tot}} = \kappa_{\text{int}} + \kappa_1 + \kappa_2$ , and we assume the cavity is driven only via one port such that  $b_{\text{in}} = 0$ . In the steady state  $\dot{a} = 0$ , the cavity amplitude becomes

$$a = \frac{\sqrt{2\kappa_1} a_{\text{in}}}{i\Delta_c + \kappa_{\text{tot}}}. \quad (2.56)$$

The in- and outgoing fields on both ports are related via

$$\begin{aligned} a_{\text{in}} + a_{\text{out}} &= \sqrt{2\kappa_1} a, \\ \underbrace{b_{\text{in}}}_{=0} + b_{\text{out}} &= \sqrt{2\kappa_2} a. \end{aligned} \quad (2.57)$$

We can therefore calculate the transmission  $|T|^2$  as the absolute squared ratio of input amplitude on one side over output amplitude at the other side as

$$|T|^2 = \left| \frac{b_{\text{out}}}{a_{\text{in}}} \right|^2 = \frac{4\kappa_1\kappa_2}{\Delta_c^2 + \kappa_{\text{tot}}^2}. \quad (2.58)$$

The resulting function is a Lorentzian with a half-width at half-maximum (HWHM) of  $\kappa_{\text{tot}}$ . We can relate the steady state cavity photon number  $n = |a^\dagger a|$  on resonance ( $\Delta_c = 0$ ) to the squared field amplitude  $|a_{\text{in}}|^2 = P_{\text{in}}/\hbar\omega_p$  in terms of the input power per photon of the probe frequency as

$$n = \frac{2\kappa_1}{\kappa_{\text{tot}}^2} \frac{P_{\text{in}}}{\hbar\omega_p}. \quad (2.59)$$

Here, we see that the cavity photons are maximized when the cavity is over-coupled such that external losses dominate the internal losses  $\kappa_{\text{ext}} = (\kappa_1 + \kappa_2) > \kappa_{\text{int}}$ . Conversely, they are minimized in the under-coupled regime when  $\kappa_{\text{ext}} < \kappa_{\text{int}}$ . In most cases, it is favorable to have an appreciable number of photons in the cavity (to interact with the spin ensemble), but at the same time, low total losses  $\kappa_{\text{tot}} = \kappa_{\text{int}} + \kappa_{\text{ext}}$  might be desirable, which makes the photons stay around for longer times, thereby amplifying the interactions. A suitable trade-off depends on the experimental requirements. In general, it is easier to tune the external coupling rates, for example by changing the length of microwave coupling pins, rather than the internal losses, which depend on the material properties of the cavity.

## 2.8 Maxwell-Bloch equations

Finally, we have almost all the ingredients to fully describe our system of  $N$  spins coupled to the cavity. The last step is to include the Hamiltonian for driving the cavity at frequency  $\omega_p$ , as given by

$$\mathcal{H}_{\text{drive}} = i\hbar\eta(a^\dagger e^{i\omega_p t} - a e^{-i\omega_p t}). \quad (2.60)$$

The driving amplitude  $\eta$  is related to the incident field at port 1 of the cavity from Eq. (2.55) above via  $\eta = \sqrt{2\kappa_1} a_{\text{in}}$ .

Now, we can calculate the equations of motion for the expectation values of cavity and spin operators in a frame rotating with the drive frequency. We use the Tavis-Cummings Hamiltonian (2.40) including the driving term (2.60) and the full Lindblad

operator (2.53) to incorporate losses. For these calculations, we utilize the definition for the expectation value of an observable  $A$  of the system  $\langle A \rangle = \text{Tr}(\rho A)$  and similarly for its time derivative  $\langle \dot{A} \rangle = \text{Tr}(\dot{\rho} A)$ . We also employ the commutator relations for the cavity,  $[a, a^\dagger] = 1$ , and the spin ladder operators,

$$[\sigma_+, \sigma_-] = \sigma_z \quad \text{and} \quad [\sigma_z, \sigma_\pm] = \pm 2\sigma_\pm, \quad (2.61)$$

along with the invariance of the trace under cyclic permutations. Then, after some juggling around we arrive at a set of equations that fully describe the dynamics of the system:

$$\langle \dot{a} \rangle = -(\kappa + i\Delta_c)\langle a \rangle + \sum_{j=1}^N g_j \langle \sigma_-^j \rangle + \eta \quad (2.62a)$$

$$\langle \dot{\sigma}_-^j \rangle = -(\gamma_\perp + \frac{\gamma_\parallel}{2} + i\Delta_s^j)\langle \sigma_-^j \rangle + g_j \langle a \sigma_-^j \rangle \quad (2.62b)$$

$$\langle \dot{\sigma}_z^j \rangle = -\gamma_\parallel(1 + \langle \sigma_z^j \rangle) - 2g_j (\langle a^\dagger \sigma_-^j \rangle + \langle a \sigma_+^j \rangle) \quad (2.62c)$$

Here, the detunings of the cavity  $\Delta_c = \omega_c - \omega_p$  and the  $j$ -th spin  $\Delta_s^j = \omega_s^j - \omega_p$  are both with respect to the drive frequency  $\omega_p$ . This is not a closed set of equations, as the second-order cumulants on the right-hand side are again expressed in terms of higher-order operators and so on, ad infinitum. Altogether, these never-ending coupled equations would contain the full quantum description of the system — but solving them all is impossible.

The simplest way of dealing with this issue is breaking the chain after the first link: we will use a semi-classical approximation by splitting the second-order cumulants into products of their first-order counterparts, neglecting higher-order correlations. The closed set of  $(2N + 1)$  equations attained in this way is known as the Maxwell-Bloch equations (MBE) of motion:

$$\langle \dot{a} \rangle = -(\kappa + i\Delta_c)\langle a \rangle + \sum_{j=1}^N g_j \langle \sigma_-^j \rangle + \eta \quad (2.63a)$$

$$\langle \dot{\sigma}_-^j \rangle = -(\gamma_\perp + \frac{\gamma_\parallel}{2} + i\Delta_s^j)\langle \sigma_-^j \rangle + g_j \langle a \rangle \langle \sigma_-^j \rangle \quad (2.63b)$$

$$\langle \dot{\sigma}_z^j \rangle = -\gamma_\parallel(1 + \langle \sigma_z^j \rangle) - 2g_j (\langle a^\dagger \rangle \langle \sigma_-^j \rangle + \langle a \rangle \langle \sigma_+^j \rangle) \quad (2.63c)$$

These equations form the basis for simulating the time evolution of the spin ensemble coupled to the cavity. Strategies for solving these equations in practice to model the experiment are discussed below.

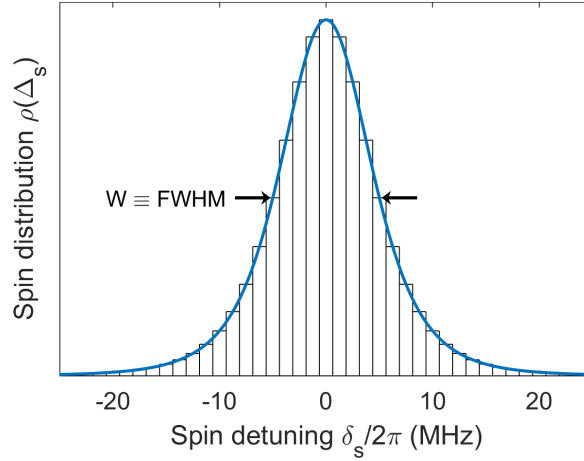


**Figure 2.8** Discretized  $q$ -Gaussian spin distribution.

### Numerical methods of solving the Maxwell-Bloch equations

As it is impractical to numerically solve a set of equations for  $5 \times 10^{12}$  spins — roughly the number of NV spins in our samples — we will make simplifying assumptions to bring the number of equations down to a solvable level: We assume a smooth distribution of spin frequencies represented by the function  $\rho(\omega_s)$ . This function is discretized into  $N_\rho$  spin packets, indexed by  $j$ , with weights  $\rho_j = \rho(\omega_s^j)$  sampled at the linearly spaced spin frequencies  $\omega_s^j = \bar{\omega}_s + \Delta_s^j$ , see Fig. 2.8. The discrete distribution is normalized to  $\sum_j^{N_\rho} \rho_j = 1$  and the sum over all spins in Eqs. (2.63) is replaced by  $\sum_j^N \rightarrow N_\rho \sum_j^{N_\rho} \rho_j$ . The cavity is designed to realize homogeneous single-spin couplings  $g_0$  throughout the sample volume, as detailed in Ch. 5. Then, the single-spin couplings  $g_j$  in Eq. (2.63a) can be factored out and replaced by  $g_\rho = g_{\text{coll}}/\sqrt{N_\rho}$ . Thus, spins that fall into the same frequency packet will behave identically, which reduces the number of coupled equations to  $2N_\rho + 1$ :

$$\langle \dot{a} \rangle = -(\kappa + i\Delta_c)\langle a \rangle + g_\rho N_\rho \sum_{j=1}^{N_\rho} \rho_j \langle \sigma_-^j \rangle + \eta \quad (2.64a)$$

$$\langle \dot{\sigma}_-^j \rangle = -(\gamma_\perp + \frac{\gamma_\parallel}{2} + i\Delta_s^j)\langle \sigma_-^j \rangle + g_\rho \langle a \rangle \langle \sigma_z^j \rangle \quad (2.64b)$$

$$\langle \dot{\sigma}_z^j \rangle = -\gamma_\parallel(1 + \langle \sigma_z^j \rangle) - 2g_\rho (\langle a^\dagger \rangle \langle \sigma_-^j \rangle + \langle a \rangle \langle \sigma_+^j \rangle) \quad (2.64c)$$

To model the spin distribution, we use a  $q$ -Gaussian function [20, 21]

$$\rho(\omega) = \left[ 1 - (1 - q) (\omega - \omega_0)^2 / \delta_q^2 \right]^{\frac{1}{1-q}}, \quad (2.65)$$

with  $\delta_q = W \sqrt{(q-1)/(2^{q-1}-1)}$ , where  $W$  is the full-width at half-maximum (FWHM). The parameter  $1 < q < 3$  influences the fall-off behavior to the sides of the distribution. A value of  $q = 1$  corresponds to a Gaussian,  $q = 2$  to a Lorentzian distribution, respectively. The value chosen in our models is  $q = 1.39$  following previous works on related systems [21, 22]. This exact choice is not as important for a steady-state description (a normal distribution works too) but leads to a better correspondence with the time-resolved dynamics. The set of differential equations (2.64) can now be efficiently solved numerically using the Runge-Kutta method [23] to simulate the system's evolution in time.

### Steady-state solution of the MBE

For extracting the relevant model parameters from the experiment, it is instructive to look at the steady-state solution of Eqs. (2.64). When the time derivatives on the left side become zero, these equations simplify to

$$\langle a \rangle = \eta \left[ (\kappa + i\Delta_c) - g_{\text{coll}}^2 \sum_j \rho_j \langle \sigma_z^j \rangle \frac{1}{\tilde{\gamma} + i\Delta_s^j} \right]^{-1}, \quad (2.66)$$

where we use the definition  $\tilde{\gamma} = \gamma_{\perp} + \frac{1}{2}\gamma_{\parallel}$ . In our system, we have  $\tilde{\gamma} \approx \gamma_{\perp}$ , as the NVs' decoherence rate  $\gamma_{\perp}$  is much faster than the spin-lattice relaxation  $\gamma_{\parallel}$ . Looking at this equation, we see that the spin ensemble's effect on the cavity amplitude vanishes (*i*) either when all  $\langle \sigma_z^j \rangle = 0$ , i.e. when the ensemble is in a completely mixed state (e.g. at higher temperatures or after a weak but long MW excitation pulse), or (*ii*) when the spin ensemble is far detuned such that all  $\Delta_s^j \gg g_{\text{coll}}$ . Then, Eq. (2.66) just describes the “empty” cavity's Lorentzian lineshape of width  $\kappa$ . In Fig. 2.9, we plot a simulated transmission spectroscopy measurement of the system in the ground state using Eq. (2.66), while the center spin frequency is varied across the cavity resonance frequency, corresponding to a magnetic field scan.

To better understand the effects of the other parameters, particularly the collective coupling  $g_{\text{coll}}$  and the spin-distribution width  $W$ , we plot the cavity transmission  $|T|^2 = |a|^2/\eta^2$  on resonance in Fig. 2.10(a,b). The system response exhibits a normal-mode splitting [c.f. Eq. (2.46)], with the two peaks separated by a frequency difference

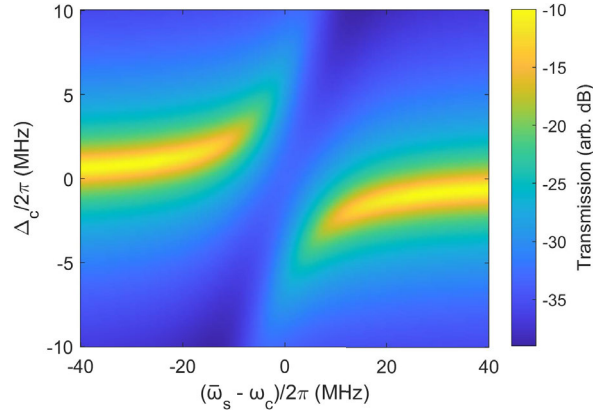


**Figure 2.9** Simulated transmission spectroscopy and magnetic field scan, i.e. the ground state polarized spins are tuned across the cavity resonance. The model parameters are  $g_{\text{coll}}/2\pi = 5$  MHz,  $\kappa/2\pi = 500$  kHz,  $W/2\pi = 10$  MHz,  $q = 1.39$ , and  $\tilde{\gamma}/2\pi = 159$  kHz.

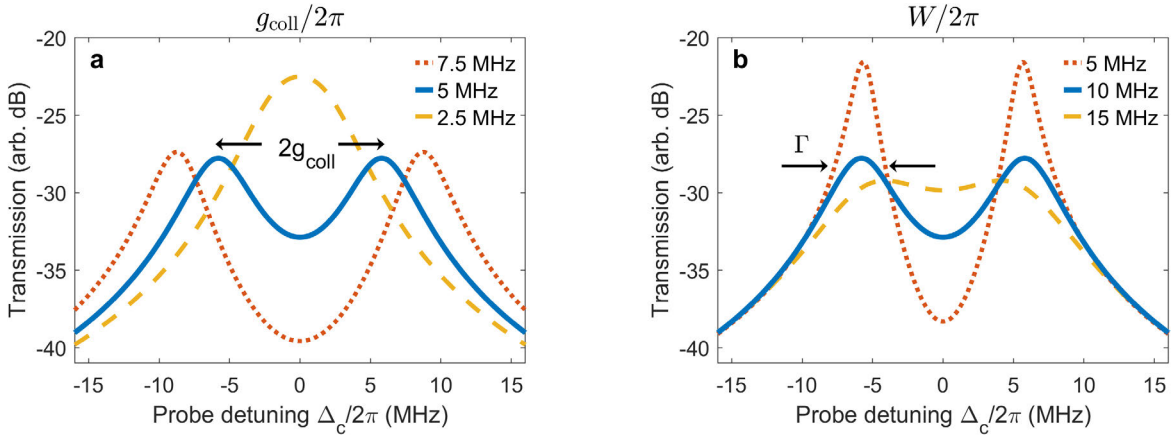


**Figure 2.10** Simulated cavity transmission on resonance  $\omega_c = \bar{\omega}_s$  using the steady-state solution of Eq. (2.66) with the spins in the ground state  $p = \langle \sigma_z^j \rangle = -1$ , varying  $g_{\text{coll}}$  in (a), and  $W$  in (b), while keeping other parameters fixed. (a) The collective coupling strength  $g_{\text{coll}}$  influences the peak-separation of the normal-mode splitting (the actual peak distance is exactly given by  $2g_{\text{coll}}$  only for a homogeneous system with  $W = 0$ ). (b) The peak widths are described by  $\Gamma$ , also referred to as the effective ensemble-linewidth, which is influenced by both the spin-distribution width  $W$  and the parameter  $\tilde{\gamma} = \gamma_{\perp} + \frac{1}{2}\gamma_{\parallel}$ .

of approximately  $2g_{\text{coll}}$ . The peak widths are determined by the effective ensemble-linewidth  $\Gamma$ , calculated as

$$\Gamma = \left[ \sum_j \rho_j \frac{1}{\tilde{\gamma} + i\Delta_s^j} \right]^{-1}. \quad (2.67)$$

In our case, the dominant contribution to this characteristic width  $\Gamma$  is the width of the inhomogeneously broadened spin distribution  $W \gg \gamma_{\perp}$ . An essential parameter characterizing the cavity-spin system is the cooperativity, defined as

$$C = \frac{g_{\text{coll}}^2}{\kappa\Gamma}. \quad (2.68)$$

This dimensionless parameter compares the rates of excitation exchange between the cavity and spins with the individual subsystem's loss rates due to dissipation and dephasing. When  $C > 1$ , the normal modes are split into two distinct peaks, and the system is said to be in the strong coupling regime.

## 2.9 Superradiance

We continue discussing a collective spin decay as a cascade through the highly symmetric subspaces — the superradiant states — of the Dicke ladder, right where we left off in Sec. 2.5.1. This collective decay, accompanied by a strong burst of emitted light, was initially predicted by Dicke in 1954 [9] and is known as a superradiant decay. A handy theory resource is the review paper by Gross and Haroche [10]. First, we will take a step back and focus on the most essential ingredients for superradiant emission, offering a qualitative description. For this, we only need a collection of  $N$  excited emitters coupled to a common mode, with the simplest case being the always-present vacuum.

The superradiant decay of this fully excited state will start with the spontaneous emission of a single photon, which has an equal probability of being emitted by any one spin — causing the total emission rate to initially scale as the number of spins  $\Upsilon \propto N$ . Now, the presence of this photon is “felt” by all the other spins and leads to the stimulated emission of other photons — generating a photon avalanche. The collective emission will speed up as long as there are more excited spins than already de-excited ones. It reaches its maximum  $\Upsilon \propto N^2$  when the collective spin vector is at the equator of the giant Bloch sphere, where the number of up-spins equals the number of down-spins. This process is depicted in Fig. 2.11(b), where a dense atomic cloud is fully excited at  $t = 0$ : The first few photons are emitted spontaneously, possibly into different competing modes (i.e. directions and frequencies). After a short period, one

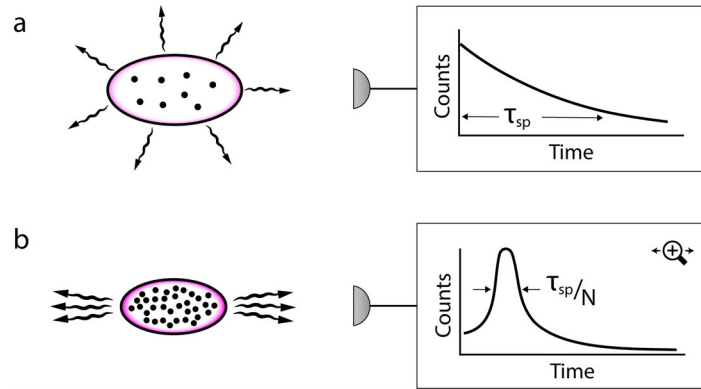


**Figure 2.11** Collective decay as the essence of superradiance: A cloud of emitters — or spins — is initialized in an excited state at  $t = 0$ . (a) When the cloud is dilute, the spins are essentially non-interacting and decay individually through spontaneous emission with the time constant  $\tau_{\text{sp}}$  by weakly coupling to the electromagnetic modes of the vacuum. (b) When the cloud is dense, the decay becomes a collective effect, accompanied by spontaneous synchronization mediated via coupling to a common mode and a speed up of the collective emission process. Figure adapted from the seminal review paper on superradiance by Gross and Haroche, Ref. [10].

of the modes will dominate and an intense burst of light is generated. If the ensemble of emitters has an elongated shape, the dominant mode aligns with this axis, and the emitted light will be directed accordingly. In some aspects, the physics of superradiance has similarities to laser physics, which also involves the synchronization of all atoms in the active medium. A key difference is that this synchronization in a conventional laser is enabled by a large number of photons in the cavity radiation field, whereas in superradiance, the coherence will be generated through the collective behavior of the excited emitters themselves.

When considering the initial fluctuations triggering the avalanche effect, we can interpret the superradiant decay as undergoing a transition from a regime dominated by quantum effects — the spontaneous emission of the first photon — to a classical regime, involving the formation of a macroscopic dipole that emits a strong burst of light. As will be discussed in Ch. 6, we realized an experiment to study the triggering of a superradiant decay using a weak microwave pulse and explore the high sensitivity offered via the amplification through the avalanche process.

The superradiant emission requires the indistinguishability of individual emitters — a necessary condition during the decay, which can only create a photon cascade when the permutation symmetry of the spin state is preserved, as discussed in Sec. 2.5.1. Only then can the amplitudes of individual emitters  $g_0 a^\dagger \sigma_-^j$  interfere constructively

and synchronize collectively. Notably, not only the Dicke states enable a theoretical description of the transition from a linear  $N$  to a quadratic  $N^2$  scaling of the superradiant decay process akin to Eq. (2.49). Also, a description in terms of spin-coherent states — the same key ingredient being indistinguishability and, thus the permutation-symmetric nature of the states — can capture these essential dynamics. The spin-coherent states are generated by the operator [24]

$$R(\vartheta, \varphi) = e^{(\zeta S_+ - \zeta^* S_-)}, \quad \text{with} \quad \zeta = \frac{1}{2}\vartheta e^{-i\varphi}, \quad (2.69)$$

using the spin ladder operators  $S_{\pm}$ . These states are coherent superpositions of Dicke states and are constructed analogously to the coherent states of the photon field [with the displacement operator (2.19) acting on the vacuum state  $|0\rangle$ ]. Spin-coherent states are generated when a classical light field interacts with a spin ensemble, causing a spin-rotation when acting on the “spin-vacuum” state, i.e. all spins down. For example, when  $\varphi = 0$ ,

$$\begin{aligned} |\Psi\rangle &= R(\vartheta, 0) |\downarrow\downarrow \dots \downarrow\rangle = e^{i\vartheta S_y} |\downarrow\downarrow \dots \downarrow\rangle \\ &= \prod_j^N \left( \cos(\theta/2) |\downarrow\rangle_j + i \sin(\theta/2) |\uparrow\rangle_j \right). \end{aligned} \quad (2.70)$$

This state, being a product state, does not exhibit any correlations between individual spins — it has no entanglement. Nevertheless, it has the required symmetry for a superradiant decay as the permutation of two spins leaves the state unchanged. In this sense, superradiance, with its hallmark  $N^2$  scaling of the maximum emitted intensity, is not inherently a quantum effect but an interference phenomenon arising from the collective decay of indistinguishable emitters.

The condition on symmetry preservation during the superradiant decay explains the requirement of a “dense” atomic cloud in Fig. 2.11(b). When the cloud is confined to a small volume  $V$ , symmetry-breaking effects such as the retardation of light, which introduces phase changes for individual spin processes, can be neglected. Therefore, a simplified condition for free-space superradiance is usually formulated as  $V \ll \lambda^3$ , where  $\lambda$  is the wavelength of the emitted light. In real examples of physical systems, there can be many effects that actively work against superradiance, dependent on the physical system. These effects include, for example, Doppler broadening in atomic gases, dipole-dipole interactions between emitters, limited lifetimes and decoherence, or other atomic transitions and modes of decay, just to name a few. Superradiance has been studied in a myriad of physical systems, e.g. ordered arrays of atoms [25],

quantum dots [26], atomic beams [27], cold atoms systems [28], atoms near optical nanofibers [29], and astrophysical masers [30].

### Superradiant threshold condition

In our system of a spin ensemble coupled to a microwave cavity, several processes compete with the superradiant decay, and have already been introduced above: photon loss with rate  $\kappa$ , and the ensemble dephasing with rate  $\Gamma$  — summarizing both the effects of inhomogeneous broadening and the individual spin decoherence rate  $\gamma_{\perp}$ . The key process to enable superradiance is the collectively enhanced coupling  $g_{\text{coll}} = g_0\sqrt{N}$  to the cavity mode. It is, therefore, natural to expect the cooperativity parameter  $C = g_{\text{coll}}^2/\kappa\Gamma$  to show up in a threshold condition for superradiance. We derive this threshold following Ref. [31]: Assuming an initial state of the spin ensemble with homogeneous polarization  $p = \langle\sigma_z^j\rangle > 0$  and zero transversal spin components  $\langle\sigma_{\pm}^j\rangle = 0$ , as well as no photons in the cavity, we insert Eq. (2.64b) above into Eq. (2.64a) (with no external cavity drive  $\eta = 0$  and on resonance  $\Delta_c = 0$ ):

$$\langle\dot{a}\rangle = \kappa\langle a\rangle \left( p \underbrace{\frac{g_{\rho}^2 N_{\rho}}{\kappa} \sum_j \rho_j \frac{1}{\tilde{\gamma} - i\Delta_s^j}}_{g_{\text{coll}}^2/\kappa\Gamma = C} - 1 \right) - g_{\rho} N_{\rho} \sum_j \rho_j \langle\dot{\sigma}_{-}^j\rangle \frac{1}{\tilde{\gamma} - i\Delta_s^j} \quad (2.71)$$

Under a quasi-steady slow initial evolution of the system from this meta-stable state, with  $\langle\dot{\sigma}_{-}^j\rangle \approx 0$ , we can interpret the expression in the large round brackets as a necessary condition on the stability of the inverted ensemble: in the case  $pC < 1$ , the cavity amplitude  $\langle a\rangle$  does not grow, and the system self-stabilizes due to the dephasing  $\Gamma$  and dissipation  $\kappa$  winning over the rate of energy exchange  $g_{\text{coll}}$ . By inverting this condition we arrive at a threshold definition for spontaneous superradiance — meaning that any fluctuation of the system will trigger a superradiant decay:

$$pC > 1 \quad (2.72)$$

We find that a cooperativity  $C > 1$  — the system being strongly coupled — is a necessary condition, as the inversion  $p$  is bounded by  $-1 \leq p \leq 1$ . However, for a system to exhibit spontaneous superradiance the system also needs a minimum homogenous inversion  $p > 1/C$ . We can drop the requirement on homogeneity of the

inversion by employing a generalization

$$\overline{pC} = N_\rho \sum_j \rho_j \langle \sigma_z^j \rangle C_j, \quad (2.73)$$

using the spin frequency distribution  $\rho_j$ , where we have introduced the definition of single-spin cooperativities

$$C_j = \frac{g_\rho^2}{\kappa} \left| \frac{1}{\tilde{\gamma} - i\Delta_s^j} \right| = \frac{g_\rho^2}{\kappa} \left( \tilde{\gamma} + \frac{\Delta_s^{j2}}{\tilde{\gamma}} \right)^{-1}. \quad (2.74)$$

These frequency-dependent contributions to the total cooperativity  $C = N_\rho \sum_j \rho_j C_j$  are peaked for spins with zero detuning  $\Delta_s^j$ . As expected, spins that are closer to the center frequency contribute more to the threshold for spontaneous superradiance

$$\overline{pC} > 1. \quad (2.75)$$

Below this threshold, the formation of a collective dipole  $|S_-|$  during the superradiant decay is hindered via dissipation through  $\Gamma$  and  $\kappa$ .

### Delay time of the superradiant emission

We now turn our attention to the delay time of the superradiant burst. This delay time is defined as the time it takes for the superradiant emission to reach its maximum amplitude  $\max(|a|)$  when starting from an inverted state with an initial tipping angle  $\theta = \arctan(|S_-|/S_z)$  and no cavity photons  $|a| = 0$ . To derive an analytic result, we start with a major simplification of the system, now recalling the Hamiltonian (2.42), where inhomogeneous broadening is neglected and the spin system can be accurately described by the collective operators  $S_z$  and  $S_\pm$ . The Heisenberg-Langevin equations of motion are given by

$$\dot{a} = -\kappa a + g_0 S_-, \quad (2.76a)$$

$$\dot{S}_- = -\gamma_\perp S_- + g_0 a S_z, \quad (2.76b)$$

$$\dot{S}_z = -g_0 (a^\dagger S_- + a S_+). \quad (2.76c)$$

Here, we assume the system is on resonance  $\Delta_c = \Delta_s = 0$ , is not driven  $\eta = 0$ , and has infinite spin lifetime  $\gamma_\parallel = 0$ . Inserting Eq. (2.76a) into Eq. (2.76c), we arrive at the result

$$\dot{S}_z = -\frac{g_0^2}{\kappa} (S_+ S_- + S_- S_+) - \frac{i g_0}{\kappa} (S_+ \dot{a} - \dot{a}^\dagger S_-). \quad (2.77)$$

Now, we will neglect the term on the right, assuming that  $\dot{a} \approx 0$ . This assumption is known as the *fast* cavity limit — photons leave the cavity on a faster timescale than the decaying spin system generates them. While not technically true for our system, this simplification offers an easy way to derive an analytic expression of the delay time — which is later confirmed by numerical simulations. By using this approximation, we ignore the cavity backaction on the spins, which becomes important for the dynamics only at later times. As we will see, the cavity will act as a reservoir and cause the energy emitted during the superradiant decay to oscillate back and forth between the two subsystems. Continuing the derivation, we assume the system is in a state  $|J, M\rangle$ , where  $J \gg 1$  and the time-ordering of the operators is not crucial, and evaluate

$$\langle \dot{S}_z \rangle = -\frac{2g_0^2}{\kappa} \langle S_+ S_- \rangle. \quad (2.78)$$

We parametrize the initial  $z$ -projection  $\langle S_z \rangle = M = J \cos(\theta)$  with the tipping angle  $\theta$  at time  $t = 0$ , further using a magnitude of the giant spin vector  $J = pN/2$  dependent on the initial polarization. Then, utilizing Eq. (2.43), we get

$$\frac{d\langle S_z \rangle}{dt} = -\frac{2g_0^2}{\kappa} (J + \langle S_z \rangle)(J - \langle S_z \rangle + 1). \quad (2.79)$$

We solve<sup>2</sup> for the delay time  $t_D$ , where the emitted intensity is maximum and the spin state points towards the equator of the Bloch sphere such that  $\langle S_z \rangle = 0$ . We end up with the result

$$t_D = t_0 - \frac{\kappa}{2g_0^2 N} \frac{1}{p} \log \left( \tan^2 \left( \frac{\theta}{2} \right) \right). \quad (2.80)$$

As a last step, we linearize  $\tan(\theta/2) \approx (\theta/2)$  and neglect the constant time offset to arrive at our final result

$$t_D = -2T_R \frac{1}{p} \log \left( \frac{\theta}{2} \right), \quad (2.81)$$

where we introduce the superradiant timescale  $T_R = \frac{\kappa}{2g_{\text{coll}}^2}$  following Refs. [10, 27].

Finally, we note that the prefactor  $2g_0^2/\kappa$  in Eq. (2.78) represents the Purcell enhancement [32], which describes the enhancement of the single spin spontaneous

<sup>2</sup>Using shorthand notation  $z = \langle S_z \rangle$  the result of Eq. (2.80) follows via

$$t_D - t_0 = -\frac{\kappa}{2g_0^2} \int_{z=J \cos(\theta)}^{z=0} dz \frac{1}{(J+z)(J-z+1)} = -\frac{\kappa}{2g_0^2} \frac{1}{2J} \log \left( \frac{1 - \cos(\theta)}{1 + \cos(\theta)} \right),$$

in the limit of large  $J \gg 1$ .

emission rate due to the coupling to the resonant cavity mode (as opposed to the vacuum field).

### Comparison with numerical simulations

Let us now compare these results with numerical simulations using the Maxwell-Bloch equations (2.64). With these simulations, we include inhomogeneous broadening and the cavity's backaction on the spins, using the same parameters as in the experiment.<sup>3</sup> We initialize all spins with uniform initial inversion  $\langle \sigma_z^j \rangle = p$  and a small tipping angle<sup>4</sup>  $\theta = \arctan(|S_-|/S_z)$  and then numerically evolve the system in time, plotting the simulated cavity amplitude  $|a|$  in Fig. 2.12(a,b).

The first noticeable difference to the “textbook” superradiant decay illustrated in Fig. 2.11 — which shows a single burst — is that each simulated decay has multiple peaks. These peaks correspond to the emitted photons being reabsorbed by the spins and oscillating back and forth between cavity and spins multiple times before being gradually lost due to dissipation and dephasing. They are, essentially, damped Rabi oscillations between the two subsystems with the oscillation frequency  $\Omega$ , appearing because the cavity acts as a reservoir for the photons emitted by the spin ensemble when we are not in the fast cavity limit.

We will now analyze the simulation runs and discuss several observations, where the simulated system's behavior either confirms or deviates from the simplified theory expectation Eq. (2.81). For these comparisons, we extract three parameters from the simulations, including the maximum cavity amplitude  $\max(|a|)$ , the time of its appearance defined as the delay time  $t_D$ , and the inverse time between consecutive cavity maxima, defined as the Rabi frequency  $\Omega$ . We then will fit these extracted parameters with simple polynomial functions and discuss the observed trends.

In Fig. 2.12(a), where the initial inversion  $p$  is varied and the tipping angle is fixed, we see a confirmation of the threshold behavior  $pC > 1$  — when the initial inversion approaches this threshold, the emitted pulses become weaker and appear at later times — below it, a superradiant decay would eventually not be able to form. From the polynomial fit, we see that the delay time  $t_D$  is inversely proportional to  $x = p - 1/C$ , where the minimum inversion threshold is subtracted from  $p$  to

<sup>3</sup>The parameters are determined for the N-diamond sample coupled to the DCR cavity as  $g_{\text{coll}}/2\pi = 4.6$  MHz,  $\kappa/2\pi = 420$  kHz,  $W/2\pi = 9.2$  MHz,  $q = 1.39$ ,  $\gamma_{\perp}/2\pi = 177$  kHz and  $\gamma_{\parallel} = 0$ , see steady-state coupling fit in Fig. 6.5(b).

<sup>4</sup>If the tipping angle was exactly zero, the equations would not show any decay — all spins would stay perfectly upright. In a real experiment, there is always a noise source present (e.g. thermal and/or quantum fluctuations) that would eventually trigger a superradiant decay.

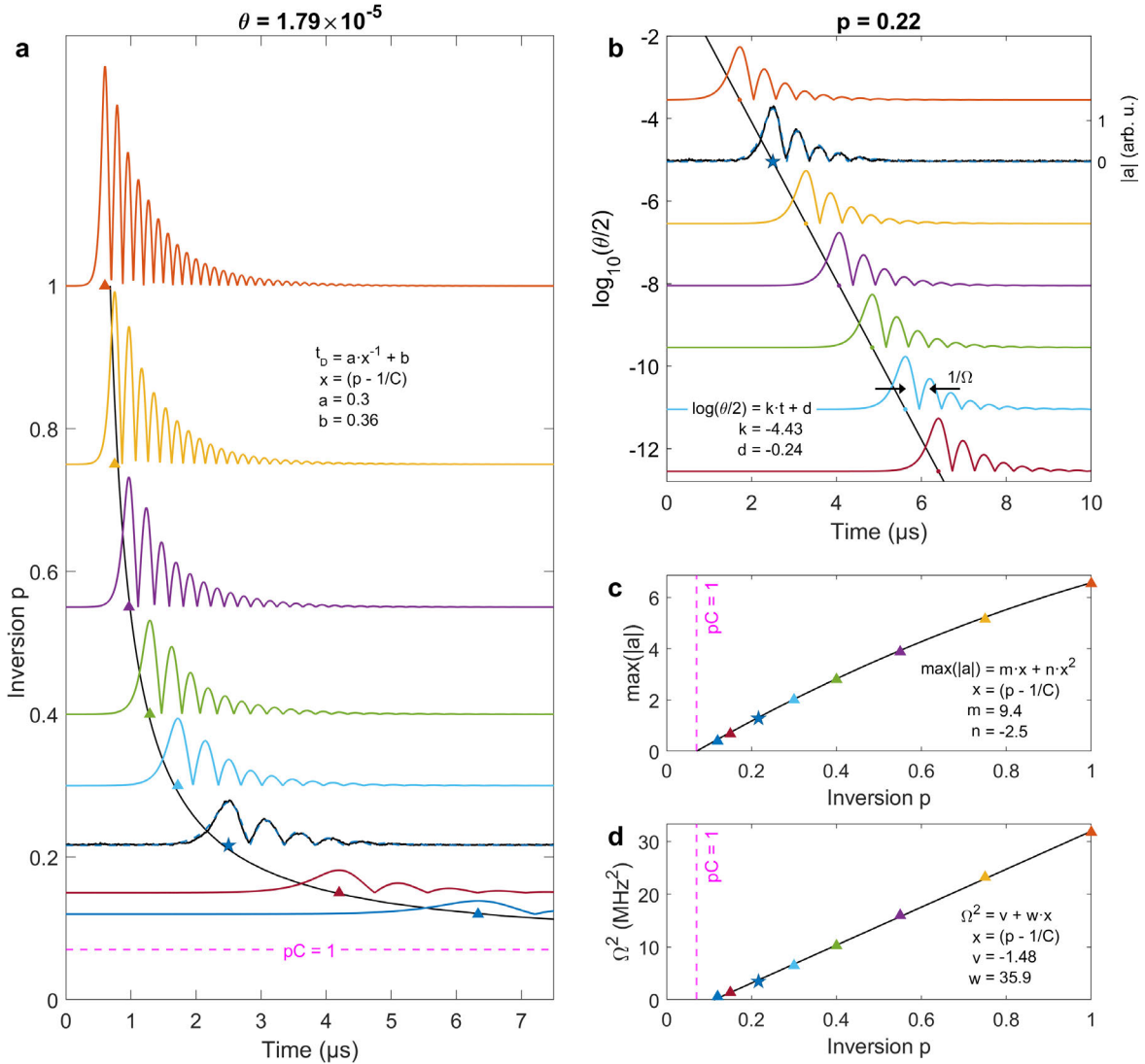


**Figure 2.12** Numerical simulations of superradiant decay using model parameters as determined from the experiment. The signal marked with a blue star in (a,b) is a single-shot time-resolved measurement — the experimental data (black line) is overlaid with the simulation result (dashed blue line). (a) Scan of  $p$  for fixed tipping angle  $\theta$ . The  $y$ -axis offset corresponds to the value of  $p$  in the simulation. (b) Logarithmic scan of tipping angle  $\theta$  for fixed  $p$ , confirming the linear dependence of the delay time  $t_D \propto -\log(\theta/2)$ . In (c), the maximum cavity amplitude  $\max(|a|)$  in arbitrary units as determined from the runs shown in (a), is plotted against the inversion  $p$ . Similarly, in (d), the squared frequency  $\Omega^2$  of the damped Rabi oscillations [graphically defined in (b)] is plotted against  $p$ .

recreate the delay time divergence to infinity when  $p = 1/C$ . This precisely follows the expected behavior  $t_D \propto -1/p$  from Eq. (2.81). Along the same lines, the logarithmic dependence  $t_D \propto -\log(\theta/2)$  is perfectly confirmed by the simulation runs with fixed  $p$  in Fig. 2.12(b).

Another expectation is confirmed, at least to a high degree, when we plot the maximum cavity amplitude of the numerical runs against the initial inversion in Fig. 2.12(c), and observe an almost linear relationship,  $\max(|a|) \propto p$ . This is, essentially, the hallmark  $N^2$  scaling of the emitted intensity, as quantified by the maximum photon number  $|a|^2$  in a superradiant decay, where the number of participating spins is directly proportional to  $p$ . Not reverting to previous definitions, we can also motivate this expectation with a simple argument: When the cavity amplitude reaches its maximum, its change  $\langle \dot{a} \rangle = 0$  becomes zero. Rearranging Eq. (2.76a), we get  $\langle a \rangle \propto S_-$ . The cavity amplitude is, therefore, proportional to the transversal component of the collective spin vector. However, this vector's initial orientation was along  $+z$ , and its length corresponded to the initial inversion  $p$ , subsequently having performed a rotation towards the equator during the superradiant decay. This establishes the expected dependence  $\max(|a|) \propto p$ . Notably, this argument also works for the inhomogeneously broadened case, where the collective spin vector would experience a length reduction due to fanning out of fast and slow spins during the decay process, which nonetheless is always proportional to its starting length and does not change our result. The deviations from the ideal superradiant emission where  $\max(|a|) \propto p$ , particularly for higher values of  $p$ , can be explained by the cavity backaction on the spins. Faster dynamics of  $|a|$  and  $S_-$  occur with higher  $p$ , making the system deviate from the adiabatic approximation  $\dot{a} \approx 0$  (i.e., the fast cavity limit).

Next, we look at the Rabi frequency  $\Omega$  extracted from the simulations [how it is extracted can be seen in Fig. 2.12(b)], plotted against the initial inversion  $p$  in Fig. 2.12(d). A natural assumption is that this frequency is proportional to the collective coupling strength  $g_{\text{coll}} = g_0\sqrt{N}$ . By definition, this coupling strength describes the rate of energy exchange between the two subsystems of cavity and spins. When including the inversion  $p$  in this picture, it should appear as a square root — in the same way as the number of spins  $N$  would — leading to our expectation  $\Omega \propto \sqrt{p}$ , or this expression squared:  $\Omega^2 \propto p$ , as shown in the plot. The slight rightward shift of the linear fit towards higher inversion than the threshold value of  $p = 1/C$  is attributed to the fact that the oscillation frequency  $\Omega$  is somewhat ill-defined in the regime of a critically damped emission, particularly when the inversion is only slightly above the minimum threshold.

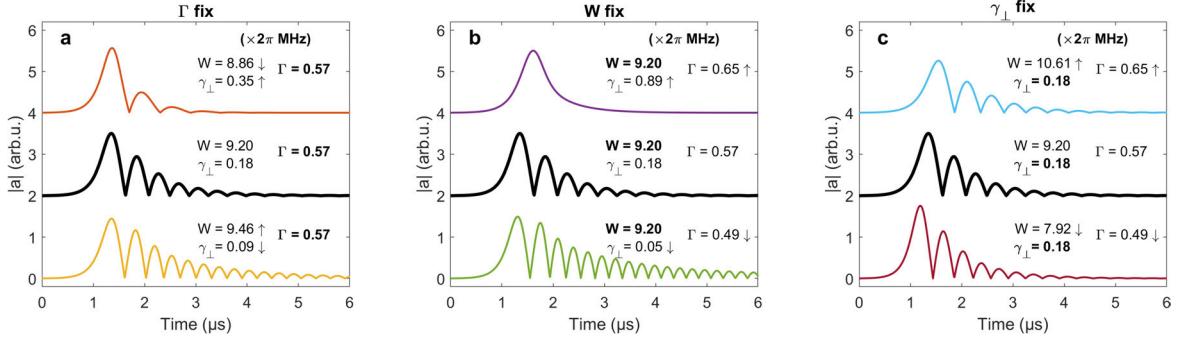


**Figure 2.13** Simulated superradiant decays with initial inversion  $p = 0.25$ , comparing different combinations  $W$ ,  $\gamma_{\perp}$ , and  $\Gamma$ . In the three panels, the middle row is identical, and one of the parameters is always fixed, while the remaining two are varied. Other simulation parameters as used for Fig. 2.12.

Finally, to further explore the influence of inhomogeneous broadening  $W$  and single spin dephasing  $\gamma_{\perp}$ , and how these two are combined in the effective ensemble linewidth  $\Gamma$ , we compare superradiant decay simulations for different combinations of these parameters in Fig. 2.13. For fixed  $\Gamma$  [but increasing  $\gamma_{\perp}$  while decreasing  $W$ , or vice versa, see Fig. 2.13(a)] we observe a very similar behavior of the first cavity peak. This is consistent with the threshold formula for the superradiant decay  $p = 1/C$ , which depends only on  $\Gamma$  (via  $C = g_{\text{coll}}^2/\kappa\Gamma$ ) and not on the specific values of  $W$  and  $\gamma_{\perp}$ . However, the later dynamics of the damped Rabi oscillations differ significantly under varying combinations of these parameters, see also Figs. 2.13(b,c). As we will discuss in Ch. 6, the spin distribution width  $W$  can be measured directly and independently. The parameter  $\gamma_{\perp}$  is then estimated by adjusting the simulations to align with the experimentally observed superradiant decay dynamics.

To summarize, the numerical simulations confirm the delay time formula (2.81). In place of the initial inversion  $p$ , the numerical results suggest using a value of  $p - 1/C$ , reduced by the superradiant threshold  $p = 1/C$  for an inhomogeneously broadened spin system. This comes as no surprise, as the simplified derivation of Eq. (2.81) above neglects all effects that would keep a giant spin of any non-zero positive inversion from decaying via a superradiant burst.

We conclude our discussion on superradiant decay here and will revisit this topic when discussing the experiments in Ch. 6.



# Chapter 3

## Experimental Setup and Instrumentation

### *Using fridges and microwaves*

This chapter provides an overview of our experimental setup, beginning with an introduction to our cryogenic systems. We then discuss the microwave devices and techniques used for both spectroscopic and time-resolved measurements, concluding with a pulse power (photon number) characterization.

### 3.1 Cryostats

#### Dilution fridge

The main experiments discussed in this thesis are carried out at extremely low temperatures in the millikelvin range, achieved using a dilution refrigerator (Oxford Instruments, model Triton 400), see Fig. 3.1. A low-temperature environment is essential for initializing our spin system in the ground state and minimizing thermal noise. To maintain minimal thermal contact with the outside, the fridge has to maintain a vacuum inside. It is constructed from several temperature stages (concentric cylinders) with limited thermal contact between them, creating a stepwise temperature gradient from the lowest temperature at the core to room temperature at the outermost layer [nominal temperature values for each stage are shown in Fig. 3.1(left)].

A dilution fridge's operation relies on the properties of a  $^3\text{He}/^4\text{He}$  mixture at low temperatures, contained in a separate closed tubing system extending from the room-temperature environment into the cryostat's vacuum chamber. Below a critical

temperature of 870 mK, the  $^3\text{He}/^4\text{He}$  mixture undergoes phase separation, forming a  $^3\text{He}$ -rich phase and a  $^3\text{He}$ -dilute phase. The core of the cooling process occurs in the mixing chamber, where these two phases meet. By continuously removing  $^3\text{He}$  from the dilute phase through pumping (using two turbo pumps outside the fridge),  $^3\text{He}$  from the rich phase is forced to cross the phase boundary to maintain equilibrium. This process of  $^3\text{He}$  moving from the concentrated phase to the dilute phase absorbs heat, cooling the system [33]. A key advantage of this system is its ability to provide continuous cooling: A minimum concentration of roughly 6.5%  $^3\text{He}$  will always remain in the dilute phase, even as temperatures approach absolute zero. Our dilution fridge can reach a minimum temperature of 24 mK (which is actually the minimum displayed value, the real temperature could be slightly lower), limited by the small but unavoidable heat influx from the environment.

To reach the low temperature required for this  $^3\text{He}/^4\text{He}$  cooling mechanism to work, the fridge is equipped with additional cooling systems: a pulse tube cooler [34] for reaching down to around 2.7 K, and the Helium gas itself. Even above the condensation temperature, the system can achieve cooling through compression and expansion of the gas mixture, similar to a conventional fridge.

The fridge's multiple temperature stages are also used to mount the coaxial MW wires (50  $\Omega$  impedance) and various active and passive MW components to control the MW signals entering and exiting the cavity-spin system. These cables are made from either steel (with better thermal isolation) or copper (lower absorption losses). To reduce heat intake on the lower stages and allow for thermal expansion and contraction, the cable routing includes additional bends, extending the heat gradient over longer distances. The total cable length of roughly 1.5 m for each line inside the fridge adds approximately 10 dB of attenuation.

Passive components include attenuators, MW isolators, and a DC block (essentially a tiny capacitance for both inner and outer conductors between coaxial wires), all used to provide thermal photon isolation. We also employ a power splitter to connect cavity port 2 to both the probe and out-line. Active components inside the fridge include a low-noise amplifier in the out-line and a high-isolation MW relay switch in the pump-line. More details on the MW setup are provided below.

The cavity box is placed within a vector magnet mounted at the coldest temperature stage. This vector magnet consists of three intermeshed Helmholtz coils (a home-built setup using superconducting NbTi wire). A crucial aspect of the magnet setup is the heat-anchoring of its wires at every temperature stage. The wire is wrapped around small copper cylinders multiple times to ensure good thermal contact.

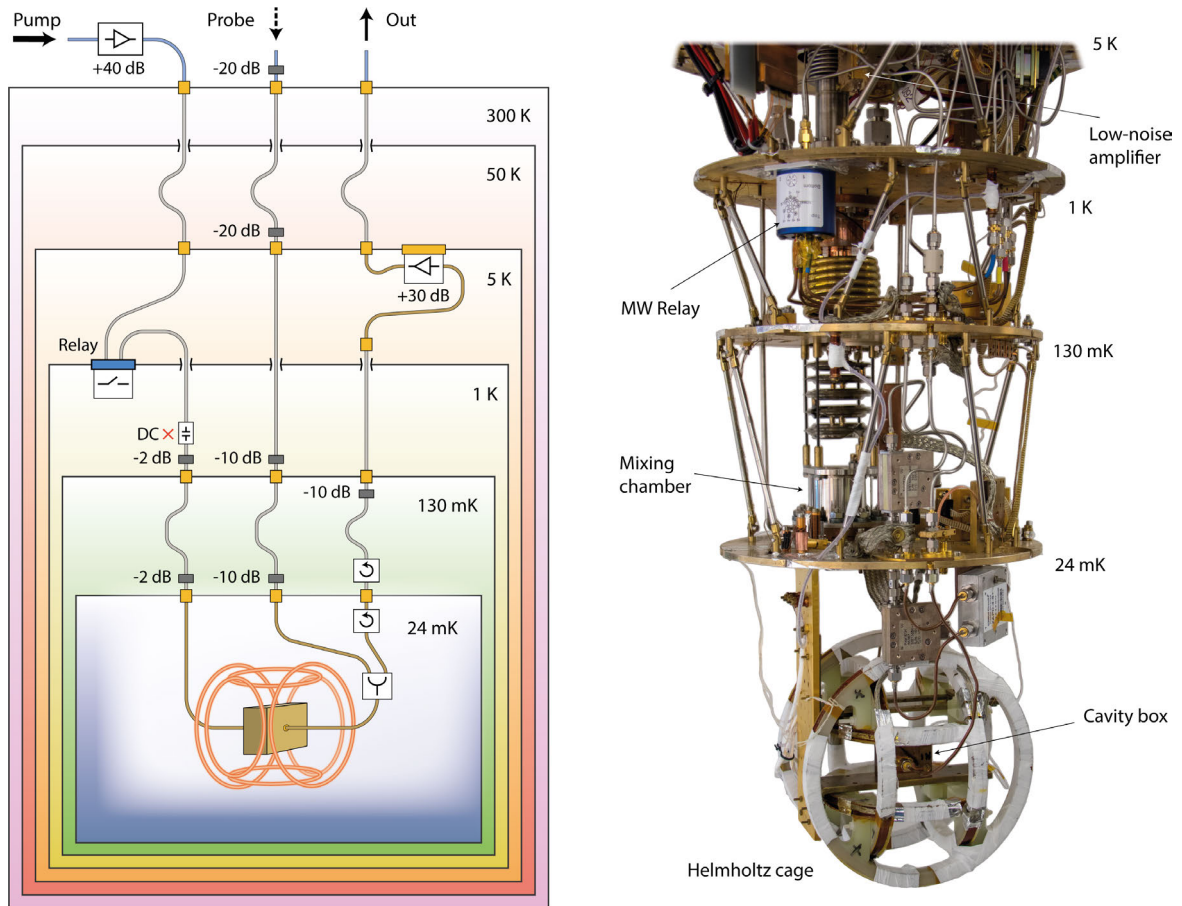


**Figure 3.1** The dilution fridge and its temperature stages. (Left) The cavity box, housed within a vector magnet (Helmholtz coils along  $x$ ,  $y$ , and  $z$ -axes), is located at the lowest stage (24 mK). Three MW lines (pump, probe, and out-line) connect to the lowest stage, assembled from steel and copper coaxial wires with various passive elements: attenuators (dark gray), DC block, power splitter/combiner (Y-shape), and isolators (round arrow). MW inversion pulses sent through the pump-line to cavity port 1 are amplified by a high-power amplifier (+40 dB, right outside the fridge), with a solenoid switch at the 1 K stage acting as a MW relay. Cavity port 2 connects via a splitter to the probe line (for applying weak pulses) and the out-line, which carries the measurement signal, amplified by a low-noise amplifier (+30 dB) at the 5 K stage. (Right) Photograph of the dilution fridge's insides.

## Adiabatic demagnetization refrigerator

For some of the experiments, particularly those focused on cavity characterization and collective coupling measurements, we employ a different cryostat: a pulse-tube pre-cooled Adiabatic Demagnetization Refrigerator (ADR, HPD Model 103 Rainier). This system operates based on the magnetocaloric effect. In contrast to the continuous cooling offered by the dilution refrigerator, the ADR provides non-continuous cooling in a single-shot mode down to a slightly higher minimum temperature of around 50 mK. Each cooling cycle takes approximately 1 h, followed by a gradual warm-up over several hours. The microwave setup in the ADR is similar to that of the dilution fridge but simpler, consisting of only a single microwave input and output line. This configuration is primarily used for spectroscopy measurements, where the system is kept in a steady state.

## 3.2 Microwave techniques

### 3.2.1 IQ-mixing

As we have seen in Sec. 2.8 of the last chapter, our hybrid system is governed by transition frequencies of the cavity and of the spin ensemble,  $\omega_c$  and  $\bar{\omega}_s$ , respectively. Although these frequencies in our experiments are in the gigahertz range, with  $\omega_c \approx \bar{\omega}_s \approx 2\pi \times 3$  GHz, the relevant dynamics occur in the rotating frame with rates of change given by their mutual detunings  $\Delta_{sc} = \bar{\omega}_s - \omega_c$ , which are in the megahertz range — three orders of magnitude slower. Consequently, to control our system in practice, the modulation of external MW drives needs to occur only over a timescale of microseconds. This is where IQ mixing becomes essential.

IQ mixing employs a high-frequency signal that is modulated in time — including both amplitude and phase modulation — on a slower timescale (the baseband) using two inputs: the in-phase component  $I(t)$ , and the quadrature component  $Q(t)$ . Given the widespread use of gigahertz frequencies in modern technology, such as cellphone networks, devices for signal synthesis are readily available. In practice, an IQ mixer is a simple building block featuring four ports for coaxial connections: the Local Oscillator (LO) port, which carries the continuous wave high-frequency signal; the I and Q ports, used for modulating the signal; and the output port, where the upconverted signal exits.

Mathematically, the process of IQ mixing can be formulated as follows:

$$s(t) = I(t) \cos(\omega_{\text{LO}}t) - Q(t) \sin(\omega_{\text{LO}}t) \quad (3.1)$$

Here,  $s(t)$  is the output signal,  $\omega_{\text{LO}}$  is the frequency of the local oscillator, and  $I(t)$  and  $Q(t)$  are the in-phase and quadrature components, respectively. Let us now go through the down-conversion step, where the same operation as Eq. (3.1) is effectively performed in reverse. The signal  $s(t)$  is mixed separately with the in-phase and quadrature components of the same local oscillator frequency,  $\sin(\omega_{\text{LO}}t)$  and  $\cos(\omega_{\text{LO}}t)$ , respectively — this is essentially called a homodyne detection scheme. For the in-phase component, one of the two output channels of the down-conversion operation, we get:

$$\begin{aligned} I'(t) &= s(t) \cdot \cos(\omega_{\text{LO}}t) \\ &= I(t) \cos^2(\omega_{\text{LO}}t) - Q(t) \sin(\omega_{\text{LO}}t) \cos(\omega_{\text{LO}}t). \end{aligned} \quad (3.2)$$

We will use these trigonometric identities:

$$\begin{aligned} \cos \alpha \cos \beta &= \frac{1}{2} [\cos(\alpha + \beta) + \cos(\alpha - \beta)] \\ \sin \alpha \cos \beta &= \frac{1}{2} [\sin(\alpha + \beta) + \sin(\alpha - \beta)] \end{aligned} \quad (3.3)$$

Substituting these, we continue as

$$I'(t) = I(t) \cdot \frac{1}{2} [1 + \underbrace{\cos(2\omega_{\text{LO}}t)}_{\text{low-pass} \rightarrow 0}] - Q(t) \cdot \frac{1}{2} \sin(2\omega_{\text{LO}}t). \quad (3.4)$$

By applying a low-pass filter, we remove the high-frequency oscillations and are left with the original in-phase part (up to a factor 1/2). The same is true for the quadrature component  $Q(t)$ .

Often, it is more convenient to express the baseband signal in a complex form as

$$y(t) = I(t) + iQ(t), \quad (3.5)$$

where we now also consider the up-conversion process as a complex multiplication

$$y(t)e^{i\omega_{\text{LO}}t} = [I(t) + iQ(t)] \cdot [\cos(\omega_{\text{LO}}t) + i \sin(\omega_{\text{LO}}t)], \quad (3.6)$$

and down-conversion becomes trivial. The actual transmitted signal corresponds to the real part of this expression (similar to the use of phasor notation in electronics),

resulting in the modulated signal  $s(t)$ , as above. Using the complex form, it is also easy to see how the cavity drive  $\eta$ , introduced in Eq. (2.60), corresponds to the  $I(t)$  and  $Q(t)$  quadratures in the rotating frame of the driving frequency  $\omega_p$  as

$$\eta(t) = I(t) + iQ(t). \quad (3.7)$$

Instead of relying on homodyne detection, where up- and down-conversion are performed using the same frequency  $\omega_{\text{LO}}$ , we can also employ heterodyne detection by demodulating at an intermediate frequency  $\omega_{\text{IF}}$ . This shifts the baseband from being centered at zero to a slightly higher range (e.g. in the kilohertz range), thereby avoiding issues with DC leakage.

### 3.2.2 Time-resolved and spectroscopy measurement setup

This subsection details the setup's equipment — a comprehensive, though not exhaustive, list intended for readers with an interest in the technical details.

The time-resolved measurements described in this thesis are primarily conducted in the dilution fridge. To synthesize the spin-inversion pulses (see Sec. 6.0.2), we use an arbitrary waveform generator (AWG, Tabor Electronics model WX2182B) to generate the I/Q signals, and a frequency source (Anritsu MG3692C) to produce the high-frequency signal. The actual mixing is performed using an IQ mixer (Marki IQ1545LMP).

To minimize unwanted MW leakage, we apply DC offset correction to the I/Q input signals using a spectrum analyzer (Agilent E4440A) and employ a series of microwave switches (various models at different stages of the pulse synthesis chain) to block the MW drive when it should be inactive. Before entering the dilution fridge's pump-line, the MW signal passes through a series of digital attenuators, allowing for precise control of the MW power in  $-0.5$  dB steps. The signal is then amplified by a high-power amplifier ( $+40$  dB, Mini-Circuits ZHL-16W-43-S+).

To block residual amplifier noise, which can persist even after conventional MW switches, we employ a mechanical MW switch at the 1 K stage inside the dilution fridge. This switch utilizes a solenoid mechanism to open and close a mechanical MW relay connection, providing approximately  $-100$  dB isolation in about 1 ms.

After passing through the cavity — entering at port 1 and exiting at port 2 — the MW signal travels up and out of the fridge, passing through two MW isolators (each having  $-16$  dB isolation and  $-7$  dB insertion loss). It is then amplified by a cryogenic low-noise amplifier ( $+30$  dB, LNF-LNC4\_8A) located at the 5 K stage. The signal

exits the fridge, undergoes further amplification and IQ demodulation, and is finally recorded using a digitizer (Acqiris U1084).

For the measurements on triggered superradiance (see Sec. 6.1), we send in very weak MW pulses to probe the system. To achieve this, cavity port 2 is connected to both the out-line and a highly attenuated probe-line via a power splitter. This setup allows us to inject the probe pulses while simultaneously blocking amplifier noise from the pump-line using the relay switch. The weak pulses are generated by simply gating the continuous-wave signal from a second frequency source.

When not conducting time-resolved measurements, but instead focusing on the steady-state spectroscopic response of the system under study, we use a vector network analyzer (VNA, Rohde&Schwarz ZNB8). The VNA measures scattering parameters, such as  $S_{21}$  — the (steady-state) transmission from port 1 to port 2 in a two-port network, a complex quantity that carries amplitude and phase information — to determine the transmission and reflection characteristics of the microwave signal through the system. The MW setup is illustrated schematically in Fig. 3.2.

### 3.2.3 Pulse photon number calibration

An important aspect of our experiment is the careful control of the microwave pulse power reaching our coupled cavity-spin system. This aspect is crucial in the experiment on triggered superradiance (see Sec. 6.1 and Ref. [35]), where we study the influence of trigger pulses, injecting different numbers of trigger photons into the cavity, on the system's behavior. The following passage is adapted from the Supplemental Material of Ref. [35].

To estimate the number of photons contained in a probe pulse we do a calibration measurement of the attenuation  $A_2 = -54.5 \text{ dB} + 5 \text{ dB}$  at room temperature for the probe-line inside the fridge up to port 2 of the cavity, where an estimated increased transmittance of  $+5 \text{ dB}$  is added to account for the lowered resistance of the lines when cold. We determine the MW power at the strongest setting for pulses that enter the probe-line outside the fridge using the power spectrum analyzer,  $P_{\text{max}} = -58 \text{ } \mu\text{W}$ . The other power settings used in the experiment have variable attenuation decrements of  $-5 \text{ dB}$  each, so the photon numbers change accordingly down to  $-45 \text{ dB}$  relative to the highest power value.

Next, we determine the values of  $\kappa_1$  and  $\kappa_2$ , the external coupling rates at both ports. For that, we measure the  $S$ -parameter traces of our system at  $24 \text{ mK}$  with the spins far detuned using the VNA. These traces are shown in Fig. 3.2(b). By fitting the measured traces with the expected results from cavity input-output theory (shown

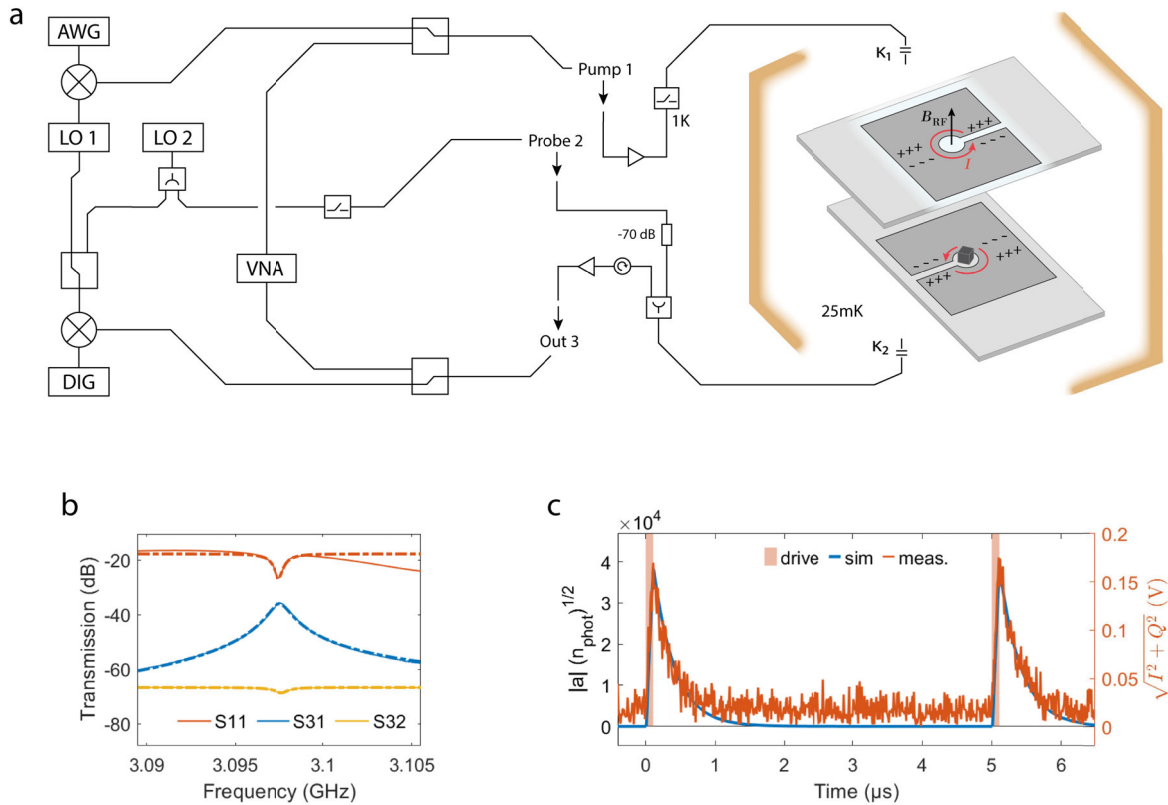


**Figure 3.2** MW lines schematic and trigger pulse photon-number estimation measurements. (a) Schematic illustration of the MW setup connected to the DCR cavity (c.f. Sec. 5.2.3) in the cryostat. (b) VNA traces of the  $S$ -parameters with far-detuned (uncoupled) spins. (c) Time-resolved measurement of a sequence of 100 ns pulses injected into the uncoupled cavity, which allows to relate the measured I/Q amplitudes to the known injected pulse power.

here for  $\Delta_c = 0$ , i.e., on resonance condition, c.f. Sec. 2.7) we obtain  $\kappa_1$  and  $\kappa_2$ .

$$\begin{aligned} |S_{11}|^2 &= A_1^2 (2\kappa_1/\kappa_{\text{tot}} - 1)^2 \\ |S_{31}|^2 &= A_1 A_3 (2\sqrt{\kappa_1 \kappa_2}/\kappa_{\text{tot}})^2 \\ |S_{32}|^2 &= A_2 A_3 (2\kappa_2/\kappa_{\text{tot}} - 1)^2 \end{aligned} \quad (3.8)$$

Here, the subscripts in  $A_{1,2,3}$  refer to the fixed MW line attenuations inside the cryostat for pump-, probe-, and out-line, respectively.

The time-dependent cavity amplitude  $|a|$  can be determined by solving the differential equation (2.64a) [with the spins far detuned, we ignore their contributions by letting  $g_p = 0$ ] and assuming a constant drive  $\eta_d = \sqrt{2\kappa_{\text{in}} P_{\text{in}}/\hbar\omega_c}$  that starts at time  $t = 0$  as

$$a(t) = \frac{\eta_d}{\kappa_{\text{tot}}} (1 - e^{-t\kappa_{\text{tot}}}),$$

with the incident power  $P_{\text{in}}$  and the appropriate port's coupling rate  $\kappa_{\text{in}}$ .

In a pulse injected via port 2, with duration  $\Delta t = 100$  ns, as used in the experiment, the number of photons  $n = |a|^2$  in the cavity charges up to a maximum value of

$$n_{\text{trig}}^{\text{min}} = \frac{P_{\text{max}}^{-45\text{dB}}}{\hbar\omega_c} A_2 \frac{2\kappa_2}{\kappa_{\text{tot}}^2} (1 - e^{-\Delta t\kappa_{\text{tot}}})^2 \approx 50,$$

where the power  $P_{\text{max}}^{-45\text{dB}}$  measured outside is attenuated by an additional factor  $A_2$  inside of the cryostat (c.f. Table 3.1).

For the pulse train measurements in the reduced cooperativity regime we use the same procedure to calculate the number of photons per 100 ns pulse entering through the pump-line (c.f. Table 3.2),

$$n_{\text{trig}}^{\text{min}} = \frac{P_{\text{MW}}}{\hbar\omega_c} A_1 \frac{2\kappa_1}{\kappa_{\text{tot}}^2} (1 - e^{-\Delta t\kappa_{\text{tot}}})^2 \approx 1.5 \times 10^9.$$

These pulses are also used to calculate the  $|a|$  units given as the square root of the cavity photon number  $n^{1/2}$  from the voltages of the time-resolved I/Q measurement, see Fig. 3.2(c).

Lastly, we estimate the number of thermal photons in the cavity, when the solenoid switch at the 1 K stage is open to decouple the higher temperature stages. We use the

values of Table 3.3 and evaluate according to

$$n_i = n_{\text{th}}(T_i) + A_{i-1,i} n_{i-1},$$

$$n_{\text{th}}(T) = \frac{1}{\exp(\hbar\omega_c/k_{\text{B}}T) - 1}, \quad (3.9)$$

going down the stages for all MW lines. The dominant contribution is thermal photons from the 1 K stage of the pump-line, which result in a value of  $n_{\text{th}} \approx 3$  photons.

Notably, the calculated number of photons depends on the actual attenuation of the MW lines in the cryostat, which decreases from the room-temperature values when cooled. To account for this, we have estimated a +5 dB change due to the temperature effects, which agrees well with the estimated number of decaying spins as shown in Fig. 6.16(c) in Sec. 6.1. However, we acknowledge that the photon numbers may be subject to a factor of two uncertainty.

**Table 3.1** Summary of the parameters used to estimate the number of photons entering the cavity via the 100 ns trigger pulses through the probe-line.

$\kappa_2/2\pi$	$\kappa_{\text{tot}}/2\pi$	$A_2$	$P_{\text{max}}^{-45\text{dB}}$
59 kHz	586 kHz	-49.5 dB	1.83 nW

**Table 3.2** Parameters used to estimate the number of photons per pulse in the pulse sequences injected via the pump-line. This experiment was done in another cool-down of our cryostat, so the Q-factor of the resonator, therefore the  $\kappa_{\text{tot}}$  value, exhibits some deviations from the ones above.

$\kappa_1/2\pi$	$\kappa_{\text{tot}}/2\pi$	$A_1$	$P_{\text{MW}}$
182 kHz	516 kHz	-10.6 dB	2.1 $\mu\text{W}$

**Table 3.3** Temperatures of the various stages inside the dilution fridge and corresponding attenuations (in the direction of lowering temperatures) between the respective stages to estimate the number of thermal cavity photons, when the solenoid switch at the nominal 1 K stage is disconnected.

stage $i$	1	2	3	4	5	6
$T_i$ (K)	296	42	4	0.9	0.12	0.025
$A_{i,i+1}$ (dB)						
pump	–	–	–	-1.5	-2	
probe	-1.5	-21.5	-1.5	-11.5	-13.5	
out	-1.5	-1.5	-1.5	-1.5	-30	



# Chapter 4

## Spin Systems

### 4.1 Nitrogen-vacancy center in diamond

The spin system central to most experimental results presented in this thesis is the negatively charged nitrogen-vacancy center in diamond (NV center<sup>1</sup>) [5]. It is a point defect in the diamond crystal, consisting of a substitutional nitrogen atom and an adjacent lattice vacancy. In many ways, this defect can be thought of as a molecule trapped in the diamond lattice — although held in place and without rotational degrees of freedom. With the diamond lattice as its host matrix, the NV center sits in a highly stable and inert place and is well-isolated from its surroundings. This leads to well-protected quantum properties with coherence times  $T_2$  reaching up to 1 s [36] and  $T_1$  lifetimes of up to 8 h [37] at millikelvin temperatures. However, these record values can be substantially lower in practice, depending on the diamond quality and the method of NV creation, as is the case for the NV sample used for the experiments in this work.

Another clear advantage of diamond — in a quite literal sense — is its optical transparency in a wide spectral range. Combined with the NV centers' optical addressability, allowing initialization and readout of the spin state at room temperature using green pump light and red fluorescence detection, the NV center is a useful tool for quantum technologies, particularly quantum sensing applications [38–41]. Although optical addressability is of minor concern for the experiments presented here, which explore phenomena arising from the collective coupling to a microwave cavity, an

---

<sup>1</sup>The superscript “-” to indicate the charge state, as in  $NV^-$ , is sometimes used in the literature, but will be omitted here for better readability.

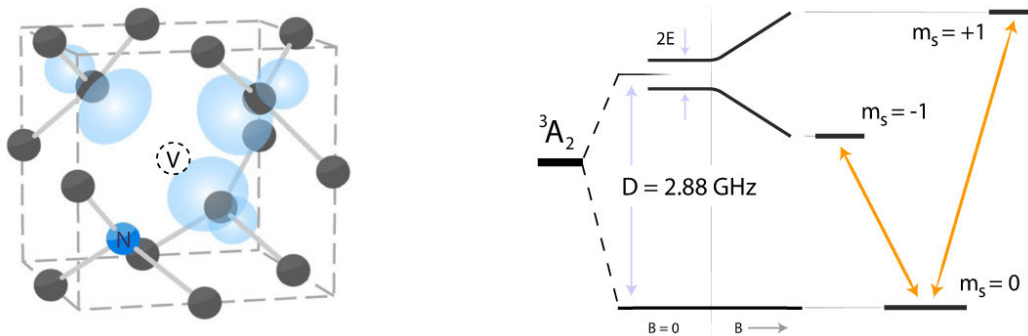


**Figure 4.1** (Left) Unit cell of the diamond crystal hosting the NV center, consisting of a lattice vacancy in the center and neighboring substitutional nitrogen atom. (Right) Ground state manifold (carrying the name  ${}^3A_2$ , following molecular symmetry naming conventions) of the negatively charged NV center with spin  $S = 1$  and V-level structure. The  $m_S = 0$  state is the lowest level, separated by a zero-field splitting of 2.88 GHz from the almost degenerate  $m_S = \pm 1$  upper states. The degeneracy is lifted when an external  $B$  field is applied and the  $m_S = \pm 1$  states are Zeeman-shifted up/down.

introduction of the NV center cannot omit this aspect, which forms the basis of the NV center’s relevance today.

The NV center, as a solid-state emitter, is a powerful platform for a variety of vibrant research fields, such as quantum information processing [42–44] and quantum networks [45], and fundamental studies of disordered spin systems [46, 47]. Especially in biomedical sensing applications [48, 49], the NV center has attracted interest in recent years due to the bio-compatibility of diamond [50, 51] and the possibility to incorporate nanodiamonds in living cells [52].

In the following, we delve into the fundamental properties of the NV center, laying the groundwork for understanding the cavity QED experiments presented later. Details about the specific NV diamond sample used in the experiments will be discussed together with the measurements for characterizing its relevant properties in the experiment chapter.

#### 4.1.1 Structure and ground state level scheme

The NV center, as a point defect in diamond, is a spin  $S = 1$  system that is created when a substitutional nitrogen atom sits next to a lattice vacancy, see Fig. 4.1. The nitrogen atom has 3 covalent bonds to the neighboring carbon atoms in the diamond lattice, which leaves 2 electrons free of the total 5 valence electrons of nitrogen. The three carbon atoms next to the vacancy each have one dangling electron that is not

bound to a neighboring carbon atom, which gives another 3 electrons. Now, yet another electron is “borrowed” from the diamond lattice - which is the reason for the attribute *negatively charged* — summing up to a total of 6 electrons. Two electron pairs, so in total 4, will form stable bonds within the diamond lattice. This finally leaves 2 unpaired electrons to contribute to the electronic properties of the NV center, forming the spin-triplet ground state  ${}^3\mathbf{A}_2$ . Notably, also other charge states of the NV center exist, such as the neutrally charged  $\text{NV}^0$ , but their uses are less common.

The spin Hamiltonian for this ground state is denoted as

$$\mathcal{H}_{\text{NV}} = \hbar D (S_z^2 - 2/3) + \hbar E (S_x^2 - S_y^2) - \hbar \gamma_e \vec{B}_{\text{ext}} \cdot \vec{S}, \quad (4.1)$$

where  $\vec{S} = (S_x, S_y, S_z)^T$  are the  $S = 1$  spin operators in the reference frame of the NV center, with the  $z$ -axis aligned parallel to the N-V-axis. The parameter  $D/2\pi \approx 2.88$  GHz [5] represents the zero-field splitting between the  $m_S = 0$  and  $m_S = \pm 1$  states, which arises from the anisotropic interaction of the electrons with the crystal field. The parameter  $E/2\pi \approx 8$  MHz is due to strain in the diamond crystal [53] and is highly sample dependent. An external magnetic field  $\vec{B}_{\text{ext}}$  allows to further tune the  $m_S = \pm 1$  levels via the Zeeman effect. In the experiment,  $\vec{B}_{\text{ext}}$  is chosen such that one of these transitions is resonant with the microwave frequency of the driving field, i.e. the cavity frequency.

In the Hamiltonian (4.1), we neglect contributions from hyperfine interactions with nuclear spins, such as  ${}^{14}\text{N}$  (about 99.6% natural abundance),  ${}^{15}\text{N}$  (0.4%), and  ${}^{13}\text{C}$  (1%). In real diamond samples, the NV center can interact with many different spin species, including the P1 center, a point defect with spin-1/2 formed by only a substitutional nitrogen atom (no adjacent vacancy). All of these interactions, along with the presence of strain-inducing lattice defects, will lead to shifts in the NV center’s level structure. However, for the purpose of this thesis, we are concerned with the effective description of a whole ensemble of around  $10^{13}$  NV centers. Hence, we assume that all NV centers are effectively described by the level structure of Eq. (4.1) although the individual NVs energy levels can be shifted by up to  $\pm 5$  MHz, depending on the local environment of each NV center. These individual energy shifts can be modeled statistically with a spin frequency distribution  $\rho(\omega_s)$ .

## NV directions

The NV center comes in four possible orientations with respect to the diamond unit cell shown in Fig. 4.1. These orientations correspond to the tetrahedral symmetry of

diamond and are given in terms of the unit cell axes as  $[1, 1, 1]$ ,  $[1, -1, -1]$ ,  $[-1, 1, -1]$ , and  $[-1, -1, 1]$ . It is useful to think of NV centers that have the same orientation as belonging to a subgroup of the whole ensemble. By carefully aligning the external field, it is possible to effectively control the number of subgroups — between 1, 2, 3, and 4 — that experience the same Zeeman shifts and therefore share identical transition frequencies between the states  $m_S = 0$  and  $m_S = \pm 1$ .

- The external field direction can be chosen to have an equal projection on all four subgroups of NVs when it is aligned along the edges of the unit cell crystal axis, e.g.  $[1, 0, 0]$ . Then, all NV centers in the diamond are affected by the same Zeeman shift.
- When  $\vec{B}_{\text{ext}}$  is aligned at an angle in the plane spanned by one side of the unit cell cube, e.g. somewhere between  $[1, 0, 0]$  and  $[0, 1, 0]$ , then two subgroups will have one value for the Zeeman shift, whereas the two other subgroups have another value.
- By aligning the external field along one of the NV axes, e.g.  $[1, 1, 1]$ , the subgroups are split into one and three.
- In the general case with an arbitrary direction of the external field, each subgroup will experience a different Zeeman shift.

### Optical transitions

As mentioned above, the profound interest in NV centers for both research and technological applications, besides having highly coherent microwave transitions, stems mostly from their optical addressability. The optical transitions between the ground and excited state manifolds are shown in Fig. 4.2. The excited state  ${}^3\mathbf{E}$  exhibits a similar fine structure as the ground state  ${}^3\mathbf{A}_2$ , with a zero-field splitting and spin  $S = 1$ . The optical transitions between these manifolds are spin-state preserving. Using red 637 nm light, the zero-phonon line is targeted. When green light is used, the additional energy is dissipated via phonon excitations in the diamond crystal lattice. From the  $m_S = \pm 1$  spin-states in the excited state manifold, the NV center is more likely to decay via intermediate states to the ground state manifold [54]. This decay via the meta-stable intermediate states can be radiative in the infrared or non-radiative and is not spin-state preserving. Conversely, the  $m_S = 0$  spin-state in the excited state manifold has a higher likelihood of reverting back to the ground state manifold, while preserving its  $m_S = 0$  projection and emitting a red fluorescence photon. When

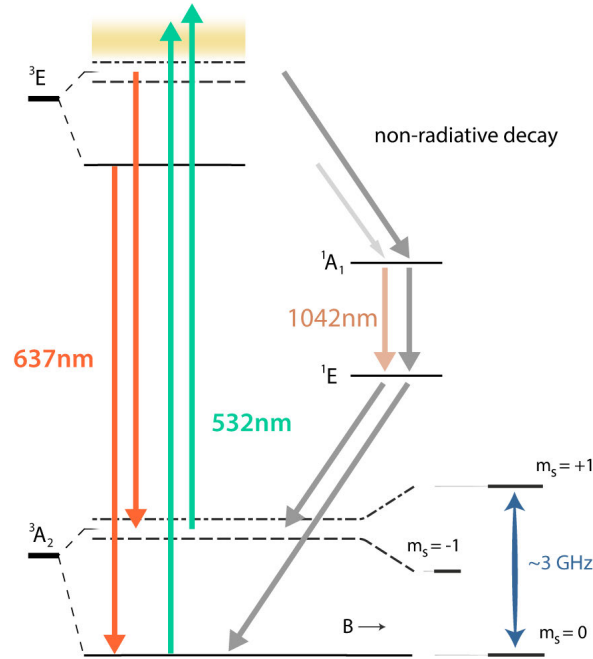


**Figure 4.2** Spin-state preserving optical transitions between the ground state manifold  ${}^3A_2$  and excited state manifold  ${}^3E$ , both having spin  $S = 1$  and a zero-field splitting. The excited state can cycle back to the ground state by emitting red fluorescence light. When green light excites the ground state, the surplus energy is dissipated in the phonon sideband. The  $m_S = \pm 1$  states are more likely to decay via the intermediate states  ${}^1A_1$  and  ${}^1E$  (either non-radiatively or by emitting in the infrared) to the ground state manifold  ${}^3A_2$  — over a few cycles this leads to a net polarization in the  $m_S = 0$  state. Higher transition probabilities for the decay pathways via the intermediate states are indicated by the darker gray arrow shadings. Figure adapted from Ref. [55].

driving the optical transition, the system is therefore initialized in the ground state with  $m_S = 0$  after a few cycles. By using green light for the optical state initialization, it is easy in practice to distinguish the pump light from the red fluorescence signal, which conveniently allows to measure the polarization in the  $m_S = 0$  state by counting the red fluorescence photons.

Notably, the optical properties of the NV center enable the operation of an NV diamond maser, as experimentally demonstrated in Ref. [56]. In principle, such a maser could function in a superradiant regime [57], where the spin ensemble is strongly coupled to the cavity — although this is still awaiting experimental realization. This regime has the potential to dramatically narrow the linewidth to the benefit of microwave quantum technology applications. However, for such a maser to work, the external tuning field must be sufficiently high and well-aligned with one of the NV axes. Then, the optically

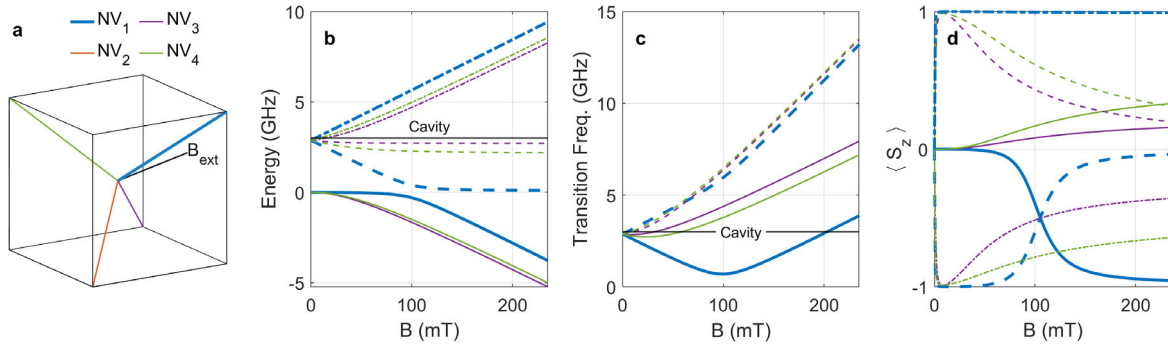


**Figure 4.3** (a) Alignment of the external magnetic field for masing operation, with a  $10^\circ$  deviation from the optimal orientation, chosen here for demonstration purposes. (b) Energy eigenstates of the NV Hamiltonian for varying field strength. (c) Transitions between these levels by subtracting the lowest energy value. At a high field value of roughly 200 mT, the  $m_S = -1$  to  $m_S = 0$  transition crosses the cavity frequency, assumed to be at 3 GHz. (d) Around this field value, the  $\langle S_z \rangle$  eigenvalue is again sufficiently well defined in the  $m_S = 0$  state for efficient optical pumping.

pumped  $m_S = 0$  state is a well-defined  $\langle S_z \rangle$  eigenstate and becomes an excited state when the zero-field splitting is overcome, and the  $m_S = -1$  state crosses below; see Fig. 4.3. Only in this case will optical pumping supply the population inversion required for maser operation. Consequently, instead of all 4 NV orientations, only one of the NV subgroups can be selected, reducing the total number of coupled spins. Another complication is that increased NV center densities in diamonds lead to a loss of optical transparency, posing a challenge for efficient optical pumping, particularly with larger diamond samples. Achieving the necessary conditions for optical pumping and strong coupling to the cavity RF field becomes a delicate balance, making the realization of a superradiant diamond maser a problem of finding the right cavity design.

### Thermal occupancy of the NV levels

In the main experiments of this thesis, we couple a superconducting microwave cavity to an NV diamond in a cryostat at millikelvin temperatures. Therefore, we rely on the cold environment to initialize the spins in the ground state, which is the  $m_S = 0$  state. Besides this convenient way of state initialization, the low-temperature regime offers other advantages, such as enabling superconductivity of the cavity in the first place and reducing the number of thermal photons to a minimum. A clear disadvantage for relying on the thermal occupation of the ground state is the long lifetime of the NV center with  $T_1 \gtrsim 100$  s for the diamond sample mainly used. However, combining the

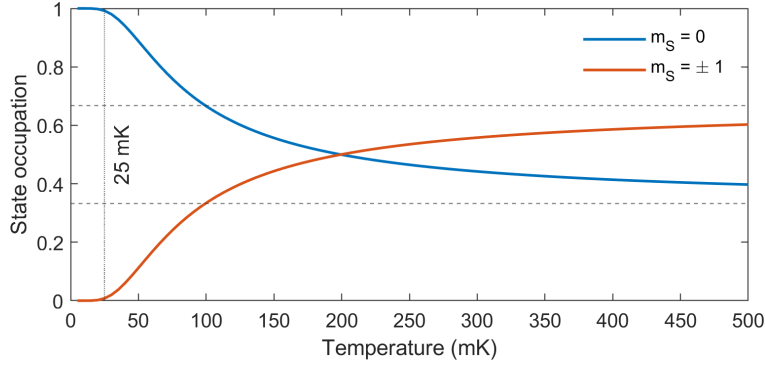


**Figure 4.4** Thermal occupation of the NV center’s  $m_S$  levels. At  $T = 25$  mK, the temperature of our dilution refrigerator’s lowest stage, the ground state polarization is more than 99%. In the high-temperature limit, all three available states are equally populated, leading to  $1/3$  occupation probability for the ground state, and  $2/3$  for the degenerate excited states, respectively.

use of lasers for optical initialization with superconducting circuits is technically hard — as the comparatively high energy optical photons tend to break the Cooper pairs in the superconductor — although not impossible as e.g. employed in Ref. [58].

The thermal occupation probability for a state with energy  $\hbar\omega_s$  is proportional to the Boltzmann factor  $\exp(-\hbar\omega_s/k_B T)$ . It is straightforward to calculate the thermal occupation of the NV’s  $m_S$  states as a function of the temperature, see Fig. 4.4, where we assume the  $m_S = \pm 1$  states to be degenerate and have energy  $\hbar\omega_s = \hbar 2\pi \times 2.88$  GHz and the  $m_S = 0$  state to have zero energy (only the difference matters). The occupation probabilities are given by

$$P_{m_S=0}(T) = \frac{1}{1 + 2e^{-\hbar\omega_s/k_B T}}, \quad \text{and} \quad P_{m_S=\pm 1}(T) = 1 - P_{m_S=0}(T). \quad (4.2)$$

At the low cryogenic temperatures of around 25 mK in the experiment, more than 99% of NVs are polarized in the ground state. By applying an external magnetic field on the order of 10 mT, we split up the (almost) degenerate  $m_S = \pm 1$  states by roughly  $2\pi \times 400$  MHz, allowing us to tune one transition into resonance with the cavity. As a result, when considering interactions with the cavity, we can neglect the off-resonant transition of the  $S = 1$  spin system and approximately describe the NV centers as effective two-level systems thermally polarized in the ground state.

### 4.1.2 NV samples used in this work

#### N-diamond sample

The roughly 200  $\mu\text{m}$  sized diamond sample utilized in the main experiments in Ch. 6 will be referred to as **N**-diamond — where **N** is short for *neutron irradiated* diamond, referring to the method for creating the lattice vacancies, making up one-half of the essential ingredients to form NV centers.

It was cut from a larger piece of single-crystal Type Ib diamond synthesized using the high-pressure-high-temperature (HTHP) method. The parent sample had an initial nitrogen concentration of approximately 200 ppm and naturally occurring  $^{13}\text{C}$  isotopes, and was sourced from the company Element-6. This parent sample underwent neutron irradiation at the Atominstitut's TRIGA Mark II reactor with a fluence of  $5 \times 10^{17} \text{ cm}^{-2}$  for 50 h to induce lattice vacancies. It was subsequently annealed at 900 °C for 3 h to facilitate the formation of NV centers. The heightened annealing temperatures cause the mobility of vacancies, which then move around and bind to the nitrogen atoms in the crystal lattice. Details of the parent sample creation are reported in Ref. [59], where the parent sample is referred to as “H4b”. Around 80 identical small diamond cubelets were cut from the parent sample by the company Delaware Diamond Knives using a  $\text{CO}_2$  laser.

The extensive lattice damage resulting from neutron irradiation leads to a significant inhomogeneous broadening with an FWHM of  $W/2\pi = 9.2 \text{ MHz}$  for the  $q$ -Gaussian shaped spin distribution, modeled with a shape parameter of  $q = 1.39$ . An estimated short  $T_2$  coherence time of approximately 0.9  $\mu\text{s}$  is in good agreement with the time-resolved collective ensemble behavior. The spin-lattice relaxation time was measured at  $T_1 \approx 134 \text{ s}$ . Details on the experimental characterization methods of these parameters are presented in Ch. 6. The shape of the small diamond is roughly cube-like but is described more precisely as a truncated rectangular pyramid with dimensions of approximately  $210 \times 190 \mu\text{m}^2$  for the base,  $120 \times 100 \mu\text{m}^2$  for the top face, and a height of 210  $\mu\text{m}$ , resulting in a volume of  $V = 5.16 \times 10^6 \mu\text{m}^3$ .

The number of spins in the **N**-sample is estimated at roughly  $N = 5.3 \times 10^{12}$ . This estimate results from a comparison of the measured collective spin-cavity coupling strength  $g_{\text{coll}} = g_0 \sqrt{N}$  to the simulated single-spin coupling  $g_0$  obtained with reliable finite-element simulations of the microwave cavity, as detailed in Ch. 5. Using the sample volume  $V$ , we calculate the NV density  $n_{\text{NV}} = n_c 6 \times 10^{-6}$  at approximately 6 ppm of the carbon density of diamond  $n_c = 1.755 \times 10^{23} \text{ cm}^{-3}$ . The resulting

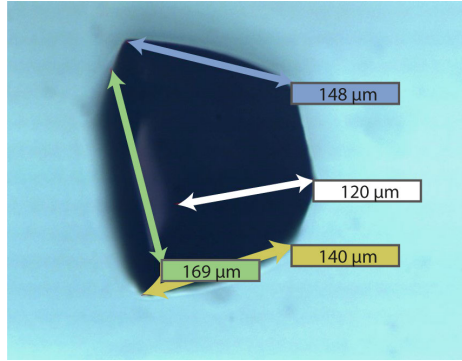


**Figure 4.5** Microscope image of the **E**-diamond sample. It is optically more transparent as the **N**-sample [shown in Fig. 5.8(b) in the next chapter], as can be seen from the internal light reflections visible on the left side of the image. This sample is also a bit smaller than the **N**-sample.

typical nearest-neighbor distance between neighboring NV centers then follows as  $r_{\text{typ}} = \sqrt[3]{n_{\text{nv}}} \approx 10 \text{ nm}$ .

### **E**-diamond sample

Another diamond sample employed in an attempt at realizing a superradiant diamond maser (details on this experiment are presented in the next chapter, Sec. 5.2.4) is the **E**-diamond, which was irradiated with electrons for lattice vacancy formation. A microscope image of this sample is shown in Fig. 4.5. The parent sample was created in a similar fashion as the sample “E1” employed in Ref. [37]. It was created from a type-Ib HPHT diamond with an initial nitrogen concentration of 100 ppm and irradiated with electrons accelerated to 2 MeV at a total dose of  $5.6 \times 10^{18} \text{ cm}^{-2}$  at temperatures of 800 °C and later annealed multiple times at 1000 °C. This larger sample was similarly cut to cubelets of nominally 200 μm, although these cubelets happened to be a bit smaller than the **N**-diamond samples.

The relevant parameters for the **E**-diamond, such as inhomogeneous broadening and coherence time, as well as spin lifetime, are not well-known. The sample was used in the superradiant maser attempt for its higher optical transparency due to having less lattice damage, as electron irradiation is a gentler method for the creation of lattice vacancies. The increased transparency helps for more efficient optical pumping of the NV transitions. Comparison with finite-element simulations of the maser cavity suggests that the spin density is also around 6 ppm. Presumably, the inhomogeneous

broadening is smaller and the spin coherence time is higher than for the N-diamond sample.

## 4.2 Molecular spins

While the primary focus of this thesis lies in exploring collective phenomena that arise from the coupling of NV ensembles to a microwave cavity, another avenue of my research, touched upon lightly here, focuses on molecules as spin systems. These molecular spins have the potential to be building blocks for encoding and manipulating quantum information, i.e. for use as qubits [6]. The spin physics of such molecular spins is very similar to the physics described by the NV center's ground state Hamiltonian (4.1). In general, there are multiple levels with different  $S_z$  projections on the molecular quantization axis, a zero-field splitting due to internal molecular anisotropies, and tunability with an external magnetic field. Additionally, hyperfine interactions with nuclear spins in the molecule can give rise to further complexities that allow for the engineering of molecular spins with tailored properties. The advantages that molecular spin systems can offer for quantum applications are summarized in the following, non-extensive list:

- High spin species  $S$  for higher magnetic moments  $|\mu| = g\mu_B S/\hbar$  to enhance spin-photon coupling. The single spin coupling scales linearly with  $S$ .
- Molecules are the largest singular physical building blocks that can be made to be completely identical — one molecule is exactly like any other molecule of the same kind — as opposed to, e.g., superconducting qubits, which have device-dependent differences due to fabrication imperfections.
- Tailored level structures for specific applications: Rich molecular level structures can be exploited, e.g. using internal error correction protocols due to redundancy in the way the information is encoded [60]. Another example is engineered clock transitions that are robust to magnetic field inhomogeneities and imperfect control [61].
- Molecular spins profit from the vast possibilities offered by chemical synthesis, e.g. controlling isotope composition and molecular architecture. Tailoring the ligands — chemists speak for molecular appendages or exchangeable parts of a molecule — offers control over the exact ways these molecules coordinate to

make, for example, two-dimensional layers for interfacing with superconducting circuits on a chip.

These advantages make molecular spins, when interfaced with superconducting circuits, a potential candidate system for building a quantum computer. A proposal [62] for such a quantum computer imagines this system as follows (see Fig. 4.6): Molecular spins act as the qubits (or in general: qudits with a  $d$ -level structure) and are the nodes where the information is stored and processed. Photons couple to the molecular spins and serve to read out and manipulate the internal states, as well as to transport and share the information, by mediating an effective coupling between spatially separate molecules to create entanglement. The photons live in superconducting circuits, which are nothing else than resonant circuits (or  $LC$  circuits) with low losses. One of the challenges for realizing such a proposal lies in engineering a coupling between photons and spins that is sufficiently strong. The coupling rate needs to overcome the information loss rate, i.e., decoherence in the molecular spins — which is, in general, worse than in solid-state spin systems. A possible strategy to increase the single-spin coupling strength is to place the molecules at certain spots in these circuits, where the oscillating current associated with the photonic excitations is forced to pass through a nanowire or *nanoconstriction*. Then, the magnetic field created by this current is locally increased, possibly by many orders of magnitude, due to the spatial confinement. This spatial confinement is equivalent to a local decrease of the effective mode volume, which increases the oscillating magnetic field as in  $\mathcal{B}_0 = \sqrt{\mu_0 \hbar \omega / 2V}$ , see Eq. (2.26).

Although there are many other challenges with this proposal for a quantum computer based on molecular spins — e.g. the low spin coherence times and the problem of reliably placing a single molecular spin at a desired location in the circuit and keeping it there — the challenge of reaching the strong coupling regime is one of the recurring themes of research presented in this thesis. My efforts in this direction have culminated in our publication *Enhanced Molecular Spin-Photon Coupling at Superconducting Nanoconstrictions* [63], which will be further discussed in the following chapter on microwave cavities. The molecular spin system employed for this work is a very simple one, and was decidedly chosen for its simplicity and for being a standard material for electron paramagnetic resonance spectroscopy: the organic free-radical molecule with the pleasant name **2,2-diphenyl-1-picrylhydrazyl** and the common abbreviation DPPH [64]. The spin Hamiltonian for this molecule is, as the byname free-radical suggests, that of a single electron with  $S = 1/2$  and therefore tunable with an external magnetic field,  $\mathcal{H} = -(g_e \mu_B / \hbar) \vec{S} \cdot \vec{B}$ . The molecules form a crystal structure with a higher spin density than usually attainable for NV diamonds, which helps with

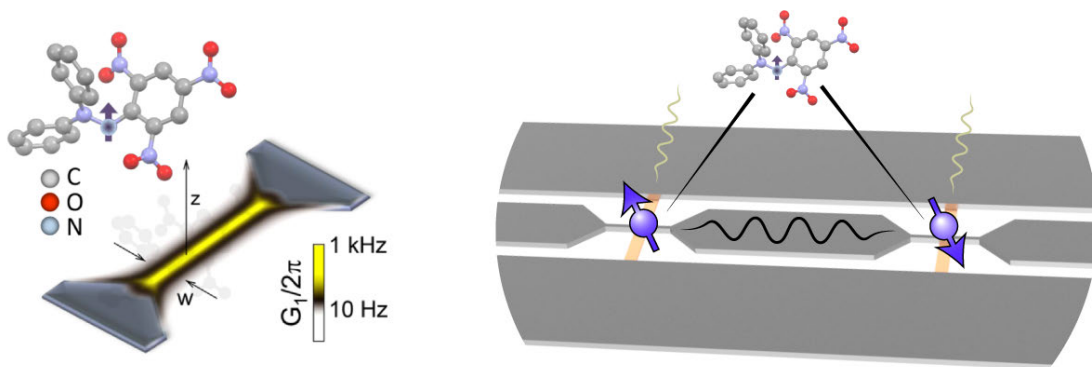


**Figure 4.6** Molecular spins for quantum applications. (Left) Molecular structure of the model system DPPH and schematic of a nanowire, where the single spin coupling (here referred to as  $G_1$ ) is locally enhanced. (Right) Proposal for a quantum computing architecture using molecular spins. The schematic shows a detail view of a superconducting circuit — a wire with two constrictions — where the magnetic field is locally enhanced. At these two nodes, the molecular spins are placed and couple to the photons in the circuit. Additional wires (shown below) allow for independent manipulation of the spin states.

detecting the influence of spatial confinement in the nanowire, i.e. variations in its width, on the spin-photon coupling strength. The molecular structure of DPPH and the nanowire are illustrated in Fig. 4.6.

# Chapter 5

## Microwave Cavity Designs

### *How to catch a wave*

Cavities, as the name suggests, are an essential part of the field of cavity quantum electrodynamics. They help to interface with the quantum emitters and facilitate coupling to, as well as manipulation and readout of the spins. The outgoing microwave signal of a cavity, after being converted to time-varying voltages by the use of IQ-mixing, is also what is ultimately measured in the experiment, allowing us to draw conclusions on the dynamics of the coupled system of cavity and spins. In this chapter, we will lay down my thoughts on how to design a microwave cavity.<sup>1</sup> After discussing some basic principles accompanied by simple formulas, we introduce simulation tools that help to guide the design process before a cavity is finally manufactured and its properties are determined by experiment. Then, we will consolidate the discussion by means of several cavity designs that were built and characterized experimentally during my PhD. The focus of all these cavity designs is to reach the strong coupling regime — where energy exchange between the coupled systems happens at a faster rate than the respective losses:  $g_{\text{coll}} > \kappa, \Gamma$  — with a small number of spins. In the case of molecular spins, the ultimate goal would be to strongly couple to a single spin. Admittedly, this task poses a significant experimental challenge.

---

<sup>1</sup>The words cavity and resonator are sometimes used interchangeably in this thesis but essentially mean the same thing. It could be said that the word resonator applies very generally — extending its meaning to the fields of electronics and acoustics — and the term cavity is more specific in that it refers to a hollow space or negative volume inside a conducting material, e.g. bulk copper, where the electromagnetic mode is confined.

## 5.1 Design principles for microwave resonators

Resonant phenomena are ubiquitous in physics — every object, depending on its shape and composition, will have several acoustic and electromagnetic resonances, although sometimes these spectral features are hard to detect, as they may appear very broadband due to damping. Often, these resonances can be grasped with the simple intuition of a standing wave, e.g., a vibrating guitar string, or the fundamental mode of a box cavity as discussed in Sec. 2.3. For more complicated geometries, the oscillation patterns of a resonant mode are less obvious. To conceptualize microwave resonances, I find it easiest to adopt a viewpoint of electronics: resonant circuits.

### LC-resonators

Under this perspective, the total energy stored in the electric and magnetic fields, expressed as an integral over the cavity mode volume, is recast into a simple formulation involving two numbers, the capacitance  $C$  and the inductance  $L$ . These two constants absorb all the geometric intricacies of the field distributions:

$$\mathcal{H} = \frac{1}{2} \int (\epsilon_0 \vec{E}^2 + \frac{1}{\mu_0} \vec{B}^2) dV = \frac{1}{2} CV^2 + \frac{1}{2} LI^2 \quad (5.1)$$

In simple terms, capacitance is a measure of the total energy that can be stored in an electric field, whereas inductance quantifies the amount of magnetic energy. However, when considering actual realizations of microwave resonators, the simplest case of a coiled-up wire constituting an inductance, and two metal surfaces forming a capacitance — archetypical examples of so-called lumped-element circuits, see Fig. 5.1 — may not always hold. In such cases, it becomes necessary to consider capacitance and inductance as a sum of individual parts:  $L = \sum l_i$  and  $C^{-1} = \sum c_i^{-1}$ . This line of thinking will eventually end in a distributed element picture, where each volume element has capacitive and inductive characteristics and an integral formulation can again be required.

Nevertheless, it is essential to keep in mind that an LC circuit has a simple property: energy oscillates between being stored electrically in the total capacitance and magnetically in the total inductance. The frequency of this oscillation — the resonance of the system — is given by

$$\omega = \frac{1}{\sqrt{LC}}. \quad (5.2)$$

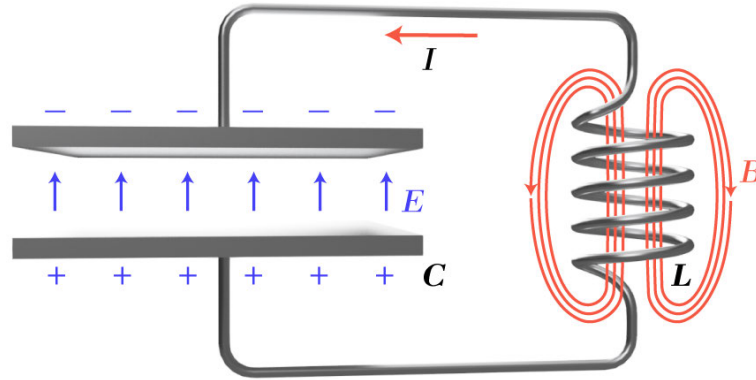


**Figure 5.1** Electric and magnetic fields in an LC circuit. Every half oscillation period, positive and negative charges in the capacitor switch places, leading to a current flowing over the inductor. Consequently, the stored energy oscillates between electric and magnetic fields.

In a real LC circuit, there will always be resistive elements present, causing the dissipation of electromagnetic energy, which is eventually turned into heat. The way to incorporate their effective description has already been discussed in Sec. 2.6 and is simply accomplished with the cavity loss rate  $\kappa$ . The formula (5.2) is key to designing microwave resonators for specific purposes. When the goal is to achieve a high coupling strength to spins — magnetic dipoles — the magnetic field strength has to be maximized in a volume where the spins are positioned. The desired resonance frequency of the microwave cavity is dictated by the spin system. For NV diamonds a resonance of around 3 GHz is a useful goalpost, as then the spins can be Zeeman tuned into resonance with the cavity by moderate external fields of roughly 10 mT. With this goal in mind, our freedom in designing the cavity is already restricted; we can choose a value for  $C$ , and the required  $L$  will follow from Eq. (5.2). It may seem paradoxical at first glance, but to maximize the RF magnetic field at the spin site, it is necessary to maximize the capacitance  $C$  and to minimize the total inductance  $L$ . In other words, a low impedance  $Z = \sqrt{L/C}$  circuit is desired for coupling to a small number of spins [65]. A simple argument for this is given by Ampère’s law — the magnetic field produced by a one-dimensional wire carrying the current  $I$  is calculated as

$$\vec{B}(r) = \frac{\mu_0 I}{2\pi r} \vec{e}_\varphi, \quad (5.3)$$

where the magnetic field strength is proportional to  $I$ . In an ideal LC circuit, the energy oscillates back and forth between the inductor and the capacitor. When the energy is

maximum in one component, it is zero in the other. Therefore, the maximum values for current and voltage are related by the equation  $\frac{1}{2}CV_{\max}^2 = \frac{1}{2}LI_{\max}^2$ . To maximize magnetic coupling to the spins, a high current maximum needs to be generated in a small inductance, resulting in high magnetic fields. Then, the magnetic energy in a microwave resonator will be focused down to a small volume, where the spins reside. Another perspective is provided by the expression for the magnetic field amplitude associated with the cavity vacuum fluctuations, discussed in Sec. 2.3,  $\mathcal{B}_0 = \sqrt{\mu_0 \hbar \omega / 2V}$ . The smaller the effective magnetic mode volume  $V$  can be engineered, the higher the magnetic field amplitude will be. It is worth noting that this effective volume can take different values within the same electromagnetic mode, depending on whether electric or magnetic contributions are considered. In general, it is more challenging to spatially focus magnetic fields than electric fields, as the magnetic field lines need to form closed loops *around* conductors, whereas electric field lines originate and terminate in charges *between* conductors. A useful visualization of this difficulty is the shape of a needle: the tip is always smaller than the overall width of the needle's body. In this picture, the tip is where electric field lines originate, whereas the magnetic field lines are formed around the body.

A possible strategy to create the desired spatial focusing of magnetic fields in a resonator is then to approximate an ideal plate capacitor geometry with a high capacitance and connect the plates with a short current path to minimize inductance. Here comes the crux of the problem: Every capacitive element inevitably introduces a parasitic inductance, and vice versa. The challenge in designing a microwave cavity is, therefore, to minimize these unwanted parasitic effects by tinkering with the exact geometry. Another problem arises when we consider Ohm's law:  $P = RI^2$ . The dissipated power in a resistance  $R$  goes with the square of the current  $I$ . A current-carrying metal surface made of a normal conducting material like copper will always have a finite resistance. As discussed above, we want to maximize the current — or more accurately, the current density — to create the magnetic fields for strong spin-photon coupling. This can lead to significant losses, as quantified by a large dissipation rate, or equivalently a large Lorentzian linewidth  $\kappa$ , see Eq. (2.58). A solution is offered by other material choices — superconductors — that have zero electrical resistance below a critical temperature and magnetic field strength. This in turn can create a new challenge: field expulsion via the Meißner–Ochsenfeld effect, which complicates the application of homogeneous external magnetic fields for frequency tuning of the spin system. As will be laid out on the basis of experimentally tested cavity designs

below, informed design choices can help to achieve desired outcomes, depending on the specific experimental requirements.

### Simulation techniques

To make informed design decisions effectively, it is essential to play around with different geometries. However, manually manufacturing each design iteration to assess the outcome would be very inefficient. Therefore, including simulation tools in the design process is crucial. For this purpose, the finite-element simulation suite COMSOL<sup>®</sup> [66] is used, specifically the “*Electromagnetic Waves, Frequency Domain*” module.<sup>2</sup> The problem of simulating the electric and magnetic fields for a given cavity geometry is essentially defined by the boundary conditions. The simulation software triangulates the surface elements of the geometry (either constructed in the program or imported from a file) and applies material properties as specified, see Fig. 5.2. It then can search for resonant modes in a specified frequency range, or even simulate a broadband transmission or reflection spectrum of a microwave resonator, see Fig. 5.3.

When comparing different cavity designs, the main figure of merit is the single spin coupling strength  $g_0 = |g_e \mu_B (\vec{B}_0 \times \vec{e}_s) / \hbar| S$ . In the case of NV centers with  $S = 1$  it is given by  $g_0 = \alpha \gamma_e B_0$ , where  $\alpha$  is a geometric factor that describes the orthogonal projection of the field  $\vec{B}_0$  at the location of the spin onto the spin quantization axis  $\vec{e}_s$ , and  $\gamma_e / 2\pi \approx 28 \text{ MHz mT}^{-1}$  is the electron gyromagnetic ratio. When equal couplings to all four sub-directions of NV centers in a diamond are desired, this factor is  $\alpha = \sqrt{2/3}$ . As the simulated magnetic field  $\vec{B}_{\text{sim}}$  of the mode is not normalized to anything, one has to take an extra step to get the cavity’s vacuum magnetic field fluctuations  $B_0$  — the field strength associated with a “half-photon”  $\hbar\omega/2$ . It is calculated using the time-averaged total magnetic energy  $\tilde{E}_B$  (half of the maximum magnetic energy), which is conveniently simulated by the program, as  $B_0 = |\vec{B}_{\text{sim}}| / \sqrt{4\tilde{E}_B / \hbar\omega}$ . For the experiments on superradiance, another important characteristic of the cavity is the uniformity of the RF magnetic field across the spin sample. Achieving homogeneous fields involves designing current paths that mimic the geometry of a Helmholtz coil. A discussion on this approach will be provided based on real cavity designs later in this chapter.

The other significant metric is the cavity’s quality factor  $Q = \omega / 2\kappa$ , as given by the frequency  $\omega$  and the total loss rate  $\kappa$ . It is generally not accessible by simulation

<sup>2</sup>A very good starting point for doing simulations of microwave resonators is the tutorial simulation of a *Coplanar Waveguide Bandpass Filter*, which is currently accessible under the link [www.comsol.com/model/coplanar-waveguide-bandpass-filter-12099](http://www.comsol.com/model/coplanar-waveguide-bandpass-filter-12099) at the time of writing.

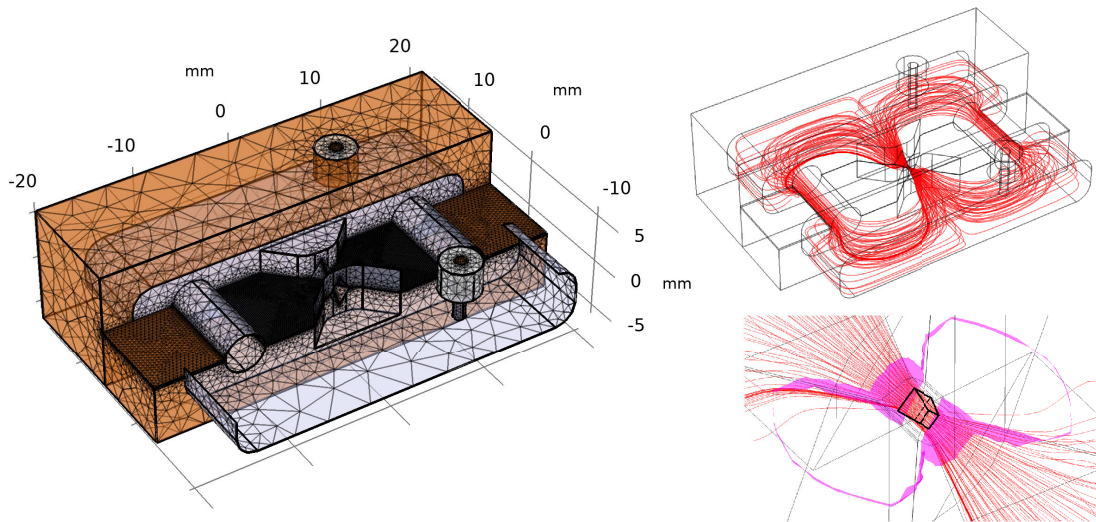


**Figure 5.2** Finite-element simulations of the LGW cavity using COMSOL. (Left) Triangulation of the surface elements and material selection for the surfaces and bulk components, with some parts hidden for visual clarity. (Top right) Streamline plot of the magnetic field distribution of the cavity mode around 3.3 GHz. The magnetic field lines form closed loops around the plate capacitances positioned symmetrically on both sides. (Bottom right) The field lines squeeze through a small opening in the center, where the cube-like NV diamond sample sits. The region inside the pink surface contains more than ten thousand times the average energy density in the simulation volume.

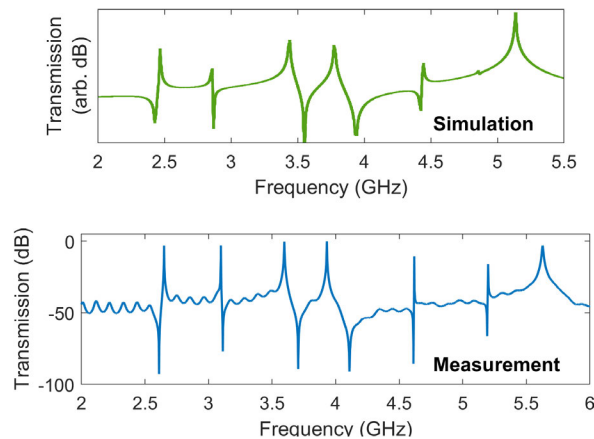


**Figure 5.3** Simulated vs. measured broadband transmission spectrum of the DCR cavity. Comparison between the simulated and measured two-port transmission shows good qualitative agreement, with all resonant features appearing in both. The main resonance of interest is around 3 GHz. The measurement's background waviness is caused by partial reflections at impedance jumps between MW line connections, with the distance between jumps given by  $L = c^*/2\Delta f$ , where  $c^* \approx 2 \times 10^8 \text{ m s}^{-1}$ .

in the same way as  $g_0$ , which is effectively a geometric quantity. The Q factor depends on specific material properties — particularly the surface conductivity — of the cavity walls and other conductive surfaces. These properties are not fully known, as they depend on material composition, as well as on surface quality. They are influenced by several factors, including surface smoothness and level of oxidation, which are hard to characterize in the cryogenic environment. In simulations, I mostly used the material properties of the standard COMSOL material library. Ultimately, only the experiment can tell the Q factor of a real cavity.

## 5.2 Microwave resonators

### 5.2.1 Enhancing the single spin coupling with nanoconstrictions

The discussion here is based on the following publication:

- **Enhanced Molecular Spin-Photon Coupling at Superconducting Nanoconstrictions**

Ignacio Gimeno\*, Wenzel Kersten\*, María C. Pallarés, Pablo Hermosilla, María José Martínez-Pérez, Mark D. Jenkins, Andreas Angerer, Carlos Sánchez-Azqueta, David Zueco, Johannes Majer, Anabel Lostao, and Fernando Luis  
ACS nano, 14(7), 8707-8715 (2020); arXiv:2006.03386

As already outlined in Sec. 4.2, a way to increase the coupling strength to a single spin lies in approximating the geometry of a one-dimensional wire, see Eq. (5.3). The magnetic field strength in such a configuration then scales as  $r^{-1}$ . However, a real wire has a finite width, setting a natural limit to the infinite magnetic field divergence at zero distance. In our publication *Enhanced Molecular Spin-Photon Coupling at Superconducting Nanoconstrictions* [63], we investigated this approach to enhance the coupling by decreasing the width of a wire using nano-fabrication techniques. The experiments and calculations were carried out in collaboration with the research group of Fernando Luis at *Instituto de Nanociencia y Materiales de Aragón* (ICMA) in Zaragoza, Spain. Here at the Atominstitut, we conducted spectroscopy measurements of DPPH molecules (a simple  $S = 1/2$  spin, see Sec. 4.2) deposited on a nanoconstriction in a coplanar-waveguide resonator. In the following, we will discuss the main results of this study, as well as further ideas on resonator designs towards the realization of strong coupling to single molecules.

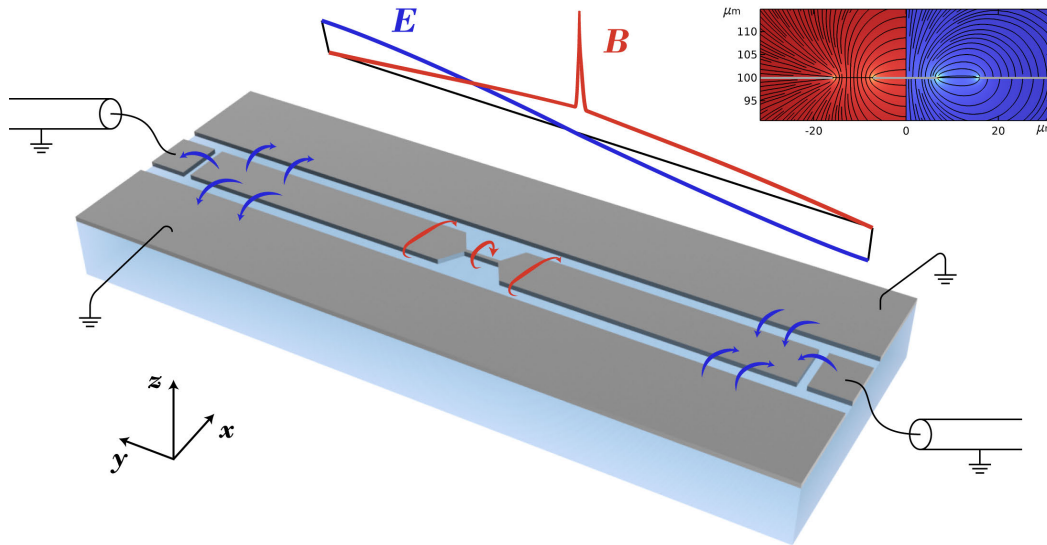


**Figure 5.4** Schematic representation of a CPW resonator with a nanoconstriction in the center, fabricated from superconducting niobium on a sapphire substrate. The nano-fabricated constriction at the center of the CPW resonator significantly enhances the local magnetic field strength. Arrows indicate the directions of the resonator's electric (shown in blue) and magnetic (shown in red) fields. The field magnitudes along the longitudinal  $y$ -axis are sketched on the right, representing a  $\lambda/2$  standing wave, while a simulated cross-section of the fields (in the  $xz$ -plane far from the constriction) is shown in the top-right corner. Microwave input and output cables depict schematically the capacitive coupling to the resonator's central wire strip.

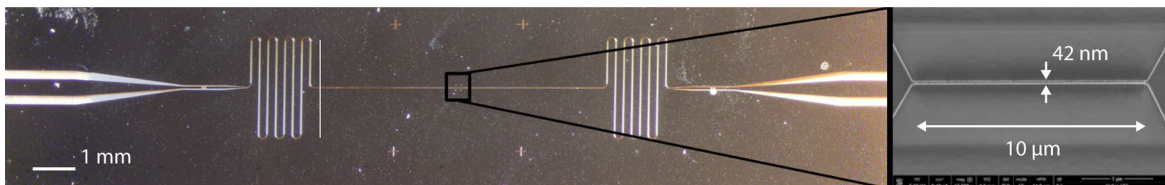


**Figure 5.5** CPW resonator with nanoconstriction in the center. (Left) Microscopy image of the superconducting niobium chip, showing the CPW resonator, with the meander structures on both sides effectively shrinking its dimensions to fit on the chip, and the in- and out-coupling ports left and right. (Right) SEM image of the nanoconstriction with a length of  $10\ \mu\text{m}$  and width  $42\ \text{nm}$  in the center of the resonator.

First, let us discuss the type of microwave resonator utilized in this study, a commonly employed resonator architecture for microwave circuit QED experiments, particularly in connection with superconducting qubits. A coplanar waveguide (CPW) — not yet a CPW *resonator* — is a type of microwave transmission line resembling a flattened coaxial cable with a central wire positioned between two ground planes and separated by a gap. When the center conductor is cut at two points, a standing wave is supported between these two points of reflection, see Fig. 5.4. The principal resonance frequency is determined by the distance  $L$  between the cut points:  $\omega_c/2\pi = c^*/2L$ . Here,  $c^*$  is the effective speed of light in the medium, which is a property influenced by the substrate material (sapphire with  $\epsilon_r \approx 12$ ) and the cross-sectional geometry of the CPW [67]. In the experiments, we use a CPW resonator made of a 150 nm superconducting niobium thin film. The middle strip has a width of 14  $\mu\text{m}$  and gap separation from the ground planes on both sides of 7  $\mu\text{m}$ , with a length of approximately 44  $\mu\text{m}$ , resulting in a fundamental resonance frequency of around  $\omega_c/2\pi \approx 1.4$  GHz.

In the center of the resonator, a 10  $\mu\text{m}$  long section of the middle strip is thinned down to a width of 42 nm using a *focused ion beam* for nano-machining. Using this technique, the niobium layer is bombarded with  $\text{Ga}^+$  ions to ablate the thin film with nanometer resolution, creating a thin wire structure — the nanoconstriction — shown in Fig. 5.5. This alteration does not have a strong effect on the CPW resonator’s frequency and Q factor, as demonstrated in Ref. [68]. However, it leads to a localized increase in the resonator’s magnetic field close to the nanoconstriction, as the RF current is concentrated to a smaller cross-section. The goal of our study is now to quantify this increase and its effect on the local single-spin coupling strength.

After this fabrication step, a droplet of DPPH solution is deposited on the nanoconstriction using *dip-pen nanolithography* [69]. This involves an atomic force microscopy (AFM) tip that carries a droplet of molecules in solution and is able to precisely deposit a defined volumetric quantity at the nanoconstriction site. The solution is prepared by dissolving the DPPH spin-1/2 molecules in the solvent N,N-Dimethylformamide with added glycerol to increase the viscosity and keep the solution from evaporating too quickly, which helps with the deposition. The distribution of deposited DPPH spins in the active coupling areas of the resonator is later determined using a combination of AFM and scanning electron microscopy (SEM) measurements at INMA.

A low-temperature spectroscopy measurement at 44 mK is carried out in our ADR fridge at the Atominstiut to investigate the collective coupling strength to the DPPH molecules after deposition at the 42 nm nanoconstriction. We use our vector network analyzer to measure in transmission while magnetically tuning the spins across

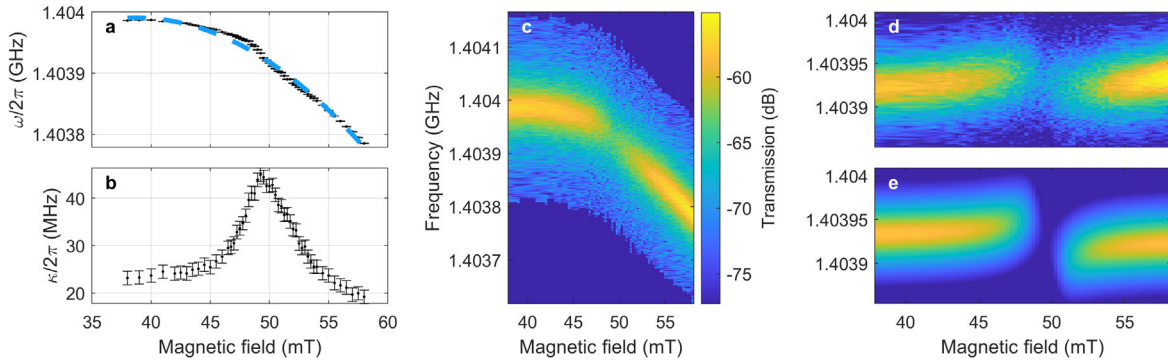


**Figure 5.6** Transmission spectroscopy versus magnetic field scan of DPPH molecules, deposited at a nanoconstriction of a superconducting CPW resonator at 44 mK. Resonance frequency (a) and linewidth (b), as determined from Lorentzian fits of the data shown as a color plot in (c). After correcting for the cavity’s magnetic field dependent resonance peak shifts with a polynomial fit, the corrected data (d) can be readily compared with the simulation (e) to estimate the collective coupling strength.

resonance with the cavity. The results are shown in Fig. 5.6. The system is weakly coupled, such that the avoided crossing on resonance is not readily observable; rather, we see an apparent broadening of the cavity linewidth. The external magnetic field direction, which is scanned along the  $x$ -axis as indicated in Fig. 5.4, is chosen due to size constraints in the cryostat. It is actually not the optimal direction for the strongest coupling, which would be the  $y$ -direction, where all spins have a quantization axis perpendicular to the resonator’s RF magnetic fields. The microwave power at the cavity input port is  $-80$  dBm, with a total downline attenuation inside the cryostat of  $-60$  dB. The resonator has a quality factor of around  $Q \approx 35\,000$  with the spins far detuned from resonance.

The first prominent feature is the shifting of the resonator peak with the external magnetic field strength, see Fig. 5.6(a,c). This effect likely arises from the type-II superconducting nature of the resonator’s niobium thin film, particularly in conjunction with the narrow dimensions of the nanoconstriction. In type-II superconductors, magnetic flux vortices can penetrate the superconducting phase above a critical field. These vortices become trapped near local defects in the superconductor, such as impurities or grain boundaries. Notably, the nanoconstriction, due to it being much narrower than the surrounding niobium structures, serves as a site for trapping these vortices, a phenomenon known as flux pinning [70]. This flux pinning introduces an effective resistance in the superconductor, leading to a shift in the resonance frequency. This shift is observed in the scans shown in Fig. 5.6, where the coupled resonator-spin

system is thermally cycled to above 5 K before it is brought to 44 mK during the cooldown procedure of the ADR fridge (see Sec. 3.1). Throughout this cooldown, the external fields are held constant at the starting value for the scan. After the thermal cycling, the system has likely settled into a “relaxed” configuration of pinned fluxes. Any change of the external field from the starting value — an unavoidable occurrence during a magnetic field scan — will then shift the resonance frequency to lower values.

Therefore, to analyze the spectroscopy results and enable comparison with a theoretical model for estimation of the collective coupling strength, this frequency shift is corrected. For this correction, a simple 2nd-order polynomial is fitted to the frequency peaks and later subtracted from the data, see Fig. 5.6(a). The model used for simulation of the corrected spectroscopy, see Fig. 5.6(d,e) for a comparison of data and simulation, is a steady-state solution of the Maxwell-Bloch equations (2.63). Instead of  $N$  spins, the ensemble of  $S = 1/2$  DPPH molecules is modeled with a single “giant” spin in the ground state, having a collective coupling strength  $g_{\text{coll}} = \sqrt{\sum g_j^2}$  and a combined decoherence rate  $\gamma = (\gamma_{\perp} + \gamma_{\parallel}/2)$ . This is a valid approximation when the effects of inhomogeneous broadening for the DPPH sample can be neglected as compared to the large linewidth  $\gamma$ . The cavity transmission then becomes

$$|T|^2 \propto \left| \frac{\langle a \rangle^2}{\eta} \right| = \left| \frac{(\gamma + i\Delta_s)}{(\gamma + i\Delta_s)(\kappa + i\Delta_c) - g_{\text{coll}}^2} \right|^2, \quad (5.4)$$

where  $g_{\text{coll}}/2\pi \simeq 1.2$  MHz and  $\gamma/2\pi \simeq 65$  MHz. The cavity linewidth  $\kappa/2\pi \simeq 20$  kHz is determined for the “empty” cavity, with the spins far detuned. The spin system, due to the low transition frequency around 1.4 GHz, is not fully polarized in the ground state at 44 mK. Therefore, the average single spin coupling strength  $g_0$  at zero temperature is calculated via the relation  $g_0^2(T=0\text{K})N_{\downarrow}(T=44\text{mK}) = g_{\text{coll}}^2$ , where  $N_{\downarrow}(T) = N[1 + \tanh(\hbar\omega_s/k_B T)]/2$ . This is the typical scaling of the collective coupling with the square root of the number of emitters  $N$  — which is effectively controlled by the temperature.<sup>3</sup>

After the cryogenic spectroscopy measurement, the spatial distribution of molecular spins is determined with a combination of AFM and SEM high-resolution imaging techniques. It is compared to a three-dimensional simulation of the magnetic fields

<sup>3</sup>The temperature dependence of the polarization for the spin-1/2 molecules is given by

$$\langle S_z(T) \rangle = \frac{\hbar}{2} N \left( \frac{e^{+\epsilon}}{e^{+\epsilon} + e^{-\epsilon}} - \frac{e^{-\epsilon}}{e^{+\epsilon} + e^{-\epsilon}} \right) = \frac{\hbar}{2} (N_{\uparrow} - N_{\downarrow}) = -\frac{\hbar}{2} N \tanh(\epsilon), \quad (5.5)$$

where  $\epsilon = \hbar\omega_s/k_B T$ .

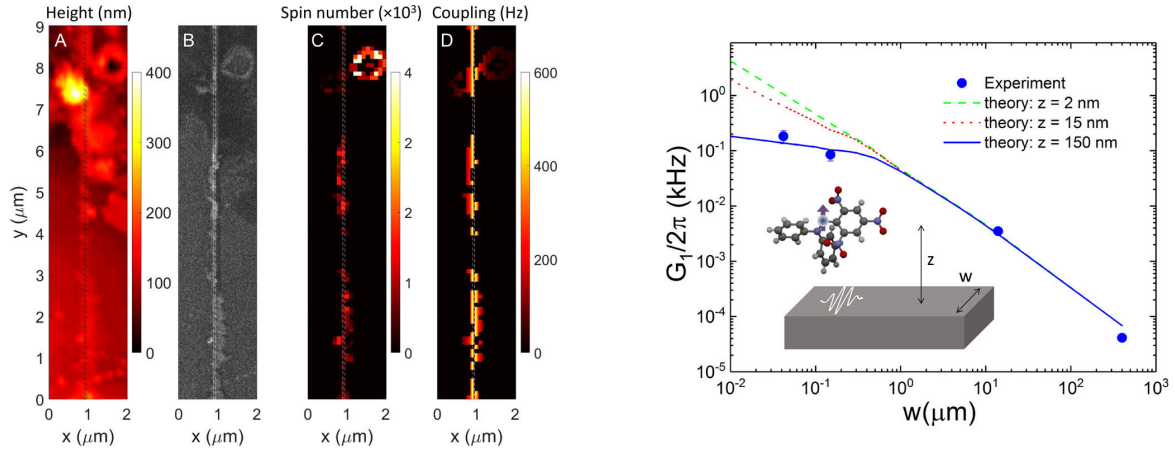


**Figure 5.7** Enhanced single spin coupling along the nanoconstriction. (Left) AFM data (A) and SEM image (B) for estimating the spatial spin distribution along the nanoconstriction. From the imaging data, a 3D map of the spin distribution (C) and in combination with a magnetic field simulation, an estimate of the spatial distribution of spin couplings (D) is attained. (Right) Combined data of the average single spin coupling (here referred to by the symbol  $G_1$ ) near the nanoconstriction from all measurements with different constriction widths. Widths other than 42 nm were measured at INMA under elevated temperature conditions of 4.2 K. The solid and dashed lines correspond to theory predictions with different distances  $z$  of the spins above the nanoconstriction.

around the nanoconstriction with a cubic cell resolution of 3 nm, to estimate the individual contributions of spins depending on their location to get an estimate of the single-spin coupling strengths  $g_0(\vec{r})$ , see Fig. 5.7 on the left. The exact methodology is described in detail in the paper [63] and will not be covered here further, as this part of the research is conducted by other co-authors.

The main results of the study are summarized in Fig. 5.7 on the right, showing a comparison of the measured average single spin coupling strength  $g_0$  across varying nanoconstriction widths  $w$ . Beyond the  $w = 42$  nm constriction measurements discussed here, the study explored other widths ranging from 158 nm to 400 μm. These experiments, similar to the ones described here although at elevated temperatures of 4.2 K, were carried out at INMA. Overall, the results show that the nanoconstriction approach is a valid method of reaching high spin-photon couplings. The average measured single spin coupling scales consistently as  $1/w$  over more than three orders of magnitude, with some spins approaching maximum couplings in the kHz range. The experimentally estimated coupling strengths only start to deviate from the  $1/w$  trend when the constriction width becomes comparable to the thickness of the su-

perconducting niobium layer. This study paves the way toward the goal of strong single-spin coupling to superconducting microwave resonators. Nevertheless, challenges remain, such as the precise delivery of the spin molecules as close to the surface of the nanoconstriction as possible. Other efforts towards this goal — on the molecular side of things — involve improving the spin molecules' coherence times, as well as increasing couplings via the dipole moment with high spin  $S$  species, as has been discussed in Sec. 4.2. Realistically, values for  $g_0$  on the order of 100 kHz are required for quantum technology applications of single molecular spins.

On the resonator side, a possible way to increase the single spin-photon coupling  $g_0$  is to use low impedance LC resonators, with maximum  $C$  and minimum  $L$  for a given resonance frequency, as already mentioned in Section 5.1 above. This approach will be further discussed below on the basis of experimentally tested cavity designs, based on both 3D bulk-machined metal cavities and 2D chip-based microwave resonators, for which the nanoconstriction approach is straightforwardly applicable.

### 5.2.2 Loop-Gap-Wedge cavity

An example of a low-impedance cavity design is shown in Fig. 5.8, given the name Loop-Gap-Wedge (LGW) cavity after the two wedge-shaped plate capacitors as the most prominent circuit elements. The LGW cavity is a 3D lumped-element resonator, where capacitance and inductance are separate structures, and draws inspiration from Ref. [71] and also from the cavity design outlined in Ref. [72].

This cavity is designed to facilitate strong and spatially homogeneous coupling to a mesoscopic diamond sample that has a cube-like shape of roughly 200  $\mu\text{m}$  size hosting approximately  $5 \times 10^{12}$  NV spins, with a resonance frequency of around 3 GHz. The reason to use a diamond sample that is three orders of magnitude smaller than the samples previously used in our lab (having typical dimensions of  $4 \times 4 \times 0.5 \text{ mm}^3$ , see e.g. in Refs. [22, 37, 73]) follows a simple logic: fewer spins means more photons per spin to cause interactions. This way, we make more efficient use of the microwave power achievable in our setup within cryogenic constraints. The intended use case for the LGW cavity is to study superradiance effects, necessitating homogeneous spin-photon couplings throughout the sample volume.

To realize these requirements, the LGW cavity design relies on short current paths with low inductance around the square-shaped center hole, where the diamond sample is placed, see Fig. 5.8(d). These short current paths connect two large capacitor structures on both sides, having an air gap of around 20  $\mu\text{m}$  and a pointed wedge shape towards the center to further narrow down the current paths. When the capacitor

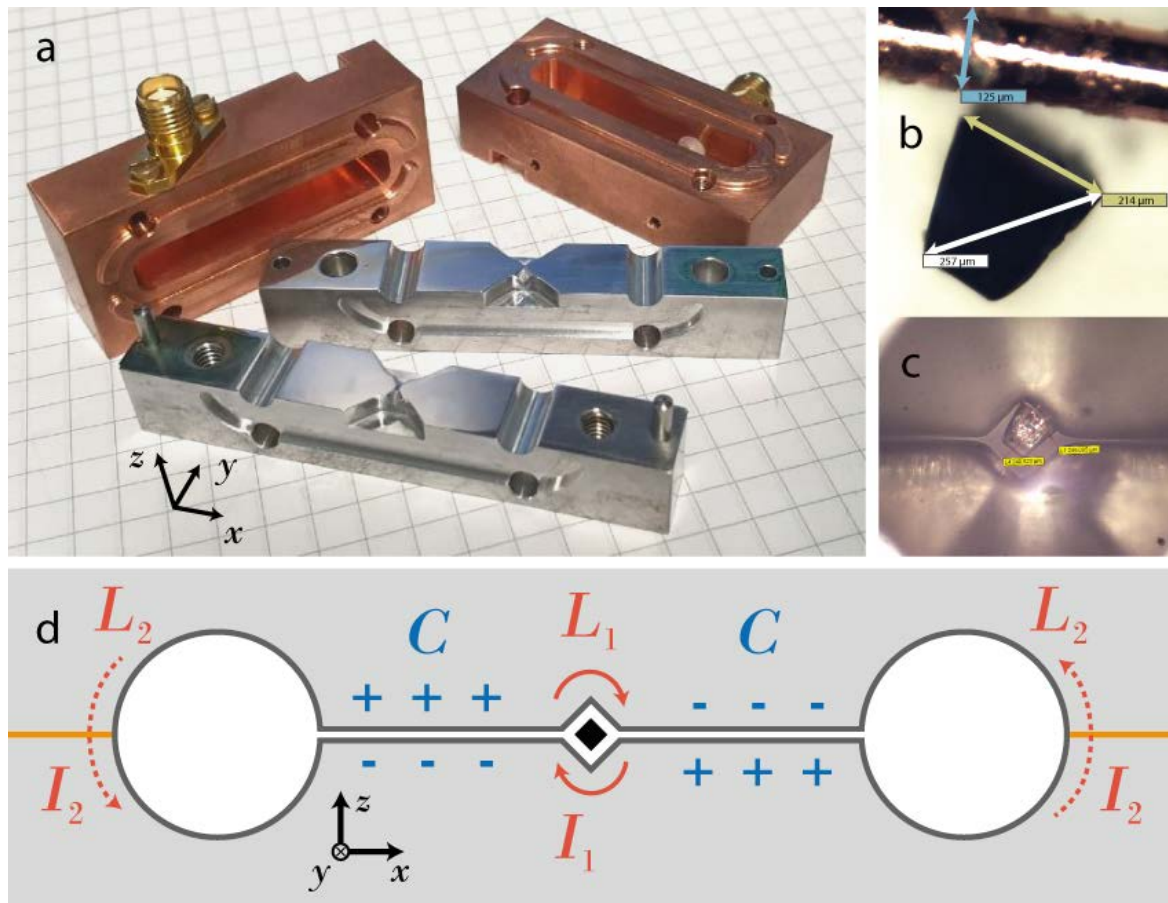


**Figure 5.8** Loop-Gap-Wedge 3D cavity. (a) Photograph of the disassembled cavity. The central part of the cavity assembly is made of two polished niobium pieces. The flat wedge-shaped mirror surfaces come together to form two plate capacitors with an air gap of  $20\ \mu\text{m}$ . Between the two capacitors, there is a small slot machined, that holds the  $200\ \mu\text{m}$  sized diamond sample. When assembled, the niobium pieces are separated by a thin isolation layer left and right, so as to not close a superconducting current loop. The assembly is completed with the copper parts on both sides, which also hold the microwave ports for in- and out-coupling, extending with little antenna pins into the cavity volume. (b) Microscope image of the diamond sample next to a  $125\ \mu\text{m}$  diameter copper wire, and (c) diamond placed inside the sample volume. (d) Schematic drawing of the capacitances and inductances in the circuit. As the current path for the inductance loop  $L_1$  in the center is much shorter than for  $L_2$ , we have  $L_1 \ll L_2$  and thus  $I_1 \gg I_2$ , leading to high RF magnetic field strengths in the center volume.

charges flow as a current from one side to the other during one-half of an oscillation period, an RF magnetic field is created in the sample hole. As the surface current is highly concentrated around the center hole, with its narrowest patch having a width only slightly larger than the sample dimensions, a normal conducting metal like copper would cause significant ohmic losses limiting the cavity's quality factor, as outlined in Section 5.1. Therefore, the choice of material fell on superconducting niobium for the two halves that make up the core of the microwave cavity. The surface currents around the walls of the sample hole mimic the current distribution of a multi-turn coil and thus create a homogeneous RF magnetic field inside the hole. Additionally, the capacitor plates on both sides are connected through significantly longer current paths on the outsides as shown in Fig. 5.8(d). These outer current paths have considerably larger inductance and contribute minimally to the total circuit inductance — a reciprocal sum for the parallel inductances — which is dominated by the currents around the center hole. The simulated RF magnetic field distribution is shown in Fig. 5.2 above.

The niobium (sourced from Xian Ocean Material Technology Co., Ltd.) and copper pieces of the LGW cavity were machined by our in-house machine shop at the Atominstitut. The niobium pieces, particularly the capacitor surfaces and the sample hole, were then polished to a mirror finish. The cavity is loaded with the N-diamond sample (c.f. Sec. 4.1.2), which is “glued” to the walls of the central hole with a small amount of vacuum grease, see Fig. 5.8(b,c). The diamond sample is oriented such that the cavity's RF magnetic field [along the  $y$ -axis in Fig. 5.8(d)] is parallel to the edges of the diamond unit-cell cube, having equal projections on all four diamond axes. A correspondence between the cube-like shape of the sample and the unit-cell cube helps with the difficult tasks of positioning the sample using a toothpick and a microscope.

An experimental characterization of the LGW cavity under millikelvin temperatures in the ADR cryostat is presented in Fig. 5.9(a,b). A magnetic field scan shows a nice avoided crossing of the coupled NV spins — a hallmark sign of the strong coupling regime. The external magnetic field in this scan is oriented parallel to the cavity RF field. This arrangement, where the normal projection of the RF field and the parallel projection of the external field have the same value of  $\sqrt{2/3}$  on the NV axes of all four sub-groups, is only possible because the NV center spin Hamiltonian has a zero-field splitting. Notably, we also see the weak coupling of another spin transition to the left of the avoided crossing in Fig. 5.9(a), caused by NV centers coupling to nearest-neighbor  $^{13}\text{C}$  nuclear spins [74]. The “empty” cavity with spins far detuned is fitted by a Lorentzian with a center frequency of  $\omega_c/2\pi = 3.093$  GHz and a linewidth of  $\kappa/2\pi = 970$  kHz, yielding a quality factor of  $Q \approx 1600$ , see Fig. 5.9(b). Notably,

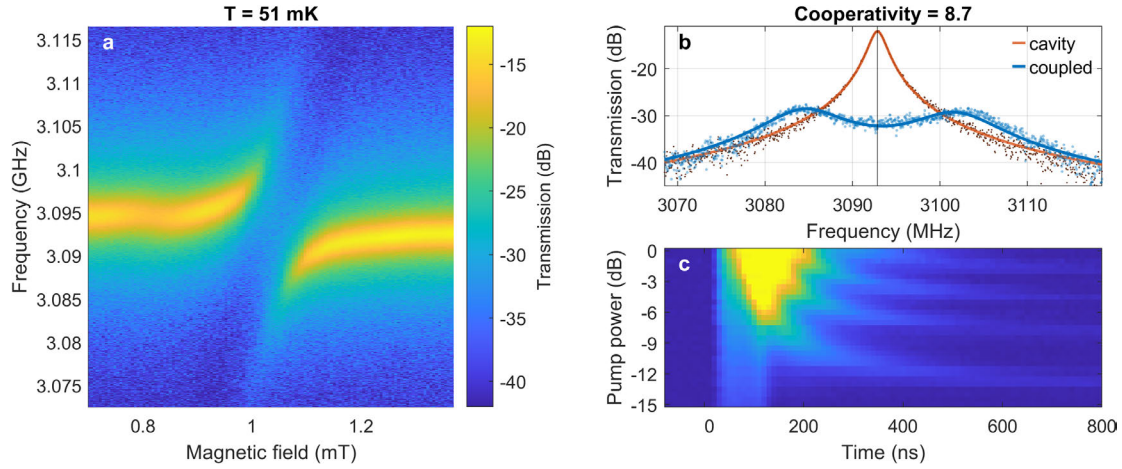


**Figure 5.9** LGW cavity: Measured collective coupling and superradiant emission. (a) Scan of the external Magnetic field showing the avoided crossing of the strongly coupled cavity-spin system. The magnetic field values are significantly lower than a naive expectation, due to the magnetic field expulsion by the superconductor. (b) Lorentzian fit of the “empty” cavity (red line) and fit of the normal mode splitting on resonance (blue line) with  $B_{\text{ext}} \approx 1$  mT. (c) Time-resolved superradiant emission dynamics after a 100 ns inversion pulse with increasing power measured in the dilution fridge, cf. Sections 2.9 and 6.0.2.

during other cooldowns, a higher Q factor of around 3000 is achieved with the diamond sample present — the quality factor is highly dependent on the surface quality of the niobium and also influenced by the amount of vacuum grease used for holding the diamond in place. The unloaded cavity initially had  $Q \approx 8000$ , suggesting that the sample introduces significant photon loss.

The normal-mode splitting of the system with the spin ensemble on resonance is fitted with a steady-state solution of the Maxwell-Bloch equations, see Fig. 5.9(b). The parameters for the fit reveal a collective coupling strength of  $g_{\text{coll}}^{\text{fit}}/2\pi = 7.4$  MHz, using a  $q$ -Gaussian spin distribution of width  $W/2\pi = 17$  MHz and shape parameter  $q = 1.39$  (see Sec. 2.8 for details on the simulation method, other model parameters are  $\gamma_{\perp}/2\pi = 177$  kHz and  $\gamma_{\parallel} = 0$ ). Correcting for the reduced NV ground state polarization at the scan-temperature of 51 mK, with  $P_{m_S=0}(T = 51 \text{ mK}) \approx 90\%$  [see Eq. (4.2)], yields a slightly higher experimental value of the collective coupling  $g_{\text{coll}}/2\pi = 7.7$  MHz.

A comparison of the measured coupling strength to the COMSOL simulation and to a simple geometric estimate is presented in Table 5.1 together with a measure of the field homogeneity calculated from the simulated field distribution. The sample shape in the simulation is a truncated pyramid with rectangular bottom and top faces

**Table 5.1** Simulated parameters of the LGW cavity. The collective coupling strength is evaluated as an integral over the sample volume using the spin density and the simulated distribution of the vacuum fluctuation RF magnetic field  $B_0^{\text{sim}}$  as outlined in Section 5.1, taking the NV orientations into account. The simulated value of  $\overline{B_0^{\text{sim}}}$ , averaged over the sample volume, can be readily compared to the estimated theory result  $\mathcal{B}_0 = \sqrt{\mu_0 \hbar \omega_c / 2V_{\text{eff}}}$ , where an effective mode volume  $V_{\text{eff}} = 300 \times 300 \times 400 \mu\text{m}^3$  is used, which approximately corresponds to the sample hole size. The field homogeneity is quantified using the standard deviation of the RF field in the sample volume  $\sigma(|B^{\text{sim}}|)$ , or in more simple terms, as the ratio of minimum over maximum.

$\omega_c^{\text{sim}}/2\pi$	$g_{\text{coll}}^{\text{sim}}/2\pi$	$\overline{B_0^{\text{sim}}}$	$\mathcal{B}_0(V_{\text{eff}})$	$\sigma( B^{\text{sim}} )$	$\frac{\min  B^{\text{sim}} }{\max  B^{\text{sim}} }$
3.3 GHz	6.8 MHz	128 pT	195 pT	$8.7 \times 10^{-3}$	92%

of roughly  $210 \times 190 \mu\text{m}^2$ , and  $120 \times 100 \mu\text{m}^2$  respectively, and a height of  $210 \mu\text{m}$ , resulting in a volume of  $5.16 \times 10^6 \mu\text{m}^3$  [see Fig. 5.8(b)]. The number of NV spins in the simulation follows from the density of carbon in diamond  $n_c = 1.755 \times 10^{23} \text{cm}^{-3}$  and an NV concentration of 6 ppm.

The coupling comparison agrees well with the measurement within 88%, with the simulation slightly underestimating the measured collective coupling. This could have many reasons, the most critical being likely the unknown exact dimensions of the diamond sample — for a fair comparison of different cavity design simulations below, we will keep these dimensions fixed from now on. Moreover, the simulated and measured cavity resonance frequencies agree even better within 94%. Notably, the cavity frequency is tunable by varying the torque on the screws used to hold the two niobium pieces together. This changes the gap size  $d$  of the capacitors, thus the total capacitance with a  $1/d$  dependence.

A surprising result is the low external magnetic field value  $B_{\text{ext}} \approx 1 \text{mT}$  on resonance, see Fig. 5.9(a). A rough estimate for the expected resonance magnetic field strength is calculated as  $B_{\text{ext}} \approx (\omega_c - D_{\text{zf}}) / \sqrt{\frac{2}{3}} \gamma_e \approx 9.6 \text{mT}$ , using the zero-field splitting parameter  $D_{\text{zf}}$  and the gyromagnetic ratio  $\gamma_e$  from Sec. 4.1.1. An explanation for the factor 10 difference is offered by the superconductivity of the niobium: it acts like a perfect diamagnet at low fields and will sustain surface currents that shield the bulk from having a non-zero magnetic flux density. Therefore, the magnetic fields in the vicinity of the niobium surface will be “deformed”, as shown in Fig. 5.10, leading to focussing and amplification of the static field in the sample hole. This property of the LGW cavity is also its biggest drawback, as it makes it impossible to change the field orientation

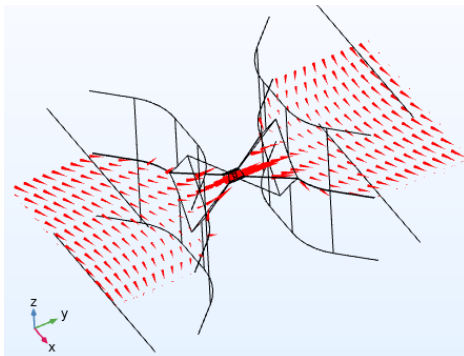


**Figure 5.10** Static magnetic field deformation near a perfect diamagnet superconductor in the Meissner phase. Vector field plot of the simulated external magnetic fields in the  $z = -50 \mu\text{m}$  plane ( $z = 0$  corresponds to the center of the sample volume). The magnetic field direction far away from the superconductor in this simulation is along  $(1, 1, 0)^T$ , but in the small sample hole, it is only along the  $y$ -axis. To simulate this effect, the niobium material has an almost zero relative permeability of  $\mu_r = 1 \times 10^{-5}$ .

for tuning the NV spins into resonance — only fields passing straight through the sample hole are possible. In order to have the four sub-groups of NV directions nicely aligned, one has to perfectly place the sample with the correct orientation. This is very challenging, as the only feedback one can get is the cryogenic experiment with cooldown times lasting at least a day. Imperfect alignment leads to a splitting of the NV sub-groups and a broadening of the spin distribution width  $W/2\pi = 17 \text{ MHz}$  in the fits shown in Fig. 5.9(b), which is almost twice as large as the later determined value of  $9.2 \text{ MHz}$ . For this reason, the LGW cavity design is abandoned in favor of the next cavity design presented below. Nevertheless, we were able to successfully measure superradiant dynamics as teased here in Fig. 5.9(c). The curious reader is referred to the later treatment of this type of measurement results in Ch. 6.

### 5.2.3 Double-Chip resonator

To combat the unwanted effect of magnetic field expulsion by the bulk niobium, while realizing the same design requirements of strong and homogeneous coupling to a  $200 \mu\text{m}$  sized diamond sample, I came up with the Double-Chip resonator (DCR) design. This design proved to be very useful and is the cavity utilized in the main publications covered in this thesis, Refs. [35, 75]. My idea was to realize a similar configuration as the LGW cavity — large capacitor pads and a small current loop to create a low-impedance circuit — in a 2D superconducting chip assembly.

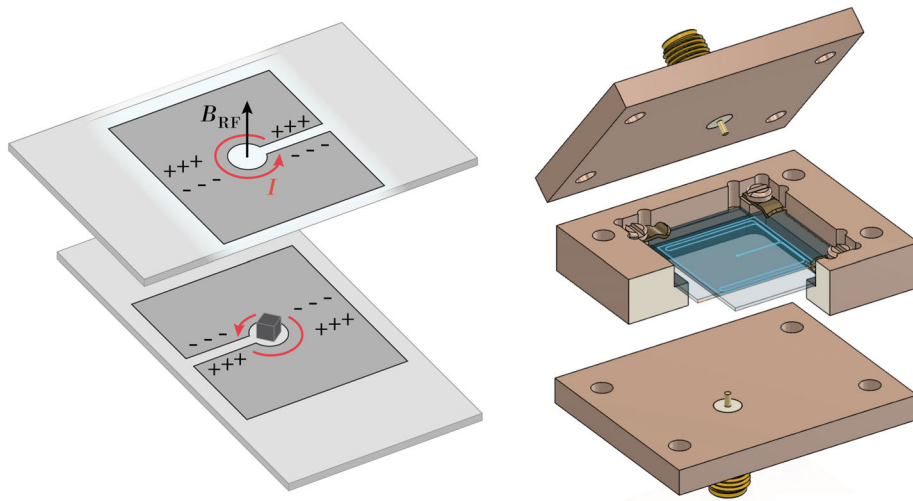


**Figure 5.11** Double Chip Resonator. (Left) Schematic illustration of the double chip assembly with inward-facing split-ring structures made of a superconducting niobium thin film (exploded view). During one half-oscillation period, a charge imbalance is accumulated on the large capacitor surfaces, creating an edge current around the center hole, when the charges swap sides. This current creates a homogeneous RF magnetic field throughout the diamond sample in the center. (Right) The two chips, with the diamond sample sandwiched between them, are enclosed inside a copper box, shown with open top and bottom lids, along with in- and out-coupling antenna pins.

The DCR cavity, illustrated in Fig. 5.11, consists of two superconducting chips mounted inside a copper box, arranged in parallel with a gap of  $250\ \mu\text{m}$  between them. Each chip is patterned with a split-ring structure, featuring an approximately  $16 \times 16\ \text{mm}^2$  square shape with a small  $380\ \mu\text{m}$  diameter hole at its center. The circular hole is partially opened on one side by a  $4\ \mu\text{m}$  slit extending outwards. This slit divides the plane into two sides, thereby creating two large capacitive surfaces. A split-ring resonator [76] is a planar realization of the archetypical LC circuit diagram, as illustrated in Fig. 5.1. However, the capacitance in a planar circuit is inherently limited by the dimensionality.<sup>4</sup> Hence, to create the desired combination of high capacitance and low inductance, the planar structure is extended into the third dimension, thereby realizing two plate capacitors, as shown in Fig. 5.11 on the left. The short current paths around the center holes serve as inductive elements on both sides, where the RF current is pushed towards the hole perimeter due to the skin effect. This creates a current geometry that is reminiscent of a one-turn Helmholtz coil, thus generating a homogeneous RF magnetic field in the center, oriented perpendicular to the chip planes. The chip layout for the patterned niobium layer with  $200\ \text{nm}$  thickness is presented in Fig. 5.12(a). It features an additional large inductance connecting the two capacitor pads on each chip through an outer current loop. Since this current path is considerably longer than the small center hole, it contributes minimally to the overall inductance. The reason for including it in the design is twofold: (i) both DCR chips resemble the layout of the established LGW resonator, particularly its cross-section in Fig. 5.8(d); and (ii) it is thought to confine the RF fields closer to the chip planes. In this configuration, the total magnetic flux remains constant inside a superconducting loop. Consequently, the RF field lines passing through the small center hole need to re-enter through the two larger holes on both sides and are held closer together. This is expected to reduce the amount of eddy currents in the copper walls, thus leading to an improved Q factor.

The copper housing of the DCR cavity consists of three parts, as shown in Fig. 5.11 on the right: a central frame, a top cover, and a bottom cover. The center box has two sets of shelves at different levels rotated  $90^\circ$  relative to each other. On these shelves, the sapphire chips with  $0.5\ \text{mm}$  thickness are held in place using copper clamps and screws, see Fig. 5.12(c). The in- and out-coupling ports are coaxial MW antennas, which capacitively couple to the mode. They are placed diagonally opposite to each other, with the antennas positioned to one side of the slit structure in the pattern on each

---

<sup>4</sup>Increasing capacitance in a planar metalized structure can be achieved using interdigit-finger capacitors, although this comes at the expense of increased parasitic inductance, as each finger forms a small wire.

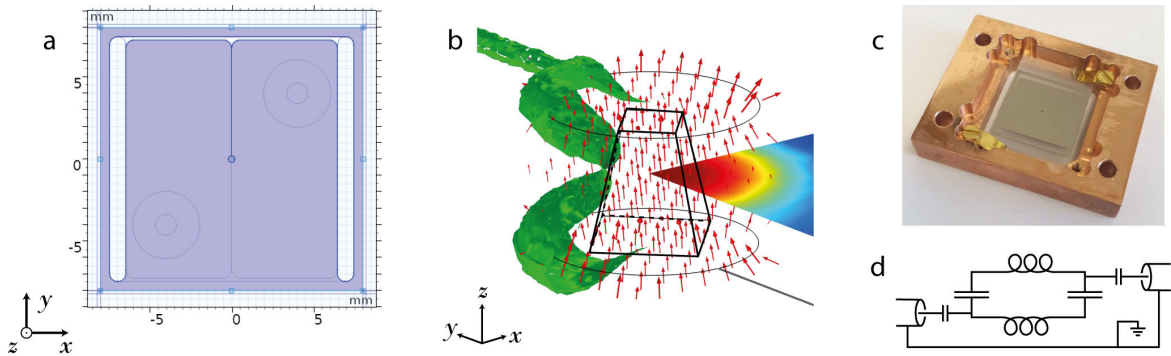


**Figure 5.12** DCR chip layout and field homogeneity. (a) Niobium pattern of a single chip with  $380\ \mu\text{m}$  diameter hole in the center and  $4\ \mu\text{m}$  slit reaching outwards. The air gap between both resonator chips is  $250\ \mu\text{m}$ . Note that the placement of the second chip results from a  $180^\circ$  rotation around the  $x$ -axis. (b) COMSOL simulation of the RF magnetic field in the sample volume between the center holes of both chips. Red arrows indicate the field direction and strength (also shown by the color plot inset). The green surface encloses a region with a less than 5% deviation from the average  $|B_{\text{osc}}|$  in the sample volume. (c) Photograph of the copper holder with only the bottom chip shown. (d) Equivalent circuit diagram of the DCR cavity.

chip. This configuration is designed to minimize direct cross-talk between the ports, which could otherwise produce a distinctly asymmetric Fano-lineshape [77] in the DCR cavity resonance. The copper parts were machined by our in-house machine shop at the Atominstitut, and the chips were sourced from the company Star Cryoelectronics.

The big advantage of the DCR cavity design, as compared to the LGW cavity, is that the external magnetic tuning field is not deformed, at least when it is applied parallel to the chip planes. In this orientation, field lines can pass virtually unchanged above and below the superconducting niobium thin film. This allows changing the angular orientation of the tuning field in the chip plane, which makes it much easier to align all 4 NV sub-groups and tune them into resonance with the cavity, when the cube-shaped diamond sample is placed flat onto the “bottom” chip. Other orientations are also possible, which result in equal projections of the tuning field for 2 and 2 NV sub-groups. For 1 and 3 NV sub-groups, a magnetic field component out of the chip planes is needed, which is not favorable in the planar superconducting configuration.

In Fig. 5.13, experimental results are presented, which characterize the DCR cavity coupled to a roughly  $200\ \mu\text{m}$  sized N-diamond sample at 24 mK, where the NV ground state polarization is more than 99%. The magnetic field direction for the scan in Fig. 5.13(a) is parallel to the chip plane, oriented along the  $xy$ -direction in Fig. 5.12(a,b) and has equal projections onto all 4 NV directions. The “empty” cavity

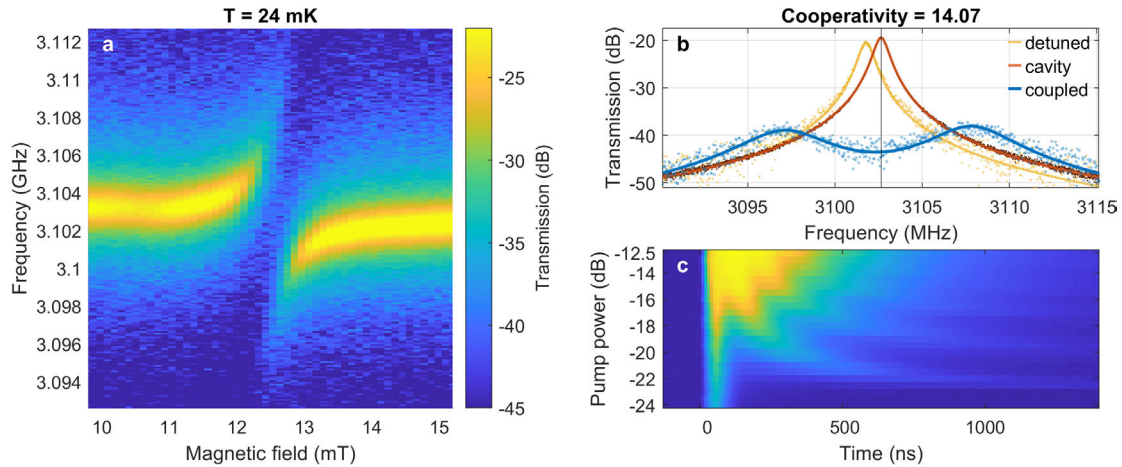


**Figure 5.13** DCR cavity: Measured collective coupling and superradiant emission. (a) Avoided crossing in the transmission spectroscopy versus magnetic field scan, measured in the dilution fridge. (b) Using high MW input power, the “empty” cavity is measured and fitted with a Lorentzian (red line). At low MW input power, the normal-mode splitting is measured and fitted for the system on resonance (blue line), and with the detuning loop current switched off (yellow line, see discussion below). (c) Time-resolved superradiant emission dynamics after a 100 ns inversion pulse with increasing power, cf. Sections 2.9 and 6.0.2.

signal is obtained by measuring the transmission at a high MW input power, thus driving the spin ensemble into a mixed state with net polarization zero, which effectively decouples the spin system and the cavity. In Fig. 5.13(b), it is fitted by a Lorentzian with a center frequency of  $\omega_c/2\pi = 3.103$  GHz and a linewidth of  $\kappa/2\pi = 420$  kHz, yielding a quality factor of  $Q \approx 3700$ . Again, the Q factor is highly dependent on the surface cleanliness. Initially, pristine chips directly from the factory yielded quality factors exceeding 10 000 for the DCR cavity when loaded with the sample. The quantity of vacuum grease utilized as a sample “glue” also plays a role. Through successive cooldown cycles, the DCR cavity with internal detuning loop (see discussion below) experienced a gradual increase in its Q factor, rising from approximately 1500 to higher values around 3700. This enhancement is likely a result of the gradual evaporation of excess grease. The transmission spectroscopy with the spins in the ground state on resonance is fitted with a steady-state solution of the Maxwell-Bloch equations in Fig. 5.13(b), revealing a collective coupling strength of  $g_{\text{coll}}^{\text{fit}}/2\pi = 4.6$  MHz, using a  $q$ -Gaussian spin distribution of width  $W/2\pi = 9.2$  MHz and shape parameter  $q = 1.39$  (the simulation method is detailed in Sec. 2.8, other parameters are  $\gamma_{\perp}/2\pi = 177$  kHz and  $\gamma_{\parallel} = 0$ ).

**Table 5.2** Simulated parameters of the DCR cavity. Compare with Table 5.1, where the same evaluation method is used for the LGW cavity design. The geometric estimate  $\mathcal{B}_0^{\text{geom}}$  is calculated by assuming a perfect plate capacitor geometry and circular current paths around the center holes, see text.

$\omega_c^{\text{sim}}/2\pi$	$g_{\text{coll}}^{\text{sim}}/2\pi$	$\overline{B}_0^{\text{sim}}$	$\mathcal{B}_0^{\text{geom}}$	$\sigma( B^{\text{sim}} )$	$\frac{\min  B^{\text{sim}} }{\max  B^{\text{sim}} }$
3.0 GHz	4.7 MHz	92 pT	108 pT	$42.3 \times 10^{-3}$	63%

A comparison of these experimentally determined values with the COMSOL simulation is offered in Table 5.2, showing a very good agreement. For the DCR cavity, it is possible to calculate a “geometric” estimate of the magnetic field’s vacuum fluctuations, denoted as  $\mathcal{B}_0^{\text{geom}}$ . We assume the LC circuit diagram shown in Fig. 5.12(d), and an ideal plate capacitor geometry with  $C_1 = \epsilon_0 A/d$ . The area for one capacitor plate — roughly half of the blue shaded area in the chip layout of Fig. 5.12(a) — is approximately  $A = 8 \times 16 \text{ mm}^2$  and the plate distance is  $d = 250 \text{ }\mu\text{m}$ , resulting in  $C_1 \approx 4.53 \text{ pF}$ . The total circuit capacitance, with both plate capacitors  $C_1$  in series, is given by  $C = C_1/2$ . Then, we combine the formula for the LC resonance frequency with the total energy in an LC circuit, where the magnetic half of the vacuum energy will be produced by the root-mean-square RF current  $I_0$ , arriving at

$$\left. \begin{aligned} \omega_c &= \frac{1}{\sqrt{LC}} \\ \frac{1}{4} \hbar \omega_c &= \frac{1}{2} L I_0^2 \end{aligned} \right\} I_0 = \sqrt{\frac{\hbar \omega_c^3 C}{2}} \approx 28 \text{ nA}, \quad (5.6)$$

where we use the value  $\omega_c/2\pi = 3 \text{ GHz}$ . From this estimate, we can calculate the magnetic field produced by a circular current loop, which represents the current flow around the center hole on each chip. While the details of this calculation are well-documented in textbooks (e.g. Ref [78]) and will not be elaborated on here, the key parameters used include a radius of  $r = 190 \text{ }\mu\text{m}$ , a distance from the circle plane of  $z = 125 \text{ }\mu\text{m}$ , and a configuration with two one turn coils with a separation  $2z$ . This yields an estimated geometric field strength of  $\mathcal{B}_0^{\text{geom}} \approx 108 \text{ pT}$ . Remarkably, this estimate closely aligns with the simulated value, indicating that the DCR cavity concept represents a near-optimal realization of a 2D low-impedance circuit design. The simulated RF field homogeneity within the sample volume is slightly lower compared to that of the LGW cavity, with the ratio of minimum over maximum field strength approximately at 63%, although this ratio is influenced by the most extreme spots. However, the local

deviation from the average field strength within the sample volume remains below 5% across almost all areas, as depicted in the isosurface plot in Fig. 5.12(b).

### Rapid magnetic field switching inside the DCR cavity

A very useful feature of the DCR cavity design is its compactness. As the magnetic mode is spatially confined close to the chips, and the electric fields are enclosed even tighter between the capacitor plates, it is possible to wind a small coil directly around the chip stack, without negatively impacting the cavity resonance, as shown in Fig. 5.14 on the left. This coil is used for rapidly tuning the spins in and out of resonance with the cavity mode in about 200 ns. In our setup, a current of 1 A passing through this low-inductance coil, made of four coil turns of superconducting wire, can be switched off in roughly 200 ns using a semiconductor switch. The field created by this current in the sample volume is sufficiently homogeneous and has a strength of  $B_{\text{loop}} \approx 1.1$  mT. The experimental characterization of the DCR cavity in Fig. 5.13 were measured with the detuning loop in place. For tuning all four NV sub-directions into resonance with the cavity while  $B_{\text{loop}}$  is maintained [blue curve in Fig. 5.13(b)], the sample and the external field direction are aligned within the chip plane at  $45^\circ$  relative to the rectangular chips, to match the loop orientation. When the loop current is switched off [yellow curve in Fig. 5.13(b)], the spins are detuned by  $\delta/2\pi \approx 25$  MHz, and the spin ensemble is effectively decoupled from the cavity — the transmission signal then looks similar to the empty cavity resonance, but having a finite dispersive-shift [c.f. Sec. 2.4]. This rapid detuning capability is useful for protocols that rely on storing the spin inversion after an inversion pulse. Subsequently, after a variable storage time, the ensemble can be brought back into resonance to release the stored inversion in a superradiant pulse, see Ch. 6.

### Integrating a nanoconstriction into the DCR cavity

As previously mentioned, the DCR cavity design is a near-optimal realization of a low-impedance circuit design.<sup>5</sup> Naturally, the nanoconstriction approach lends itself to be used for such a cavity design, when the goal is to achieve strong single

---

<sup>5</sup>Even better would be to have only two capacitor plates connected by a single wire — the simplest form of an LC circuit — instead of an arrangement of effectively four plates connected with two separate current paths on both sides as in the DCR design. However, this is much harder to achieve with a 2D design approach. It would necessitate a multilayer pattern on a chip with a dielectric separation layer between the capacitor pads and a wire-like inductance loop, as proposed in Ref. [79]. In this case, dielectric losses need to be considered and could potentially limit the achievable Q factors. Generally, the fabrication of such a design is much more technically demanding.

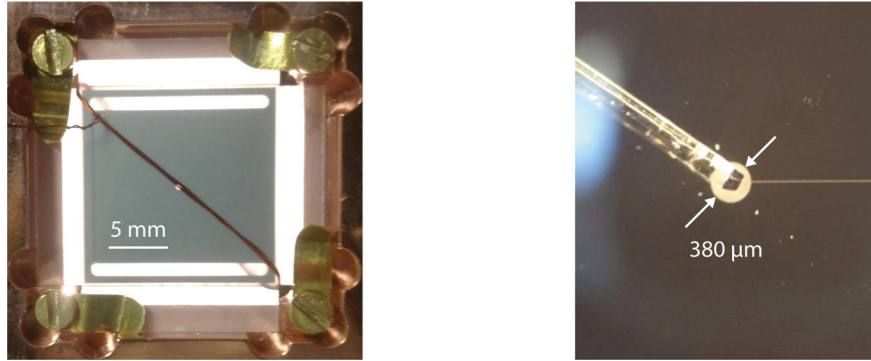


**Figure 5.14** DCR cavity: detuning loop and optical fiber access. (Left) A magnetic detuning loop, consisting of 4 windings of superconducting wire, can be wrapped directly around the double chip assembly. In the experiment it is used for rapidly detuning the spins from resonance and back again. (Right) An attempt at building a superradiant maser: the diamond sample is glued to the tip of an optical fiber, which enters through a small hole in the copper housing. The fiber is sandwiched between the two chips and oriented to align one NV direction with the external tuning field — in this case along the slit structure to the right.

spin-photon coupling, see Fig. 5.15. To investigate the feasibility of integrating a nanoconstriction into a DCR cavity, superconducting chips were fabricated by the company Star Cryoelectronics and later nano-machined with the focused ion beam technique at INMA in Zaragoza. For these chips, designed to operate at around  $\omega_c/2\pi \approx 2.5$  GHz with the help of COMSOL simulations, the dimensions for the capacitor surfaces (half of one chip square) are  $A = 16 \times 8 \text{ mm}^2$  and the plate separation is  $d = 50 \text{ }\mu\text{m}$ . The bottom chip pattern of the two DCR chips, see Fig. 5.15(a), features a  $1 \text{ }\mu\text{m}$  slit and a circular  $150 \text{ }\mu\text{m}$  hole. The upper chip has the same hole, but the slit extends on the other side as well, and the two capacitor surfaces are only connected via a narrow bridge of width  $1 \text{ }\mu\text{m}$ , see Fig. 5.15(c,d). This bridge is later thinned down to a width of only  $\sim 100 \text{ nm}$  to create the nanoconstriction. The nanoconstriction DCR cavity is designed to minimize the ratio  $L/C$  even further than the previous DCR chips, and the outer large current loop [see Fig. 5.12(a)] is left out completely.<sup>6</sup>

The nanoconstriction DCR cavity is characterized experimentally in our ADR refrigerator at around  $60 \text{ mK}$  and showed a strong coupling of  $g_{\text{coll}}/2\pi \approx 30 \text{ MHz}$  to a large ensemble of approximately  $1 \times 10^{16}$  DPPH molecules covering a large  $\sim 1.5 \text{ mm}$  area in the center of the “upper” chip with the  $\sim 100 \text{ nm}$  constriction, see Fig. 5.15(b,e).

<sup>6</sup>This leaving out of the large outer current loop likely gives rise to the asymmetric Fano resonance of the nanoconstriction DCR cavity, as shown in Fig. 5.15(b).

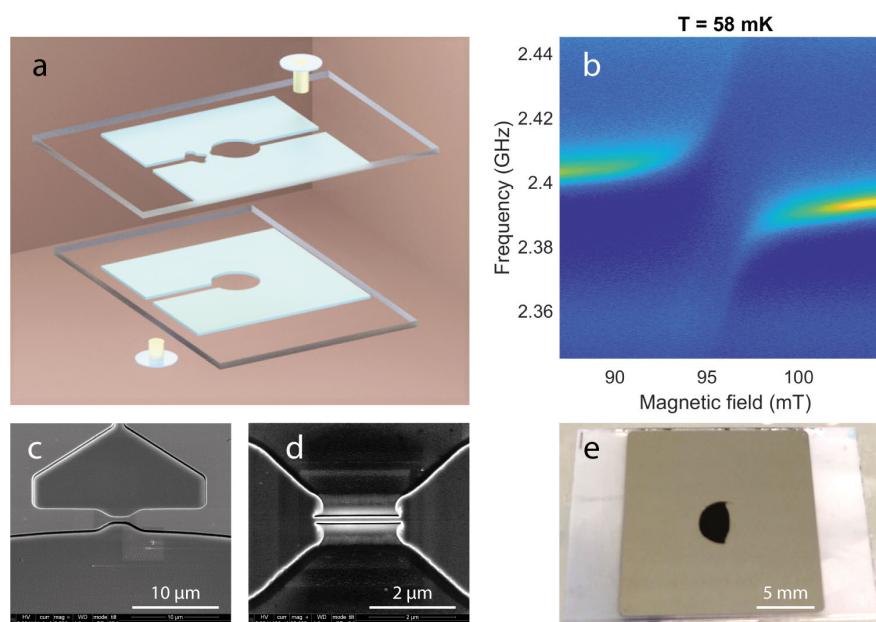


**Figure 5.15** DCR cavity with nanoconstriction. (a) Schematic layout of the two chips. The upper chip has only a single wire next to the center hole that connects the two capacitor sides, whereas the lower chip is similar to the DCR design discussed above. (b) Magnetic field scan of DPPH molecules coupled to the DCR cavity, measured in the ADR fridge. SEM image before (c) and after (d) a nanoconstriction of width  $\sim 100$  nm is machined. (e) Photograph of the  $16 \times 16$  mm<sup>2</sup> chip (nanoconstriction side) with a dried droplet of DPPH solution containing approximately  $1 \times 10^{16}$  spins.

The maximum quality factor for the DCR cavity with nanoconstriction is measured at  $Q \approx 12000$ . Unfortunately, the large deposition area of the DPPH molecules does not allow us to estimate the contributions of individual spins at the constriction — the DCR chips are too large for an AFM scan - and is only an experimental proof of the general feasibility of this approach.

We can still directly calculate the expected increase of the spin-photon coupling  $g_0 \propto I_0$  in the vicinity of the nanoconstriction for a low-impedance DCR design as compared to a CPW resonator, with a typical impedance  $Z_{\text{CPW}} = 50 \Omega$ , as the CPW resonator from Ref. [63] discussed above. We revisit this topic by looking at the zero-point fluctuation current  $I_0$  of Eq. (5.6), slightly rewritten using the definition for the circuit impedance  $Z_0 = \sqrt{L/C}$

$$I_0 = \sqrt{\frac{\hbar\omega_c^2}{2Z_0}}. \quad (5.7)$$

The circuit impedance for the DCR design is calculated as  $Z_{\text{DCR}} = 1/\omega_c C$ , with the total circuit capacitance given by  $C = C_1/2 = \frac{1}{2}\epsilon_0 A/d$  (see discussion above), resulting in  $Z_{\text{DCR}} \approx 5.6 \Omega$ . This leads to an expected increase of the current  $I_0$  and thus the RF magnetic field at the nanoconstriction by a factor of roughly  $\sqrt{Z_{\text{CPW}}/Z_{\text{DCR}}} \approx 3$  when the resonance frequency  $\omega_c$  is assumed to be the same. While not enough to reach the strong coupling regime to a single spin, this estimated increase — and the experimental evidence as feasibility proof — marks another step towards achieving this goal. Notably, a circuit impedance of  $5.6 \Omega$  does not constitute the ultimately achievable value and can be further decreased by reducing the chip distance and the inner hole diameter. Additionally, increasing the resonance frequency  $\omega_c$  is another possible avenue for improvement of  $g_0$ .

### **Attempt at realizing a superradiant diamond maser with the DCR cavity**

Finally, to conclude this exploration of potentials offered by the DCR cavity design, I discuss an attempt at realizing a superradiant diamond maser with the DCR cavity as shown in Fig. 5.12(a). A 200  $\mu\text{m}$  optical fiber enters the cavity through a small hole in the copper housing. The diamond sample is glued on the flat tip of the fiber using an optically clear ultraviolet curing adhesive. The fiber is oriented between the chips at an angle that allows to approximately find a good alignment of the NV diamond with the external field; see Fig. 5.14. This alignment of the NV axis parallel to the external field and orthogonal to the cavity's RF field is a necessary requirement for achieving a superradiant maser, as discussed in Sec. 4.1.1. This attempt turned out to be unfruitful,

as the intense green laser light used for optical pumping completely destroyed the cavity resonance peak. This effect is attributed to a breakdown of superconductivity, as the high-energy photons break apart the Cooper pairs.

A possible way to mitigate this problem is to have the fiber enter from the “top” in a direction perpendicular to the chip planes, requiring a borehole in the sapphire chips. This configuration would allow the pump light to exit on the opposite side without hitting the niobium layer. Unwanted light on the superconducting layer could be further prevented by a reflective coating around the diamond and the fiber tip. Additionally, the boreholes in the chips’ sapphire substrate would allow the placement of the chips closer together than the diamond sample size — where the sample now extends partially outside the niobium layers — and the RF magnetic field is even more strongly focused. In conclusion, although not successful, this initial attempt at building a superradiant maser provided many valuable insights for future explorations.

#### 5.2.4 3D-Cavity towards a superradiant diamond maser

The development of a superradiant diamond maser represents a significant step forward in quantum technologies with solid-state spin platforms, providing a robust and compact system with the potential for room-temperature operation. Its potential applications include precise microwave frequency sources with ultra-narrow linewidths, quantum-limited microwave amplification [80], and new possibilities for studying quantum effects in microwave cavities at room temperature [81]. Progress towards this goal includes the first continuous-wave room-temperature diamond maser in 2018 [56]. However, this system did not reach the high-cooperativity regime ( $C > 1$ ) needed for superradiant emission. Recent theoretical work suggests that a carefully designed system of NV centers strongly coupled to a microwave cavity could achieve continuous wave superradiant emission with optical pumping [57]. With these considerations in mind, I developed a new microwave cavity design called the Maser-3D (M3D) cavity. This design aims to create the conditions necessary for a superradiant maser: the strong and uniform cavity-spin coupling, combined with optical access for pumping of the masing transition. The M3D cavity combines elements from both the LGW and DCR cavities, integrating the strengths of 2D and 3D lumped element cavities. A key feature of this new design is the incorporation of an optical fiber, which is crucial for its intended operation.

This cavity design is shown in Fig. 5.16(a). At its heart, the M3D cavity shares a fundamental concept with the DCR cavity: two flat metal surfaces, separated by a small air gap, form mirrored capacitor structures and allow the RF magnetic field lines

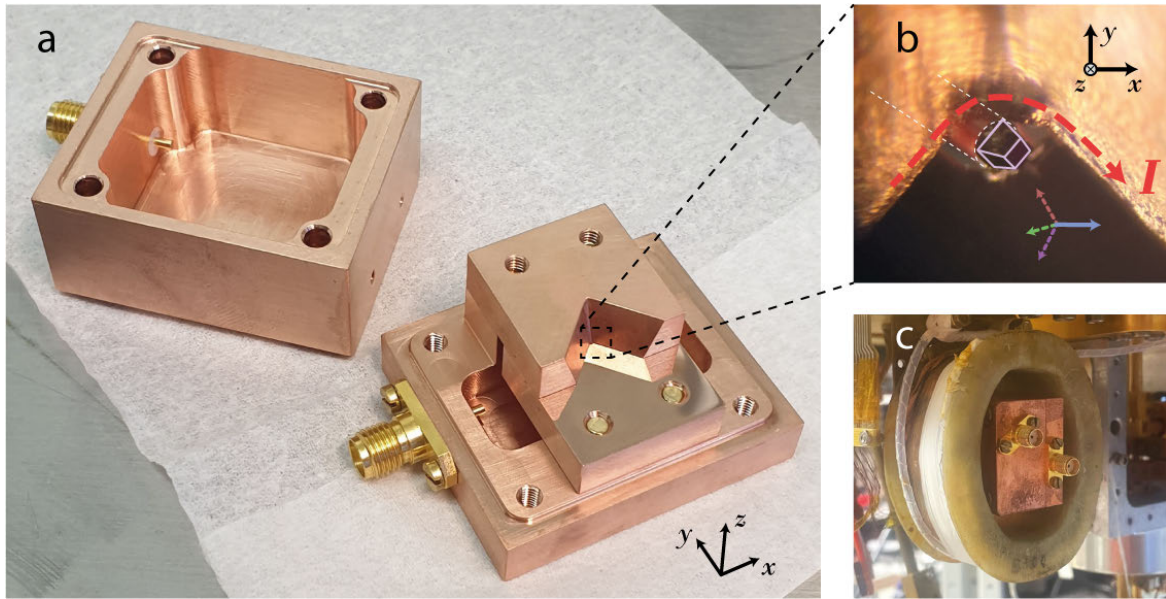


**Figure 5.16** Photographs of the M3D cavity. (a) The M3D cavity is assembled from four machined copper parts: a base part, a box cover, and two identical copper blocks with a wedge-cut machined in the center. The polished flat faces of the two blocks come together to form a pair of capacitances that are connected via short current paths around a small hole in the center — where the diamond sample is held in place on the tip of an optical fiber, see microscope image in panel (b). The diamond is oriented to align one NV-axis along the  $x$ -direction. (c) A home-built superconducting wire coil is able to create high magnetic fields of more than 200 mT.

to only squeeze through a small hole in the center. In the M3D cavity, these surfaces are the inward-facing sides of two copper blocks with a wedge-shaped cutout in the center. An essential feature of this cavity, crucial for its intended masing application, is the integration of an optical fiber, uniquely made possible by the space created by the wedge cutout. For the diamond samples we have, which are cut along the (100) planes, the fiber needs to enter at an angle.

Current paths along the sharp inner edges of the wedge cutouts on both sides form a loop around the diamond sample, which is glued on the tip of an optical fiber, and shown in Fig. 5.16(b). These current paths connect the two plate capacitors and are the source of the homogeneous RF field in the sample volume, penetrating the sample volume along the  $yz$ -plane, as shown in Fig. 5.17. The bulk copper is very efficient in squeezing the magnetic field lines through the small sample hole, which makes it possible to only use an easy-to-machine wedge cutout instead of a narrow slit as on the DCR chips. At the same time, the flat sides of the copper parts' capacitor

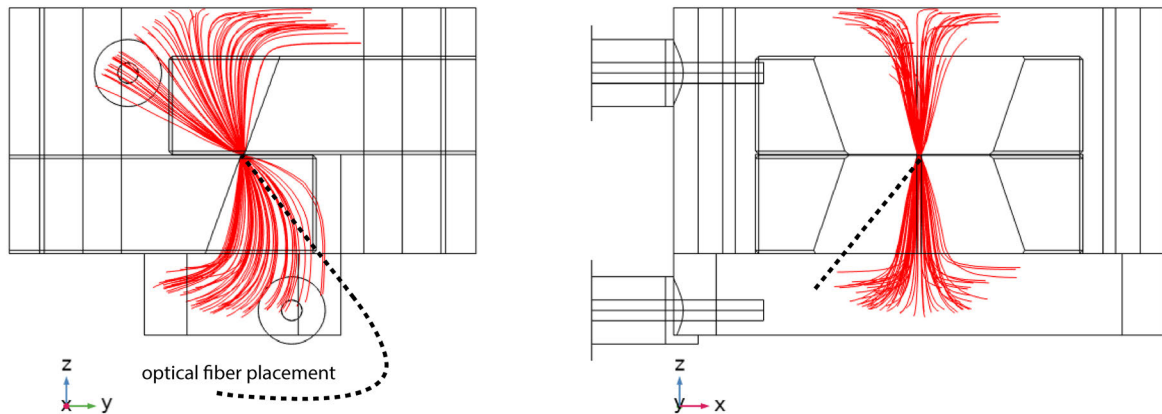


**Figure 5.17** RF magnetic field of the M3D cavity. Streamline plot of the RF magnetic field distribution inside the M3D cavity at a resonance frequency of around 3.5 GHz, simulated with COMSOL. A dashed line indicates the placement of the optical fiber through a small hole in the copper walls of the base piece.

surfaces are well-suited for polishing to a mirror finish. Dimensions for the copper blocks are approximately  $20 \times 20 \times 6 \text{ mm}^3$ , with a nominal capacitor gap of  $50 \mu\text{m}$  and a center hole diameter of roughly  $350 \mu\text{m}$ . The orientation of the optical fiber with a core diameter of roughly  $200 \mu\text{m}$ , reaching into the center hole at an angle, is chosen such that the strong external field along the  $x$ -direction is parallel to one of the four NV-axes, as required for efficient optical pumping (c.f. Sec. 4.1.1). The M3D cavity fits snugly into a superconducting coil with around 6000 windings that is custom-built<sup>7</sup> for this application. At current values of around 2 A, it generates fields upwards of 200 mT.

In Fig. 5.18, a transmission spectroscopy measurement of the M3D cavity coupled to an NV diamond sample is presented. The magnetic field is scanned and the NVs'  $m_S = -1$  to  $m_S = 0$  transition crosses the cavity resonance when the system is cold at around 65 mK, with the spins polarized in the ground state to approximately 93%, and with the green pump laser turned on at around 4 K. The green laser light is produced from a laser diode with a nominal wavelength of 520 nm, using a home-built temperature-controlled diode driver setup. The output power of the laser at the tip of the fiber is measured at approximately  $700 \mu\text{W}$ . The experiment is carried out in the ADR cryostat because its single-shot cooldown operation allows for sudden warming up due to a sustained heat intake from the pump laser. With the laser turned on,

<sup>7</sup>The coil body fabrication process is quite interesting: I created a 3D printed mold and laminated the body using a composite material mix of glass-fiber sheets and two-component epoxy glue, sourced from a local hardware store. This finished coil turned out to be well-suited for the cryogenic conditions.

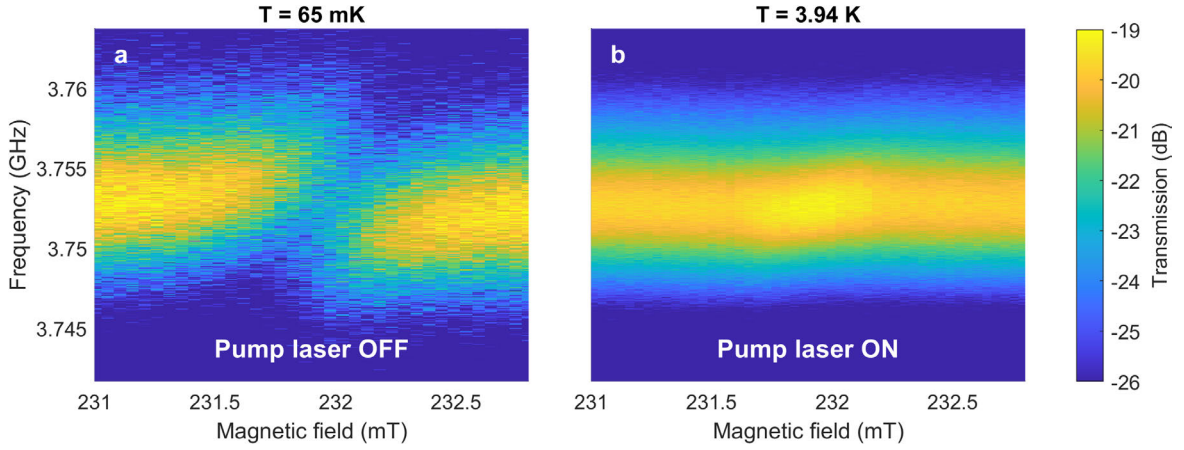


**Figure 5.18** Magnetic field scan of NV diamond coupled to the M3D cavity. (a) Avoided crossing of the  $m_S = -1$  to  $m_S = 0$  transition at cryogenic temperatures. (b) When the pump laser is on, the temperature rises to around 4 K, and the coupled system shows an amplification of the probe MW signal on resonance.

the temperature quickly rises but stabilizes as continuous cooling is provided by the pulse tube cooler at the 4K stage. The diamond sample used for this experiment is an **E** diamond sample, as it is optically more transparent than the **N**-sample, and thus better suited for optical pumping.

The “empty” cavity, with the spins far detuned, is fitted by a Lorentzian with a center frequency of roughly  $\omega_c/2\pi = 3.75$  GHz and a linewidth of  $\kappa/2\pi = 3720$  kHz, yielding a quality factor of  $Q \approx 500$ , see Fig. 5.19(a). Although an avoided crossing at 65 mK is observed, a coupling fit using the Maxwell-Bloch equations in the steady state reveals that the system does not enter the strong coupling regime. For this fit, we assume the same parameters for the spin ensemble as for the **N**-sample in the DCR cavity — this way we can directly compare the fitted collective coupling strength, as the specific parameters such as  $\gamma_\perp$  and the  $q$ -Gaussian FWHM for the **E**-sample are not known. The collective coupling strength is determined as  $g_{\text{coll}}^{\text{fit}}/2\pi = 2.6$  MHz (fixed model parameters are:  $q = 1.39$ ,  $W/2\pi = 9.2$  MHz,  $\gamma_\perp/2\pi = 177$  kHz, and  $\gamma_\parallel = 0$ ).

In Fig. 5.19(b,c) a simulated magnetic field scan is shown that replicates the measurements in Fig. 5.18(a,b), with all spins polarized in the ground state  $p = \langle \sigma_z^j \rangle = -1$ , and with a constant polarization of  $p = +0.1$  to simulate the effect of the optical pumping. With the pump laser turned on, the absorption dip of the cold spin system on resonance turns into a peak, resulting in weak amplification of the transmitted MW signal.

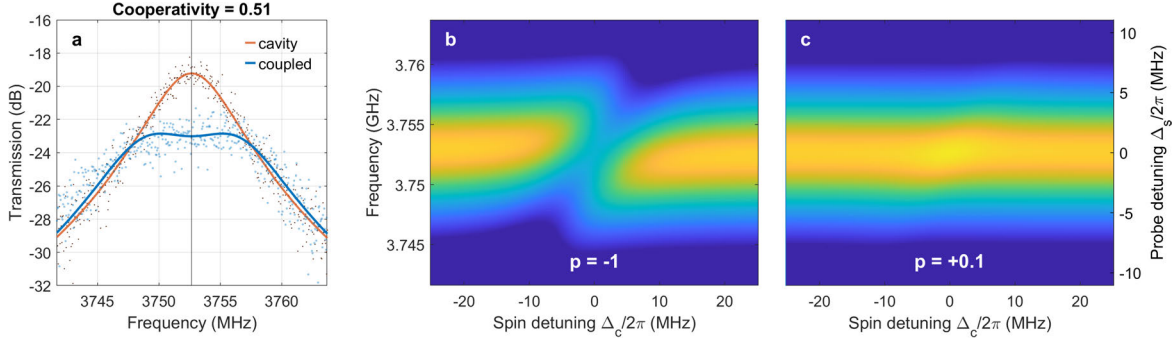


**Figure 5.19** M3D cavity coupling fit and magnetic field simulation. (a) Lorentzian fit of the far-detuned cavity and MBE-steady-state fit of the ground-state polarized spin ensemble. Simulated magnetic field scan using the same fit parameters with a polarization  $p = \langle \sigma_z^j \rangle = -1$  (b) for the effective two-level-system, and with  $p = 0.1$  (c) to simulate the effect of optical pumping. Compare with Fig. 5.18(a,b).

**Table 5.3** Simulated parameters of the M3D cavity. Compare with Table 5.1 and 5.2, where the same evaluation method is used for the other cavity designs. The spin density used to simulate  $g_{\text{coll}}^{\text{sim}}$  is taken to be 1/4 of the usual value of 6 ppm NV concentration with  $n_c = 1.755 \times 10^{23} \text{ cm}^{-3}$  carbon density in diamond.

$\omega_c^{\text{sim}}/2\pi$	$g_{\text{coll}}^{\text{sim}}/2\pi$	$\overline{B_0^{\text{sim}}}$	$\sigma( B^{\text{sim}} )$	$\frac{\min  B^{\text{sim}} }{\max  B^{\text{sim}} }$
3.5 GHz	3.35 MHz	102 pT	$99 \times 10^{-3}$	36%

For the sake of comparison, the COMSOL simulation results shown in Table 5.3 use the same sample dimensions as the other cavity simulations above, although a spin density that is reduced to  $1/4$ , as only one of the four NV-directions is tuned into resonance with the cavity due to the optical pumping requirements. The simulation results — usually trustworthy as the experimental comparisons for the other cavity designs suggest — show a higher simulated coupling strength than measured in the experiment. This is likely caused by a lower spin density in the **E**-sample and its slightly smaller size than the **N**-sample [shown in Fig. 4.5, and Fig. 5.8(b), respectively]. The M3D cavity design sacrifices some field homogeneity to allow for good integration of the optical fiber. Additionally, the very simple geometric structure makes it easier to polish the copper surfaces to improve the Q factor. As the cavity-spin system is only weakly coupled, it does not function as a superradiant maser. Still, it is worthwhile to explore how far away the system is from this regime — and to discover the roadblocks and possible strategies to overcome them.

A complete model of superradiant masing dynamics, including a theoretical prediction of the continuous-wave emission’s linewidth, requires a second-order cumulant expansion of the relevant operators for spin and cavity degrees of freedom. This approach leads to quadratic scaling of numerical complexity with the number of spin frequency packets — the number of equations to solve grows as  $\mathcal{O}(N^2)$  instead of  $\mathcal{O}(N)$  when using standard Maxwell-Bloch equations. While such a full treatment is beyond the scope of this thesis, interested readers can find practical information on numerically simulating higher-order cumulant expansions in Ref. [82].

For our purposes, we employ simplified simulations of the steady-state solution for the cavity amplitude  $|a|$  using a modified set of Maxwell-Bloch equations. These equations are adapted with a pumping term and take the contributions of thermal photons into account, causing a non-negligible contribution at elevated temperatures of 4 K. The equations follow from the Tavis-Cummings Hamiltonian (2.40), using a

modified Lindblad operator of Eq. (2.53),

$$\begin{aligned}
\mathcal{L}(\rho) = & \kappa(n_{\text{th}} + 1) (2a\rho a^\dagger - a^\dagger a\rho - aa^\dagger\rho) \\
& + \kappa n_{\text{th}} (2a^\dagger\rho a - aa^\dagger\rho - a^\dagger a\rho) \\
& + \frac{\gamma_{\parallel}}{2}(n_{\text{th}} + 1) \sum_j^N (2\sigma_-^j \rho \sigma_+^j - \sigma_-^j \sigma_+^j \rho - \rho \sigma_+^j \sigma_-^j) \\
& + \frac{1}{2} [\gamma_{\parallel} n_{\text{th}} + w] \sum_j^N (2\sigma_+^j \rho \sigma_-^j - \sigma_+^j \sigma_-^j \rho - \rho \sigma_-^j \sigma_+^j) \\
& + \frac{\gamma_{\perp}}{2} \sum_j^N (\sigma_z^j \rho \sigma_z^j - \rho),
\end{aligned} \tag{5.8}$$

with the addition of two new processes, the creation and annihilation of either a photonic or spin excitation by interacting with the bath of  $n_{\text{th}}$  thermal photons with operators  $a^{(\dagger)}$  and  $\sigma_{\pm}^j$ , and the creation of an excited spin by the optical pumping with rate  $w$  and operator  $\sigma_+^j$ . Then, the steady-state equations ( $\langle \dot{a} \rangle = 0$ ,  $\langle \dot{\sigma}_-^j \rangle = 0$ , and  $\langle \dot{\sigma}_z^j \rangle = 0$ ) simplify to

$$0 = -(\kappa + i\Delta_c)\langle a \rangle + \eta + g_{\rho}^2 N_{\rho} \langle a \rangle \sum_j^{N_{\rho}} \rho_j \left( \frac{1}{\tilde{\gamma} + i\Delta_s^j} \right) \langle \sigma_z^j \rangle, \tag{5.9a}$$

$$\langle \sigma_z^j \rangle = \frac{-\gamma_{\parallel} + w}{[\gamma_{\parallel}(2n_{\text{th}} + 1) + w] + 4g_{\rho}^2 |a|^2 \tilde{\gamma} / (\tilde{\gamma}^2 + \Delta_s^{j2})}, \tag{5.9b}$$

using  $N_{\rho} = 501$  spin packets following the discretization method outlined in Sec. 2.8, and  $\tilde{\gamma} = \gamma_{\perp} + \frac{1}{2}\gamma_{\parallel}(2n_{\text{th}} + 1) + w/2$ . The number of thermal photons at the relevant frequency of  $\omega_c/2\pi \approx 3.75$  GHz and temperature  $T \approx 4$  K is evaluated with the Bose-Einstein distribution as  $n_{\text{th}}(\omega_c, T) = [\exp(\hbar\omega_c/k_B T) - 1]^{-1} \approx 22$ .

The numerical steady-state solution for  $|a|$  is then calculated as a 2D plot for three different scenarios, shown in Fig. 5.20(a,b,c). The  $x$ -axis is the rate of optical pumping  $w$ , while the  $y$ -axis represents either the cavity's quality factor  $Q = \omega_c/2\kappa$ , the collective coupling  $g_{\text{coll}}$ , or the effective ensemble-linewidth  $\Gamma$ . While the Q-factor and the collective coupling strength need no further explanation, the value of  $\Gamma$  is varied by changing the width  $W$  of the  $q$ -Gaussian spin distribution, appearing in the model via  $\rho_j$  and the spin packet's detunings  $\Delta_s^j$ . The exact values chosen for  $\gamma_{\perp}/2\pi = 177$  kHz and  $\gamma_{\parallel}/2\pi = 20$  Hz are mostly inconsequential for the effective linewidth  $\Gamma$ , as it is dominated by the inhomogeneous broadening  $W$ , but are still required for the numerical model. They are taken from simulations of the N-diamond coupled to the DCR cavity

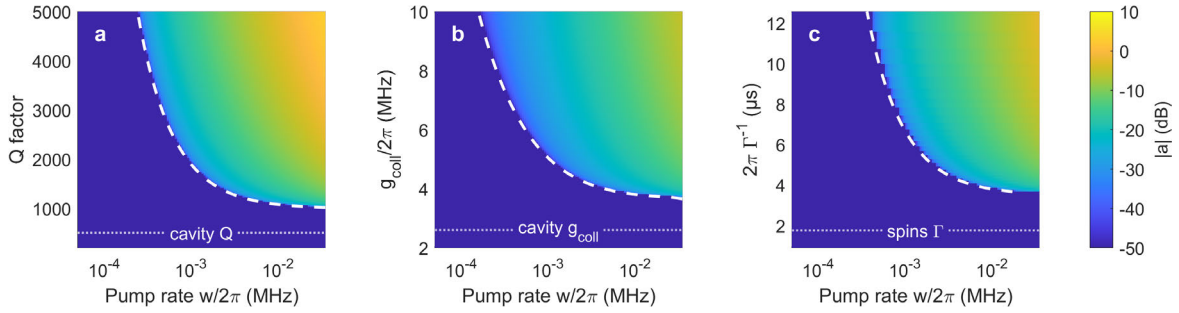


**Figure 5.20** Simulated steady-state cavity amplitude  $|a|$  during optical pumping of the spin-ensemble. Color-plots of the cavity amplitude as a function of pump rate  $w$  versus the cavity’s quality factor  $Q = \omega_c/2\kappa$  (a), versus the collective coupling strength  $g_{\text{coll}}$  (b), and versus the inverse effective ensemble-linewidth  $\Gamma$  (c), while the other parameters, taken from the experiment, are held constant. The superradiant threshold prediction (dashed-line) follows from Eq.(5) of Ref. [57].

and make sense in the context<sup>8</sup> of the experiments presented in Ch. 6. For numerical stability, and to bypass the need for a second-order cumulant expansion — essentially to prevent  $|a| = 0$  as a solution — a very low value for the external MW cavity drive of  $\eta \approx 2 \times 10^{-15}$  is used in the simulations.<sup>9</sup> In the plots of Fig. 5.20, we see a clear signature of the superradiant masing regime: when the optical pumping crosses a threshold value given by

$$\frac{w}{\gamma_{\parallel}} \geq \frac{2n_{\text{th}} + C + 1}{C - 1}, \quad (5.10)$$

the cavity amplitude will grow exponentially. This threshold formula is taken from Eq. (5) of Ref. [57] (where a true second-order cumulant expansion is used) and adapted to work with our choice of definitions.

With these results, we see that the M3D cavity in its current state is actually not too far from the superradiant masing regime. The most straightforward way to get into this regime is to increase the  $Q$  factor, where an improvement of slightly more than factor 2 is needed. Improving the single-spin coupling is much harder, as it is limited by the ability to constrain the effective mode volume to ever smaller dimensions

<sup>8</sup>The value of  $\gamma_{\parallel} = 1/\tau$  here represents the lifetime of a spin-ensemble having a net polarization  $p > 0$ , which is measured to be  $\tau \approx 8$  ms for the **N**-sample, as opposed to the long lifetime  $T_1 > 100$  s of a completely mixed ensemble with  $p < 0$ . This discrepancy is attributed to the effect of spin-spin interactions within the diamond. A detailed discussion will be given in the next chapter.

<sup>9</sup>Our trick to avoid a second-order cumulant expansion is to treat the system as a microwave amplifier for an extremely weak signal, rather than as a maser that spontaneously emits radiation. In essence, spontaneous emission can be viewed as amplification of an *intrinsic* signal: noise. Noise-driven terms are part of the second-order cumulant expansion but are absent in the first-order treatment. More on this in Sec. 6.1.

by the relation  $g_0 \propto \mathcal{B}_0 = \sqrt{\mu_0 \hbar \omega_c / 2V_{\text{eff}}}$ . To have a high collective coupling strength  $g_{\text{coll}} = g_0 \sqrt{N}$ , one needs a filling ratio of sample volume over mode volume  $V/V_{\text{eff}}$  and a high spin density  $n$  to get large  $N = nV$  — which inevitably makes the diamond sample more opaque, limiting the optical pumping efficiency. The effective ensemble linewidth  $\Gamma$ , on the other hand, depends mostly on the degree of inhomogeneous broadening, which is a highly sample-dependent quantity.

As an improved Q factor seemed to be the clearest path forward to realize the superradiant maser, some attempts were made to improve it further, such as trying harder at polishing all internal copper surfaces, annealing the copper parts for hours at around 900 °C and subsequently etching the surface to improve the surface conductivity, and even trying to coat the flat capacitor surfaces with a thin superconducting niobium layer, using an electron evaporation machine at the Atominstitut — although niobium sputtering seems to be a more suitable coating technique [83]. Unfortunately, none of these attempts led to any substantial improvements. A possibility that has not been explored yet is electropolishing as a surface treatment. Notably, using bulk superconducting niobium for the cavity parts is out of the question, as it leads to large deformations of the external fields, which are required to be homogeneous, as shown in Fig. 5.10.

Another question is, if our setup's optical pumping rate is strong enough to achieve masing, even if the Q factor is twice its actual value. A very simple estimate is given by the steady-state solution of Eq. (5.9b) when the cavity influence is neglected ( $g_\rho = 0$ ). Then, we can assume all spins have the same inversion, resulting in  $p = \langle \sigma_z^j \rangle = (-\gamma_{\parallel} + w) / [\gamma_{\parallel}(2n_{\text{th}} + 1) + w]$ . For a value of  $p = 0.1$  [see simulation in Fig. 5.19(c) and compare with measurement in Fig. 5.18(b)] and using the model parameters above, this results in a value of  $w/2\pi = 4.7 \times 10^{-5}$  MHz, which is below the threshold everywhere in Fig. 5.20. This estimate is not very reliable, (*i*) as it is based on oversimplified assumptions about a homogeneous steady-state inversion and unknown effective value of  $\gamma_{\parallel}$ , and (*ii*) as the actual sample temperature, and therefore value of  $n_{\text{th}}$ , is likely higher than measured by the thermo-sensor, which is mounted at the coldest cryostat stage, far away from the small diamond sample. This sensor is only reliable when the pump laser is off and the system is in equilibrium. The laser power in the experiment is not a bottleneck and could be substantially increased by using a commercial green fiber laser.

Notably, after the design and testing of the M3D cavity, I stumbled upon an interesting cavity design reported in Ref. [80], which claims to have realized superradiance effects, although in a short offhand remark at the end.

If I were to try again to realize a superradiant diamond maser, I would focus on the following improvements:

- Work at a higher cavity frequency upwards of 10 GHz, as the single spin coupling scales as  $g_0 \propto \sqrt{\omega_c}$ . This would necessitate higher external magnetic fields larger than 450 mT, currently not possible with our coil setup.
- Use a slightly bigger diamond sample with high NV density, e.g.  $(500 \mu\text{m})^3$  — this should come with an improved Q factor, as the surface currents at the bigger sample hole, and therefore the ohmic losses scaling as  $I^2$ , would be reduced. On the other hand, a bigger sample makes optical pumping less efficient. A delicate balance must be found, or possibly an optimal sample shape with decreased thickness in one dimension.
- Generally, work with a larger physical design volume for the total cavity dimensions — this would help tremendously with the awkwardness of assembling everything in a small space, and could also help to improve the Q factor when the RF fields do not reach outwards into the cavity walls, effectively reducing parasitic inductance.
- The ultimate goal would be to realize a superradiant diamond maser at room temperature, so maybe an optical fiber is actually not needed, and direct illumination with green laser diodes from two sides is a possibility.
- Use a better quality NV diamond to reduce the inhomogeneous broadening and thereby  $\Gamma$ .
- A diamond cut square along the (111) plane would remove the need to orient the sample at an awkward angle and could at the same time help to achieve a higher filling factor of the cavity's mode volume.

In summary, my efforts in exploring different cavity designs have culminated in many insights and new ideas to try in the future. My experimentalist's trial-and-error approach led me somewhat close to the lofty goal of realizing a continuous-wave superradiant diamond maser. As it turned out, the experiments accomplished with the DCR cavity, in particular, enabled by its rapid magnetic detuning capabilities, have actually realized a quasi-continuous superradiant maser. This quasi-continuous emission is driven not by the optical pumping of NV centers but by an effective internal pumping mechanism attributed to spin-spin interactions within the dense diamond sample — and opens up a completely new window for looking at spin-spin many-body

physics through the lens of collective superradiant dynamics. This aspect, among other superradiant phenomena, will be the topic of the next chapter.

# Chapter 6

## Experiments

### *Explorations with a superradiant diamond*

After introducing the theoretical tools in Ch. 2, as well as the technical and setup-related details in Ch. 3, we now turn our focus on the experiments realizing superradiant emission from our diamond sample coupled to the microwave cavity. In these experiments, we use the N-diamond sample (see Section 4.1.2) and the DCR cavity (see Section 5.2.3). The hybrid system of cavity and spins is illustrated in Fig. 6.1, which schematically highlights the key aspects of our system. The system is essentially characterized by three rates: the rate of collective energy exchange between the spin ensemble and the cavity  $g_{\text{coll}}$ , the cavity dissipation rate  $\kappa$ , and the spin ensemble's effective linewidth  $\Gamma$ .

We begin this chapter with an experimental characterization of our system, particularly the NV diamond's inhomogeneously broadened spin distribution, the main contributor to the parameter  $\Gamma$ . We then explore superradiant dynamics by inverting the spin ensemble using simple rectangular microwave pulses. As we will demonstrate, higher initial spin inversion, and crucially, the homogeneous inversion over the full range of frequencies of the broadened ensemble, can be achieved with a specially designed chirped pulse. By combining this improved pulse design with a rapid detuning protocol using the magnetic detuning loop inside the DCR cavity, we achieve an initial state of the inverted ensemble that closely approximates the ideal situation of all spins inverted with a vanishing tipping angle, i.e., oriented only along the  $+z$ -direction.

Upon tuning the inverted spin system back into resonance with the cavity, the system enters a metastable initial state. This inversion and detuning protocol, which offers a high level of control over the spin ensemble's initial state, allows us to study in detail the crucial moment at the beginning of the superradiant decay, where small

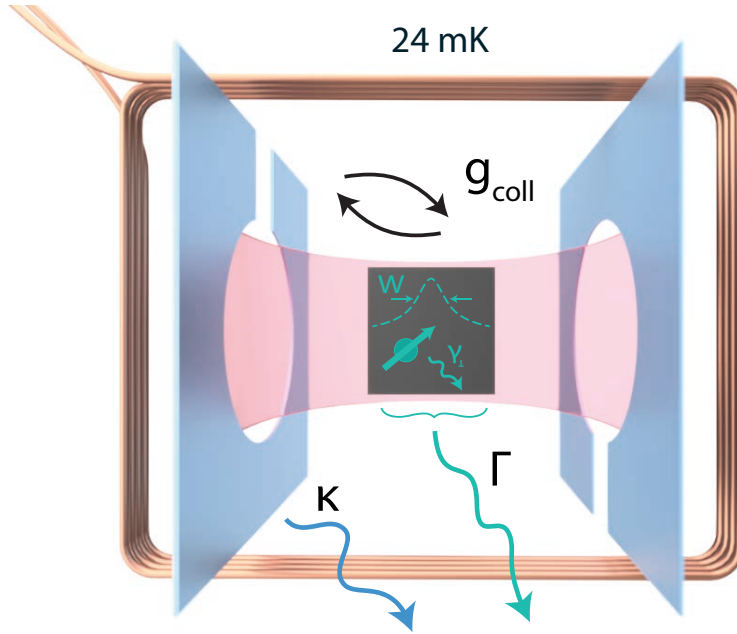


**Figure 6.1** Hybrid system at the heart of our experiment. The homogeneously coupled spin ensemble exchanges excitations with the cavity mode at a rate  $g_{\text{coll}}$ , while the cavity loses photons with rate  $\kappa$  and the spin system dephases with the effective rate  $\Gamma$ . This effective rate encompasses both the individual spin dephasing  $\gamma_{\perp}$  and the fanning out of fast and slow spins due to inhomogeneous broadening of width  $W$ .

causes have significant effects and minute fluctuations are subsequently amplified by the superradiant avalanche process. We reveal the inverted spin system's high sensitivity to weak microwave trigger pulses, which influence both the delay time and the phase of the superradiant decay.

Lastly, we focus on a novel phenomenon at the intersection of superradiance and many-body spin-spin interactions. After the initial superradiant decay, we observe a series of revival pulses and a subsequent regime of sustained quasi-continuous masing. After presenting several experimental pieces of evidence, we conclude that dipolar coupling between the disordered spins in the ensemble is directly responsible for driving these dynamics.

### 6.0.1 Hybrid system characterization

#### Measuring the spin distribution $\rho(\omega)$ and lifetime $T_1$ in the dispersive regime

We begin our characterization of the spin distribution by scanning the external magnetic field, as shown in Fig. 6.2, with the field oriented to have equal projections along all 4

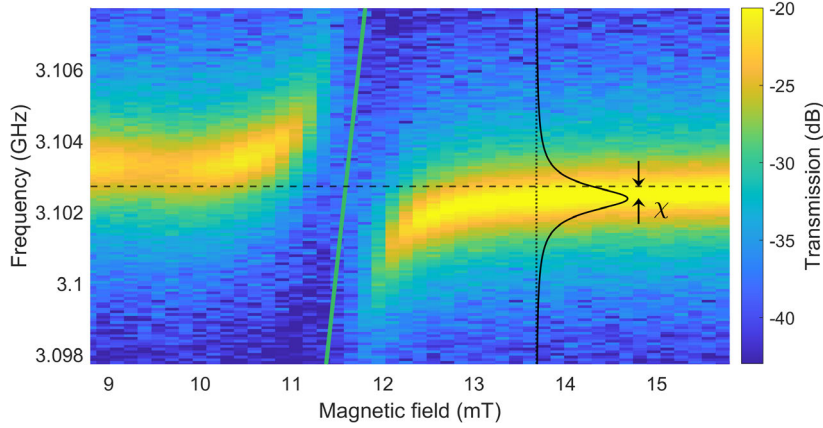


**Figure 6.2** Transmission spectroscopy and external magnetic field scan with equal projections on all 4 NV sub-groups, with the spin system in the ground state. When tuning the spin center frequency (green line) across the “empty” cavity resonance (dashed black line), we observe an avoided crossing of the coupled system. Off resonance, the spin ensemble’s coupling to the cavity causes a dispersive shift  $\chi$  of the Lorentzian response relative to the bare resonator frequency.

NV axes. For the next set of measurements, we detune the spins by about  $\Delta = 50$  MHz from the cavity frequency, as indicated by the dotted vertical line in Fig. 6.2. In this dispersive regime, where  $\Delta \gg g_{\text{coll}}$ , the apparent cavity peak is shifted from the “empty” cavity frequency by an amount

$$\chi = \frac{g_{\text{coll}}^2}{\Delta} \langle S_z \rangle, \quad (6.1)$$

depending on the polarization of the spin ensemble (using a generalized form of Eq. (2.39) for the collective spin operator). We will now frequency-selectively alter the spin polarization  $p(\omega_p) = \langle \sigma_z(\omega_p) \rangle$ .

To this end, we use a highly-attenuated 100 ms long microwave pulse of probe frequency  $\omega_p$  to drive spins in a narrow frequency range around  $\omega_p$  into a mixed state with partial inversion, while maintaining the initial polarization in the ground state for the other spins. We then measure the cavity transmission spectrum over time using the VNA while the spin system slowly relaxes to the ground state with the spin-lattice relaxation rate  $\gamma_{\parallel} = 1/T_1$ . These measurements allow us to determine the dispersive shift depending on the number of spins targeted by the probe pulses, thereby mapping the frequency distribution of the detuned spin system, as shown in Fig. 6.3. Each run with a different probe frequency is fitted with an exponential decay function to extract data points for the spin distribution, which is shown in Fig. 6.4(a), and fitted with

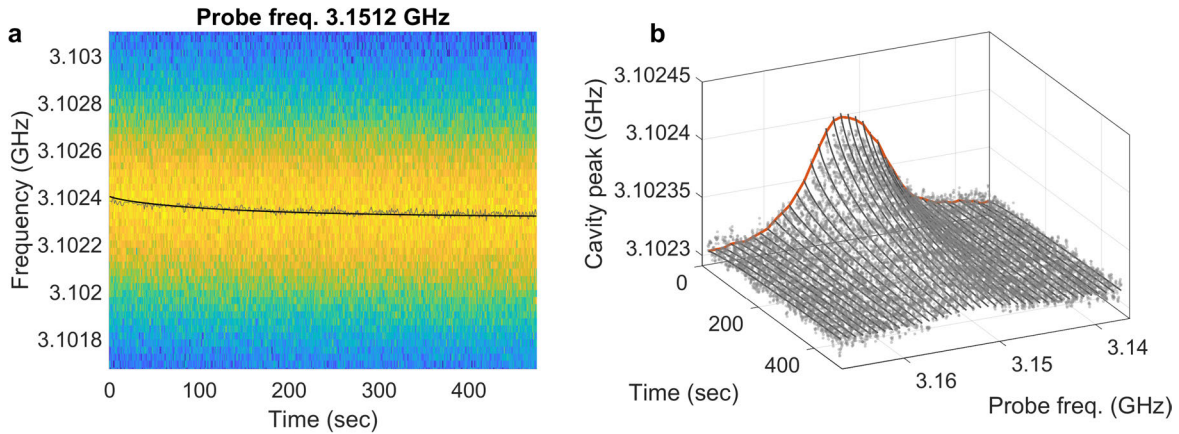


**Figure 6.3** Relaxation dynamics after 100 ms low-power probe pulse with a set probe frequency is applied to the system, measured with the VNA. (a) Color plot of a single run with exponential decay fit. (b) Repeating the measurement while scanning the probe frequency reveals the spin distribution.

a  $q$ -Gaussian function of width  $W/2\pi = 9.2$  MHz and shape parameter  $q = 1.39$ , see also discussion in Sec. 2.8. Additionally, this measurement allows us to evaluate the spin-lattice relaxation time  $T_1 = 150$  s, as shown in Fig. 6.4(b).

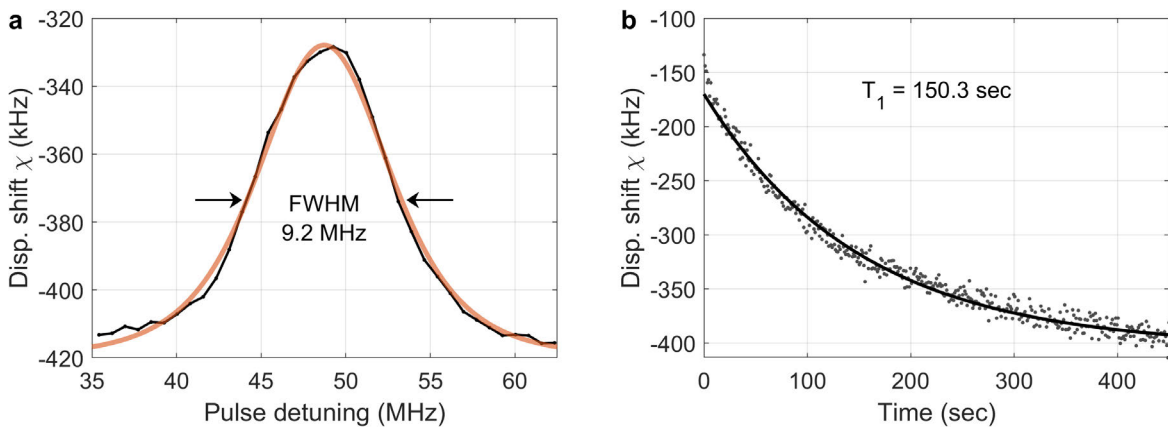


**Figure 6.4** Spin distribution and relaxation time  $T_1$ . (a) Data points for the spin distribution follow from exponential fits of each run shown in Fig. 6.3(b), and fitted with a  $q$ -Gaussian of width  $W/2\pi = 9.2$  MHz and shape parameter  $q = 1.39$ . (b) Using a higher-power probe pulse, the entire ensemble is brought into a mixed state with partial inversion, generating a larger signal. An exponential decay with a characteristic timescale of around  $T_1 = 150$  s is observed.

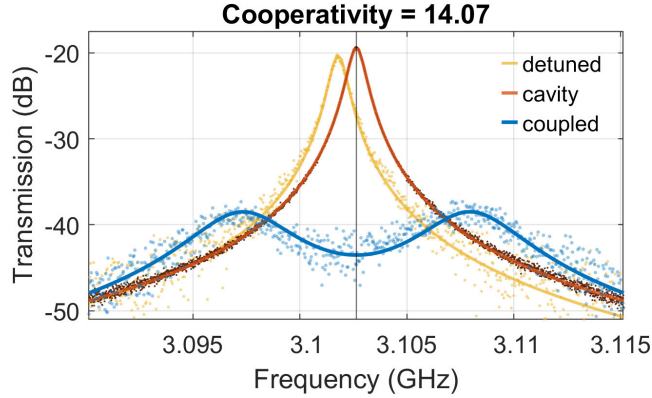


**Figure 6.5** Transmission spectroscopy measured with the VNA and fitted using steady-state MBE solutions. The coupled system on resonance exhibits a normal mode splitting (blue), allowing the extraction of the collective coupling strength  $g_{\text{coll}}/2\pi = 4.6$  MHz. At high measurement power of the VNA, we measure the “empty” cavity signal (red). The yellow curve is measured at low power with the detuning loop switched off and fitted by using a detuning of roughly  $\Delta/2\pi \approx 20$  MHz between cavity and spins. The detuning loop will be used for the experiments presented below.

### Determining the cavity linewidth $\kappa$ , the coupling strength $g_{\text{coll}}$ , and estimating the spin linewidth $\gamma_{\perp}$

We continue our system characterization by magnetically tuning the spins back on resonance. Using a high-power setting on the VNA and tracing over the cavity resonance several times, we bring all spins into a fully mixed state. This leaves only the cavity Lorentzian response, which directly yields the cavity linewidth  $\kappa/2\pi = 420$  kHz, as shown in Fig. 6.5.

After allowing the spin system to relax to the ground state, we measure the steady-state response to reveal the normal-mode splitting of the coupled system. From this, we extract the collective coupling strength using our semi-classical model in the steady-state, Eq. (2.66). By inputting the  $q$ -Gaussian spin distribution from Fig. 6.4(a), we achieve good agreement with a parameter value of  $g_{\text{coll}}/2\pi = 4.6$  MHz.

The last system parameter is the estimated spin coherence time  $T_2 = 1/\gamma_{\perp} \approx 900$  ns, corresponding to an individual spin linewidth of  $\gamma_{\perp}/2\pi = 177$  kHz. This value is, in principle, accessible via direct measurement. Typically this is achieved through a spin-echo experiment, such as a Hahn-echo sequence [17] or a more robust CPMG pulse sequence [84]. However, direct measurement of  $T_2$  proved to be challenging for our system for two reasons: (i) the relatively short coherence time is difficult to measure accurately, and (ii) the superradiant nature of our system — enabled by the spatially

homogeneous spin coupling to the cavity — complicates the application of  $\pi$  and  $\pi/2$  pulses without releasing a superradiant burst, thereby preventing spin refocusing to create an echo pulse.

Despite these challenges, the parameter  $\gamma_{\perp} = 1/T_2$  is crucial for our model and generates a distinctive signature in the time-resolved dynamics, as seen in Fig. 2.13 and discussed in Sec. 2.9. Our estimated value for  $\gamma_{\perp}$  is in good agreement with the observed dynamics in the main experiments of this work, particularly the superradiant decay of our uniformly inverted spin ensemble.

Combining all parameters, we calculate the cooperativity parameter of our hybrid system to be approximately  $C = 14$ , see Eq. (2.68).

## 6.0.2 Inversion pulses

### Superradiant emission after a rectangular inversion pulse

We start our experimental exploration of superradiance with all NV spins, including those along all 4 diamond axes, magnetically tuned into resonance with the cavity, and thermally polarized in the ground state.

Now, to bring the spin system into an inverted state — an essential step for the subsequent superradiant decay — the simplest way to achieve this is to apply a constant microwave drive for a fixed time, i.e. using a rectangular pulse. We drive the system with a 50 ns pulse of constant phase (only using one quadrature channel) on resonance with the cavity via the pump line.

To reduce waiting times between multiple experimental runs, we use a special protocol to initialize our spin system close to the ground state. First, we use a high-power setting on the VNA to repeatedly trace over the cavity resonance, effectively bringing the spin ensemble into a completely mixed state of spins up and down. We then wait for a fixed period of  $\Delta t = 3$  min, allowing the spins to relax with the time constant  $T_1$ . This protocol prepares the spin system in a state with an initial spin inversion of  $p = \exp(-\Delta t/T_1) - 1 \approx -0.7$ , based on our  $T_1$  estimate. In practice, the value of  $p$  is even closer to  $-1$ , as the resonant ensemble undergoes faster decay via Purcell enhancement due to its coupling to the resonant cavity mode (see Sec. 2.9). Using this method, we avoid waiting several  $T_1$  periods to reach the complete ground state and still prepare the system in a repeatable initial state.

We conduct a power scan of the 50 ns pulses using a stack of digital attenuators, which can vary the power in increments of 0.5 dB, similar to the experiments of Ref. [73]. In Fig. 6.6(a), we plot the cavity amplitude for the run with a nominal attenuation value

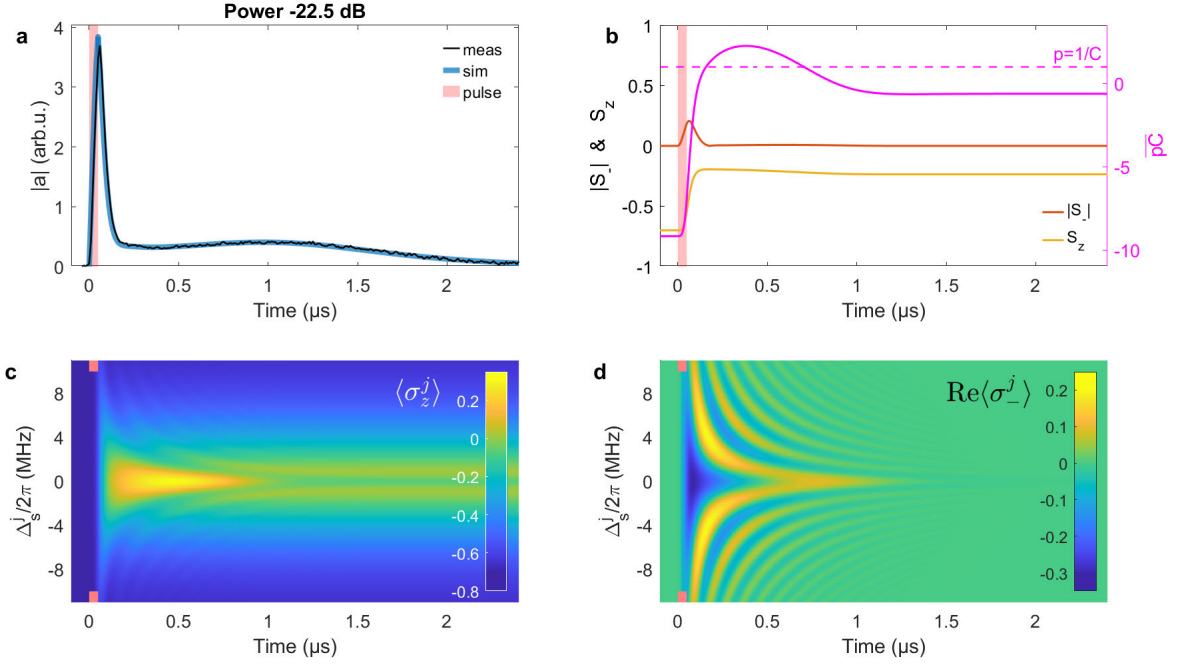


**Figure 6.6** Rectangular excitation pulse for superradiant emission. (a) Measured and simulated cavity amplitude for a nominal attenuation of  $-22.5$  dB of the setup's maximum power for the  $50$  ns inversion pulse. This power corresponds to the lowest value for which the system exhibits superradiance. In (b), we plot the collective spin dynamics, evaluated as  $S_z = \sum \rho_j \langle \sigma_z^j \rangle$  (yellow line) and similarly for  $|S_-|$  (red line). Additionally, the magenta line illustrates the system crossing the instability threshold  $\overline{pC} = 1$ , leading to the observed superradiant emission after the excitation pulse. (c,d) Color plots of the simulated spin system dynamics, showing  $\text{Re}\langle \sigma_-^j \rangle$  and  $\langle \sigma_z^j \rangle$ , respectively, for different spin packet detunings  $\Delta_s^j$ .

of  $-22.5$  dB, the lowest power at which the system subsequently decays by emitting a superradiant burst. The driving pulse appears as a large narrow peak, after which the cavity amplitude drops quickly but then gradually rises again, forming a long, drawn-out superradiant emission pulse with its maximum around the  $1 \mu\text{s}$  mark.

We use our semi-classical model [see Eqs. (2.63)] to numerically simulate the observed cavity dynamics of the driven coupled system, starting from an initial state of the system with inversion  $p = -0.7$ . The excitation pulse is modeled as a rectangular function for the cavity drive  $\eta(t)$ , with its constant amplitude adjusted to replicate the measurement. Most parameters for the simulation are as given above and used for the steady-state fit in Fig. 6.5, except  $\gamma_{\perp}$ . To achieve good correspondence between measurement and simulation, we use a relatively large value for the single-spin decoherence rate,  $\gamma_{\perp}/2\pi \approx 555$  kHz. This value is roughly three times larger than the rate used to accurately model our system during a free, undriven superradiant decay from a uniformly inverted state, as seen in subsequent experiments. Additionally, this high  $\gamma_{\perp}$  is inconsistent with our steady-state measurements. A discussion on this discrepancy will be given below.

The simulation provides indirect insights into the dynamics of the spin system, where we plot the longitudinal and transversal components of the collective spin vector in Fig. 6.6(b), together with an evaluation of the superradiant instability threshold  $\overline{pC}$ , for which the spins resonant with the cavity contribute most, see Eq. (2.73) and discussion there. Although the value of  $S_z = \sum \rho_j \langle \sigma_z^j \rangle$  is never above zero, the inverted center spins push the system above the threshold  $\overline{pC} > 1$ , leading to a superradiant decay in the form of an extended shallow bump in the cavity amplitude. The dynamics of individual spin packets with different detunings  $\Delta_s^j$  is shown in Fig. 6.6(c,d). The striped pattern, most clearly visible in the plot of  $\langle \sigma_z^j \rangle$ , is a result of the inhomogeneous broadening, where the phase of spin packets with larger detunings on both sides changes significantly faster in time than the resonant center packets.

In Fig. 6.7(a), the cavity dynamics for the full power scan are shown as a color plot, revealing several branches of superradiant pulses. When the spin system is inverted substantially above the superradiance threshold, the energy transferred into the cavity mode during the spin decay can oscillate back and forth between the two subsystems multiple times. In Fig. 6.7(b), we present an attempt at recreating these dynamics in the simulation. The basis for this recreation is the fit run at  $-22.5$  dB, only adjusting the constant amplitude for  $\eta(t)$ . The measurement deviates from the simulation, with the branch structure appearing significantly more washed out in the experimental data.

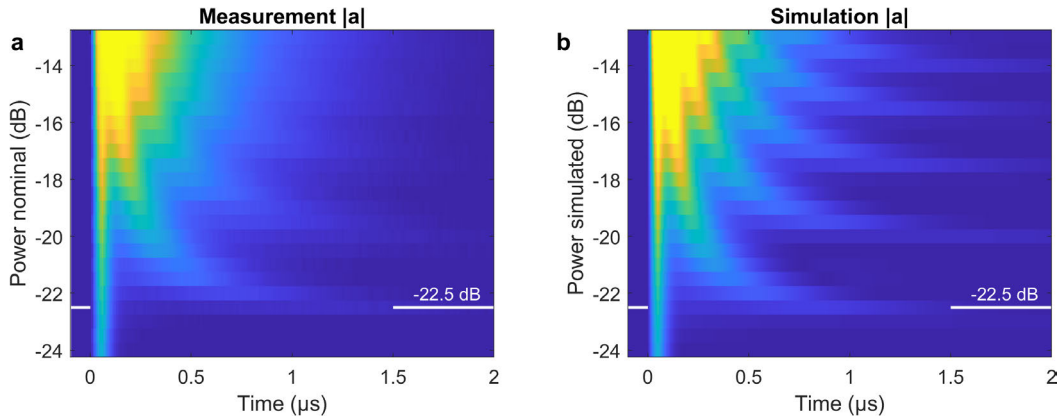


**Figure 6.7** Rectangular excitation pulses for superradiant emission. (a) Color plot of the measured cavity amplitude when scanning the rectangular pulses’ power in logarithmic increments of 0.5 dB using the digital attenuators. (b) Simulation of the dynamics that attempts to recreate the measurements. The simulated power scan is based on a fit of the lowest power at 22.5 dB attenuation, as described in the text.

Particularly in the higher-power runs, individual branches merge into a single blurred, colorful blob without any oscillatory structure visible.

This discrepancy is possibly connected with the overestimation of  $\gamma_{\perp}$  in the simulation. We offer a possible explanation: The semi-classical description provided by the Maxwell-Bloch equations, which uses a first-order cumulant expansion, fails to accurately capture the dynamics. A higher-order cumulant approach is required. While this is not critical during the driven part of the sequence — where a strongly driven system behaves classically and not quantum mechanically — it becomes crucial during the free evolution that follows. Effectively modeling these two regimes with the same set of parameters results in a discrepancy, particularly for higher-power pulses.

To summarize this section on rectangular excitation pulses, we emphasize their main drawback: the inversion is highly inhomogeneous across the frequencies of the broadened ensemble. Off-center spins are rotated to different angles compared to resonant spins, leading to a state far from the desired uniform inversion  $p = \langle \sigma_z^j \rangle$  discussed in Sec. 2.9. To achieve this ideal initial state, which is crucial for exploring the superradiance phenomena central to this thesis, we developed a protocol combining a modified chirped pulse for uniform inversion with a rapid detuning and inversion storage sequence. The design approach for the chirped microwave pulse will be discussed next.

## Design of a chirped microwave pulse for uniform spin inversion

The starting point for our chirped pulse design process begins with a simple question: “How can we achieve homogeneous inversion over a whole range of spin frequencies in free space?” Initially, we disregard the cavity environment and focus on this challenge. Only later will we modify the microwave pulse to “work around” the cavity filter function. This filter not only causes the photonic amplitude to react to the driving amplitude  $\eta$  with a certain delay — manifesting itself for the cavity field’s loading and its dissipation, determined by the linewidth  $\kappa$  — but also selectively transmits frequencies: resonant ones are transmitted maximally, while off-resonant ones are attenuated.

A possible approach to invert an inhomogeneously broadened spin ensemble in a free space environment — or, in other words, under a high bandwidth filter function — is to use *rapid adiabatic passage* pulses. These pulses were originally developed for nuclear magnetic resonance experiments to achieve efficient ensemble inversion despite field inhomogeneities. With such pulses, the RF pulse frequency is swept across the spin center frequency in such a way that the effective magnetic field vector in the rotating frame moves slowly enough for the spin magnetization vector to adiabatically follow, but still faster than decoherence effects can occur [85].

Our approach is simple: we want to design a continuous pulse that sweeps linearly across the spin frequencies. Specifically, the pulse envelope should be smooth, avoiding steep gradients and sudden jumps. These criteria ensure that the pulse can later be adapted for use in the cavity, as will be discussed below. The pulse we have chosen is a chirped pulse, which involves a frequency sweep over a range of 20 MHz, with a 400 ns Gaussian envelope, shown in Fig. 6.8(a).

We solve the dynamics of the spin ensemble in response to this pulse using the optical Bloch equations. These equations are derived from our semi-classical model by substituting the cavity amplitude in Eqs. (2.63) with a classical driving field,  $g_0\langle a \rangle \rightarrow \Omega(t)$ , resulting in the following coupled equations:

$$\langle \dot{\sigma}_-^j \rangle = -(\gamma_\perp + i\Delta_s^j)\langle \sigma_-^j \rangle + \Omega(t)\langle \sigma_z^j \rangle, \quad (6.2a)$$

$$\langle \dot{\sigma}_z^j \rangle = 2\left(\Omega(t)\langle \sigma_-^j \rangle + \Omega^*(t)\langle \sigma_+^j \rangle\right). \quad (6.2b)$$

The drive amplitude is expressed as a sum of the time-dependent field quadratures  $\Omega(t) = I(t) + iQ(t)$  in the rotating frame of the drive frequency  $\omega_p$ . In Fig. 6.8(b), we perform a numerical scan of the chirped pulse power to determine the pulse amplitude

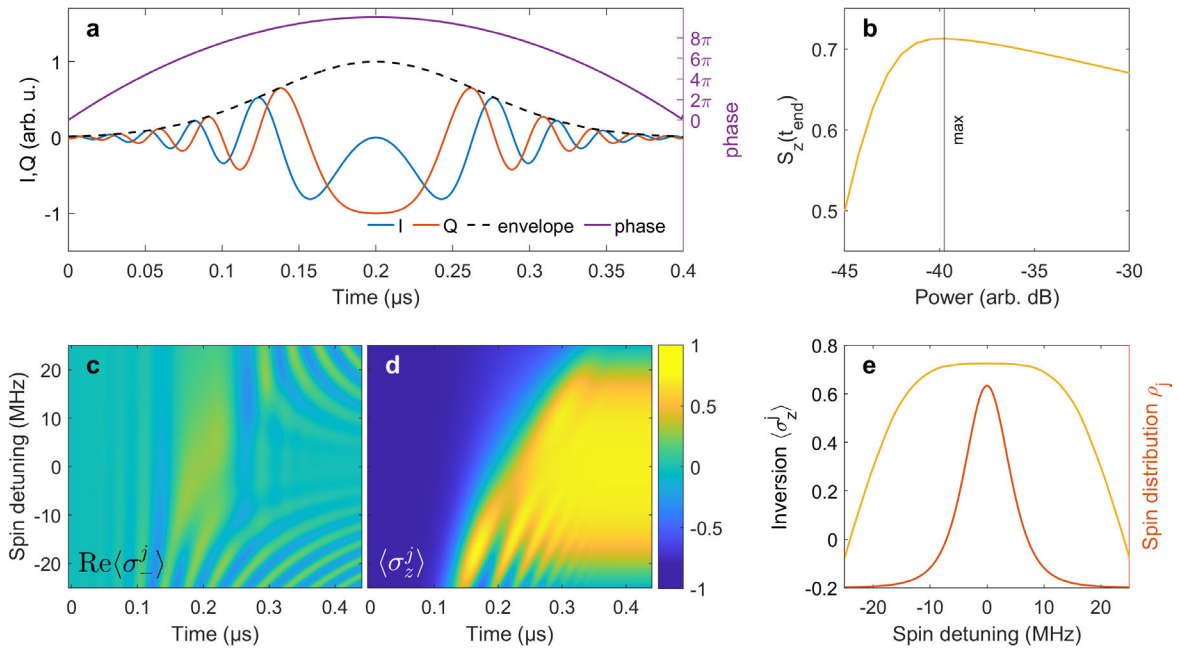


**Figure 6.8** Simulation of a chirped pulse with a 400 ns Gaussian envelope. (a) Quadratures and phase of the chirped pulse  $\Omega(t) = I + iQ$ . The phase is evaluated as  $\arg(\Omega(t))$ , displaying a parabolic shape as expected from a linearly swept frequency. (b) Numerical scan of the ensemble inversion  $S_z = \sum \rho_j \langle \sigma_z^j \rangle$  for different powers of the chirp pulse. (c,d) Color plots of the simulated spin system dynamics at the pulse power for maximum  $S_z$ , showing  $\langle \sigma_z^j \rangle$  and  $\text{Re}\langle \sigma_-^j \rangle$ , respectively, across the ensemble frequencies. (e) Efficient uniform inversion over the spin distribution is achieved at the end of the chirped pulse.

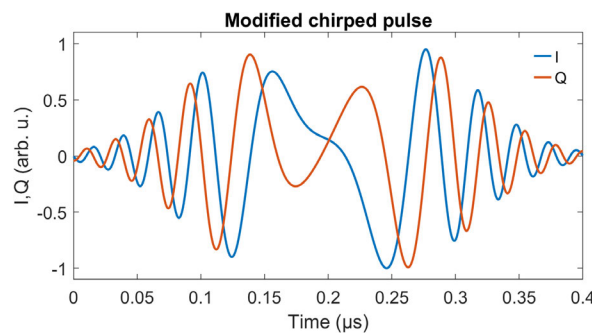


**Figure 6.9** Quadratures  $I$  and  $Q$  of the modified 400 ns chirped pulse  $\eta(t)$  for uniform spin inversion, attained by the “reverse engineering” method described in the text.

that maximizes the ensemble inversion  $S_z$ . Specifically, in Fig. 6.8(e), we observe that this pulse in “free space” achieves a uniform final inversion of  $\langle \sigma_z^j \rangle \approx +0.7$  for nearly all spins, starting from an initial inversion of  $p = \langle \sigma_z^j \rangle = -0.8$ .

Now that we understand the necessary driving amplitude in free space, we can revert our earlier simplification  $\Omega(t) \rightarrow g_0 \langle a \rangle$  and attempt to account for the cavity. When (numerically) solving a system of coupled differential equations, one usually assumes some initial conditions and an external drive, in this case,  $\eta(t)$ , and then solves for the dynamics. Here, we will do the opposite: We assume the intended system dynamics (and also know how to calculate their derivatives), particularly the cavity and the spin components  $\langle \sigma_-^j \rangle$  plotted in Fig. 6.8(a,c), and then solve for the required drive that is necessary to generate them. We invert Eq. (2.64a), assuming a drive frequency on resonance with the cavity ( $\Delta_c = 0$ ):

$$\eta = \kappa \langle a \rangle - g_\rho N_\rho \sum_{j=1}^{N_\rho} \rho_j \langle \sigma_-^j \rangle + \langle \dot{a} \rangle. \quad (6.3)$$

This results in the modified chirped pulse shown in Fig. 6.9. We then perform a numerical power scan of our specially designed microwave pulse, plotting the cavity amplitude  $|a|$  and the ensemble inversion  $S_z$  in Fig. 6.10(a,b). The pulse power that achieves the best inversion leads to a superradiant emission with maximum cavity amplitude, as shown in Fig. 6.11(a). Here, we also recognize the “free space” chirped pulse with Gaussian envelope of Fig. 6.8(a) during the first 400 ns of the cavity dynamics, confirming that our pulse design method is self-consistent, at least in the simulation. The superradiant decay is followed by a sequence of damped Rabi oscillations. The uniform inversion at the end of the pulse ( $t = 400$  ns) is also visible in the color plot of  $\langle \sigma_z^j \rangle$  across different spin frequencies, as shown in Fig. 6.11(c).

The final step is to test our modified chirped pulse in the experiment. As usual, we start with a power scan, which is shown in Fig. 6.12(a). We observe some similarities with the simulation in Fig. 6.10(a), but the experimental data does not fully replicate the simulation. Notably, the detected signal is most likely somewhat saturated at amplitudes higher than around 5 arbitrary units. The discrepancy between measurement and simulation is ultimately not a surprise, as we observed a similar issue with the rectangular pulses. For the simulations shown here, we have reverted to the “default” value of  $\gamma_\perp/2\pi = 177$  kHz. Despite the differences, we can be very satisfied with our results. Our pulse achieves the desired outcome: it generates the superradiant decay of a uniformly inverted ensemble with initial inversion  $p$ , similar to the simulated

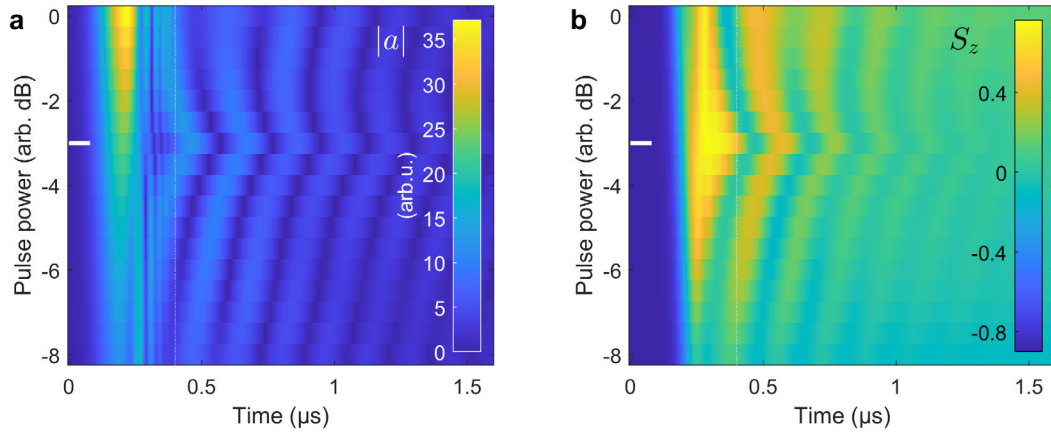


**Figure 6.10** Numerical simulations with the modified 400 ns chirped pulse. Color plots of (a) the cavity amplitude  $|a|$ , and (b) the ensemble inversion  $S_z$  over time, for different pulse powers in logarithmic increments. At the nominal value of  $-3$  dB, the ensemble inversion reaches its maximum value near the end of the pulse.

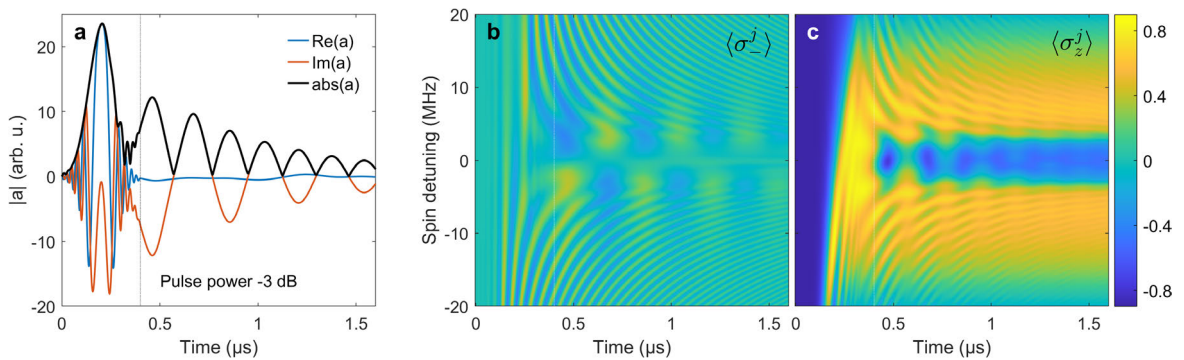


**Figure 6.11** Numerical simulation of the cavity dynamics in (a) for the optimal inversion pulse. Color plots of the spin packet's dynamics, illustrating the real part of the transversal component in (b) and the  $z$ -projection in (c). Around the 400 ns mark, the spin ensemble is almost uniformly inverted.

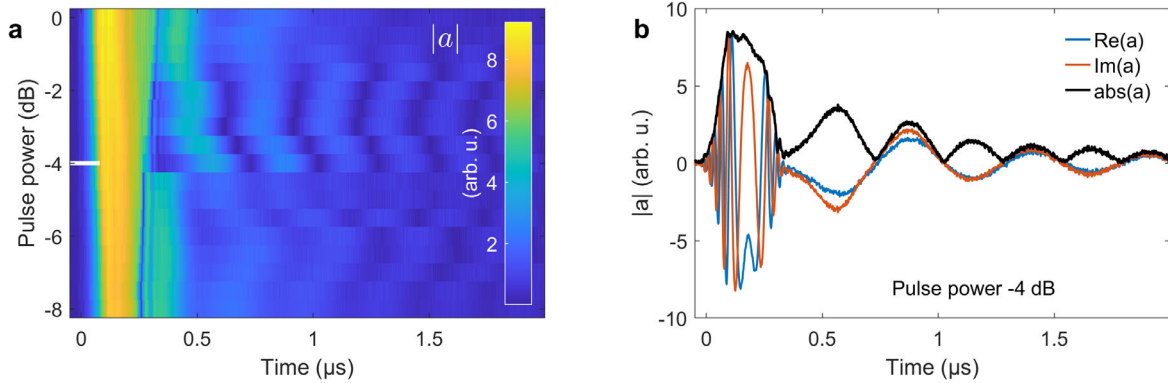


**Figure 6.12** Using the modified 400 ns chirped pulse in the experiment. (a) Cavity amplitude for a pulse power scan in 0.5 dB increments. (b) Detailed plot of the cavity dynamics at the optimal power setting.

dynamics discussed in Sec. 2.9. This will be the microwave inversion pulse we use for the main experimental results below.

### 6.0.3 Inversion storage using the rapid detuning loop

We now have an inversion pulse that works well to almost uniformly invert spins over the whole range of frequencies in the inhomogeneously broadened ensemble. But looking closely at the cavity dynamics in Fig. 6.12(b) and comparing with the simulations, particularly the simulated spin packet's dynamics  $\langle \sigma_-^j \rangle$  in Fig. 6.11(b), we see that the spin system has already started its motion of falling down the giant Bloch sphere while emitting a superradiant burst. The chirped inversion pulse alone just does not offer enough control over the spin system to perfectly align all spins along  $+z$  and momentarily freeze the dynamics in the metastable inverted state discussed in Sec. 2.9.

Simply stated, while it does create a mostly uniform inversion  $p = \langle \sigma_z^j \rangle$ , the transversal spin components are not uniformly zero  $\langle \sigma_-^j \rangle \neq 0$ . To combat this effect, we devised a simple method that yields a perfectly upright condition for each spin packet with vanishing  $\langle \sigma_-^j \rangle \approx 0$ . It relies on using the detuning loop, a small loop of superconducting wire directly wrapped around the parallel chip assembly of the DCR resonator (see Sec. 5.2.3): right after the chirped pulse, we rapidly detune the whole spin ensemble from the cavity resonance by an amount of  $\delta/2\pi \approx 20$  MHz. This detuning is achieved by switching off the loop current of 1 A in about 200 ns using a semi-conductor switching setup developed by the university's electronics workshop.

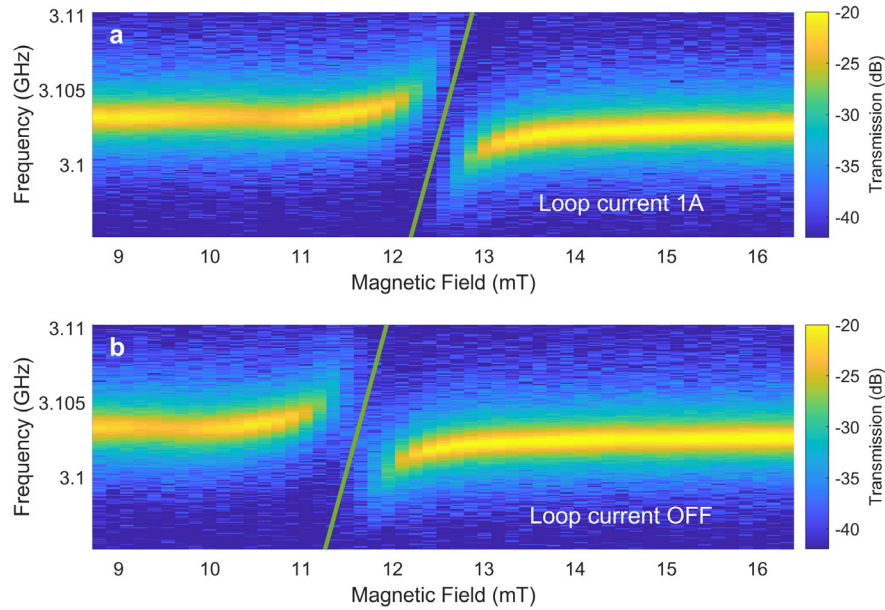


**Figure 6.13** External magnetic field scan and transmission spectroscopy in the ground state, with loop current at 1 A in (a) and with loop current switched off in (b).

The offset magnetic field of the detuning loop  $|\vec{B}_{\text{loop}}| \approx 1$  mT is oriented anti-parallel to the external field of the 3D Helmholtz coil cage  $|\vec{B}_{\text{ext}}| \approx 12.5$  mT, see Fig. 6.13, where we show a magnetic field scan with loop current on and off. With the loop current switched off, the system is now in a detuned state where the superradiant dynamics are fully suppressed. This way, the spin system maintains its inversion, which is expected to only slowly decay via the long characteristic timescale  $T_1$  on the order of seconds, while the transversal components quickly vanish with the short microsecond timescale  $T_2$ .

When tuning the spins back into resonance with the cavity by switching the loop current back on, the system is in a metastable inverted state. The stored inversion will always eventually decay via a superradiant burst when the threshold condition for superradiance,  $pC > 1$ , is fulfilled. However, it does so from a very controlled initial state of the spin ensemble. This carefully prepared initial state will allow us to study the crucial moments right at the onset of superradiance and investigate mechanisms that trigger the collective decay.

An example run using this inversion pulse and loop-switching protocol is shown in Fig. 6.14. When the inversion is stored for a short hold time of only  $60 \mu\text{s}$ , the superradiant emission that occurs upon tuning the spins back into resonance reaches a maximum cavity amplitude that is comparable to the first peak after the inversion

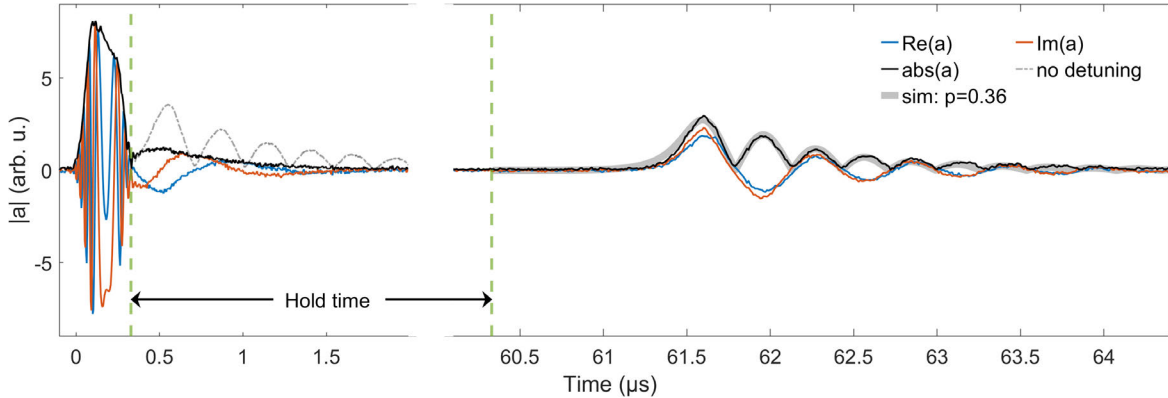


**Figure 6.14** Single run of the experiment using our inversion pulse and loop detuning/retuning protocol with optimized settings, plotting the measured cavity dynamics. The duration between the switch-off and switch-on triggers (dashed green lines) — where the superradiant dynamics are suppressed and the spin inversion is effectively stored — is defined as the hold time, shown here for a hold time value of  $60 \mu\text{s}$ . The cavity dynamics of the superradiant decay are simulated using an initial state with uniform inversion  $p$  and a small tipping angle, with only  $p$  and a time offset as free parameters.

pulse without detuning. This shows that our loop-switching protocol works as intended to store the inversion and later release it in a controlled way. Comparison with the numerical simulation also allows us to estimate the spin inversion efficiency of the full protocol from the simulation value  $p \approx 0.36$  as the ratio of spins in the excited state as  $N_{\uparrow}/N = (p + 1)/2 \simeq 68\%$ . Notably, the pulse does not appear immediately, but it takes a time of around  $1 \mu\text{s}$  to reach its maximum — this is the delay time of the superradiant burst, discussed in Sec. 2.9.

In reality, the current switching in the loop is not a perfectly rectangular function, as can be seen in Fig. 6.15(a) for both the switch-off flank and the switch-on flank of the loop current. We measure this loop current as the voltage drop over a series resistor in the loop switching circuit. The length of wire inside the cryostat ( $\sim 2 \text{ m}$ ) adds some parasitic capacitance to the loop circuit, causing the oscillations due to unwanted LC characteristics. The reason for using the loop with the default setting of  $1 \text{ A}$  for the on-resonance condition and  $0 \text{ A}$  to detune (instead of the opposite) is that the switch-off is much quicker. We simply do not care about the rapid fluctuations afterward, as the spins are already detuned far enough. The detuning loop alone, having an inductance of roughly  $L = 3 \mu\text{H}$  measured directly at the two leads into the cryostat, has a self-resonance frequency around  $7.5 \text{ MHz}$  [86] due to its LC behavior.

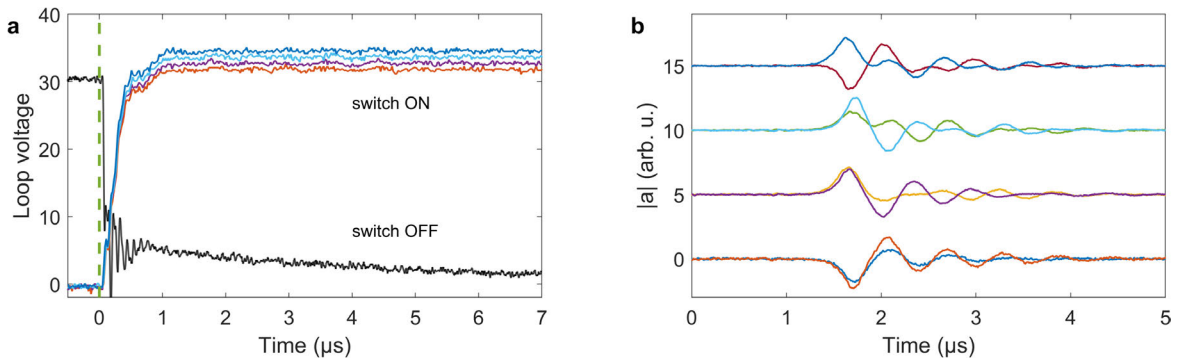


**Figure 6.15** Details of the loop switching dynamics. (a) Loop current over time, measured as a voltage over a series resistor in the loop circuit. (b) Depending on the loop current level reached upon tuning the spins back into resonance, the superradiant emission has its  $I$  and  $Q$  quadratures in phase or undergoing a phase rotation — a beating signal — during the emission process.

We chose a rather high series resistor value of around  $R = 30 \Omega$  to achieve a short rise time  $\tau = L/R$ , thus approximating the ideally rectangular switching behavior.<sup>1</sup>

An intuitive expectation is that when tuning the spins almost back into resonance but not quite, with a small detuning  $|\delta| \gtrsim 0$  left between the radiating spin system and the cavity frequency, the superradiant decay would still happen. However, this finite offset  $\delta$  would be visible as a beating signal in the  $I$  and  $Q$  quadratures. In Fig. 6.15(b) we see exactly this effect happening. It turns out that for the beating frequency to be exactly zero, the apparent loop current upon switching back — i.e. the voltage level measured at the resistor — needs to rise higher than the initial on-resonance setting prior to the inversion pulse. This peculiar behavior is most likely caused by the LC characteristics of the loop circuit.

Additionally, the optimal level to suppress the beating — to have the cavity quadratures in phase — even needs to be adjusted for different hold times. We attribute this effect to the current-limiting electronics in the power supplies generating the loop current, which presumably have some finite reaction time. We found the easiest solution to this problem is to use two sets of power supplies and current switches — one for switching off and one for switching back on resonance. The value of  $\delta$  when

<sup>1</sup>The measured rise time in Fig. 6.15(a) of around  $1 \mu\text{s}$  seems to contrast the statement above, that the superradiant decay does not appear immediately after switching back on resonance, but only after a certain delay time. As we will see below — especially for slightly reduced initial inversion  $p$  after a longer hold time — we can exert good control over the observed delay time by influencing the magnitude of fluctuations that trigger the superradiant avalanche effect. The delay time of around  $1 \mu\text{s}$  for the run in Fig. 6.14 is particularly short, as we start with a high initial inversion, and the superradiant decay is triggered by the noise photons of the high-power amplifier in the pump line.

tuning back can be adjusted by choosing the correct set voltage for the switch-on power supply, while the set current is always 1 A.

At this point in the experimental chapter, we are finished with the preliminary discussions, which were carried mostly by considerations about the protocol to create a uniformly inverted spin state. We continue with the main results of this thesis, investigating some intriguing aspects of our superradiant system, where the discussion will be based on two of my first-authored publications in chronological order.

## 6.1 Triggered superradiance

The discussion here is based on the following publication:

- **Triggered Superradiance and Spin Inversion Storage in a Hybrid Quantum System**

Wenzel Kersten, Nikolaus de Zordo, Oliver Diekmann, Tobias Reiter, Matthias Zens, Andrew N. Kanagin, Stefan Rotter, Jörg Schmiedmayer, and Andreas Angerer

Phys. Rev. Lett., 131, 043601 (2023); arXiv:2301.04100

In this work, we investigated the controlled triggering of superradiant emission from a metastable inverted spin state with uniform inversion  $p$ , following our inversion pulse and rapid-detuning protocol. The word “triggering” has a twofold meaning: *(i)* The superradiant decay is triggered by bringing the inverted spins back into resonance using the detuning loop, as the system is fundamentally unstable above the inversion threshold  $pC > 1$  on resonance. In this state, even the smallest fluctuation — in principle the presence of even a single microwave photon — will eventually set the collective superradiant avalanche process into motion. *(ii)* The superradiant decay is triggered by a microwave trigger pulse, which provides the initial kick to the collective spin vector, initiating the superradiant decay from the metastable inverted state. When the intrinsic fluctuations — the thermal background noise and quantum fluctuations — are well-controlled and small, the spontaneous formation time of the collective decay can be long. A coherent microwave pulse injected prior to self-decay will then influence the delay time and phase of the subsequent superradiant emission. Depending on the trigger pulse strength, the superradiant decay is shifted to earlier times, and its phase, as measured by the I/Q quadratures, is inherited from the trigger pulse.

Before investigating the system’s sensitivity to the number of trigger photons in the metastable state, let us examine the basis of our study — the superradiant decay from the uniformly inverted state — and compare it with our numerical simulations. In this first experiment, the decay is triggered by the high-power amplifier noise of the microwave pump line. Fig. 6.16(a) shows the cavity dynamics, with the  $y$ -axis in units of the square root of the estimated number of intra-cavity photons, using the calibration method outlined in Sec. 3.2.3. In this figure, we also give a visual definition of the delay time  $t_D$ , the time of maximum cavity amplitude during the superradiant emission. The cavity linewidth during this cooldown was measured at  $\kappa/2\pi = 516$  kHz, and the system’s cooperativity is  $C \approx 12$ . The simulation data is

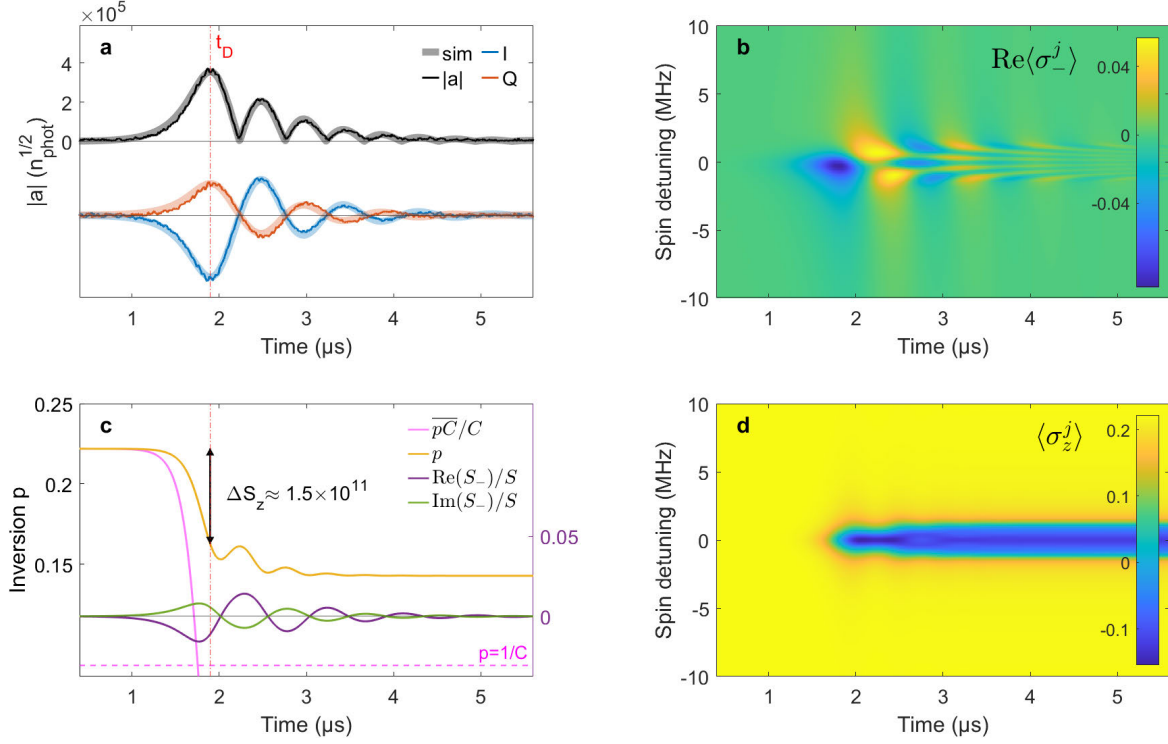


**Figure 6.16** Superradiant decay of the uniformly inverted spin-ensemble after a hold time of 3 ms, triggered by the high-power amplifier noise in the pump line. (a) Measured cavity dynamics, plotted as the absolute value of  $|a|$  and as the field quadratures  $I = \text{Re}(a)$  and  $Q = \text{Im}(a)$ . In this experiment, we plot  $|a|$  in units of square root number of photons  $n^{1/2}$  after calibrating our microwave setup. (b) A color plot of the simulated spin packet's dynamics for the transversal components  $\text{Re}\langle\sigma_-^j\rangle$ . (c) Dynamics of the spin ensemble averages: the inversion  $p = \langle S_z \rangle / S$  and the normalized transversal component of the collective spin vector, evaluated as  $S_- = \sum_j \rho_j \langle \sigma_-^j \rangle$  using the discrete distribution weights  $\rho_j$  of the numerical model. (d) Similar as in (b) but for the  $z$ -component  $\langle\sigma_z^j\rangle$ . Notably, only spins within a narrow frequency window as determined by the cavity linewidth  $\kappa$  participate in the dynamics. After the superradiant decay, a spectral hole in the spin inversion profile is created.

created by time-evolving an initial state with uniform inversion  $p \approx 0.22$  and a small initial tipping angle  $\theta = \arctan(|S_-|/S_z) \approx 4.3 \times 10^{-4}$ .

The number of photons that are generated by the superradiant decay,  $\max(|a|)^2 \approx 1.6 \times 10^{12}$ , agrees well with the number of decaying spins  $\Delta S_z = \Delta p N / 2 \approx 1.5 \times 10^{12}$ , see Fig. 6.16(c). We evaluate this number as the difference between the initial inversion  $p$  and the value at time  $t_D$ , using the estimated number of spins in the sample of  $N \approx 5.3 \times 10^{12}$ , see Sec. 4.1.2.<sup>2</sup>

An interesting observation from the dynamics in Fig. 6.16(d) is that the majority of spins, particularly the off-resonant spin packets, do not decay but remain inverted; only the spins close to the cavity resonance do. This creates a spectral hole of de-excited spins after the superradiant decay. It becomes particularly evident that the total spin inversion  $p$  is still above the threshold (dashed pink line) in Fig. 6.16(c), implying that the inverted ensemble still carries enough energy to generate another superradiant decay. However, the non-uniformity of the inversion profile, with the resonant spin packets depleted, stabilizes the partially inverted state and prevents an immediate subsequent decay. This spectral hole formation is a crucial observation to keep in mind for the discussion of the second main experimental result presented in this thesis, focused on the paper "Self-Induced Superradiant Masing" described below.

Quite naturally, the next step was to scan the hold time - the duration for storing the inverted ensemble using the detuning loop. Fig. 6.17(a) shows the result of this scan, where the superradiant decays are again triggered by the high-power amplifier noise. We use our semi-classical model to simulate the data, adjusting only the uniform initial inversion  $p$  and a time offset, using the same procedure mentioned above. A plot of the simulated values of  $p$  versus hold time will be presented below, along with another experiment demonstrating "superradiant amplification" of injected MW pulses, allowing us to estimate  $p$  even when  $p < 1/C$ , where the ensemble dephasing and other losses overpowered the formation of a superradiant decay.

For increasing hold times, the maximum cavity amplitude  $\max(|a|)$ , which has the expected proportionality  $\max(|a|) \propto p$  (see Sec. 2.9), decreases roughly exponentially, as shown in Fig. 6.17(b). This indicates that the spin inversion is gradually lost during the hold time. While this result is to be expected, the timescale  $\tau = 7.6$  ms comes as a surprise, being five orders of magnitude faster than the slow longitudinal spin

---

<sup>2</sup>Notably, the values of our best estimates for some parameters ( $g_{\text{coll}}$ ,  $W$ ,  $\gamma_{\perp}$ , and  $N$ ) have undergone slight changes within 20% as compared to the paper [35], and a keen reader might notice single-digit number changes compared to the original publication. This is of no further consequence to the main results, where the focus is mainly on a qualitative description. For the remaining discussion of the paper's results, I will stick to the original analysis.

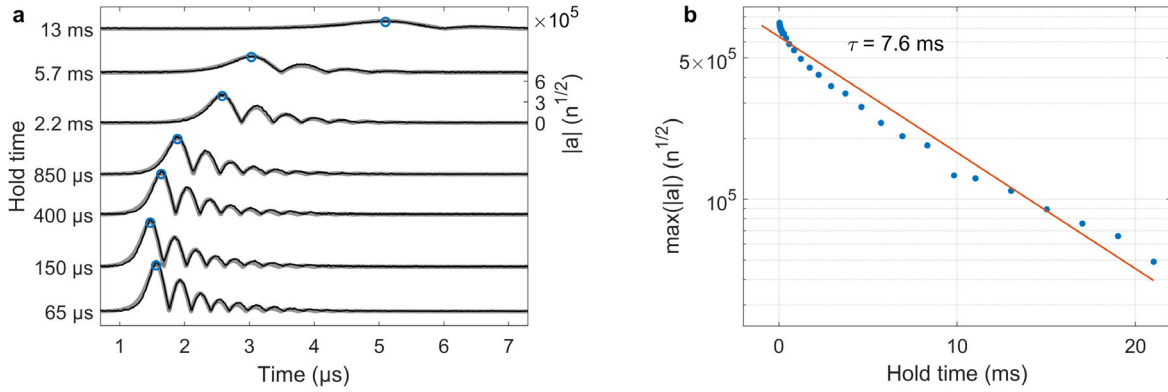


**Figure 6.17** Hold time scan of the spins in the inverted state. (a) Multiple experimental runs (black) of the cavity amplitude dynamics are shown, where the  $y$ -offset corresponds to the different hold times in logarithmic scale. Gray curves represent semi-classical model simulations of the data. (b) Maximum cavity amplitudes of the superradiant decays plotted versus the hold time on a semi-log scale, exhibiting an exponential decay behavior.

relaxation  $T_1 > 100$  s. For hold times above  $\sim 20$  ms, the inversion has dropped below the threshold  $p = 1/C$ , and we no longer observe any superradiant emission.

These results suggest two distinct timescales for spin inversion loss: a faster millisecond process, followed by the slower  $T_1$  relaxation to the ground state. Our proposed mechanism for the faster process is direct dipole-dipole coupling between neighboring spins. Flip-flop processes driven by these spin-spin couplings cause the exchange of excitations between neighboring spins. Among the trillions of NV spins in the diamond, a sizeable number have exceptionally short lifetimes due to their local crystal environment. These are described as “fluctuator NVs” in Ref. [87].<sup>3</sup> Once an excitation is transferred to a fluctuator spin, it is quickly lost. Thus, the fluctuators act as local sinks for the spin polarization. The transfer of excitations into these sinks — a diffusive process — is driven by the spatial polarization gradient. Once an average inversion level  $p = 0$  is reached throughout the sample, the gradient vanishes, and diffusion can no longer sustain the accelerated inversion loss. At this point, the slow  $T_1$  relaxation of individual spins takes over. The role of these spin-spin interactions —

<sup>3</sup>The fluctuator NVs owe their short lifetimes to fluctuations of their charge state from  $\text{NV}^-$  to  $\text{NV}^0$  and back, which does not preserve the spin state. These experiments, which consolidated the fluctuator model, were conducted at room temperature using optical initialization and readout (crucially, of both the spin and charge state) in combination with MW pulses for spin state manipulation. In their paper, the authors report an extracted fluctuator density of approximately 16 ppm out of a very high density of 45 ppm NV spins in their sample. The charge state dynamics are postulated to arise from electron tunneling between NVs in close proximity to each other.

also acting as a driving force for superradiant dynamics — will be explored further when discussing the second publication.

Leaving the “mystery” of spin-spin interactions and the fast relaxation dynamics behind us for now, we return to another aspect in Fig. 6.17(a). Looking at the stacked superradiant decay signals, we notice a trend of the delay time increasing with the hold time (or decreasing with the inversion), confirming the expected  $t_D \propto p^{-1}$  dependence derived in Eq. (2.81). We restate the delay time equation:

$$t_D = -2T_R \frac{1}{p} \log\left(\frac{\theta}{2}\right), \quad (6.4)$$

where  $\theta = \arctan(|S_-|/S_z)$  is the initial tipping angle of the collective spin vector, and  $T_R$  is the characteristic timescale of the superradiant emission, a fixed parameter to be determined experimentally.

The logarithmic dependence on the initial tipping angle  $\theta$  suggests a potential application as a microwave detector: Once the inverted spin state is tuned back into resonance, it has zero tipping angle, apart from the unavoidable intrinsic quantum and thermal fluctuations. A microwave signal injected before the spin ensemble eventually decays on its own will cause a rotation of the collective spin vector from its starting position. This will change the vector’s azimuthal coordinate  $\theta$  contingent on the signal’s amplitude, therefore influencing the delay time  $t_D \propto -\log(\theta)$ . Additionally, the microwave signal’s phase will influence the spin vector’s polar coordinate  $\phi = \arg(S_-)$ , consequently determining the phase  $\varphi = \arctan(Q_D/I_D)$  as measured by the quadratures of the cavity amplitude at time  $t_D$ . In theory, this could result in a highly sensitive detection scheme, sensitive to both the amplitude and phase of microwave signals.

To test this concept, we must first isolate the cavity, located at the 24 mK stage of the cryostat, from the noise of the pump line’s high-power amplifier at room temperature. We implemented an isolation switch at the 1 K stage, which mechanically decouples cavity port 1 from the microwave pump line using a solenoid mechanism. Fig. 6.18 compares the superradiant decay dynamics with this switch open and closed. We clearly see that, on average, the delay times with the open switch are roughly 500 ns earlier than for the closed switch, indicating that the noise isolation works as intended.

We now proceed to evaluate the sensitivity of the inverted spin state experimentally. We fix a constant hold time of 2 ms, allowing sufficient time for the isolation switch operation and subsequent system equilibration, with an estimated remaining thermal photon population of  $\bar{n} \approx 3$ . At  $t = 150$  ns after the detuning loop is switched

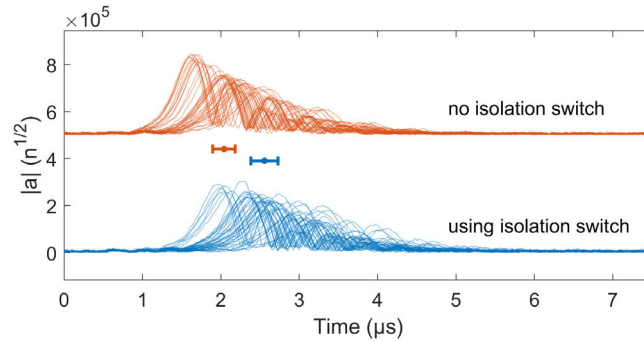


**Figure 6.18** Repeated runs with a hold time of 5 ms, where the isolation switch is either open or closed. The red and blue horizontal error bars indicate the position of the mean delay time and its standard deviation.

back ( $t = 0$ ), we inject a 100 ns trigger pulse via the highly attenuated probe line (approximately  $-70$  dB attenuation). This pulse is resonant with the cavity and introduces a calibrated number of trigger photons. Our methods for estimating both thermal and trigger photon numbers are discussed in Sec. 3.2.3.

The experiment is repeated many times, adjusting the trigger photon number  $n_{\text{trig}}$  by modifying the pulse power in 5 dB steps using digital attenuators, including runs without a trigger pulse ( $n_{\text{trig}} = 0$ ). For each iteration, we determine the delay time  $t_D$  and the  $I_D/Q_D$  quadrature values of the superradiant decay peak. As shown in Fig. 6.19, the superradiant decay amplitudes  $\max(|a|) = \sqrt{I_D^2 + Q_D^2}$  exhibit variations of  $\pm 10\%$  between runs. These variations are likely caused by timing and amplitude imperfections of the inversion pulse generation, and variability of the mechanical connection opened and closed by the isolation switch.

To focus only on the trigger photon number’s impact on delay times, we compensate for the systematic dependence of  $t_D \propto \max(|a|)^{-1}$  by rescaling the  $t_D$  data. Additionally, we apply an independent correction to the superradiant decay phases  $\varphi = \arctan(Q_D/I_D)$  to account for a linear phase drift with  $t_D$ , which results from a slight constant detuning of the spins relative to the cavity. A visual representation of these correction methods is presented in Fig. 6.19(a,b).

After applying these corrections, we plot the rescaled delay times and phases of all superradiant cavity pulses in Fig. 6.20. We see a clear trend: with higher numbers of trigger photons  $n_{\text{trig}}$ , the distributions of  $t_D$  shift towards earlier times and become narrower. Similarly, the  $\varphi$  distributions change from initially random at low trigger photon counts to more well-defined and centered around zero for stronger trigger pulses.

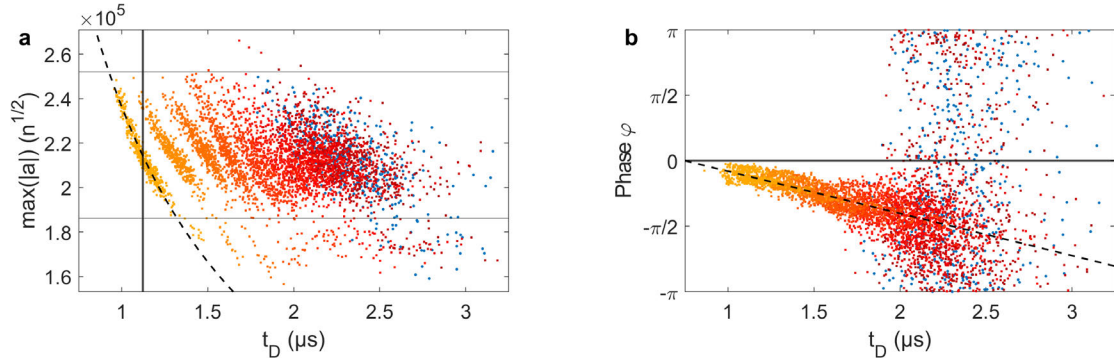


**Figure 6.19** Raw data from the detector experiment showing delay times, amplitude maxima, and phases. Different color dots indicate the trigger photon numbers: brighter yellow for higher, darker red for lower, and blue for thermal and quantum noise triggering. (a) Delay time versus maximum superradiant decay amplitude, showing  $\max(|a|) = \sqrt{I_D^2 + Q_D^2}$  variations within  $\pm 10\%$ . We compensate for systematic effects due to the amplitude variations. This involves removing outliers beyond the horizontal black lines and adjusting for the  $t_D \propto \max(|a|)^{-1}$  dependence by shifting  $x$ -coordinates to transform the fitted function  $x = ay^{-1} + b$  (dashed line) to the vertical black line. (b) Superradiant emission phases  $\varphi = \arctan(Q_D/I_D)$  are independently corrected for a linear drift with  $t_D$  by shifting  $y$ -coordinates from the dashed line to  $y = 0$ .

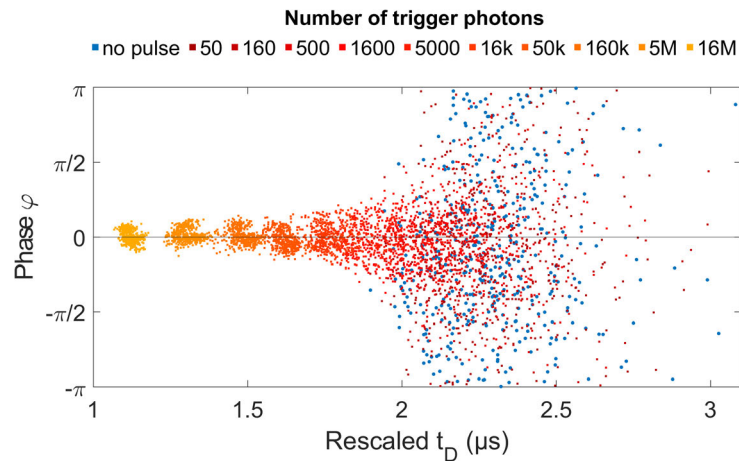


**Figure 6.20** Rescaled delay times and phases, color-coded by trigger photon number (“no pulse” indicates  $n_{\text{trig}} = 0$ ). Each dataset is comprised of over 400 runs. Higher trigger photon numbers result in earlier  $t_D$  distributions and narrower  $\varphi$  distributions.

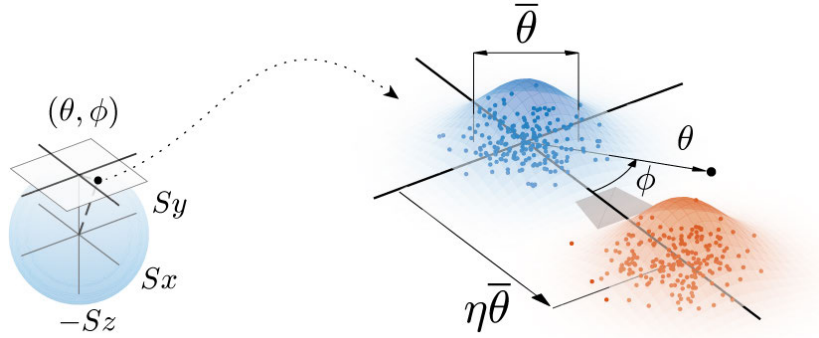


**Figure 6.21** Collective spin vector coordinates  $(\theta, \phi)$  during the linear stage of the superradiant decay. Prior to the trigger pulse, the vector is located near the origin of a plane with a  $z$  offset determined by the inversion  $p$ . The initial state distribution (blue) is a 2D Gaussian with width  $\bar{\theta}$ . The trigger pulse displaces this distribution by length  $\eta$  (in  $\bar{\theta}$  units) towards  $\phi = 0$  (red).

To understand this behavior intuitively, consider a mechanical analogy: a well-balanced inverted pendulum. Left undisturbed, it would eventually topple, brought out of balance by a slight air current. The direction of its fall would be random, and the process would take longer. However, when deliberately pushed, the pendulum falls sooner and in the direction of the applied force. This mental image captures the essence of the data presented in Fig. 6.20, where intrinsic fluctuations play the role of air currents, and the trigger pulse acts as the deliberate push.

Now, for a more quantitative analysis, we want to understand the distributions of the measured  $t_D$  and  $\varphi$  data. The observed randomness is not part of our theoretical model, which only offers a fully deterministic description to calculate the evolution starting from a well-defined initial state. The easiest way to incorporate the effect of intrinsic thermal and quantum fluctuations is to introduce it via randomness in the initial conditions. To this end, we conceptually split the dynamics of the superradiant decay into two stages [10, 88].

The superradiant decay process begins with a linear phase, during which the total emission rate of the decaying spin ensemble scales linearly with the number of emitters,  $\Upsilon \propto N$  (see Sec. 2.9). Initially, the collective spin vector with a length given by the initial inversion  $p$  is oriented upwards along  $+z$ . Intrinsic fluctuations of the system induce a small tipping angle  $\theta = \arctan(|S_-|/S_z) \approx 0$  and a random polar angle  $\phi = \arg(S_-)$ . Given that  $\cos(\theta) \approx 1$  throughout this linear phase, we model the spin vector's movement as confined to the offset plane  $z = p$ , see Fig. 6.21. The spin vector's

initial state, incorporating the random intrinsic fluctuations, is then simply described by a 2D Gaussian distribution of width  $\bar{\theta}$  centered at the origin on this “map of the north pole” [27].

Now, the trigger pulse induces a coherent rotation of the collective spin vector about an axis determined by the phase of the trigger pulse, which is held constant across all experimental runs. This rotation corresponds to a displacement  $\eta$  within the plane,<sup>4</sup> chosen to be in the  $\phi = 0$  direction. The rotation angle — and therefore the displacement length  $\eta$ , expressed in units of  $\bar{\theta}$  — corresponds to the magnetic amplitude of the trigger pulse. This establishes the relationship  $\eta \propto B_{\text{trig}} \propto \sqrt{n_{\text{trig}}}$ .

After the trigger pulse’s displacement action, the “radial” coordinate in the offset plane, i.e. the tipping angle  $\theta$ , follows the Rician distribution [89]

$$f_{\Theta}(\theta, \eta, \bar{\theta}) = \frac{\theta}{\bar{\theta}^2} \exp\left(-\frac{1}{2} \left(\frac{\theta^2}{\bar{\theta}^2} + \eta^2\right)\right) I_0\left(\frac{\theta\eta}{\bar{\theta}}\right), \quad (6.5)$$

with the modified Bessel function of the first kind  $I_0$ . For  $\eta \gg 1$  this distribution  $f_{\Theta}$  becomes a Gaussian with mean value  $\langle \theta \rangle = \eta\bar{\theta}$  and variance  $\text{Var}(\theta) = \bar{\theta}^2$ .

As  $\eta$  increases with higher trigger photon numbers, the initially random polar angles converge towards a narrower distribution around  $\phi = 0$ . This is illustrated by the gray shaded angular spread of the coordinate  $\phi$  for dots sampled from the red Gaussian distribution, see Fig. 6.21. The angular distribution for  $\phi$  is given by [90]

$$f_{\Phi}(\phi, \eta) = \frac{\eta}{\sqrt{2\pi}} \tilde{\varphi}(\eta) \left(1 + \eta \cos(\phi) \frac{\tilde{\Phi}(\eta \cos(\phi))}{\tilde{\varphi}(\eta \cos(\phi))}\right), \quad (6.6)$$

where  $\tilde{\varphi}$  is the standard normal distribution and  $\tilde{\Phi}$  its cumulative distribution function. As  $\eta$  increases, the initially randomly distributed angle  $\phi$  becomes more and more well-defined and approaches  $\phi = 0$ .

Following this linear stage, the system transitions into a nonlinear regime dominated by the superradiant avalanche dynamics. Collective stimulated emission will accelerate the spin vector’s rotation towards the equator of the giant Bloch sphere, where the total emission rate reaches its maximum and scales as  $\Upsilon \propto N^2$ . The emitted decay pulse’s phase  $\varphi$  corresponds directly to  $\phi$  at the onset of the nonlinear stage.

---

<sup>4</sup>Notably, we use here the same symbol  $\eta$  as for the cavity drive in the Maxwell-Bloch equations, particularly in the first line of Eq. (2.76a). This usage is in line with Refs. [27, 88]. The displacement  $\eta$  in the context of this section has units of a linearized angle in radians, in contrast to the cavity drive which is a rate with units of inverse seconds.

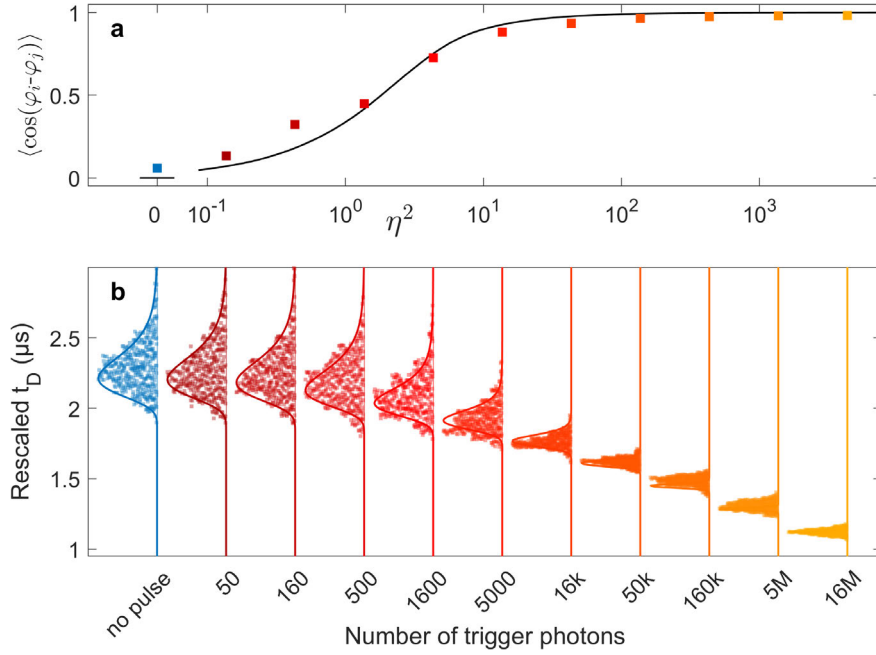


**Figure 6.22** (a) Cosine of phase differences  $\langle \cos(\varphi_i - \varphi_j) \rangle$ , averaged over all runs with identical  $n_{\text{trig}}$ , quantifying the phase randomness from the measured sets of  $\varphi$ . (b) Swarm plots of the delay time  $t_D$  data. The solid lines in (a) and (b) are obtained from our theoretical description, varying only the parameter  $\eta^2 \propto n_{\text{trig}}$ .

Less directly, the initial tipping angles  $\theta$  follow from the delay times  $t_D$  using the relation Eq. (6.4) by applying a change of variables

$$f_{t_D}(t_D, \eta, \bar{\theta}) = f_{\Theta}(\theta(t_D, \tilde{T}_R), \eta, \bar{\theta}) \left| \frac{d\theta(t_D, \tilde{T}_R)}{dt_D} \right|, \quad (6.7)$$

where  $\tilde{T}_R = T_R/p$ . Using this relationship, we model the histograms of  $t_D$  in Fig. 6.22(b), by fixing  $\tilde{T}_R = 142 \text{ ns}$  and  $\bar{\theta} = 5.85 \times 10^{-4}$  and varying  $\eta^2$  linearly. To quantify the phase randomness, we average the cosine of mutual phase differences  $\langle \cos(\varphi_i - \varphi_j) \rangle$  over all runs with identical trigger photon numbers  $n_{\text{trig}}$ . Using the same  $\eta^2$  scaling as for the delay time data, we calculate the black line in Fig. 6.22(a) by evaluating the cosine average with Eq. (6.6). Since  $\eta^2$  is proportional to the energy imparted to the spin system during the linear stage, we can use it interchangeably with  $n_{\text{trig}}$  on the  $x$ -axes of Figs. 6.22(a,b), confirming the expected result  $n_{\text{trig}} \propto \eta^2$ .

Notably, even a weak microwave pulse of approximately  $10^{-11}$  photons per spin can significantly affect the superradiant decay. This high sensitivity demonstrates the potential of our system as a detector for weak microwave signals. We expect that

the system’s sensitivity to both amplitude and phase could be further enhanced by reducing the number of spins while maintaining high cooperativity. However, a clear drawback of the current system is the requirement for statistics to differentiate pulse powers and phases. For any practical application, the averaging time needs to be reduced significantly from the current roughly 3 min per run. Potentially, this could be implemented using optical pumping of NV spins to create the inverted state, enabling dramatically increased experimental repetition rates. Furthermore, critical coupling of the cavity to the signal entry port is required to avoid parts of the signal being reflected and lost for detection. In the experiment presented here, we only refer to the number of intra-cavity trigger photons and disregard any prior signal losses. Lastly, the frequency range of detectable MW signals, currently limited by the cavity bandwidth of roughly 1 MHz around a resonance frequency of approximately 3 GHz, could be tuned in-situ using piezo-actuators to vary the chip distance and adjust the cavity’s circuit capacitance, combined with Zeeman tuning the spin ensemble. These improvements could potentially open up new avenues for quantum sensing applications, making our system a candidate for detecting weak microwave signals with both amplitude and phase sensitivity.

Having explored our system as a sensitive probe for weak microwave signals, we now shift our focus to the regime of reduced effective cooperativity  $pC < 1$  below the superradiant threshold. In this regime, dissipation processes dominate over the spontaneous build-up of coherence in the spin system, preventing the generation of superradiant emission (see also Sec. 2.9). However, we demonstrate that by injecting a sequence of moderate-power MW pulses, we can externally seed coherence in the system. This process generates a form of “stimulated superradiant emission”, observable as an effective amplification of the injected pulse sequence with the partially inverted spins acting as an effective gain medium.

We probe the system by injecting a sequence of resonant MW pulses via the pump line at 5  $\mu$ s intervals, each with a duration of 100 ns. As illustrated in Fig. 6.23, this results in an amplification of the pulses compared to the “empty” cavity response (with far-detuned spins). Notably, tens of injected MW pulses can be amplified in succession, see Fig. 6.24. We find good agreement of the measured dynamics with our numerical simulations, using only two free parameters: the amplitude of the incident pulses (held constant for all fits) and the ensemble inversion  $p$ .

Finally, we combine our results above and below the superradiance threshold  $pC = 1$ , demonstrating that our semi-classical model seamlessly captures the system’s behavior in both regimes. In Fig. 6.25, we plot the inversion  $p$  extracted with our

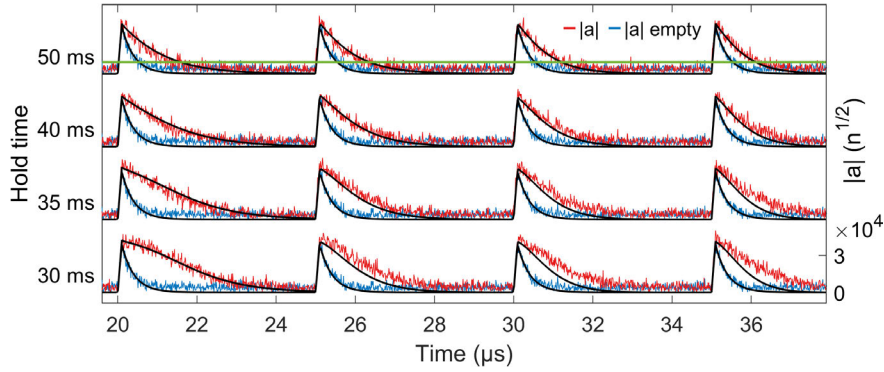


**Figure 6.23** Cavity amplitude  $|a|$  for a series of 100 ns pulses, each injecting  $n_{\text{trig}} \approx 1.5 \times 10^9$  photons, amplified by the partially inverted spin ensemble below the spontaneous superradiant threshold  $pC < 1$  for different hold times (red). In comparison, we plot the signal obtained with an “empty” cavity, where the spins are far detuned (blue). For finding the parameters in our semi-classical model (black), we ignore noise below a certain threshold (green line at the top).

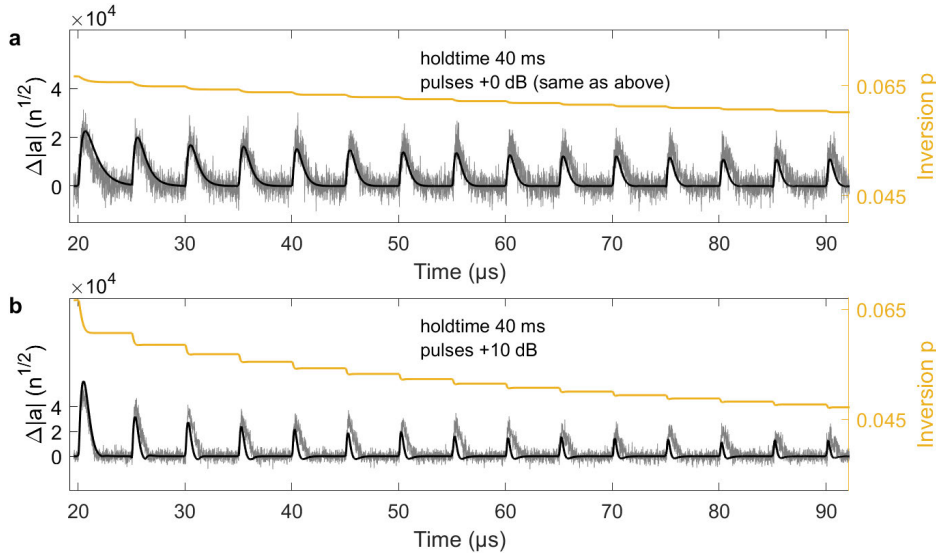


**Figure 6.24** Pulse amplification plotted as the difference of a measurement with partially inverted spins ( $pC < 1$ ) and “empty” cavity  $\Delta|a| = |a| - |a_{\text{empty}}|$  (c.f. Fig. 6.23). (a) Longer section of the dynamics for the run with a hold time of 40 ms in Fig. 6.23, with the measured data plotted in gray and the simulation result in black. Additionally, we plot the simulated inversion dynamics, where the value of  $p$  decreases as a step-like function with each pulse. (b) Similar measurement, but for a 10 dB higher pulse power than in (a).

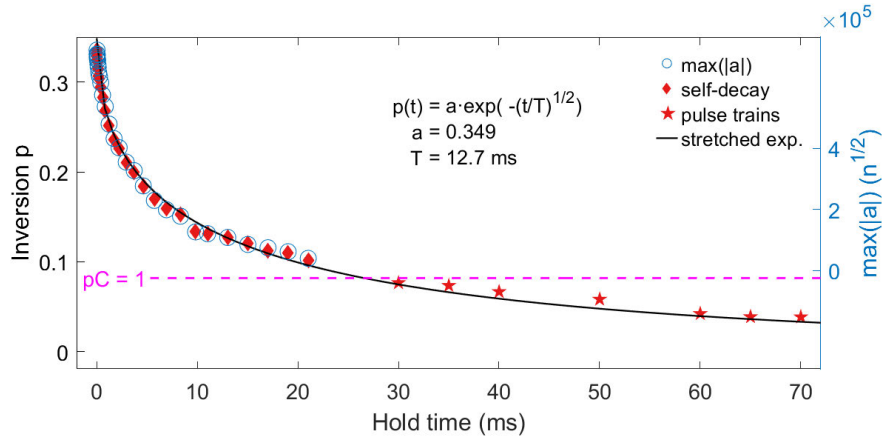


**Figure 6.25** Ensemble inversion as a function of hold time, extracted by simulations in the two regimes above and below  $pC = 1$ . Above this threshold, the pulse maxima (right  $y$ -axis) follow the values of  $p$  from simulations of the self-decays shown in Fig. 6.17. A stretched exponential with exponent  $1/2$  is fitted to the inversion.

numerical simulations over the hold time. In the regime  $pC > 1$  this confirms the relation  $\max(|a|) \propto p$ . Furthermore, the  $p$  values derived from simulated pulse train amplification measurements provide insight into the time evolution of the ensemble inversion below the superradiance threshold  $pC < 1$ . We fit these data with a stretched exponential function, using an exponent of  $1/2$ . Notably, this fit achieves good agreement without requiring an offset term, as  $p = 0$  represents the natural endpoint of this rapid inversion loss process, in contrast to the slow  $T_1 > 100$  s decay. The  $1/2$  exponent is characteristic of spin diffusion in three dimensions, as demonstrated in Ref. [87] and its accompanying Supplemental Material. This suggests that the fast inversion loss is indeed driven by spin diffusion, wherein fluctuators dissipate spin excitations from their local surroundings via direct spin-spin interactions until the spin ensemble reaches a completely mixed state ( $p = 0$ ). At this point, spin diffusion becomes ineffective due to the vanishing spatial polarization gradient in the ensemble, and the slow  $T_1$  decay mechanism takes over.

Summarizing the paper's results, we have established our experimental platform — showcasing its ability to create an inverted spin ensemble and store the inversion for tens of milliseconds, before releasing it in the form of a strong superradiant burst. The observed superradiant dynamics are consistent with our numerical model, which assumes a uniformly inverted initial spin state. We observe a short lifetime of the inverted state, an effect we attribute to spin diffusion mediated by direct spin-spin coupling. Our platform exhibits remarkable sensitivity to weak microwave trigger pulses, influencing

the subsequent superradiant dynamics through amplitude and phase. Additionally, we explore a regime of reduced cooperativity without spontaneous superradiant emission, where the inverted spins effectively act as a gain medium for a series of short MW pulses. These observations showcase our ability to control superradiant emission and explore its fascinating collective behavior. Interestingly, as we will discuss in the next section based on my second paper using this platform, spin-spin interactions play a dual role. Beyond their dissipative effects, they actually drive a series of superradiant revival pulses, highlighting the complex nature of collective quantum phenomena in our system.

## 6.2 Self-induced superradiant masing

The discussion here is based on the following publication:

- **Self-Induced Superradiant Masing**

Wenzel Kersten, Nikolaus de Zordo, Elena S. Redchenko, Nikolaos Lagos, Andrew N. Kanagin, Andreas Angerer, William J. Munro, Kae Nemoto, Igor E. Mazets, Jörg Schmiedmayer  
arXiv:2402.08537

At the core of this work is an unexpected observation, shown in Fig. 6.27: After the initial superradiant decay, we observe a series of periodic revival pulses, which gradually diminish in amplitude, followed by a long period of sustained emission, decaying slowly and lasting more than 500 microseconds. Surprisingly, the pulsed emission sets in after a long break  $\Delta t$  ranging from 15  $\mu\text{s}$  up to 30  $\mu\text{s}$  following the initial, well-understood, superradiant decay.

This revival dynamics timescale  $\Delta t$  is unexpected, as it is much longer than the characteristic timescales of the cavity loss rate, the ensemble dephasing, and the collective interaction of the coupled system,  $\Delta t \gg \{\kappa, \Gamma, g_{\text{coll}}\}^{-1}$ . It also significantly exceeds the individual spin linewidth  $\Delta t \gg \gamma_{\perp}^{-1}$ . This seems to exclude any Rabi oscillations or spin-echo behavior as a possible explanation for the revivals. These peculiar dynamics were already observed early on in our exploration of this experimental system, but a suitable explanation remained elusive. Only recently, we discovered a mechanism to describe our observations: As already pointed out in Fig. 6.16, only the resonant spin packets  $j$ , having a detuning  $|\Delta_s^j|$  smaller than the cavity linewidth  $\kappa$ , participate in the dynamics and are de-excited after the initial superradiant decay, creating a spectral hole. The revival dynamics can be explained by the transport of spin excitations from off-resonant spins into this spectral hole, leading to a gradual homogenization of the spin inversion profile in frequency space. As we will discuss below, the underlying mechanism is governed by spin-spin interaction within the spin ensemble.

In the following, we will develop our discussion in this order: First, we focus on the observed dynamics and their spectral properties. Next, we study the dynamics experimentally, employing a protocol that uses a second detuning sequence after the initial superradiant decay to effectively exclude any other sources for the revival pulses other than dynamics within the spin system itself. This will be followed by a phenomenological model that captures the observed dynamics using numerical simulations, underpinned by further experimental evidence. Finally, we lay our focus

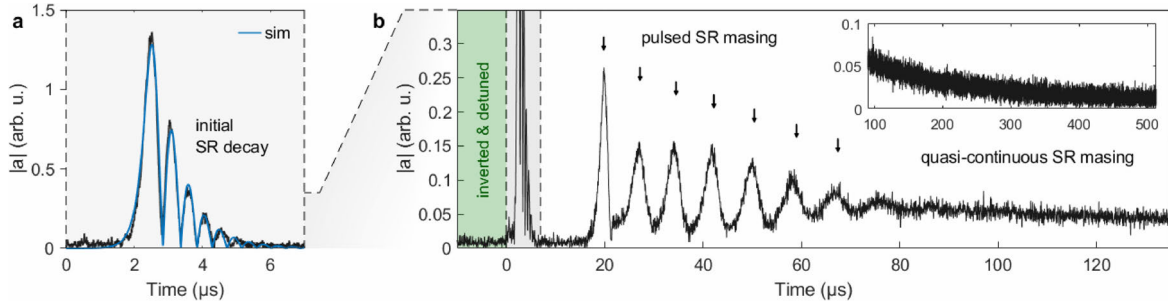


**Figure 6.26** Cavity dynamics of a single experimental run with 4 ms hold time. (a) Plot of the initial superradiant decay, triggered by the high-power amplifier noise, together with a simulation using our standard semi-classical model with uniform initial inversion  $p_0 \approx 0.22$ . (b) Details of the revival pulses and subsequent quasi-continuous superradiant emission.

on the conjectured source for our observations, direct dipole-dipole interactions in the disordered spin system as a driving force for the spectral hole-refilling, generating the pulsed and subsequent sustained superradiant emission.

The initial superradiant decay and novel subsequent dynamics are shown in Fig. 6.26, using our standard experimental protocol: We apply a microwave inversion pulse to uniformly invert all spins, starting from a relaxed spin ensemble in resonance with the cavity. After the inversion pulse, we store the spin inversion for a varying hold time using the detuning loop and subsequently release the superradiant emission. The initial superradiant decay is well captured by the standard semi-classical model using a numerical solution of the Maxwell-Bloch equations (2.64), starting from a uniformly inverted spin ensemble with a small initial tipping angle.

Let us now focus on the first part of the novel dynamics, a sequence of periodic revival pulses. As we saw earlier, the initial superradiant peak amplitude  $\max(|a|)$ , directly proportional to the initial spin inversion<sup>5</sup>  $p_0$ , decreases for longer hold times. The superradiant avalanche formation starting from a state with lower initial inversion  $p_0$  takes a longer amount of time to reach its maximum, as quantified by the delay time, scaling inversely with the inversion as  $t_D \propto p_0^{-1}$ . The revival timescale, on the other hand, decreases with the initial inversion  $\Delta t \propto p_0$ , with the revival pulses shifted to earlier times for lower  $p_0$ , see the hold time scan shown in Fig. 6.27.

We now discuss the time-resolved and spectral properties of the observed cavity dynamics for an exemplary single-shot experimental run. The data are recorded with

<sup>5</sup>In this section the total ensemble inversion  $p = \sum_k \rho_k \langle \sigma_z^k \rangle$  will become a dynamical quantity, and we emphasize its value as an initial condition at  $t = 0$  with the subscript zero as  $p_0$ .

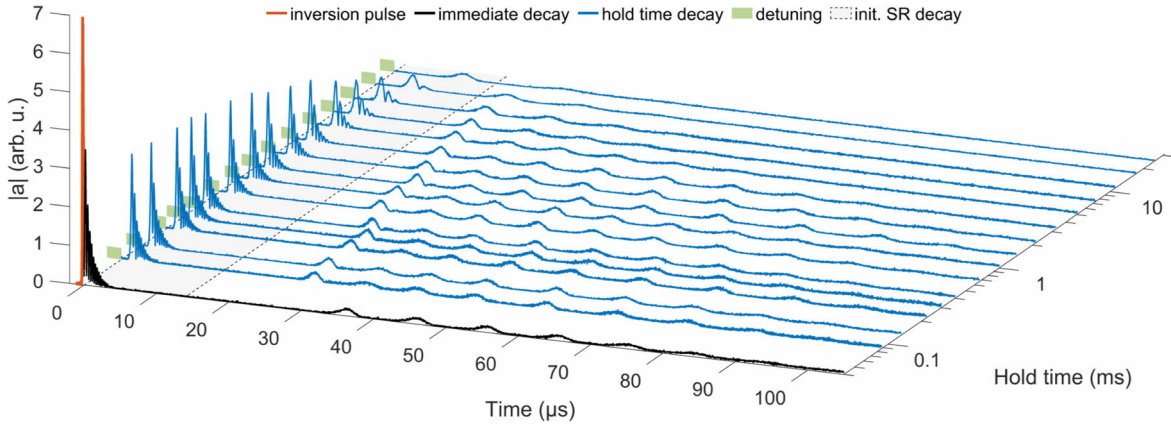


**Figure 6.27** Time evolution of the cavity emission using the standard experimental protocol: spin inversion pulse, detuning period for inversion storage (hold time), and release as superradiant emission. Following the initial superradiant decay, we observe a series of unexpected revival pulses, appearing at earlier times  $\Delta t$  for longer hold times, i.e. decreasing initial inversion  $p_0$ .

the same measurement settings as for the run in Fig. 6.26, using a hold time of 4 milliseconds, corresponding to an initial inversion of approximately  $p_0 \approx 0.22$ . Only the digitizer sample rate is halved, extending the measured time window to capture the subsequent quasi-continuous regime lasting up to roughly one millisecond. The recorded quadratures  $I$  and  $Q$  of the cavity amplitude are demodulated at an intermediate frequency of 5 MHz detuned from the cavity resonance. This demodulation bypasses a DC noise peak, improving the signal quality. For visual clarity, the I/Q signals shown in Fig. 6.28 and other plots below are digitally demodulated in the rotating frame of the cavity resonance frequency.

The periodic pulses, which appear approximately  $\Delta t \approx 15 \mu\text{s}$  after the initial superradiant decay dynamics have subsided, manifest as approximately Gaussian envelopes of the absolute value of the cavity amplitude  $|a|$ . To extract the pulsed emission's linewidth, we employ a fast Fourier transform (FFT) analysis of the recorded I/Q data. Gaussian lineshapes are then used to fit the pulses both in the time domain and in frequency space, using a limited time window centered around each pulse to calculate the FFT results. This fitting is shown for the time-resolved data in Fig. 6.28. The analysis results in pulse widths  $\delta t$  (FWHM) ranging from approximately 1.5 to 3.8 microseconds, corresponding to bandwidths  $(\delta\omega/2\pi)$  of about 120 to 400 kHz.

The ratio of  $I$  and  $Q$  — the phase  $\varphi = \arctan(Q/I)$  of the signal — appears with a random but approximately constant value during each consecutive pulse, changing only slowly over time. The time-bandwidth product  $\delta t \cdot \delta\omega/2\pi$  of these pulses ranges in value

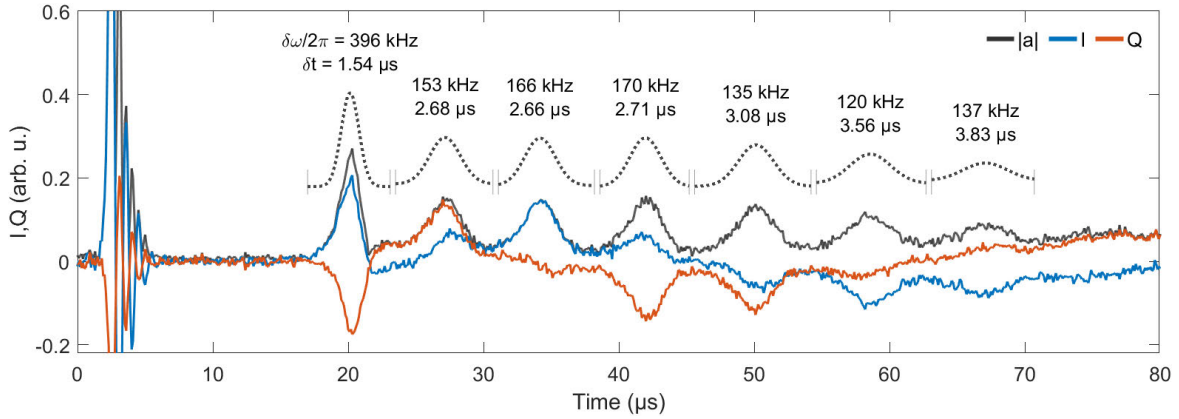


**Figure 6.28** Analysis of the pulsed emission regime, showing  $I$  and  $Q$  quadratures and spectral properties. Each pulse is fitted with a Gaussian profile in the time domain, yielding the width  $\delta t$  (FWHM). The integration window around each pulse, indicated by the vertical lines, is used for FFT analysis. The resulting frequency spectrum is also fitted with a Gaussian, yielding  $\delta\omega/2\pi$  (FWHM) values.

between roughly 0.41 and 0.61, indicating that the pulses are approximately transform-limited, with deviations likely driven by phase fluctuations and noise. This near-transform-limited nature suggests a high degree of coherence in the pulses, consistent with collective emission processes as the source of the emission. For reference, the time-bandwidth product of an ideal Gaussian pulse is  $\delta t \cdot \delta\omega/2\pi \approx 0.44$  [91].

Next, we turn to the quasi-continuous regime starting at around  $t = 100 \mu\text{s}$ , shown in Fig. 6.29(a). To characterize the linewidth of this sustained emission signal, we extend the integration window to  $200 \mu\text{s}$  and similarly employ FFT analysis, now using a Lorentzian profile to fit the spectrum, as plotted in Fig. 6.29(b). This fit function is an appropriate choice for a sustained signal with a slowly decaying amplitude. By varying the starting point  $t_F$  of the integration window, we measure the drift of the central frequency of the masing emission over time within  $\pm 25 \text{ kHz}$ ; see Fig. 6.29(c). The Lorentzian linewidth ranges from  $5 \text{ kHz}$  to  $25 \text{ kHz}$  and is significantly narrower than the cavity linewidth  $\kappa$  and the individual spin linewidth  $\gamma_{\perp}$  by one to two orders of magnitude. This linewidth narrowing highlights the importance of collective enhancement – an indicative trait of superradiance – in achieving high coherence. We attribute the linewidth variation to the emission frequency drift within the integration window, likely caused by magnetic field fluctuations. Notably, this frequency drift behavior is reproducible across repeated experimental runs using the same parameters, suggesting that the loop-switching circuitry is the likely source for the oscillations.

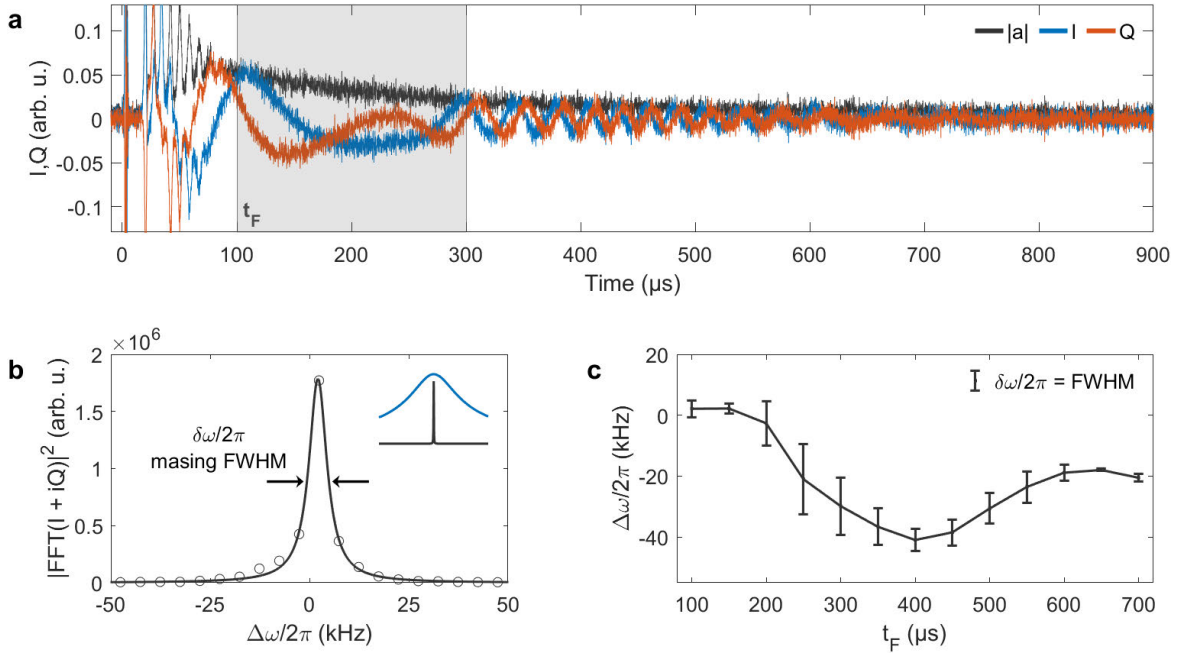


**Figure 6.29** Analysis of the quasi-continuous masing emission spectrum. (a) Extended view of the quasi-continuous masing emission, displaying the  $I$  and  $Q$  quadratures of the cavity amplitude  $|a|$ . The signal is digitally demodulated in the cavity resonance frequency's rotating frame for visual clarity. The gray area indicates the interval for calculating the Fourier spectrum, which is plotted in (b), revealing an emission linewidth significantly narrower than the cavity linewidth (see inset). The frequency difference  $\Delta\omega/2\pi$  is measured relative to the cavity frequency around 3.1 GHz. (c) Temporal evolution of the emission frequency and linewidth, obtained by shifting the Fourier analysis window in time.

Having examined the spectral characteristics of both the transient pulsed and quasi-continuous emission regimes, we now present a direct experimental test to shed light on the mechanism driving these novel dynamics. This test aims to determine whether the observed phenomena are driven by known cavity QED effects manifesting in an unusual form. Some potential explanations that come to mind include Rabi oscillations, spin-echo type behavior (see Sec. 2.5.2), or effects similar to collapse and revivals in the Jaynes-Cummings model [92].

Our experimental approach is straightforward: Following the initial superradiant decay, we rapidly detune the spin ensemble from the cavity resonance by our standard amount of  $\delta/2\pi \approx 20$  MHz using the detuning loop. During this second hold time, the superradiant interaction between the spins and the cavity mode is suppressed. Upon retuning the spins to resonance, we observe an increase in the peak cavity amplitude of the subsequent emission pulse, with the magnitude of this increase growing with the duration of the second hold time [see Fig. 6.30(a)]. The sharp initial amplitude increase exhibits a characteristic timescale of  $T = 13.7 \mu\text{s}$  followed by a long plateau, as shown in Fig. 6.30(b).

A common feature of the aforementioned cavity QED effects is that they typically involve a specific timescale associated with the dynamics, where the revival time is a characteristic of the coupled cavity-spin system. By decoupling the spins from the cavity during the second hold time, we can delay the appearance of the revival pulses. This observation leads to two key insights: (i) The emission is generated by a collective interaction between the resonant spin ensemble and the cavity, and (ii) the phenomenon does not appear to be governed by an internal clock cycle, as it can be effectively “paused and restarted” by detuning and retuning the ensemble.

These findings suggest that the cavity does not play a central role in the mechanism driving the pulsed revivals. More so, the revivals even grow after the spins have been off-resonant with the cavity. Over time, this mechanism leads to an increase in spin inversion, which is subsequently converted into cavity photons upon release of the superradiant decay. With an increased spin inversion after an extended second hold time, the first superradiant emission even returns to exhibiting damped Rabi oscillations instead of one overdamped approximately Gaussian pulse. The long-term amplitude decrease, shown in the inset of Fig. 6.30(b) is a dissipative effect arising from a diffusive spin transport into fluctuator NVs (NVs having exceptionally short lifetimes), and has already been discussed in Sec. 6.1.

We are now in a position to put the puzzle pieces together: (i) The second-hold-time experiment indicates an increase in spin inversion  $p$  over time. (ii) Our numerical

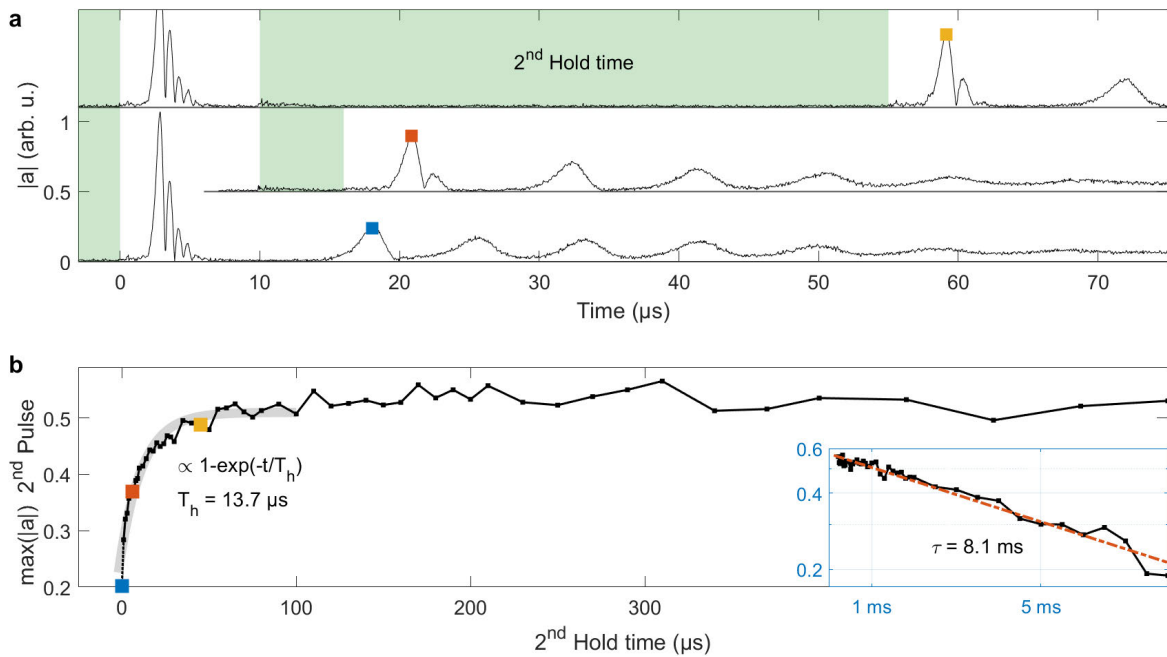


**Figure 6.30** Influence of a second hold time on revival pulse dynamics. (a) Stacked cavity signals of superradiant dynamics with a second stabilization sequence (2<sup>nd</sup> hold time), indicated by light green shading. Longer second hold times lead to an increased amplitude of the superradiant masing pulse revival. (b) Revival amplitude as a function of second hold time duration, displaying a sharp initial increase followed by an exponential decrease over extended timescales (see inset).

simulations, particularly the results presented in Fig. 6.16(d) of the previous section, demonstrate that the initial superradiant decay creates a spectral hole, reducing the ensemble below the threshold  $\overline{pC} = 1$  required for spontaneous superradiance (as derived in Sec.2.9 for the generalized case of non-uniform inversion).

Based on these observations, we propose a simple conceptual model: Over time, the spectral hole is gradually refilled, pushing the ensemble back above the superradiance threshold. At this point, the spin state becomes unstable, triggering another superradiant decay. Importantly, as we are not externally driving the spin inversion, the refilling mechanism must originate from internal dynamics within the spin system itself. This leaves direct spin-spin interactions as the primary candidate for driving this mechanism.

Without delving into the precise nature of these interactions, we introduce a phenomenological model to capture this behavior. We augment the semi-classical Maxwell-Bloch equations (2.64) with a new term that facilitates the gradual filling of the spectral hole. This additional term allows each spin packet  $j$  to slowly approach the time-dependent mean ensemble inversion  $p = \sum_k \rho_k \langle \sigma_z^k \rangle$  with a characteristic relaxation rate  $\mathcal{J}$ . Mathematically, this is expressed as:

$$\langle \dot{\sigma}_z^j \rangle = (\dots) + \mathcal{J}(p - \langle \sigma_z^j \rangle), \quad (6.8)$$

where  $(\dots)$  represents the standard coherent (relaxation-free) components of the coupled system dynamics. This new term plays the role of an effective pumping of the central spin packets, at the cost of reducing the inversion at the lobes of the spin distribution over time.

To effectively capture the observed dynamics — including the initial superradiant decay and the full subsequent dynamics — our model incorporates a free time offset parameter,<sup>6</sup> the hole-filling rate  $\mathcal{J}$ , and a small constant cavity drive  $\eta$ . This drive  $\eta$ , contributing to the right-hand side of  $\langle \dot{a} \rangle$ , represents the effects of cavity noise and intrinsic fluctuations that continuously trigger the recurring superradiant emission pulses. These fluctuations, arising from quantum, thermal, and technical noise, would typically require a higher-order cumulant expansion for a comprehensive description [93].

---

<sup>6</sup>This time offset is needed, because the constant cavity drive  $\eta$ , used to match the timing of simulated revivals with the measurement (in combination with the hole filling rate  $\mathcal{J}$ , see discussion), also affects the initial superradiant decay, shifting it to earlier times. The time offset in the simulation of Fig. 6.31 is  $t - t_{\text{sim}} = -1.27 \mu\text{s}$ . This makes the simulation start after  $t = 0$ , where the loop-switching is triggered. As the loop retuning is not instantaneous [see Fig. 6.14(a)], this is still not unphysical. In the simulation, cavity and spins are always assumed to be on resonance ( $\delta = 0$ ).

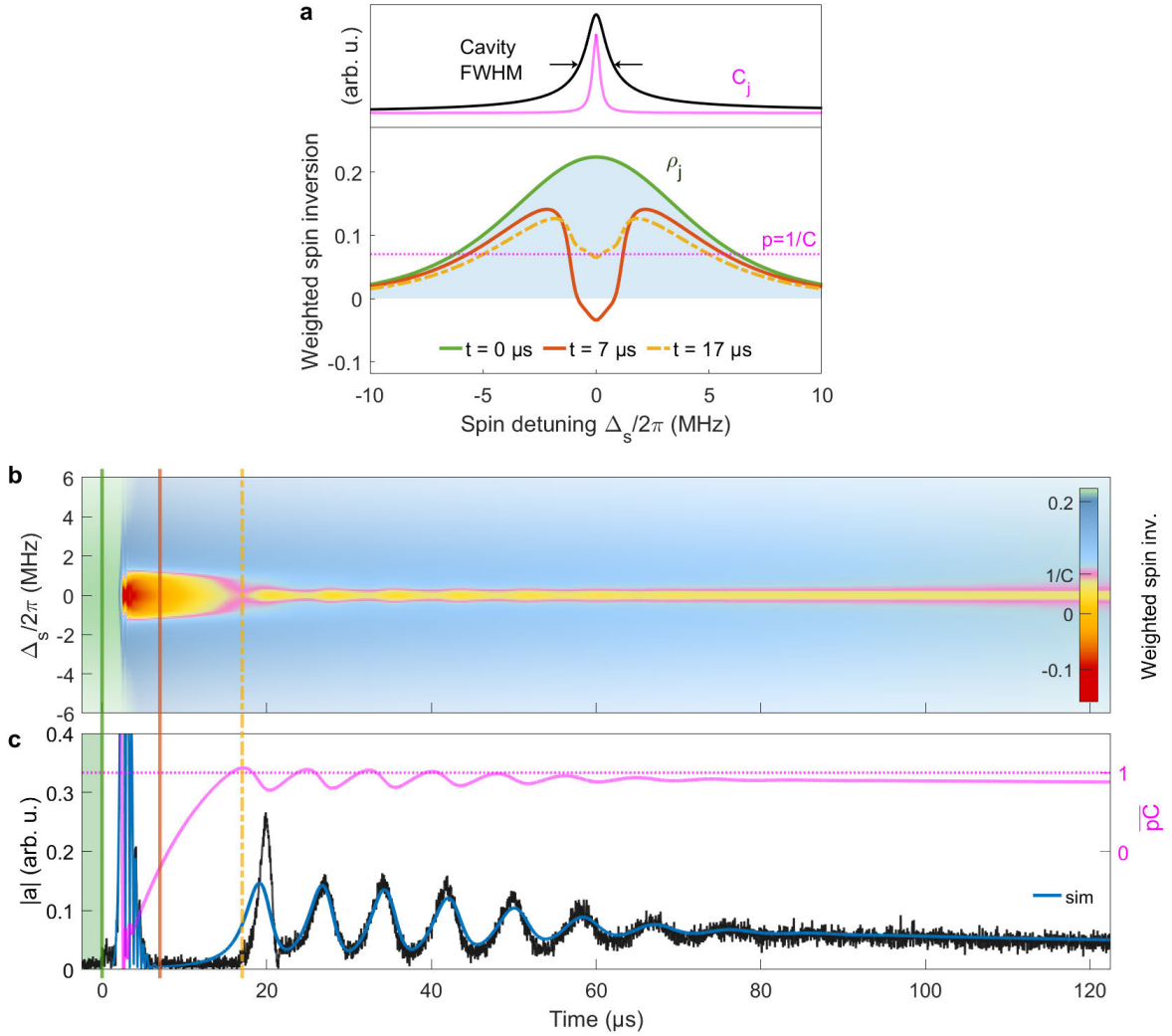


**Figure 6.31** Numerical simulation of superradiant dynamics using the effective relaxation rate model. (a) Spin distribution at key stages: uniform starting inversion (green), deep spectral hole after the initial superradiant decay (red), and partially refilled hole before the first revival pulse (yellow). The  $y$ -axis represents a weighted spin inversion  $\rho_j \langle \sigma_z^j \rangle$ , renormalized to reflect  $\langle \sigma_z^j \rangle$  of the central frequency packet. For comparison, the cavity resonance (black) and single spin packet cooperativities  $C_j$  (pink) are overlaid. (b) Color plot of simulated spin inversion dynamics across different detunings. Vertical lines correspond to the three time points highlighted in (a). (c) Comparison of measured and simulated cavity amplitude  $|a|$  using the spectral hole-filling model, alongside the temporal evolution of the weighted instability threshold  $\overline{pC}$ .

For simplicity, we employ a first-order semi-classical approach, using  $\eta$  to effectively model these stochastic processes.

Fig. 6.31(b) illustrates the simulated filling of the spectral hole over time, demonstrating the transfer of inversion from the edges toward the center of the spin distribution. The resulting simulated cavity amplitude, shown in Fig. 6.31(c), qualitatively reproduces the measured dynamics. Notably, the hole-filling rate used in this simulation,  $\mathcal{J}/2\pi = 15.6$  kHz, aligns well with the measured timescale  $T_h \sim \mathcal{J}^{-1}$  presented in Fig. 6.30. This timescale is also in reasonable agreement with the lifetime  $\tau \approx 27$   $\mu$ s of *engineered dark states* in Ref. [22]. In this study, a similar NV diamond with comparable spin density and inhomogeneous broadening was used. The engineered dark states are generated by burning two spectral holes on both sides of the spin distribution at a distance  $2g_{\text{coll}}$  and decay as the holes refill over time.

Our simulation employs a constant cavity drive of  $\eta/2\pi = 5.6$  kHz. While  $\mathcal{J}$  and  $\eta$  appear similar in magnitude, potentially contradicting the earlier characterization of  $\eta$  as small, a more appropriate comparison considers these effective pump rates relative to their associated dissipation rates. The ratio  $\mathcal{J}/\gamma_{\parallel}$  ranges from  $10^3$  to  $10^7$  (depending on whether we consider the long  $T_1 > 100$  s process or the  $\tau \sim 10$  ms “fast” inversion decay for  $\gamma_{\parallel}$ ).<sup>7</sup> In contrast, the ratio of cavity drive to dissipation is considerably smaller, with  $\eta/\kappa \sim 10^{-2}$ .

The dynamical quantity  $\overline{pC}$  — the superradiance threshold — is key for understanding how the system changes from self-pulsing behavior to quasi-continuous emission. The pulsed revivals are generated from the interplay between gradual spectral hole-filling (an effective pump) and the threshold condition  $\overline{pC} > 1$ , as shown in Fig. 6.31(c). Revival pulses start as soon as the threshold is exceeded, making the inverted spin state unstable and susceptible to triggering by cavity noise photons. Each pulse reduces the overall spin inversion  $p$  while consecutive spectral holes become shallower and need less time to refill. However, successive pulses exhibit increasing delay times to reach peak amplitude as the self-accelerating superradiant avalanche process slows down with a lower effective number of participating spins. This delay time goes inversely with  $p$ , see Eq. (2.80).

Initially,  $\overline{pC}$  clearly oscillates above and below 1, generating separated superradiant pulses. As pulses begin to merge, these oscillations get smaller. The system then reaches a quasi-steady state where energy lost through the cavity is balanced by steady inflow from the edges of the spin distribution, maintaining a threshold of just under

---

<sup>7</sup>In the simulation, we set  $\gamma_{\parallel} = 0$  and only account for spin inversion loss via cavity emission, which occurs on a much faster 10 – 100 microsecond timescale.

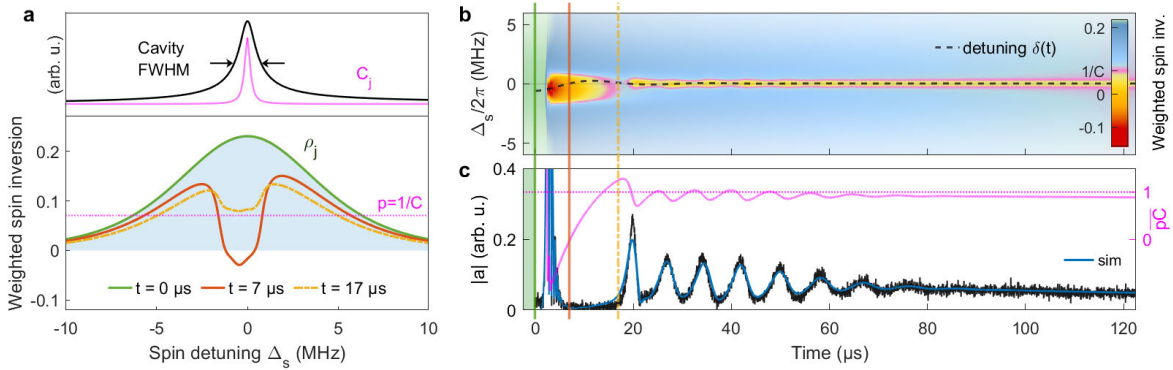


**Figure 6.32** Simulation of self-induced superradiance using the effective relaxation rate model with time-dependent detuning  $\delta(t)$ . (a) Asymmetric spectral hole (red) in the off-resonant spin ensemble after initial superradiant decay. (b) Ensemble inversion dynamics over time, with fitted damped sine wave detuning function. (c) Cavity dynamics and superradiance threshold  $\overline{pC}$ , showing improved accuracy of the initial revival peak fit around  $t = 20 \mu\text{s}$ . Compare with constant detuning ( $\delta = 0$ ) in Fig. 6.31.

1. This process continues until significant inversion loss prevents any further masing emission.

It is worth noting that the sequence of periodic pulses observed in our system is similar to recent findings in Ref. [94], where a superradiant system was externally driven via optical pumping. The interpretation of the pulsed emission in both systems is essentially the same. The system is driven above the threshold  $\overline{pC} = 1$  relatively quickly, but the subsequent superradiant decay occurs after a longer delay time. Once it does occur, it pushes the system significantly below the threshold, and the cycle starts again. However, a key distinction lies in the pumping mechanism: in an optically pumped system, the pump rate remains constant, whereas in our system the effective pumping diminishes over time as the spin inversion becomes more uniform, approaching a threshold of  $p = 1/C$  everywhere. Consequently, our system exhibits not only the initial self-pulsing behavior but also a quasi-continuous regime at later times, before the emission eventually comes to a halt.

Our simple phenomenological model can be further refined to improve the fit of the self-induced superradiant dynamics. Close examination of Fig. 6.31(c) reveals that the measured first revival pulse is significantly higher than our simple fit model predicts. To account for this discrepancy, we introduce a slight complication to the model: a time-dependent detuning function  $\delta(t)$  between the cavity and spins, as shown in Fig. 6.32. This detuning function, illustrated in Fig. 6.32(b), takes the form of a damped sine wave  $\delta(t) = \sin(\omega t + \varphi) \cdot \exp(-t/\tau) + c$ . This form is physically plausible,

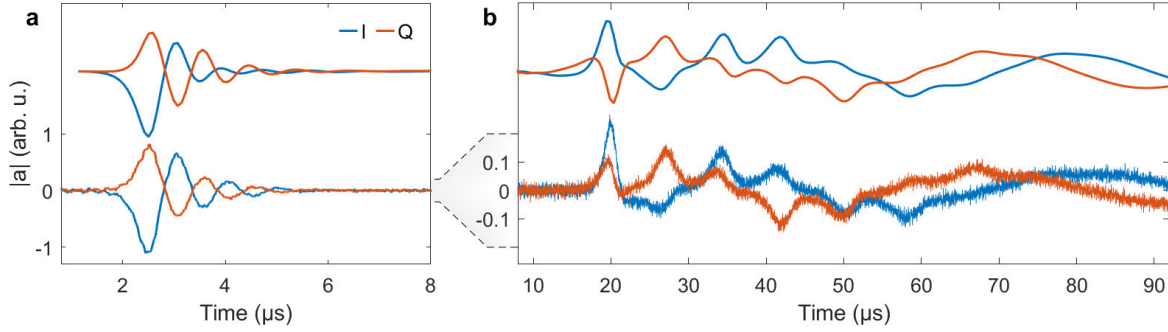


**Figure 6.33** Recreation of the phase dynamics of the measured superradiant cavity amplitude ( $a_{\text{meas}} = I + iQ$ ) from the simulated signal  $a_{\text{sim}}$  of Fig. 6.32. Simulated curves include an additional time-dependent phase factor  $e^{-i(\omega_{\Delta}t + \phi)}$  with small additional detuning  $\omega_{\Delta}/2\pi \approx 26$  kHz. Different constant phase offsets  $\phi$  are used for (a) initial superradiant decay and (b) subsequent dynamics, reflecting the stochastic nature of the noise triggering.

as the magnetic field generated by the detuning loop after rapidly switching the current back on is likely to oscillate to some extent.

Using this enhanced model, we can even recreate the phase dynamics of the measured cavity amplitude, i.e., the time evolution of the I/Q quadratures (see Fig. 6.33). To achieve the best fit, which closely matches the initial superradiant decay and provides good qualitative agreement with subsequent dynamics, we multiply the simulated (complex) cavity amplitude by a time-dependent phase factor  $a_{\text{sim}} \cdot e^{-i(\omega_{\Delta}t + \phi)}$ . This introduces a small additional detuning  $\omega_{\Delta}/2\pi \approx 26$  kHz, which was not resolved by the original fit method that only used the absolute cavity signal. In addition to the  $\omega_{\Delta}$  parameter, we apply independent constant phase shifts for the initial superradiant decay [Fig. 6.33(a)] and the later part [Fig. 6.33(b)]. These independent phase shifts confirm the stochastic nature of the superradiant emission triggering due to noise. Notably, the phase fit shows the greatest disagreement with the measurement during the first revival pulse, which could be interpreted as a separately triggered event, potentially requiring another independent phase offset.

Our spectral hole-filling model is further validated by experiments investigating the deliberate creation of spectral holes in the spin ensemble and their impact on subsequent superradiant dynamics. In Fig. 6.34(a), we apply a strong microwave pulse with a duration of  $8 \mu\text{s}$  to the spins while they are detuned from the cavity. Similar to the initial superradiant decay, this pulse generates a slice of decreased spin inversion

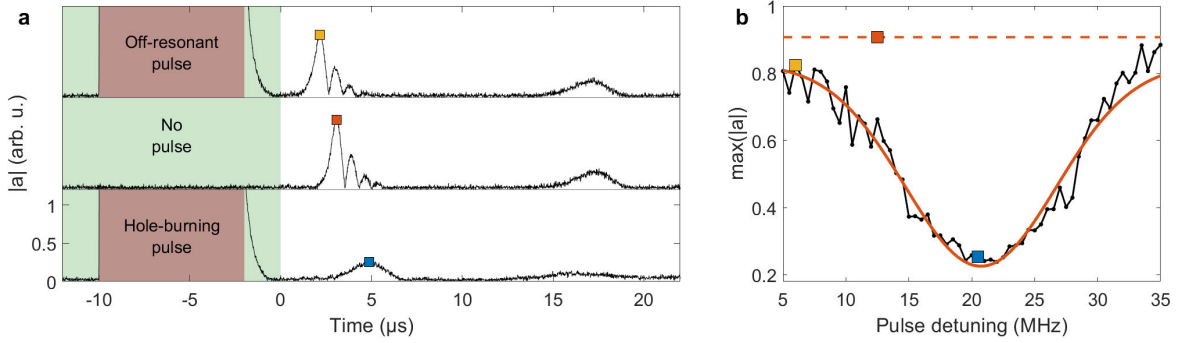


**Figure 6.34** Hole-burning pulse and subsequent superradiant dynamics. (a) Cavity dynamics when applying a strong microwave pulse (red shading) while the inverted spins are initially detuned (green shading), followed by superradiant decay and revival pulses. A resonant hole-burning pulse recreates a spectral hole similar to that generated by the initial superradiant decay without a pulse. Off-resonant pulses trigger an earlier superradiant decay but maintain similar subsequent dynamics. (b) Maximum amplitude of superradiant emission after hole-burning pulses at different frequencies, revealing the (power broadened) spin frequency distribution.

within the ensemble. Crucially, this pulse-generated spectral hole is centered at the pulse frequency, which is varied over multiple runs.

When a hole is burned at the center of the spin ensemble, the subsequent first emission pulse resembles the usual revival pulse following the initial superradiant decay without a hole-burning pulse. An off-resonant hole-burning pulse applied to the sides of the spin distribution does not significantly alter the dynamics compared to not using a hole-burning pulse. The only difference is that the delay time of the initial superradiant decay is slightly shortened, as the off-resonant pulse still generates an increased initial tipping angle (see Sec. 6.1).

The maximum amplitude of the superradiant decay pulse varies with different hole-burning frequencies, effectively mapping out the frequency distribution of the detuned spins, see Fig. 6.34(b). This distribution appears broader than the measured  $q$ -Gaussian linewidth of  $W/2\pi = 9.2$  MHz [see Fig. 6.4], which we attribute to power broadening effects. The strong microwave pulse used for hole-burning is sufficiently intense to also affect off-resonant spin packets, exciting spins that are slightly detuned from the pulse frequency. This power broadening leads to a wider apparent distribution of the spin ensemble.

To further elucidate the spectral hole-filling process, we examine the relationship between the filling time and the effective area of the spectral hole. Fig. 6.35 presents data from multiple cooldowns with different cavity linewidths  $\kappa$ . These variations in

linewidth likely stem from the gradual evaporation of the grease used to secure the diamond sample, resulting in a progressively cleaner surface over several cooldown cycles (see discussion in Sec. 5.2.3).

The effective area of the spectral hole generated by the initial superradiant decay is characterized by its depth and width. The depth correlates with the initial inversion  $p_0$ , as the spins involved in the superradiant decay effectively undergo a  $\pi$ -rotation. Its width is determined by  $\kappa$ , since only spins within the cavity linewidth interact with the mode. We extract  $p_0$  by using our numerical model to fit the initial superradiant decay signals, adjusting  $\kappa$  (per cooldown) while keeping other model parameters constant. By comparing the time difference  $\Delta t$  between the maxima of the initial superradiant decay and the first revival pulse with the effective area of the spectral hole,  $p_0\kappa$ , we uncover a consistent linear trend across different cooldowns. This time difference  $\Delta t$  serves as a measure of the duration required to fill up the spectral hole with effective area  $p_0\kappa$ , bringing the ensemble above the threshold for  $\overline{pC}$  to allow for the first superradiant revival pulse.

Upon taking a closer look, our observation of  $\Delta t \propto p_0\kappa$ , validated for linewidths  $\kappa$  in a range from roughly 400 to 700 kilohertz, reveals a more nuanced picture. The spectral hole refilling threshold to enable a superradiant revival pulse, approximately given by  $p = 1/C$ , changes for different values of  $\kappa$  as the cooperativity  $C \propto \kappa^{-1}$  is inversely proportional to the cavity linewidth. This relationship suggests that higher  $\kappa$  values should lead to longer hole-refilling times. However, this effect is counterbalanced by a decreased depth of the spectral hole, as the initial superradiant decay is increasingly damped with  $\kappa$  and, therefore, hindered from extracting more excitations from the spin system. Consequently, the spectral hole formed is shallower, partially offsetting the increased superradiance threshold.

In Fig. 6.36, we reproduce the experiment of Fig. 6.35 using numerical simulations with our phenomenological model (simple version with  $\delta = 0$ ). We fix the hole filling rate  $\mathcal{J}$  and the trigger amplitude  $\eta$  (values taken from the fit in Fig. 6.31), varying the cavity linewidth  $\kappa$  and the initial inversion  $p_0$ . Notably, the numerically simulated results of  $\Delta t$  over  $p_0\kappa$  align less well with a linear trend than the experimental data.

This discrepancy is not entirely unexpected, as the fit results of our phenomenological model (Fig. 6.38) reveal a more complex relationship between the parameters  $p_0$ ,  $\mathcal{J}$ , and  $\eta$ . Fig. 6.37 illustrates the model parameters resulting in the best fits of multiple experimental runs with fixed  $\kappa$  (same cooldown) and different initial inversions  $p_0$  (as controlled by different hold times). The fitted runs are shown in Fig. 6.38.

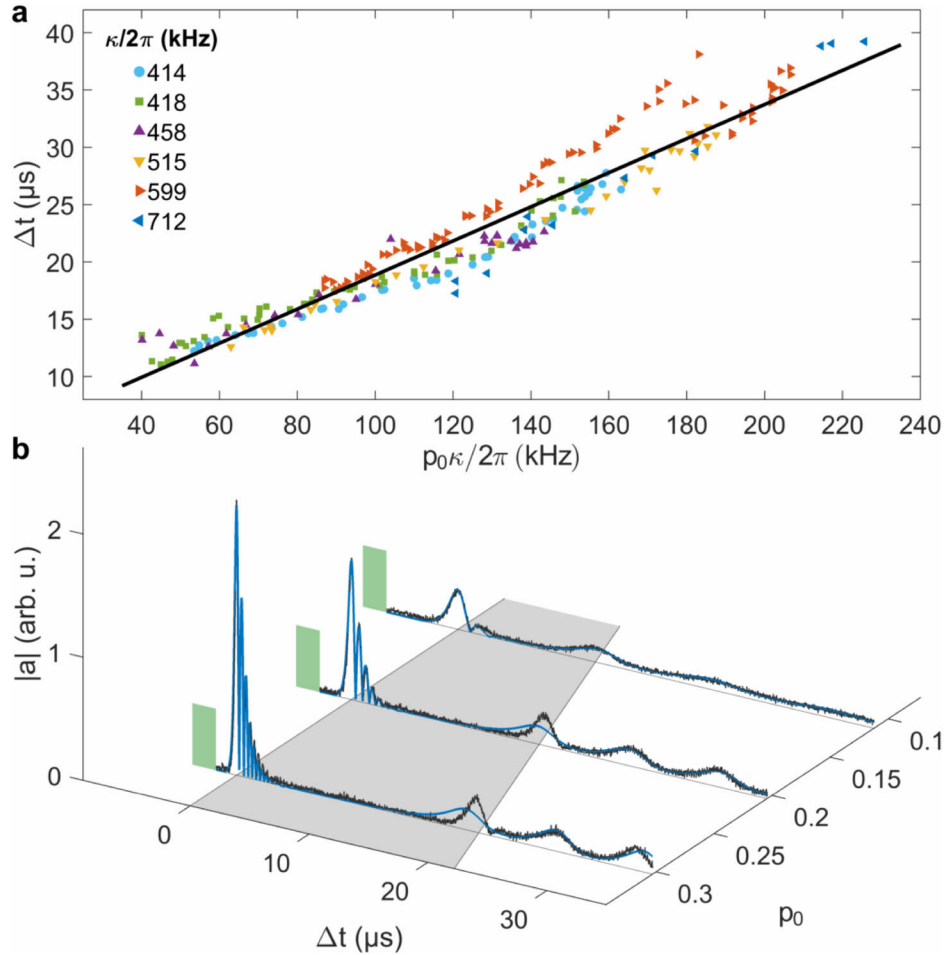


**Figure 6.35** Influence of effective spectral hole area on refilling time across multiple cooldowns. (a) Data from cooldowns with different cavity linewidths  $\kappa$ , showing the relationship between revival dynamics timescale and spectral hole area. The time difference  $\Delta t$  between initial decay and first revival pulse maxima is plotted against effective hole area  $p_0\kappa$ , revealing a consistent linear trend. Initial inversion  $p_0$  (varied via hold time) is extracted from the superradiant decay using our simple numerical model. (b) Three experimental runs with different initial inversions  $p_0$  and corresponding simulation curves for  $\kappa/2\pi = 418$  kHz, illustrating the hole refilling time  $\Delta t$  (gray shading). Measured cavity amplitude (black) is plotted alongside simulation curves (blue) using our simple phenomenological model.

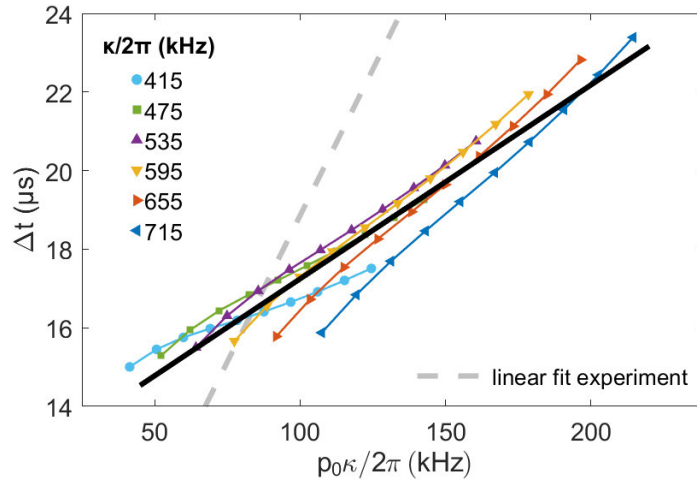


**Figure 6.36** Simulated effective-hole-area experiment with fixed hole-filling rate  $\mathcal{J}$  and trigger amplitude  $\eta$ , for varying combinations of initial inversion  $p_0$  and cavity linewidths  $\kappa$ . The hole-filling time  $\Delta t$  is extracted from the simulated runs in the same way as shown in Fig. 6.35(b) for real experimental data. For comparison, the linear fit of the experimental data from Fig. 6.35(a) is shown as a gray dashed line.

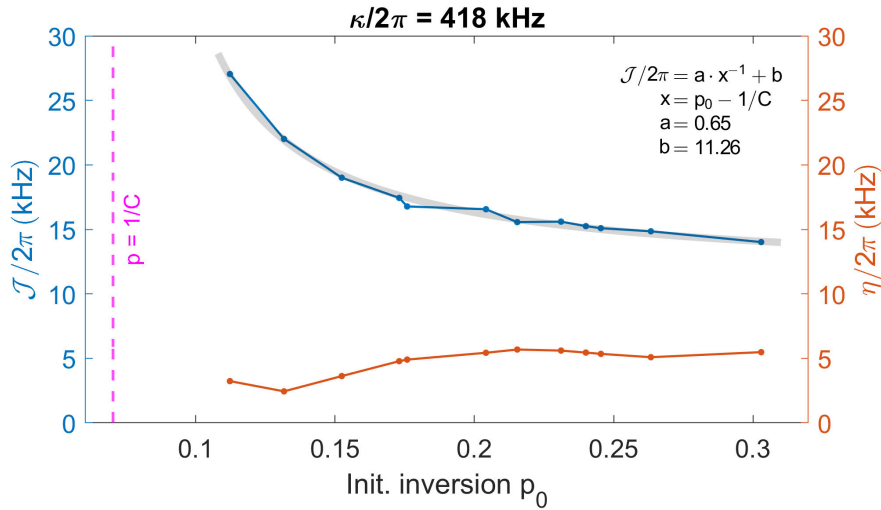


**Figure 6.37** Phenomenological model parameters obtained from fitting the measured self-induced superradiant dynamics in a hold time scan with cavity linewidth  $\kappa/2\pi = 418$  kHz. The model employs three parameters: initial inversion  $p_0$ , hole-filling rate  $\mathcal{J}$ , and constant trigger amplitude  $\eta$ . The fitted runs are shown in Fig. 6.38. The parameters  $p_0$  versus  $\mathcal{J}$  are well described by a linear fit of  $\mathcal{J}$  as a function of inverse  $x = p_0 - 1/C$ , offset by the superradiant threshold  $p = 1/C$ .

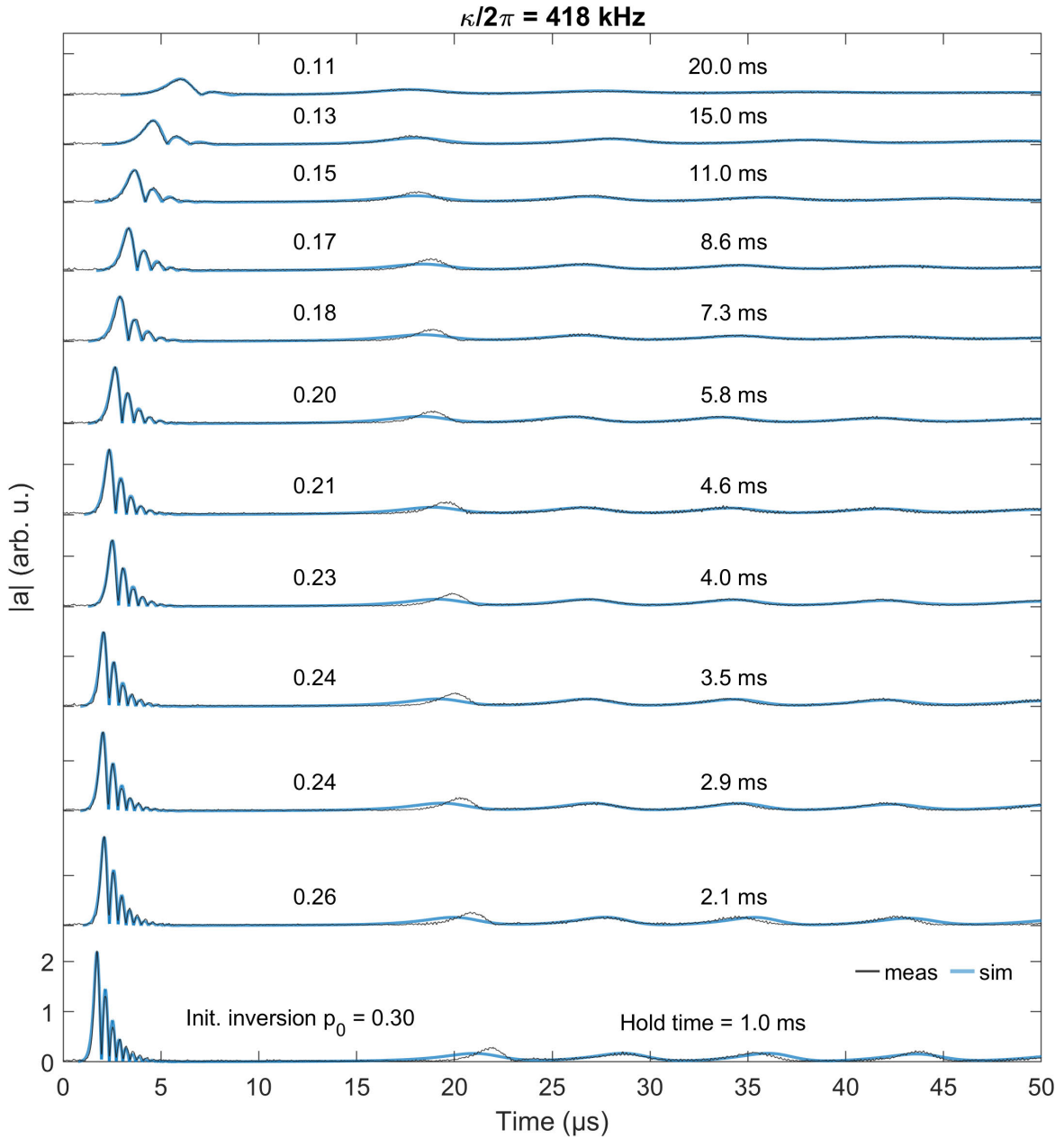


**Figure 6.38** Self-induced superradiant dynamics: measured and simulated runs in a hold time scan with cavity linewidth  $\kappa/2\pi = 418 \text{ kHz}$ . The model parameters ( $p_0$ ,  $\mathcal{J}$ , and  $\eta$ ), are plotted in Fig. 6.37. Here, we are using the simple phenomenological model ( $\delta = 0$ ).

A clear trend of  $\mathcal{J} \propto (p_0 - 1/C)^{-1}$  emerges from this analysis. Although the inclusion of an offset given by the superradiance threshold (inspired by the analysis accompanying Fig. 2.12) is not immediately obvious and might be coincidental, it leads to an excellent agreement with a linear fit of  $\mathcal{J}$  as a function of inverse  $(p_0 - 1/C)^{-1}$ , rather than requiring a quadratic fit without the offset. This also explains why the experimental linear trend  $\Delta t \propto p_0 \kappa$  in the effective-hole-area measurement (Fig. 6.35) deviates from the simulated scan with fixed  $\mathcal{J}$  (less linear, see Fig. 6.36): The hole filling rate  $\mathcal{J}$  is indeed inversion-dependent, increasing inversely proportional to  $p_0$ . On the other hand, the continuous cavity drive  $\eta$  for the recurrent triggering of the superradiant emission follows no clear trend, possibly reflecting the stochastic nature of the noise triggering that is only effectively modeled by the parameter  $\eta$ .

Having explored these experimental and model-based insights, we now turn our attention to the underlying mechanism for the spectral hole-filling: direct dipole-dipole interactions within the disordered spin ensemble. This conclusion is supported by compelling experimental evidence, including the second-hold-time and hole-burning experiments, which demonstrate the spin system's role in hole-refilling and exclude other potential sources.

Our findings strongly suggest that the hole-refilling process is primarily driven by direct spin-spin interactions among NV centers. While P1 centers are present at higher densities in our sample, their significant detuning (the P1 center's transition frequency at our operating field of  $B_{\text{ext}} \approx 10$  mT is around  $\gamma_e B_{\text{ext}} = 280$  MHz, which is more than 2 GHz detuned from the 3.1 GHz NV resonance) effectively excludes their participation in this process. Furthermore, we can confidently exclude phonon-mediated processes as the primary mechanism, supported by Ref. [37] showing extremely long  $T_1$  times even in samples with significant crystal damage (as in our neutron-irradiated sample).

In the next section, we will derive a model for effective hole-filling based on estimated NV density and spin-spin interactions, exploring the extent to which such a model is able to offer an explanation and also its limitations, including the possible need for a full many-body description beyond simple pair processes.

### 6.2.1 Spin-spin interactions

To find a suitable description for the spectral hole-filling process, we must consider the different hierarchies of timescales within our system:

1. Superradiant decay: The fastest process, characterized by time  $T_R \lesssim 1 \mu\text{s}$  (see Sec. 6.1). This is approximately the time required to create a spectral hole during the initial superradiant decay.
2. Spectral hole-filling: Occurring over  $T_h \approx 10 \mu\text{s}$  to  $100 \mu\text{s}$ . During this time, spins from different frequency packets  $i$  equalize their inversion  $\langle \sigma_z^i \rangle$ , approaching the mean ensemble inversion  $p = \sum_i \rho_i \langle \sigma_z^i \rangle$ .
3. Spin-lattice relaxation: The slowest process, with timescale  $\gamma_{\parallel}^{-1}$ . Individual spins lose energy and return to the ground state. Our results (Fig. 6.25, Sec. 6.1) indicate an initial fast decay to  $p = 0$  over a time  $\tau \approx 10 \text{ ms}$ , followed by a slower  $T_1 > 100 \text{ s}$  decay. Both these timescales can be neglected for the superradiant dynamics driven by spectral-hole filling.

These distinct timescales allow us to simplify our analysis. After the spectral hole has been created, the system falls below the superradiance threshold  $\overline{pC} = 1$ , and the spin-cavity dynamics can be ignored. Consequently, we can focus solely on processes within the spin system when modeling the spectral-hole filling process. This approach is supported by our second-hold-time measurements (Fig. 6.30), which show spectral hole refilling even when cavity-spin interaction is suppressed by a large detuning  $\delta$ .

The magnetic dipole-dipole interaction Hamiltonian between two nearest-neighbor spins at distance  $r$  is given by

$$\mathcal{H}_{\text{dipole}} = -\hbar \underbrace{\frac{\mu_0 \gamma_e^2 \hbar}{4\pi r^3}}_{J(r)} \left[ 3 (\vec{S}_1 \cdot \hat{r}) (\vec{S}_2 \cdot \hat{r}) - \vec{S}_1 \cdot \vec{S}_2 \right], \quad (6.9)$$

where  $\hat{r}$  is the unit vector connecting the spins,  $\vec{S}_j = (\sigma_x^j, \sigma_y^j, \sigma_z^j)^T$  represents the Pauli matrices for spin  $j$ , and  $\gamma_e/2\pi \approx 28 \text{ MHz mT}^{-1}$  is the electron gyromagnetic ratio. We treat NV centers as effective two-level systems (spin-1/2), justified by the large frequency difference ( $> 2\pi \times 400 \text{ MHz}$ ) between the relevant  $m_S = 0 \longleftrightarrow m_S = +1$  transition and the inactive  $m_S = 0 \longleftrightarrow m_S = -1$  transition in our experiment. We also introduce the interaction rate  $J_n = J(r_{\text{typ}})$  between nearest-neighbor spins at a typical distance  $r_{\text{typ}} = n_{\text{NV}}^{-1/3} \approx 10 \text{ nm}$ , evaluated using the density  $n_{\text{NV}}$  of NV centers in our sample of approximately  $1.05 \times 10^{-3} \text{ nm}^{-3}$  (corresponding to the estimated

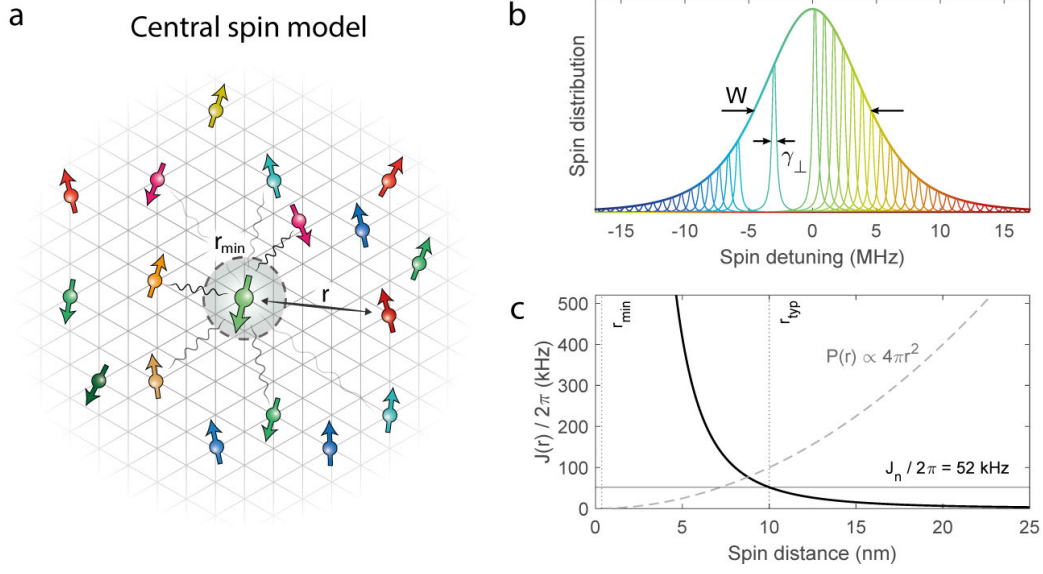


**Figure 6.39** (a) Schematic illustration of a central NV spin in the diamond crystal lattice, interacting with surrounding NVs. The evaluation of the effective hole-filling rate  $\mathcal{J}$  depends on the spin distribution (b) and the  $r^{-3}$  scaling of the spin-spin coupling (c), with the full model based on four parameters: the distribution width  $W$ , the individual spin linewidth  $\gamma_{\perp}$ , the spin density  $n_{\text{nv}} = r_{\text{typ}}^{-3}$  and a minimum cut-off distance  $r_{\text{min}}$ , taken as the diamond lattice constant.

concentration of 6 ppm in the diamond lattice, see Sec. 4.1.2). The resulting value for the typical nearest-neighbor coupling rate is  $J_n/2\pi \approx 52$  kHz.

To derive the effective hole-filling term used in Eq. (6.8), we simplify the dipole-dipole Hamiltonian by removing all directional dependencies arising from different orientations of spins. On average the terms involving products of spin operators are on the order of magnitude one. We then construct a simplified Hamiltonian that includes the on-site energies  $\omega_s^j$  (sampled from the inhomogeneously broadened spin distribution) and a flip-flop interaction between spins, taking into account the  $r^{-3}$  scaling of the coupling rate between two spins  $j$  and  $k$  [95], see Fig. 6.39 for a conceptual illustration. Having only flip-flop processes ensures that the number of spin excitations is always conserved by the Hamiltonian

$$\mathcal{H}_{\text{spins}} = \frac{\hbar}{2} \sum_j \omega_s^j \sigma_z^j + \hbar \sum_{j,k>j} J_{jk} \left[ \sigma_+^j \sigma_-^k + \sigma_-^j \sigma_+^k \right], \quad (6.10)$$

where we used  $J_{jk} = J_n/n_{\text{nv}}r_{jk}^3$ . We employ a master equation approach and include Lindblad operators for the spin dephasing with rate  $\gamma_{\perp}$  and the spin-lattice relaxation

with a very slow rate  $\gamma_{\parallel}$  (c.f. Sec. 2.6):

$$\begin{aligned} \mathcal{L}(\rho) = & \frac{\gamma_{\perp}}{2} \sum_j (\sigma_z^j \rho \sigma_z^j - \rho) \\ & + \frac{\gamma_{\parallel}}{2} \sum_j (2\sigma_-^j \rho \sigma_+^j - \sigma_-^j \sigma_+^j \rho - \rho \sigma_+^j \sigma_-^j). \end{aligned} \quad (6.11)$$

From this, we derive the equations of motion up to second order for the relevant quantities

$$\frac{d}{dt} \langle \sigma_z^j \rangle = -\gamma_{\parallel} (1 + \langle \sigma_z^j \rangle) + 2i \sum_{k \neq j} J_{jk} \left[ \langle \sigma_-^j \sigma_+^k \rangle - \langle \sigma_+^j \sigma_-^k \rangle \right], \quad (6.12a)$$

$$\begin{aligned} \frac{d}{dt} \langle \sigma_-^j \sigma_+^k \rangle = & - \left( \gamma_{\parallel} + 2\gamma_{\perp} + i(\omega_s^j - \omega_s^k) \right) \langle \sigma_-^j \sigma_+^k \rangle + \frac{i}{2} J_{jk} \left[ \langle \sigma_z^j \rangle - \langle \sigma_z^k \rangle \right] \\ & + i \sum_{l \neq j, k} \left[ J_{jl} \langle \sigma_z^j \sigma_+^k \sigma_-^l \rangle - J_{kl} \langle \sigma_-^j \sigma_z^k \sigma_+^l \rangle \right]. \end{aligned} \quad (6.12b)$$

Given that the timescale  $\gamma_{\perp}^{-1} \approx 1 \mu\text{s}$  is the fastest process in the spin system, we assume that the variable  $\langle \sigma_-^j \sigma_+^k \rangle$  reaches quasi-equilibrium rapidly [96]. This leads to the adiabatic condition

$$\frac{d}{dt} \langle \sigma_-^j \sigma_+^k \rangle \approx 0 \quad (6.13)$$

for the left-hand side of Eq. (6.12b). The third-order cumulants in the second line of Eq. (6.12b) are notoriously difficult to deal with and cannot be straightforwardly evaluated [93, 97]. One possible approach would be to split them into a product of first and second-order contributions, e.g.  $\langle \sigma_z^j \sigma_+^k \sigma_-^l \rangle \approx \langle \sigma_z^j \rangle \langle \sigma_+^k \sigma_-^l \rangle$  (splitting in this way leaves  $\sigma_-$  and  $\sigma_+$  on the same footing). Substituting this approximation into Eq. (6.12b) and applying the adiabatic condition to solve for  $\langle \sigma_-^j \sigma_+^k \rangle$ , it becomes evident that these third-order terms contribute only at higher orders of  $J_{jk}$  and will thus be neglected for simplicity. We rearrange, using  $\gamma_{\parallel} \approx 0$ ,

$$\langle \sigma_-^j \sigma_+^k \rangle = \frac{i J_{jk}}{2 \left( 2\gamma_{\perp} + i(\omega_s^j - \omega_s^k) \right)} \left[ \langle \sigma_z^j \rangle - \langle \sigma_z^k \rangle \right]. \quad (6.14)$$

Substituting this back into Eq. (6.12a), we get

$$\frac{d}{dt} \langle \sigma_z^j \rangle = \sum_{k \neq j} \frac{J_{jk}^2}{\left( \gamma_{\perp} + \frac{1}{4\gamma_{\perp}} (\omega_s^j - \omega_s^k)^2 \right)} \left[ \langle \sigma_z^k \rangle - \langle \sigma_z^j \rangle \right]. \quad (6.15)$$

This equation closely resembles the effective term in our phenomenological model, describing a relaxation of spin  $j$  towards the mean ensemble inversion  $p$  with rate  $\mathcal{J}$  [Eq. (6.8) above]:

$$\frac{d}{dt}\langle\sigma_z^j\rangle = (\dots) + \mathcal{J}(p - \langle\sigma_z^j\rangle).$$

To evaluate  $\mathcal{J}$  from Eq. (6.15), we must average over the contributions of all spin pairs  $j$  and  $k$ . Our approach is to replace the discrete sum with an integral formulation over spatial coordinates and frequencies. Importantly, we require the final result to be independent of frequency  $\omega_s^j$  and the specific shape of the inversion-over-frequency profile. This requirement marks the simplest possible description — consistent with our phenomenological model. In pursuing this approach, our underlying assumption is that the number of up spins inside and outside the spectral hole is roughly the same — effectively assuming a shallow spectral hole. This assumption is reasonably justified, as the spin inversion inside and outside the spectral hole of width  $2\kappa$  are typically  $p(|\Delta_s| < \kappa) \sim -0.1$  and  $p(|\Delta_s| > \kappa) \sim 0.2$ , corresponding to spin-up percentages of about 45% and 60%, respectively.

Rewriting the sums over spin frequencies  $\omega_{1,2}$  as integrals is straightforward, using the spin distribution  $\rho(\omega)$  as a kernel,

$$\tilde{\mathcal{J}} = J_n^2 \sum_{\mathbf{r}} \left( \frac{1}{n_{\text{nv}} r^3} \right)^2 \int_{-\infty}^{\infty} d\omega_1 \rho(\omega_1) \int_{-\infty}^{\infty} d\omega_2 \rho(\omega_2) \frac{4\gamma_{\perp}}{4\gamma_{\perp}^2 + (\omega_1 - \omega_2)^2}. \quad (6.16)$$

The sum over positions  $\mathbf{r}$  is intentionally kept discrete. Converting this sum to an integral has to be done carefully: We must account for the reduced probability of finding a spin that is both spatially close (small  $r$ ) and simultaneously close in frequency (small detuning  $\Delta = \omega_1 - \omega_2$ ). This is achieved using Poissonian statistics — describing the distributions of independent rare events. Details of this calculation, based on Ref. [98], are provided in Appendix A. It involves solving complex integrals and approximating the  $q$ -Gaussian distribution with a standard Gaussian of equivalent width  $W$  (FWHM) to achieve an analytic solution.

The final estimation, true within logarithmic accuracy, is obtained as

$$\tilde{\mathcal{J}} = \frac{32\pi J_n^2 \tilde{\Gamma}_{\perp}}{9\sigma_w} \ln \left( \frac{1}{\nu_{\text{min}}^2 \tilde{\Gamma}_{\perp}} \right) \ln \left( \frac{1}{\tilde{\Gamma}_{\perp}} \right). \quad (6.17)$$

Here, we have introduced the spin distribution's standard deviation  $\sigma_w = W/(2\sqrt{2\ln 2})$ , the small parameter  $\tilde{\Gamma}_{\perp} = \gamma_{\perp}/\sigma_w \ll 1$ , and the average number of spins  $\nu_{\text{min}} =$

$\frac{4}{3}\pi n_{\text{nv}} r_{\text{min}}^3 < 1$  in a sphere with a radius corresponding to the minimum possible NV-NV distance  $r_{\text{min}} = a$ , taken as the diamond lattice constant  $a = 0.3567$  nm.

Using the estimated parameters of our system —  $W/2\pi = 9.2$  MHz,  $\gamma_{\perp}/2\pi = 177$  kHz from the phenomenological model, and the spin-spin interaction  $J_{\text{n}}/2\pi = 52$  kHz of NVs at the typical distance  $r_{\text{typ}} \approx 10$  nm — we find that  $\tilde{\mathcal{J}}/2\pi \approx 6.85$  kHz. This estimate corresponds to a hole-filling timescale of  $T_{\text{h}} = \tilde{\mathcal{J}}^{-1} \approx 23$   $\mu\text{s}$ . This value is in good agreement with the observed revival times  $\Delta t$ , which range from approximately 10  $\mu\text{s}$  for shallow spectral holes (generated from an initial superradiant decay with low inversion) to about 40  $\mu\text{s}$  for deep spectral holes (generated from high inversion), as shown in Fig. 6.35(a).

Notably, a similar central spin model is discussed in Ref. [99], where critical (slower than exponential) relaxation with a power-law decay is observed in the limit of  $\gamma_{\perp} \rightarrow 0$ . Without decoherence, spin transport is suppressed by disorder in Hamiltonian (closed) systems, an effect known as Anderson localization [95]. This has an important implication for our simple model: It relies on the spin decoherence rate  $\gamma_{\perp}/2\pi = 177$  kHz, where the linewidth of the NV transition is broadened through the interaction with a bath, indicating that we are considering an open system. Only when the individual spin linewidths are sufficiently broad in this model can the spins inside and outside the spectral hole achieve enough “resonant” overlap to enable inversion exchange.

Our spin coherence time  $T_2 = 1/\gamma_{\perp} \approx 1$   $\mu\text{s}$  is markedly decreased from the record value of  $T_2 \approx 1$  s achieved with a less dense high-purity NV diamond [36]. It is clear that in our system, at least concerning the superradiant interactions, this value is effective in the way it models the spin coherence of *spin frequency packets*. In our diamond sample, there are many sources for the decreased spin coherence, including interactions with substitutional nitrogen spins (P1 centers),  $^{13}\text{C}$  nuclear spins in the diamond, and high amounts of lattice damage, see Sec. 4.1.2. Crucially, the most important factor is the dipolar interactions within the NV spin ensemble itself.

Here, it may be important to emphasize the distinction between the mechanisms underlying spin decoherence in our theoretical models. We use the same value  $\gamma_{\perp}$  to describe both the spin-spin interactions of individual spins (although averaged in our model) and the spin linewidth relevant for the superradiance dynamics. This assumption leads to a decent agreement for the hole-filling timescale with the experiment, and it is hardly possible to measure  $T_2$  of individual spins in our system. Nonetheless, this assumption is likely an oversimplification, as the spin-spin interactions and cavity-spin(-packet) coupling are different phenomena with different timescales.

Let us now discuss the result for the effective hole-filling rate  $\tilde{\mathcal{J}}$  in our simple model, and see how it fares against further scrutiny in the broader context of our experimental observations. We will first look at the suggested dependence of Eq. (6.17) on the spin density (neglecting the lesser logarithmic part):

$$\tilde{\mathcal{J}} \propto n_{\text{nv}}^2 \quad (6.18)$$

A natural approach would be to equate this spin density with the number of inverted spins outside the spectral hole, determined by the initial inversion  $p_0 \sim n_{\text{nv}}$ . These are the spins responsible for refilling the spectral hole via flip-flop interactions. Accordingly, we would expect the effective hole-filling rate to scale as  $\mathcal{J} \sim p_0$  (we use the " $\sim$ " notation here, as we are interested in a qualitative discussion of the suggested trends rather than the precise polynomial order).

However, the fit results presented in Fig. 6.37 suggest a different trend:  $\mathcal{J} \sim 1/p_0$ . Although the change of  $\mathcal{J}$  is at most 50%, it is quite puzzling how to reconcile this discrepancy.

A speculative explanation we can offer is as follows: The effective rate  $\mathcal{J}$  is derived from Eq. (6.15), which averages the contributions of all other (single) spins to invert a central spin. However, this formulation does not account for the fact that the other spins themselves undergo flip-flop interactions. Intuitively, it seems clear that the number of flip-flops at any given time must be determined by the number of possible spin pairs that can participate in such processes. Crucially, these processes require the spins to be in opposite states relative to each other (e.g.,  $|\uparrow\downarrow\rangle \longleftrightarrow |\downarrow\uparrow\rangle$ ), which cannot occur when both spins are in the same state. The number of available spin pairs for flip-flop interactions would be maximized as the ensemble approaches a 50/50 mixture of up and down spins, corresponding to a mean inversion of  $p = 0$ . In this scenario, the higher total rate of occurring flip-flops could facilitate a faster spectral-hole filling.

This perspective suggests that a many-body theory is required to capture the essence of such dynamics, where individual spins are considered as parts of interacting pairs, chains, or more complicated networks, rather than isolated carriers of excitations. The current single-spin-based theory appears to be insufficient in fully describing the observed trends, hinting at the possibility of a more comprehensive many-body approach to understanding the complex nature of our system.

### 6.2.2 Spin exchange between detuned sub-ensembles

To further explore the spectral spin exchange driven by direct spin-spin interactions within the disordered NV system, we present a new set of measurements featuring previously unpublished findings. These measurements introduce an additional layer of complexity by splitting the four NV subgroups (aligned along the four diamond axes) into two halves, each comprising two NV directions. By applying an off-axis magnetic field, we create a tunable splitting  $\delta_{\text{sub}}$  between these sub-ensembles, as illustrated in Fig. 6.40. This allows us to study how the splitting influences the spectral spin exchange between detuned sub-ensembles.

The experiment follows our standard protocol: (*i*) We initialize the spins in their ground state, (*ii*) invert the resonant (half) ensemble using a chirped microwave pulse, (*iii*) rapidly detune the spins to store the inversion for a variable hold time, and (*iv*) return the spins to resonance to observe the superradiant decay and subsequent self-induced dynamics. Importantly, the chirped inversion pulse only affects spins within a frequency window of approximately  $2\pi \times 20$  MHz [assumed to have smooth edges, see Fig. 6.41(a)], corresponding to the resonant half-ensemble (see Sec. 6.0.2). We focus on two key metrics: the maximum amplitude of the first superradiant decay peak  $\max(|a|)$  and the time difference  $\Delta t$  between this peak and the first revival pulse, while scanning the hold time. Evidence that the full protocol inverts the resonant spins with the same efficiency, regardless of  $\delta_{\text{sub}}$ , is shown by the fact that the maximum values of  $\max(|a|)$  differ by a factor of 1/2 between  $\delta_{\text{sub}} = 0$  and  $\delta_{\text{sub}} > 0$ . This difference occurs because the number of resonant spins within the superradiant window is halved, and  $\max(|a|) \propto p_0(\omega_s = \omega_c)$  (see Sec. 2.8). The results are shown in Fig. 6.41.

First, we focus on the influence of  $\delta_{\text{sub}}$  on the spin system's self-pulsed superradiant emission, see Fig. 6.41(b). As the detuning  $\delta_{\text{sub}}$  between the two sub-ensembles increases, the time  $\Delta t$  required for the system to fill the spectral hole and surpass the superradiant threshold becomes significantly longer. This suggests a high sensitivity of the spectral hole filling time to the sub-ensemble detuning, with a much shorter filling time observed when all four sub-ensembles are aligned [blue data in Fig. 6.41(b)]. However, the aligned configuration requires a lower inversion threshold  $p = 1/C$  for the revival pulse due to the higher cooperativity  $C$  resulting from the larger number of resonant spins. The effective halving of  $C$  with the number of resonant spins complicates the direct comparison of the different slopes for  $\delta_{\text{sub}} > 0$  and  $\delta_{\text{sub}} = 0$ . Notably, for fitting the slope in the cases  $\delta_{\text{sub}} > 0$ , we ignore the three points of highest  $\max(|a|)$ , corresponding to shortest hold times. It is reasonable to assume that these points might be outliers, as the homogenization of spin inversion over frequencies

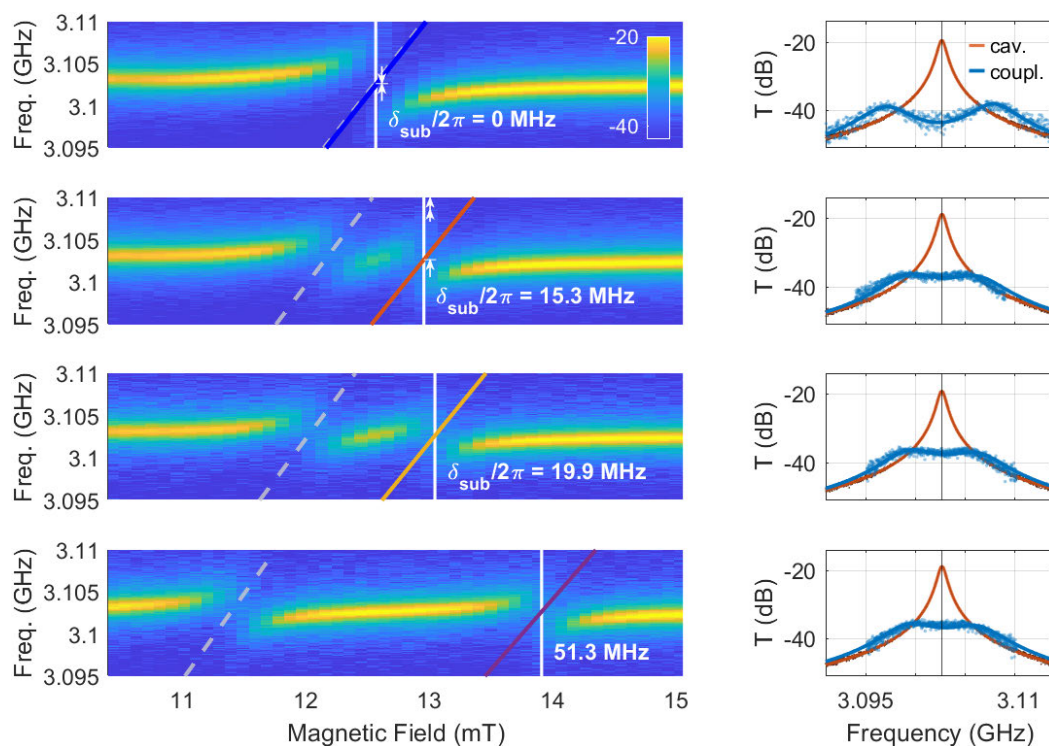


**Figure 6.40** Magnetic field scans (left) and transmission spectroscopy on resonance (right) with the spin system in the ground state. Top row: Magnetic field aligned along the (100) diamond axis, resulting in equal projection on all four NV axes ( $\delta_{\text{sub}} = 0$ ). Other rows: As the field direction rotates toward the (010) axis, the NV ensemble is split into two halves, with 2-and-2 sub-groups separated by a detuning  $\delta_{\text{sub}}$ . This detuning is measured by the distance between the two diagonal lines crossing the vertical white line. When the number of resonant spins is halved, the normal-mode splitting is reduced, as the collective coupling effectively decreases by a factor of  $1/\sqrt{2}$ .

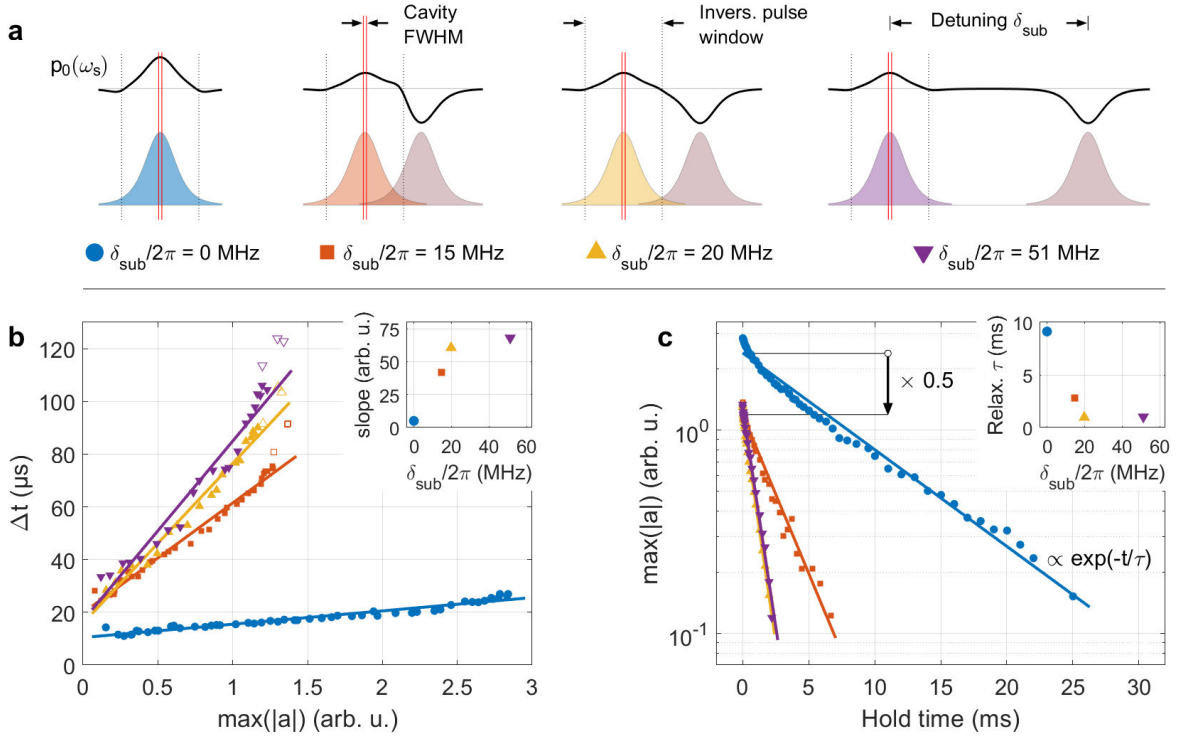


**Figure 6.41** Hold time scan results of the self-induced superradiant dynamics for varying detunings  $\delta_{\text{sub}}$  between the 2-and-2 NV sub-ensembles, showing the maximum cavity amplitude  $\max(|a|)$  and the revival time  $\Delta t$  between the initial superradiant decay and the first revival pulse [c.f. Fig. 6.35(b)]. (a) Schematic representation of the sub-ensembles separated by  $\delta_{\text{sub}}$ , illustrating the estimated initial inversion distribution  $p_0(\omega_s)$ , the superradiant window defined by the cavity linewidth, and the frequency window targeted by the inversion pulse. (b) Linear fits of revival time  $\Delta t$  versus  $\max(|a|)$ . (c) Semi-log plot of  $\max(|a|)$  versus hold time with exponential decay fits. When the number of resonant spins within the superradiant window is halved,  $\max(|a|) \propto p_0(\omega_s = \omega_c)$  also reduces by half.

(essentially the hole-filling process) has not yet fully occurred, both within the resonant half-ensemble and also between the resonant and off-resonant parts. However, we know that the inversion  $p(\omega_s)$  does not become entirely uniform over both ensemble halves, as it would then drop completely below the superradiance threshold for cases where  $\delta_{\text{sub}} > 0$  [see Fig. 6.41(a)].

As a rough estimate, the fitted slopes should correspond to the inverse hole-filling rate, with  $d(\Delta t)/d(\max(|a|)) \sim 1/\mathcal{J}$ , according to Eq. (6.8), considering that  $\max(|a|) \propto p$ . The observed dependence of the slopes increasing with detuning  $\delta_{\text{sub}}$  qualitatively agrees with Eq. (6.16):  $\mathcal{J} \propto 1/(4\gamma_{\perp}^2 + \Delta^2)$ . For very large detuning, we could assume that the off-resonant half-ensemble is mostly negligible for the spin interactions that refill the

spectral hole. Under this assumption, our existing theory of single spins interacting with the mean field generated by all other spins suggests a difference of roughly a factor of 4 between  $\delta_{\text{sub}} = 0$  and detunings much larger than the inhomogeneous broadening width ( $\delta_{\text{sub}} \gg W$ ). This factor arises from the quadratic contribution of the effectively halved spin density, as suggested by Eq. (6.18), where we approximate this contribution as  $\mathcal{J} \propto n_{\text{nv}}^2$ . However, the experiment shows an even larger difference between the slopes (up to factor  $\sim 15$ ), indicating that the spectral hole-filling rate slows more significantly with larger detuning than our current model predicts.

To compare the measured slopes with a more rigorous prediction of the simple central spin model, we introduce a new complication in the model derived from Eq. (6.15). Instead of evaluating the sum over all other spins  $k$  around the central spin  $j$  by averaging over all spectral and spatial contributions (i.e. we average over all three:  $\omega_s^j, \omega_s^k, r_{jk}$ ), we only average over the spatial parts and leave the frequency dependence intact (derived in the appendix A.1). This model replaces the hole-filling rate  $\mathcal{J}$ , previously a constant, with the matrix  $\mathcal{J}_{jk}$ . Thus, it describes a dependence of the hole-filling process on frequency  $\omega_s^j$  of the  $j$ -th spin-packet, denoted as [c.f. Eq. (A.17)]:

$$\frac{d}{dt} \langle \bar{\sigma}_z^j \rangle = \sum_{k \neq j} \mathcal{J}_{jk} \rho_k \left[ \langle \bar{\sigma}_z^k \rangle - \langle \bar{\sigma}_z^j \rangle \right], \quad (6.19)$$

where we use the notation  $\langle \bar{\sigma}_z^j \rangle$  to emphasize that we are now dealing with frequency packets and not single spins  $\langle \sigma_z^j \rangle$ . The formula for  $\mathcal{J}_{jk}$ , Eq. (A.18), is somewhat complicated — it assumes a spin-flip rate proportional to  $P_{\downarrow}(\omega_s^j) \cdot P_{\uparrow}(\omega_s^k)$  and includes a cumulative probability — but has the expected dependence on spin-packet detunings  $\mathcal{J}_{jk} \propto 1/(4\gamma_{\perp}^2 + \Delta_{jk}^2)$ . Using this model, we try to recreate the hole-filling after an initial superradiant decay of equal initial  $\overline{pC}$ , resulting in equal emission amplitudes  $\max(|a|)$ , in the different  $\delta_{\text{sub}}$  cases. This allows us to directly compare the measured  $\Delta t$  values at a fixed  $\max(|a|)$  slice in Fig. 6.41(b) with the frequency-dependent hole-filling prediction. The simulation results are shown in Fig. 6.42. In this simulation, the first 10  $\mu\text{s}$  until  $t = 0$  are simulated using the standard Maxwell-Bloch equations without hole-filling, generating the spectral hole profiles at  $t = 0$ , each well below the superradiance threshold  $\overline{pC} = 1$ . From this moment, the system is evolved using the frequency-dependent hole-filling model, excluding the cavity-spin interaction and single spin losses. In this simulation, we are interested in what time the system crosses again above the threshold, where it would emit a superradiant revival pulse, indicating the revival time (or hole-filling time)  $\Delta t$ .

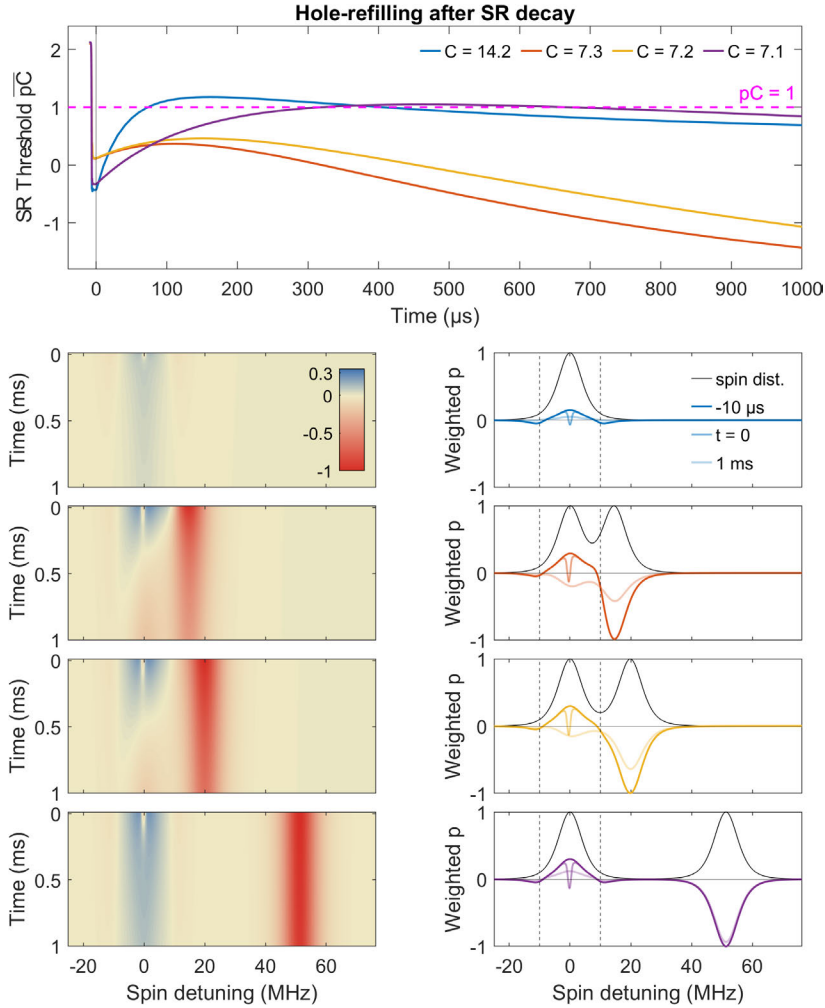


**Figure 6.42** Hole-filling simulation with the frequency-dependent central spin model. (Top) Time evolution of the superradiance threshold  $\overline{pC}$ . When  $\overline{pC} > 1$ , the system is unstable and emits a superradiant (revival) pulse. In all four cases of sub-ensemble detuning  $\delta_{\text{sub}}$ , the spin system is initialized to the same  $\overline{pC}$  state by adjusting the inversion  $\langle \bar{\sigma}_z^j \rangle$  inside the inversion-pulse window accordingly. From this starting point, the system is evolved from  $t = -10 \mu\text{s}$  to  $t = 0$  using the standard Maxwell-Bloch equations, leading to the formation of a spectral hole. In each case, at  $t = 0$ , the system is well below the superradiance threshold. From this moment, the system is evolved using the frequency-dependent central spin model, now excluding cavity coupling. Depending on the value of  $\delta_{\text{sub}}$ , it may eventually cross above  $\overline{pC} = 1$  corresponding to the revival time  $\Delta t$ . (Panels below) The time evolution of the weighted spin inversion  $p_w(\omega_s^j) = \rho_j \langle \bar{\sigma}_z^j \rangle / \max(\rho_k)$  is shown as color plots and as different snapshots in time.

Remarkably, this crossing above the threshold does not occur for the intermediate  $\delta_{\text{sub}}$  cases, where the resonant and off-resonant half-ensembles partially overlap. In these cases, even though the spectral hole initially refills to some extent, inversion from the resonant spins is quickly lost to nearby non-inverted spins due to their close proximity in frequency space. Thus, this model suggests that a revival pulse would never occur. However, for the largest detuning  $\delta_{\text{sub}}$ , where the resonant and off-resonant spins do not overlap, the spectral hole does refill, just as it does in the fully resonant case  $\delta_{\text{sub}} = 0$ . In the case of large detunings, the off-resonant spins are simply too far apart in frequency for any significant inversion exchange.

Summarizing the above, the frequency-dependent central spin model outcome is opposite to what we observed experimentally. In the experiment [see Fig. 6.41(b), for example around  $\max(|a|) \approx 1$  arb.u.], spectral holes refill across all cases and a revival pulse appears with  $\Delta t$  increasing in correlation with  $\delta_{\text{sub}}$ .

Notably, our model overestimates the refilling time by roughly a factor of 4, which is of minor concern, as we are interested in a comparison of the simulation results. The discrepancy, compared to the simpler model with a constant hole-filling rate  $\mathcal{J}$ , which showed better agreement, is likely introduced by the previous use of the shallow-spectral hole approximation and logarithmic approximations for the integral solutions. In the frequency-dependent model, we are using the same parameters as discussed in the previous chapter, including the nearest-neighbor spin-spin interaction  $J_n$ , the spin linewidth  $\gamma_{\perp}$  and  $q$ -Gaussian spin distribution width  $W$ .

Next, we examine the influence of  $\delta_{\text{sub}}$  on the lifetime of spin inversion, as measured by  $\max(|a|)$  of the initial superradiant decay and shown in Fig. 6.41(c). Surprisingly, we observe an unexpected trend: the lifetime is significantly shorter when half the ensemble is detuned. While we previously identified the nature of the initial fast spin relaxation process (as opposed to long  $T_1 > 100$  s) as connected with short-lived fluctuator NVs (see discussion in Sec. 6.1), the exact mechanism remains poorly understood.

A minor complication arises due to an additional splitting of each half-ensemble when the spin inversion is stored in the detuned state. The detuning loop is (almost) parallel with the (100) diamond direction and cannot be rotated in the same way as the external tuning field. However, this added splitting is less than 10% of  $\delta_{\text{sub}}$ , making it a secondary effect.

A simple explanation for the decreased lifetime with half the spins detuned is this: the detuned half-ensemble is not targeted by the initial inversion pulse, resulting in inversion profiles  $p_0(\omega_s)$  as shown in Fig. 6.41(a). Inversion from the resonant half could slowly — over hundreds of microseconds to single milliseconds — wander off

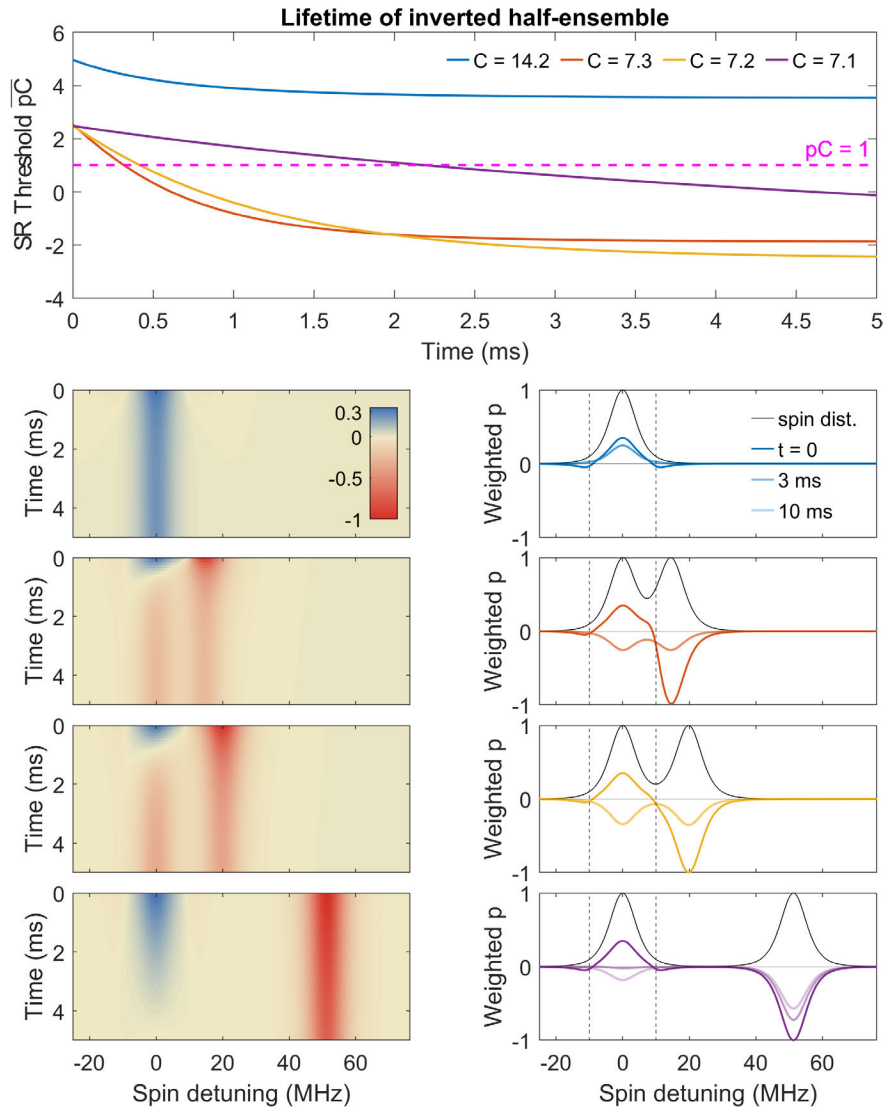


**Figure 6.43** Lifetime simulation with the frequency-dependent central spin model. (Top) Time evolution of the superradiance threshold  $\bar{p}C$  with the spins inside the inversion-pulse window initialized to the same inversion  $p_0$  at  $t = 0$ . The blue curve (fully resonant case  $\delta_{\text{sub}} = 0$ ) becomes flat after roughly 2 ms where the small valleys outside the borders of the initial inversion window have fully refilled at small cost to the central peak height. In the other cases, the system eventually drops below the superradiance threshold, as inversion wanders off to the off-resonant half-ensemble. (Panels below) Time evolution of the weighted spin inversion as color plots and at different snapshots in time. In the color plots, it is clearly visible that the non-inverted half-ensemble (red stripe) slowly draws inversion (blue) from the resonant spins, first depleting the inversion of nearby spins and later affecting the more detuned ones.

to the off-resonant half. This explanation is supported by the observed difference in slopes within the three datasets with  $\delta_{\text{sub}} \neq 0$ , where the red dataset shows a higher lifetime than the other two, while also having a larger overlapping portion of the second sub-ensemble. This overlapping part is still inverted by the initial inversion pulse, potentially contributing to the longer lifetime.

Again, we cross-check the observed lifetimes with a simulation using the frequency-dependent hole-filling model. These simulations are shown in Fig. 6.43. We initialize the resonant spins within the inversion-pulse window to a fixed initial inversion [corresponding to equal time slices in Fig. 6.41(c)] and evolve the system according to Eq. (6.19), without cavity coupling. Importantly, in this simulation, we are excluding any spin-lattice relaxation ( $T_1$  losses), such that the total inversion  $p = \sum_j \rho_j \langle \bar{\sigma}_z^j \rangle$  is conserved. For this reason, the fully resonant case ( $\delta_{\text{sub}} = 0$ ) shows an “infinite” lifetime, never dropping below  $\overline{pC} = 1$ .<sup>8</sup> Conversely, all cases  $\delta_{\text{sub}} > 0$  eventually drop below the superradiance threshold, losing inversion at the cavity resonance frequency to the non-inverted detuned half-ensemble. However, the intermediate  $\delta_{\text{sub}}$  cases drop below the threshold first, and the model suggests the longest lifetime for the largest  $\delta_{\text{sub}}$ . Again, this result is opposite to the experimental observation, where the lifetime reduces with increasing  $\delta_{\text{sub}}$ .

Further investigation with a higher degree of relative overlap between spin ensembles is needed to clarify and cement the observed experimental trends. However, at the current time, we lack a theoretical model that can fully explain these findings. Without such a theory at hand, we are left to speculate on what additional effects might need to be considered in order to capture this complex behavior. One plausible direction, already mentioned above, is the development of a many-body theory, where individual spins are no longer treated as singular units but rather as components of interacting networks. This perspective — and our experiments — suggests that the central spin model currently in use is insufficient to describe the full scope of the dynamics, hinting that collective interactions between multiple spins may hold the key to a more comprehensive understanding.

While additional data and analysis are still needed, these preliminary results hint at a rich landscape of spin-spin dynamics that extends beyond the scope of our current models. The interplay between effective spin-spin interactions — influenced by the proximity of spins both in space and the frequency domain in the disordered system —

---

<sup>8</sup>Before flattening out, the initial decrease of the blue  $\overline{pC}$  curve until around 2 ms bears some similarity to the blue data in Fig. 6.41(c), with a short non-exponential behavior at the beginning. In the simulation, this occurs due to the non-uniform initial inversion introduced by the finite inversion-pulse window approaching a uniform level over time.

causing spectral hole filling, combined with superradiance, suggests exciting avenues for future research.

In summary, this chapter presented experiments that offer key insights into controlling superradiant emission in a diamond-based hybrid cavity-spin system and revealing complex self-driven dynamics that pave the way for further exploration and practical applications. In the final chapter, we will conclude this thesis by discussing potential future experiments and extensions of the work presented.



# Chapter 7

## Conclusion and future directions

In this thesis, we have explored the fascinating realm of superradiant dynamics and the crucial role of spin-spin interactions in driving these phenomena.

We conclude with a brief summary of our results: We have demonstrated the capabilities of our hybrid cavity-spin system in observing and controlling superradiant emission. By developing a technique to store spin inversion and release it at will, we achieved precise control over both the initial inversion and the crucial moments that define the onset of superradiance. This level of control enabled us to explore the transition from quantum-dominated dynamics to the classical emission of a macroscopic radiating dipole formed by trillions of spins. Our experiments also revealed the system's remarkable sensitivity to weak microwave signals during this critical onset stage.

Additionally, we uncovered intriguing self-driven dynamics, characterized by a pulsed superradiance regime followed by a narrow-linewidth quasi-continuous emission. These phenomena are driven by the transfer of spin inversion into the active superradiant window, combined with the interplay of spectral hole formation and the superradiant threshold condition,  $\overline{pC} = 1$ . We provided a phenomenological model to simulate these self-driven superradiant dynamics and presented direct experimental evidence that this inversion transfer is mediated by spin-spin interactions within the disordered spin ensemble. A simple microscopic theory involving a central spin interacting with a mean field generated by the ensemble and requiring only a few parameters — spin linewidth, spin density, and inhomogeneous broadening — agrees well with the observed hole-filling timescale, although questions about the many-body nature of these processes remain open.

Looking ahead, we highlight a promising direction toward technological applications: the possibility of using a microwave drive on the far-detuned half of the spin ensemble to

achieve superradiant emission from the resonant half. In this scenario, spin excitations could be repumped via the detuned half-ensemble and transferred into the resonant half-ensemble through direct spin-spin interactions, where they would generate superradiant emission of microwave photons. This repumping would rely entirely on the microwave domain, bypassing the need for optical pumping of the NV centers [56]. This may potentially be achieved by repeatedly sweeping over the frequency range of the detuned spins, similar to a recurrent chirping pulse.

A first simple test to explore these possibilities — before investigating if a stable population inversion of the off-resonant spins to drive superradiant emission by the resonant spins could even be achieved — would involve sweeping a strong microwave tone across the detuned ensemble, generating a fully mixed spin state with zero net inversion. This should decrease the spectral spin excitation flow between the inverted resonant spins and the fully mixed, off-resonant spins, leading to a change of the self-induced superradiant emission dynamics and hole-filling timescale in a repeated measurement akin to Sec. 6.2.2. Achieving steady population inversion only through microwave repumping is likely challenging and may be limited to pulsed operation under carefully optimized conditions.

This speculative microwave-only pumping approach shares similarities with recent advancements in diamond-based cryogenic microwave amplifiers that exploit cross-relaxation effects between NV centers and P1 centers — where dipole-dipole interactions also play a key role — to generate a population inversion in one of the hyperfine P1 transitions [100]. In this cross-relaxation process [101], the key mechanism involves a four-spin resonance between microwave-driven P1 centers, aided by a nearby NV spin to remove an excitation, while another P1 ends up inverted. Further research in this direction offers exciting potential for diamond-based systems in quantum technologies, particularly in high-precision frequency generation with ultra-narrow linewidths [57] and quantum-limited microwave amplification [80]. Moreover, future explorations with our experimental platform may contribute to ongoing efforts in applying collectively coupled diamond-based systems and superradiant systems to enhanced metrology techniques through superradiance effects [102, 103], quantum sensing of magnetic fields [104], and the implementation of microwave mode cooling techniques [105, 106].

At last, we mention additional layers to the physics that have not been included in the discussions so far, remaining as open questions:

- What is the role of entanglement generated by superradiant emission in the spin system, and how does it influence subsequent spin-spin dynamics? While the

---

hallmark  $N^2$  of superradiance can be obtained using (classical) spin-coherent states (see Sec.2.9), it can be argued that the appearance of coherent states might be due to an experiment's inability to resolve the actual quantum aspects, as discussed in Ref. [107]. With a highly entangled spin system possibly working behind the scenes, how does the entanglement affect spin-spin interactions?

- How can we incorporate the line-broadening of single spins — partially caused by spin-spin interactions and used in our semi-classical modeling of superradiance based on spin frequency packets — into a theoretical model that focuses on these spin-spin interactions?
- What insights might be gained by treating the stochastic noise triggering of superradiant emission using a second-order cumulant description in the semi-classical model of spin-cavity dynamics, instead of the constant cavity drive  $\eta$ ?

In conclusion, the observation of self-induced superradiance driven by spin-spin interactions reveals a new phenomenon with important implications for both fundamental quantum physics and potential technological applications. Throughout this thesis, I explored key aspects of the complex interactions between spin ensembles and microwave cavities and provided insights into the intriguing dynamics of superradiance in solid-state systems. These insights span a wide range (of time), with an initial focus on the onset of superradiant dynamics — investigating the triggers that initiate emission — and later exploring the self-induced aspects of superradiant emission as it unfolds. While I have made significant progress in understanding these phenomena, many open questions remain, offering exciting opportunities for further research. As these hybrid quantum systems are further explored, I expect continuous advancement in the understanding of collective quantum effects that harness the power of superradiance and spin-spin interactions.



# Appendix A

## Integral evaluation of the spectral hole filling rate $\mathcal{J}$

In this appendix, based on calculations by Igor Mazets [98], we evaluate the spectral hole filling rate  $\mathcal{J}$  starting from the result [Eq. (6.16) in the main text]:

$$\mathcal{J} = J_n^2 \sum_{\mathbf{r}} \left( \frac{1}{n_{\text{nv}} r^3} \right)^2 \int_{-\infty}^{\infty} d\omega_1 \rho(\omega_1) \int_{-\infty}^{\infty} d\omega_2 \rho(\omega_2) \frac{4\gamma_{\perp}}{4\gamma_{\perp}^2 + (\omega_1 - \omega_2)^2}. \quad (\text{A.1})$$

One of the frequency integrals can be taken, leaving the detuning probability density

$$\mathcal{P}(\Delta) = \int_{-\infty}^{\infty} d\omega_1 \rho(\omega_1) \rho(\omega_1 + \Delta),$$

which is an even function,  $\mathcal{P}(\Delta) = \mathcal{P}(-\Delta)$ , normalized as  $\int_{-\infty}^{\infty} d\Delta \mathcal{P}(\Delta) = 1$ . To proceed from summation over NV positions to integration, we need to account for the discrete nature of spins in the crystal lattice by introducing the probability  $\mathcal{F}(r, \Delta)$  of having *no spins* within a sphere of a radius  $r$  having detunings in the range from  $-\Delta$  to  $\Delta$  relative to the central spin.

On average, there are

$$\bar{N}(r) = \frac{4}{3} \pi n_{\text{nv}} r^3 \quad (\text{A.2})$$

NVs in a sphere of a radius  $r$ . Assuming their statistical independence and, hence, Poissonian statistics, we find

$$\begin{aligned} \mathcal{F}(r, \Delta) &= \sum_{k=0}^{\infty} \frac{1}{k!} e^{-\bar{N}(r)} [\bar{N}(r)]^k [1 - \mathcal{C}(\Delta)]^k \\ &= \exp[-\bar{N}(r) \mathcal{C}(\Delta)], \end{aligned} \quad (\text{A.3})$$

where we introduce the cumulative probability

$$\mathcal{C}(\Delta) = 2 \int_0^\Delta d\Delta' \mathcal{P}(\Delta').$$

We can now replace summation in Eq. (A.1) with integration:

$$\mathcal{J} = J_n^2 4\pi n_{\text{nv}} \int_{r_{\text{min}}}^\infty dr r^2 \left( \frac{1}{n_{\text{nv}} r^3} \right)^2 2 \int_0^\infty d\Delta \mathcal{P}(\Delta) [1 - \mathcal{F}(r, \Delta)] \frac{4\gamma_\perp}{4\gamma_\perp^2 + \Delta^2}. \quad (\text{A.4})$$

Here we introduce the minimum possible distance  $r_{\text{min}} \approx a$  between NV spins, determined by the period  $a \approx 3.567 \text{ \AA}$  of the diamond crystalline lattice,  $r_{\text{min}} \ll n_{\text{nv}}^{-1/3}$ . This naturally cures the logarithmic divergence of the integral in Eq. (A.4). Using Eqs. (A.2,A.3) and integrating over  $r$ , we obtain:

$$\mathcal{J} = 2 \left( \frac{4\pi}{3} \right)^2 J_n^2 \int_0^\infty d\Delta \mathcal{P}(\Delta) \mathcal{C}(\Delta) G[\nu_{\text{min}} \mathcal{C}(\Delta)] \frac{4\gamma_\perp}{4\gamma_\perp^2 + \Delta^2}, \quad (\text{A.5})$$

where  $\nu_{\text{min}} = \frac{4}{3}\pi n_{\text{nv}} r_{\text{min}}^3$ ,

$$G(x) = \frac{1 - e^{-x}}{x} + \Gamma(0, x),$$

and  $\Gamma(a, x) = \int_x^\infty dz t^{a-1} e^{-z}$  is the incomplete gamma-function [108]. For small arguments, relevant for Eq. (A.5), we have

$$G(x) \approx 1 - \gamma - \ln x, \quad x \ll 1,$$

with  $\gamma \approx 0.577$  being the Euler-Mascheroni constant.

For ease of an analytic solution, we approximate the  $q$ -Gaussian spin distribution  $\rho(\omega)$  with a simple Gaussian of the same width  $W$  (FWHM) and standard deviation  $\sigma_w = W/2\sqrt{2\ln 2}$ . The distribution of detunings  $\Delta$  is then also Gaussian:

$$\mathcal{P}(\Delta) = \frac{\exp[-\Delta^2/(4\sigma_w^2)]}{2\sqrt{\pi}\sigma_w},$$

and  $\mathcal{C}(\Delta) = \text{erf}[\Delta/(2\sigma_w)]$  is given by the error function [108]. Changing the integration variable in Eq. (A.5) to  $\mathcal{C}(\Delta)$ , we obtain

$$\mathcal{J} = \left( \frac{4\pi}{3} \right)^2 \frac{J_n^2}{\sigma_w} \int_0^1 dy y \ln \left( \frac{1}{\nu_{\text{min}} y} \right) \frac{\tilde{\Gamma}_\perp}{\tilde{\Gamma}_\perp^2 + [\text{erf}^{-1}(y)]^2}, \quad (\text{A.6})$$

where  $\tilde{\Gamma}_\perp = \gamma_\perp/\sigma_w$  and  $\text{erf}^{-1}(y)$  is the inverse error function. In Eq. (A.6), we neglected, within logarithmic accuracy, the difference between  $e^{1-\gamma}$  and 1.

The remaining task is to evaluate two integrals:

$$\mathcal{I}_1(\tilde{\Gamma}_\perp) = \int_0^1 dy y \frac{\tilde{\Gamma}_\perp}{\tilde{\Gamma}_\perp^2 + [\text{erf}^{-1}(y)]^2}, \quad \mathcal{I}_2(\tilde{\Gamma}_\perp) = \int_0^1 dy y \ln(1/y) \frac{\tilde{\Gamma}_\perp}{\tilde{\Gamma}_\perp^2 + [\text{erf}^{-1}(y)]^2}.$$

By assumption, the transition linewidth is narrow compared to the inhomogeneous broadening, and we have  $\tilde{\Gamma}_\perp \ll 1$ . In this limit, the main contribution to these integrals comes from small  $y$ , where we can use the approximation  $\text{erf}^{-1}(y) \approx \sqrt{\pi}y/2$ . Then the first integral is elementary, yielding

$$\mathcal{I}_1(\tilde{\Gamma}_\perp) \approx \frac{2}{\pi} \tilde{\Gamma}_\perp \ln \left( 1 + \frac{\pi}{4\tilde{\Gamma}_\perp^2} \right). \quad (\text{A.7})$$

A bit more cumbersome estimation yields

$$\mathcal{I}_2(\tilde{\Gamma}_\perp) \approx \frac{1}{2} \ln(1/\tilde{\Gamma}_\perp) \mathcal{I}_1(\tilde{\Gamma}_\perp). \quad (\text{A.8})$$

Direct numerical integration confirms the fairness of the estimations Eqs. (A.7,A.8).

Finally, within logarithmic accuracy, we obtain

$$\mathcal{J} = \frac{32\pi J_n^2 \tilde{\Gamma}_\perp}{9\sigma_w} \ln \left( \frac{1}{\nu_{\min}^2 \tilde{\Gamma}_\perp} \right) \ln \left( \frac{1}{\tilde{\Gamma}_\perp} \right), \quad (\text{A.9})$$

where we assume  $\tilde{\Gamma}_\perp \ll 1$ .

## A.1 Frequency dependent spectral hole refilling

We revisit the full ‘‘microscopic’’ model of a central spin  $j$  interacting with all other spins  $k$  [c.f. Eq. (6.15)]:

$$\frac{d}{dt} \langle \sigma_z^j \rangle = \sum_{k \neq j} \left( \frac{J_n}{n_{\text{nv}} r^3} \right)^2 \frac{4\gamma_\perp}{4\gamma_\perp^2 + (\omega_j - \omega_k)^2} \left[ \langle \sigma_z^k \rangle - \langle \sigma_z^j \rangle \right]. \quad (\text{A.10})$$

Here, we attempt to incorporate the full extent of this model — suggesting a  $\omega_j$  dependent result of the sum on the right-hand side — into the description of the self-induced superradiant dynamics. Proceeding similarly to the above derivation, we separate the contributions in the sum into spatial and frequency parts. We introduce

the spectral distribution of inverted spins

$$P_{\uparrow}(\omega) = \frac{1}{N} \sum_{l=1}^N \left( \frac{1 + \langle \sigma_z^l \rangle}{2} \right) \delta(\omega_l - \omega).$$

The spin distribution is given by the sum of all up and down spins

$$\rho(\omega) = P_{\uparrow}(\omega) + P_{\downarrow}(\omega),$$

which remains constant over time. Here, we assume the spin-lattice relaxation rate  $\gamma_{\parallel} = 0$ . We now express Eq. (A.10) in its continuous form:

$$\frac{d}{dt} P_{\uparrow}(\omega) = \int_{-\infty}^{\infty} d\omega' \mathcal{J}_s(\omega, \omega') \left[ P_{\downarrow}(\omega) P_{\uparrow}(\omega') - P_{\uparrow}(\omega) P_{\downarrow}(\omega') \right]. \quad (\text{A.11})$$

This equation describes the increase of inversion  $P_{\uparrow}(\omega)$  over time, driven by the interaction between down-spins at frequency  $\omega$  with up-spins at frequency  $\omega'$ . The spectral interaction rate is given by

$$\mathcal{J}_s(\omega, \omega') = 4\pi n_{\text{nv}} \int_{r_{\text{min}}}^{\infty} dr r^2 \left( \frac{J_{\text{n}}}{n_{\text{nv}} r^3} \right)^2 \frac{4\gamma_{\perp}}{4\gamma_{\perp}^2 + (\omega - \omega')^2} \left[ 1 - \tilde{\mathcal{F}}(r, \omega, |\omega - \omega'|) \right]. \quad (\text{A.12})$$

Here,  $\tilde{\mathcal{F}}(r, \omega, \Delta)$  represents the probability of finding *no inverted spins* within a sphere of radius  $r$  around a central spin, such that their detunings are less than  $\pm\Delta = |\omega - \omega'|$ . Analogous to the above derivation, this probability is modeled using Poissonian statistics:

$$\tilde{\mathcal{F}}(r, \omega, \Delta) = \exp \left[ -\frac{4}{3} \pi n_{\text{nv}} r^3 \tilde{\mathcal{C}}(\omega, \Delta) \right], \quad (\text{A.13})$$

where the cumulative probability is calculated as:

$$\tilde{\mathcal{C}}(\omega, \Delta) = \int_{\omega-\Delta}^{\omega+\Delta} P_{\downarrow}(\omega') d\omega'.$$

The  $r$  integration can then be carried out, resulting in

$$\mathcal{J}_s(\omega, \omega') = \left( \frac{4\pi}{3} \right)^2 J_{\text{n}}^2 \frac{4\gamma_{\perp}}{4\gamma_{\perp}^2 + \Delta^2} \tilde{\mathcal{C}}(\omega, \Delta) G[\nu_{\text{min}} \tilde{\mathcal{C}}(\omega, \Delta)], \quad (\text{A.14})$$

where we use the same definitions of  $G(x)$  and  $\nu_{\text{min}}$  as in the above derivation.

To make this result useful in combination with the Maxwell-Bloch equations, we discretize the problem again into  $N_\rho$  equally spaced frequency packets using the normalized distribution weights  $\rho_j$ , see Sec. 2.8. Here, we use the notation  $\langle \bar{\sigma}_z^j \rangle$  for the averaged spin-packet inversion to distinguish the spin-packets from single spins  $\langle \sigma_z^j \rangle$ .

First, we express the up-spin and down-spin distributions as:

$$P_\uparrow(\omega_j) = \rho_j \left( \frac{1 + \langle \bar{\sigma}_z^j \rangle}{2} \right), \quad (\text{A.15})$$

$$P_\downarrow(\omega_j) = \rho_j - P_\uparrow(\omega_j) = \rho_j \left( \frac{1 - \langle \bar{\sigma}_z^j \rangle}{2} \right), \quad (\text{A.16})$$

The equation of motion for the inversion of the spin-frequency packet  $\langle \bar{\sigma}_z^j \rangle$  can then be written as:

$$\frac{d}{dt} \langle \bar{\sigma}_z^j \rangle = \sum_{k \neq j} \mathcal{J}_{jk} \rho_k \left[ \langle \bar{\sigma}_z^k \rangle - \langle \bar{\sigma}_z^j \rangle \right]. \quad (\text{A.17})$$

Here,  $\mathcal{J}_{jk}$  is the effective spin-packet interaction matrix, which we express as:

$$\mathcal{J}_{jk} = \left( \frac{4\pi}{3} \right)^2 J_n^2 \frac{4\gamma_\perp}{4\gamma_\perp^2 + (\omega_j - \omega_k)^2} \tilde{\mathcal{C}}_{jk} G(\nu_{\min} \tilde{\mathcal{C}}_{jk}). \quad (\text{A.18})$$

The cumulative discrete distribution  $\tilde{\mathcal{C}}_{jk}$  is given by:

$$\tilde{\mathcal{C}}_{jk} = \sum_{l=l_{\min}(j,k)}^{l_{\max}(j,k)} \rho_l \left( \frac{1 - \langle \bar{\sigma}_z^l \rangle}{2} \right), \quad (\text{A.19})$$

where the indices  $l_{\min} = \max(j - |j - k|, 1)$  and  $l_{\max} = \min(j + |j - k|, N_\rho)$  define the range of frequency packets  $l$  for which  $\omega_l$  lies within the interval  $\omega_j \pm |\omega_j - \omega_k|$ . In the numerical implementation of this model, we symmetrize the matrix  $\mathcal{J}'_{jk} = (\mathcal{J}_{jk} + \mathcal{J}_{kj})/2$  to account for a small boundary error, where the range from  $l_{\min}$  to  $l_{\max}$  is not symmetric around  $j$ . This way, the total inversion  $p = \sum_j \rho_j \langle \sigma_z^j \rangle$  is conserved.



# References

- [1] J. C. Maxwell, “Viii. a dynamical theory of the electromagnetic field,” *Philosophical transactions of the Royal Society of London*, no. 155, pp. 459–512, 1865.
- [2] P. A. M. Dirac, *The principles of quantum mechanics*. No. 27, Oxford university press, 1981.
- [3] R. P. Feynman, *QED: The strange theory of light and matter*. Princeton University Press, 2014.
- [4] S. Haroche and J.-M. Raimond, *Exploring the quantum: atoms, cavities, and photons*. Oxford university press, 2006.
- [5] M. W. Doherty, N. B. Manson, P. Delaney, F. Jelezko, J. Wrachtrup, and L. C. Hollenberg, “The nitrogen-vacancy colour centre in diamond,” *Physics Reports*, vol. 528, no. 1, pp. 1–45, 2013.
- [6] A. Gaita-Ariño, F. Luis, S. Hill, and E. Coronado, “Molecular spins for quantum computation,” *Nature chemistry*, vol. 11, no. 4, pp. 301–309, 2019.
- [7] A. Blais, R.-S. Huang, A. Wallraff, S. M. Girvin, and R. J. Schoelkopf, “Cavity quantum electrodynamics for superconducting electrical circuits: An architecture for quantum computation,” *Physical Review A—Atomic, Molecular, and Optical Physics*, vol. 69, no. 6, p. 062320, 2004.
- [8] A. Chiesa, S. Roca, S. Chicco, M. de Ory, A. Gómez-León, A. Gomez, D. Zueco, F. Luis, and S. Carretta, “Blueprint for a molecular-spin quantum processor,” *Physical Review Applied*, vol. 19, no. 6, p. 064060, 2023.
- [9] R. H. Dicke, “Coherence in spontaneous radiation processes,” *Physical Review*, vol. 93, no. 1, p. 99, 1954.
- [10] M. Gross and S. Haroche, “Superradiance: An essay on the theory of collective spontaneous emission,” *Physics Reports*, vol. 93, no. 5, pp. 301–396, 1982.
- [11] W. Kersten, L. Brandl, R. Wagner, C. Huber, F. Bruckner, Y. Hasegawa, D. Suess, and S. Sponar, “Additive-manufactured and topology-optimized permanent-magnet spin rotator for neutron interferometry,” *Physical Review Applied*, vol. 12, no. 1, p. 014023, 2019.

- 
- [12] H. Rauch, A. Zeilinger, G. Badurek, A. Wilfing, W. Bauspiess, and U. Bonse, “Verification of coherent spinor rotation of fermions,” *Physics Letters A*, vol. 54, no. 6, pp. 425–427, 1975.
- [13] R. Dick *et al.*, *Advanced quantum mechanics*. Springer, 2012.
- [14] M. O. Scully and M. S. Zubairy, *Quantum optics*. Cambridge university press, 1997.
- [15] J. J. Sakurai and J. Napolitano, *Modern quantum mechanics*. Cambridge University Press, 2020.
- [16] A. Klein and E. Marshalek, “Boson realizations of lie algebras with applications to nuclear physics,” *Reviews of modern physics*, vol. 63, no. 2, p. 375, 1991.
- [17] E. L. Hahn, “Spin echoes,” *Physical review*, vol. 80, no. 4, p. 580, 1950.
- [18] H. J. Carmichael, *Statistical methods in quantum optics 1: master equations and Fokker-Planck equations*, vol. 1. Springer Science & Business Media, 1999.
- [19] D. Walls and G. J. Milburn, *Quantum Optics*. Springer Berlin, Heidelberg, 2007.
- [20] C. Tsallis, “Possible generalization of boltzmann-gibbs statistics,” *Journal of statistical physics*, vol. 52, pp. 479–487, 1988.
- [21] K. Sandner, H. Ritsch, R. Amsüss, C. Koller, T. Nöbauer, S. Putz, J. Schmiedmayer, and J. Majer, “Strong magnetic coupling of an inhomogeneous nitrogen-vacancy ensemble to a cavity,” *Physical Review A*, vol. 85, no. 5, p. 053806, 2012.
- [22] S. Putz, A. Angerer, D. O. Krimer, R. Glattauer, W. J. Munro, S. Rotter, J. Schmiedmayer, and J. Majer, “Spectral hole burning and its application in microwave photonics,” *Nature Photonics*, vol. 11, no. 1, pp. 36–39, 2017.
- [23] C. Runge, “Über die numerische auflösung von differentialgleichungen,” *Mathematische Annalen*, vol. 46, no. 2, pp. 167–178, 1895.
- [24] F. T. Arecchi, E. Courtens, R. Gilmore, and H. Thomas, “Atomic coherent states in quantum optics,” *Physical Review A*, vol. 6, no. 6, p. 2211, 1972.
- [25] S. J. Masson, J. P. Covey, S. Will, and A. Asenjo-Garcia, “Dicke superradiance in ordered arrays of multilevel atoms,” *PRX Quantum*, vol. 5, no. 1, p. 010344, 2024.
- [26] M. Scheibner, T. Schmidt, L. Worschech, A. Forchel, G. Bacher, T. Passow, and D. Hommel, “Superradiance of quantum dots,” *Nature Physics*, vol. 3, no. 2, pp. 106–110, 2007.
- [27] P. Goy, L. Moi, M. Gross, J. M. Raimond, C. Fabre, and S. Haroche, “Rydberg-atom masers. II. Triggering by external radiation and application to millimeter-wave detectors,” *Physical Review A*, vol. 27, no. 4, p. 2065, 1983.

- [28] G. Ferioli, A. Glicenstein, I. Ferrier-Barbut, and A. Browaeys, “A non-equilibrium superradiant phase transition in free space,” *Nature Physics*, vol. 19, pp. 1345–1349, 2023.
- [29] R. Pennetta, M. Blaha, A. Johnson, D. Lechner, P. Schneeweiss, J. Volz, and A. Rauschenbeutel, “Collective radiative dynamics of an ensemble of cold atoms coupled to an optical waveguide,” *Physical Review Letters*, vol. 128, no. 7, p. 073601, 2022.
- [30] F. Rajabi and M. Houde, “Astronomical masers and dicke’s superradiance,” *Monthly Notices of the Royal Astronomical Society*, vol. 494, no. 4, pp. 5194–5206, 2020.
- [31] B. Julsgaard and K. Mølmer, “Dynamical evolution of an inverted spin ensemble in a cavity: Inhomogeneous broadening as a stabilizing mechanism,” *Physical Review A*, vol. 86, no. 6, p. 063810, 2012.
- [32] E. M. Purcell, “Spontaneous emission probabilities at radio frequencies,” *Physical Review*, vol. 69, p. 681, 1946.
- [33] F. Pobell, *Matter and methods at low temperatures*, vol. 2. Springer, 2007.
- [34] K. Uhlig, ““Dry” dilution refrigerator with pulse-tube precooling,” *Cryogenics*, vol. 44, no. 1, pp. 53–57, 2004.
- [35] W. Kersten, N. de Zordo, O. Diekmann, T. Reiter, M. Zens, A. N. Kanagin, S. Rotter, J. Schmiedmayer, and A. Angerer, “Triggered superradiance and spin inversion storage in a hybrid quantum system,” *Physical Review Letters*, vol. 131, no. 4, p. 043601, 2023.
- [36] M. H. Abobeih, J. Cramer, M. A. Bakker, N. Kalb, M. Markham, D. J. Twitchen, and T. H. Taminiau, “One-second coherence for a single electron spin coupled to a multi-qubit nuclear-spin environment,” *Nature communications*, vol. 9, no. 1, p. 2552, 2018.
- [37] T. Astner, J. Gugler, A. Angerer, S. Wald, S. Putz, N. J. Mauser, M. Trupke, H. Sumiya, S. Onoda, J. Isoya, *et al.*, “Solid-state electron spin lifetime limited by phononic vacuum modes,” *Nature Materials*, vol. 17, no. 4, pp. 313–317, 2018.
- [38] C. L. Degen, F. Reinhard, and P. Cappellaro, “Quantum sensing,” *Reviews of modern physics*, vol. 89, no. 3, p. 035002, 2017.
- [39] L. Trifunovic, F. L. Pedrocchi, S. Hoffman, P. Maletinsky, A. Yacoby, and D. Loss, “High-efficiency resonant amplification of weak magnetic fields for single spin magnetometry at room temperature,” *Nature nanotechnology*, vol. 10, no. 6, pp. 541–546, 2015.
- [40] K. Bian, W. Zheng, X. Zeng, X. Chen, R. Stöhr, A. Denisenko, S. Yang, J. Wrachtrup, and Y. Jiang, “Nanoscale electric-field imaging based on a quantum sensor and its charge-state control under ambient condition,” *Nature Communications*, vol. 12, no. 1, p. 2457, 2021.

- [41] Y. Nishimura, K. Oshimi, Y. Umehara, Y. Kumon, K. Miyaji, H. Yukawa, Y. Shikano, T. Matsubara, M. Fujiwara, Y. Baba, *et al.*, “Wide-field fluorescent nanodiamond spin measurements toward real-time large-area intracellular thermometry,” *Scientific reports*, vol. 11, no. 1, p. 4248, 2021.
- [42] P. C. Maurer, G. Kucsko, C. Latta, L. Jiang, N. Y. Yao, S. D. Bennett, F. Pastawski, D. Hunger, N. Chisholm, M. Markham, *et al.*, “Room-temperature quantum bit memory exceeding one second,” *Science*, vol. 336, no. 6086, pp. 1283–1286, 2012.
- [43] C. E. Bradley, J. Randall, M. H. Abobeih, R. C. Berrevoets, M. J. Degen, M. A. Bakker, M. Markham, D. J. Twitchen, and T. H. Taminiau, “A ten-qubit solid-state spin register with quantum memory up to one minute,” *Physical Review X*, vol. 9, no. 3, p. 031045, 2019.
- [44] G. Van de Stolpe, D. Kwiatkowski, C. Bradley, J. Randall, M. Abobeih, S. Breitweiser, L. Bassett, M. Markham, D. Twitchen, and T. Taminiau, “Mapping a 50-spin-qubit network through correlated sensing,” *Nature Communications*, vol. 15, no. 1, p. 2006, 2024.
- [45] B. Hensen, H. Bernien, A. E. Dréau, A. Reiserer, N. Kalb, M. S. Blok, J. Ruitenberg, R. F. Vermeulen, R. N. Schouten, C. Abellán, *et al.*, “Loophole-free bell inequality violation using electron spins separated by 1.3 kilometres,” *Nature*, vol. 526, no. 7575, pp. 682–686, 2015.
- [46] E. J. Davis, B. Ye, F. Machado, S. A. Meynell, W. Wu, T. Mittiga, W. Schenken, M. Joos, B. Kobrin, Y. Lyu, *et al.*, “Probing many-body dynamics in a two-dimensional dipolar spin ensemble,” *Nature physics*, vol. 19, no. 6, pp. 836–844, 2023.
- [47] C. Zu, F. Machado, B. Ye, S. Choi, B. Kobrin, T. Mittiga, S. Hsieh, P. Bhattacharyya, M. Markham, D. Twitchen, *et al.*, “Emergent hydrodynamics in a strongly interacting dipolar spin ensemble,” *Nature*, vol. 597, no. 7874, pp. 45–50, 2021.
- [48] R. Schirhagl, K. Chang, M. Loretz, and C. L. Degen, “Nitrogen-vacancy centers in diamond: nanoscale sensors for physics and biology,” *Annual review of physical chemistry*, vol. 65, no. 1, pp. 83–105, 2014.
- [49] N. Aslam, H. Zhou, E. K. Urbach, M. J. Turner, R. L. Walsworth, M. D. Lukin, and H. Park, “Quantum sensors for biomedical applications,” *Nature Reviews Physics*, vol. 5, no. 3, pp. 157–169, 2023.
- [50] D. R. Glenn, K. Lee, H. Park, R. Weissleder, A. Yacoby, M. D. Lukin, H. Lee, R. L. Walsworth, and C. B. Connolly, “Single-cell magnetic imaging using a quantum diamond microscope,” *Nature methods*, vol. 12, no. 8, pp. 736–738, 2015.
- [51] D. R. Glenn, D. B. Bucher, J. Lee, M. D. Lukin, H. Park, and R. L. Walsworth, “High-resolution magnetic resonance spectroscopy using a solid-state spin sensor,” *Nature*, vol. 555, no. 7696, pp. 351–354, 2018.

- [52] T. F. Segawa and R. Igarashi, “Nanoscale quantum sensing with nitrogen-vacancy centers in nanodiamonds—a magnetic resonance perspective,” *Progress in Nuclear Magnetic Resonance Spectroscopy*, vol. 134, pp. 20–38, 2023.
- [53] V. Ivády, H. Zheng, A. Wickenbrock, L. Bougas, G. Chatzidrosos, K. Nakamura, H. Sumiya, T. Ohshima, J. Isoya, D. Budker, *et al.*, “Photoluminescence at the ground-state level anticrossing of the nitrogen-vacancy center in diamond: A comprehensive study,” *Physical Review B*, vol. 103, no. 3, p. 035307, 2021.
- [54] L. Robledo, H. Bernien, T. Van Der Sar, and R. Hanson, “Spin dynamics in the optical cycle of single nitrogen-vacancy centres in diamond,” *New Journal of Physics*, vol. 13, no. 2, p. 025013, 2011.
- [55] <https://commons.wikimedia.org/wiki/File:NV-transitions.svg>. [Accessed 4-Sep-2024], Licensed under CC BY-SA 4.0, Created by BonPhire, 2021.
- [56] J. D. Breeze, E. Salvadori, J. Sathian, N. M. Alford, and C. W. Kay, “Continuous-wave room-temperature diamond maser,” *Nature*, vol. 555, no. 7697, pp. 493–496, 2018.
- [57] Q. Wu, Y. Zhang, X. Yang, S.-L. Su, C. Shan, and K. Mølmer, “A superradiant maser with nitrogen-vacancy center spins,” *Science China Physics, Mechanics & Astronomy*, vol. 65, no. 1, pp. 1–10, 2022.
- [58] C. Grezes, Y. Kubo, B. Julsgaard, T. Umeda, J. Isoya, H. Sumiya, H. Abe, S. Onoda, T. Ohshima, K. Nakamura, *et al.*, “Towards a spin-ensemble quantum memory for superconducting qubits,” *Comptes Rendus. Physique*, vol. 17, no. 7, pp. 693–704, 2016.
- [59] T. Nöbauer, K. Buczak, A. Angerer, S. Putz, G. Steinhauser, J. Akbarzadeh, H. Peterlik, J. Majer, J. Schmiedmayer, and M. Trupke, “Creation of ensembles of nitrogen-vacancy centers in diamond by neutron and electron irradiation,” *arXiv preprint arXiv:1309.0453*, 2013.
- [60] M. Chizzini, L. Crippa, L. Zaccardi, E. Macaluso, S. Carretta, A. Chiesa, and P. Santini, “Quantum error correction with molecular spin qubits,” *Physical Chemistry Chemical Physics*, vol. 24, no. 34, pp. 20030–20039, 2022.
- [61] M. Shiddiq, D. Komijani, Y. Duan, A. Gaita-Ariño, E. Coronado, and S. Hill, “Enhancing coherence in molecular spin qubits via atomic clock transitions,” *Nature*, vol. 531, no. 7594, pp. 348–351, 2016.
- [62] M. Jenkins, D. Zueco, O. Roubeau, G. Aromí, J. Majer, and F. Luis, “A scalable architecture for quantum computation with molecular nanomagnets,” *Dalton Transactions*, vol. 45, no. 42, pp. 16682–16693, 2016.
- [63] I. Gimeno, W. Kersten, M. C. Pallarés, P. Hermosilla, M. J. Martínez-Pérez, M. D. Jenkins, A. Angerer, C. Sanchez-Azqueta, D. Zueco, J. Majer, *et al.*, “Enhanced molecular spin-photon coupling at superconducting nanoconstrictions,” *ACS nano*, vol. 14, no. 7, pp. 8707–8715, 2020.

- [64] D. Žilić, D. Pajić, M. Jurić, K. Molčanov, B. Rakvin, P. Planinić, and K. Zadro, “Single crystals of dpqh grown from diethyl ether and carbon disulfide solutions—crystal structures, ir, epr and magnetization studies,” *Journal of Magnetic Resonance*, vol. 207, no. 1, pp. 34–41, 2010.
- [65] C. Eichler, A. Sigillito, S. A. Lyon, and J. R. Petta, “Electron spin resonance at the level of  $10^4$  spins using low impedance superconducting resonators,” *Physical review letters*, vol. 118, no. 3, p. 037701, 2017.
- [66] “COMSOL Multiphysics® v. 6.2.” [www.comsol.com](http://www.comsol.com). COMSOL AB, Stockholm, Sweden.
- [67] M. Göppl, A. Fragner, M. Baur, R. Bianchetti, S. Filipp, J. M. Fink, P. J. Leek, G. Puebla, L. Steffen, and A. Wallraff, “Coplanar waveguide resonators for circuit quantum electrodynamics,” *Journal of Applied Physics*, vol. 104, no. 11, 2008.
- [68] M. D. Jenkins, U. Naether, M. Ciria, J. Sesé, J. Atkinson, C. Sánchez-Azqueta, E. d. Barco, J. Majer, D. Zueco, and F. Luis, “Nanoscale constrictions in superconducting coplanar waveguide resonators,” *Applied Physics Letters*, vol. 105, no. 16, 2014.
- [69] R. D. Piner, J. Zhu, F. Xu, S. Hong, and C. A. Mirkin, ““ dip-pen ” nanolithography,” *science*, vol. 283, no. 5402, pp. 661–663, 1999.
- [70] G. Blatter, M. V. Feigel’man, V. B. Geshkenbein, A. I. Larkin, and V. M. Vinokur, “Vortices in high-temperature superconductors,” *Reviews of modern physics*, vol. 66, no. 4, p. 1125, 1994.
- [71] J. R. Ball, Y. Yamashiro, H. Sumiya, S. Onoda, T. Ohshima, J. Isoya, D. Konstantinov, and Y. Kubo, “Loop-gap microwave resonator for hybrid quantum systems,” *Applied Physics Letters*, vol. 112, no. 20, p. 204102, 2018.
- [72] A. Angerer, T. Astner, D. Wirtitsch, H. Sumiya, S. Onoda, J. Isoya, S. Putz, and J. Majer, “Collective strong coupling with homogeneous rabi frequencies using a 3D lumped element microwave resonator,” *Applied Physics Letters*, vol. 109, no. 3, p. 033508, 2016.
- [73] A. Angerer, K. Streltsov, T. Astner, S. Putz, H. Sumiya, S. Onoda, J. Isoya, W. J. Munro, K. Nemoto, J. Schmiedmayer, *et al.*, “Superradiant emission from colour centres in diamond,” *Nature Physics*, vol. 14, no. 12, pp. 1168–1172, 2018.
- [74] R. Amsüss, C. Koller, T. Nöbauer, S. Putz, S. Rotter, K. Sandner, S. Schneider, M. Schramböck, G. Steinhauser, H. Ritsch, *et al.*, “Cavity qed with magnetically coupled collective spin states,” *Physical review letters*, vol. 107, no. 6, p. 060502, 2011.
- [75] W. Kersten, N. de Zordo, E. S. Redchenko, N. Lagos, A. N. Kanagin, A. Angerer, W. J. Munro, K. Nemoto, I. E. Mazets, and J. Schmiedmayer, “Self-induced superradiant masing,” *arXiv preprint arXiv:2402.08537*, 2024.

- [76] W. Hardy and L. Whitehead, “Split-ring resonator for use in magnetic resonance from 200–2000 MHz,” *Review of Scientific Instruments*, vol. 52, no. 2, pp. 213–216, 1981.
- [77] D. Rieger, S. Günzler, M. Spiecker, A. Nambisan, W. Wernsdorfer, and I. Pop, “Fano interference in microwave resonator measurements,” *Physical Review Applied*, vol. 20, no. 1, p. 014059, 2023.
- [78] W. Demtröder, *Experimentalphysik*, vol. 2. Springer, 1998.
- [79] B. Sarabi, P. Huang, and N. M. Zimmerman, “Possible hundredfold enhancement in the direct magnetic coupling of a single-atom electron spin to a circuit resonator,” *Physical Review Applied*, vol. 11, no. 1, p. 014001, 2019.
- [80] A. Sherman, O. Zgadzai, B. Koren, I. Peretz, E. Laster, and A. Blank, “Diamond-based microwave quantum amplifier,” *Science Advances*, vol. 8, no. 49, p. eade6527, 2022.
- [81] Y. Zhang, Q. Wu, S.-L. Su, Q. Lou, C. Shan, and K. Mølmer, “Cavity quantum electrodynamics effects with nitrogen vacancy center spins coupled to room temperature microwave resonators,” *Physical Review Letters*, vol. 128, no. 25, p. 253601, 2022.
- [82] D. Plankensteiner, C. Hotter, and H. Ritsch, “Quantumcumulants.jl: A julia framework for generalized mean-field equations in open quantum systems,” *Quantum*, vol. 6, p. 617, 2022.
- [83] C. Benvenuti, D. Bloess, N. Hilleret, P. Bernard, J. Tückmantel, E. Chiaveri, G. Cavallari, E. Häbel, and W. Weingarten, “Superconducting niobium sputter-coated copper cavity modules for the LEP energy upgrade,” tech. rep., 1991.
- [84] S. Meiboom and D. Gill, “Modified spin-echo method for measuring nuclear relaxation times,” *Review of scientific instruments*, vol. 29, no. 8, pp. 688–691, 1958.
- [85] C. Hardy, W. Edelstein, and D. Vatis, “Efficient adiabatic fast passage for nmr population inversion in the presence of radiofrequency field inhomogeneity and frequency offsets,” *Journal of Magnetic Resonance (1969)*, vol. 66, no. 3, pp. 470–482, 1986.
- [86] R. Leifert – KainkaLabs (Youtube channel), “Measuring Self-Capacitance and Self-Resonant Frequency SRF of Inductors.” Available online at <https://www.youtube.com/watch?v=tjbK4LsOQRk>.
- [87] J. Choi, S. Choi, G. Kucsko, P. C. Maurer, B. J. Shields, H. Sumiya, S. Onoda, J. Isoya, E. Demler, F. Jelezko, N. Y. Yao, and M. D. Lukin, “Depolarization dynamics in a strongly interacting solid-state spin ensemble,” *Phys. Rev. Lett.*, vol. 118, p. 093601, Mar 2017.
- [88] L. Moi, P. Goy, M. Gross, J. M. Raimond, C. Fabre, and S. Haroche, “Rydberg-atom masers. I. A theoretical and experimental study of super-radiant systems in the millimeter-wave domain,” *Physical Review A*, vol. 27, no. 4, p. 2043, 1983.

- [89] S. O. Rice, “Mathematical analysis of random noise,” *The Bell System Technical Journal*, vol. 24, no. 1, pp. 46–156, 1945.
- [90] E. A. Cooper and H. Farid, “A toolbox for the radial and angular marginalization of bivariate normal distributions,” 2020.
- [91] R. Paschotta, “Time–bandwidth product.” RP Photonics Encyclopedia. Available online at [https://www.rp-photonics.com/time\\_bandwidth\\_product.html](https://www.rp-photonics.com/time_bandwidth_product.html) .
- [92] J. H. Eberly, N. Narozhny, and J. Sanchez-Mondragon, “Periodic spontaneous collapse and revival in a simple quantum model,” *Physical Review Letters*, vol. 44, no. 20, p. 1323, 1980.
- [93] R. Kubo, “Generalized cumulant expansion method,” *Journal of the Physical Society of Japan*, vol. 17, no. 7, pp. 1100–1120, 1962.
- [94] H. Hara, J. Han, Y. Imai, N. Sasao, A. Yoshimi, K. Yoshimura, M. Yoshimura, and Y. Miyamoto, “Periodic superradiance in an er: Yso crystal,” *Physical Review Research*, vol. 6, no. 1, p. 013005, 2024.
- [95] P. W. Anderson, “Absence of diffusion in certain random lattices,” *Physical review*, vol. 109, no. 5, p. 1492, 1958.
- [96] C. Gardiner and P. Zoller, *Quantum noise: a handbook of Markovian and non-Markovian quantum stochastic methods with applications to quantum optics*. Springer Science & Business Media, 2004.
- [97] P. Fowler-Wright, K. B. Arnardóttir, P. Kirton, B. W. Lovett, and J. Keeling, “Determining the validity of cumulant expansions for central spin models,” *Physical Review Research*, vol. 5, no. 3, p. 033148, 2023.
- [98] I. Mazets, “Integral evaluation of the spectral hole filling rate  $\mathcal{J}$ ,” 2024. Private communication.
- [99] G. Kucsko, S. Choi, J. Choi, P. C. Maurer, H. Zhou, R. Landig, H. Sumiya, S. Onoda, J. Isoya, F. Jelezko, *et al.*, “Critical thermalization of a disordered dipolar spin system in diamond,” *Physical review letters*, vol. 121, no. 2, p. 023601, 2018.
- [100] K. Yuimaru, J. R. Ball, P. Moroshkin, and D. Konstantinov, “Ultra-low noise cryogenic microwave amplification,” 2023. US Patent 11677206.
- [101] P. Sorokin, G. Lasher, and I. Gelles, “Cross relaxation studies in diamond,” *Physical Review*, vol. 118, no. 4, p. 939, 1960.
- [102] M. Koppenhöfer, P. Groszkowski, H.-K. Lau, and A. A. Clerk, “Dissipative superradiant spin amplifier for enhanced quantum sensing,” *PRX Quantum*, vol. 3, no. 3, p. 030330, 2022.
- [103] E. A. Bohr, S. L. Kristensen, C. Hotter, S. A. Schäffer, J. Robinson-Tait, J. W. Thomsen, T. Zelevinsky, H. Ritsch, and J. H. Müller, “Collectively enhanced ramsay readout by cavity sub-to superradiant transition,” *Nature Communications*, vol. 15, no. 1, p. 1084, 2024.

- 
- [104] H. Wang, K. L. Tiwari, K. Jacobs, M. Judy, X. Zhang, D. R. Englund, and M. E. Trusheim, “A spin-refrigerated cavity quantum electrodynamic sensor,” *arXiv preprint arXiv:2404.10628*, 2024.
- [105] E. MacQuarrie, M. Otten, S. Gray, and G. Fuchs, “Cooling a mechanical resonator with nitrogen-vacancy centres using a room temperature excited state spin–strain interaction,” *Nature communications*, vol. 8, no. 1, p. 14358, 2017.
- [106] D. P. Fahey, K. Jacobs, M. J. Turner, H. Choi, J. E. Hoffman, D. Englund, and M. E. Trusheim, “Steady-state microwave mode cooling with a diamond n-v ensemble,” *Physical Review Applied*, vol. 20, no. 1, p. 014033, 2023.
- [107] K. Mølmer, “Optical coherence: A convenient fiction,” *Physical Review A*, vol. 55, no. 4, p. 3195, 1997.
- [108] M. Abramowitz and I. A. Stegun, *Handbook of Mathematical Functions with Formulas, Graphs, and Mathematical Tables*. New York City: Dover, ninth dover printing, tenth gpo printing ed., 1964.







# Acknowledgements

Writing my PhD thesis after years of hard work is certainly one of my life's great achievements. However, it would never have been possible without the help of many dear people around me. Here, I want to issue a heartfelt *thank you* to the ones involved.

Foremost, I am grateful to my supervisor, Jörg Schmiedmayer, for his trust in his students' abilities, and for equipping us not only with contracts and experimental tools but with his invaluable physical intuition. His wisdom, always on point, often comes as a wake-up call to guide us from experiment to insight.

Also, I want to thank Johannes Majer, who took me in initially, taught me a great bit of physics, and was the one to establish the lab, laying the groundwork for many subsequent experimental endeavors.

The one who I owe the most gratitude to is my former colleague and mentor, Andreas. He taught me almost everything I know about spins, cavities, and cryostats — how to get results quickly and about the dangers of makeshift solutions. His wits, patience, and care were most appreciated, as were the beers we shared along the way. Another mentor who I am most thankful for is Tom, who held my hand right at the start of my time in the group and then went on to follow his passion for physics elsewhere. Many beers and cheerful times were also had together with Andrew, a dear colleague and the master of cryo-crystals and pucks. When Nikolaus joined, I was amazed at the extent of his abilities, both practical and theoretical, in absorbing information and participating in every project within the lab, playing a key role in our success — and being one of my favorite office buddies who will certainly tame the molecules. Then Lena came, and she was quick to extend her knowledge of qubits to our ensemble, with a sharp mind and decisive opinions, leading our lab, with a bright future ahead.

There are many others with whom I may not have worked directly on projects, but with whom I've built lasting, joyful memories. In no particular order, I will name them here, starting with Amin-joon. He, a true scholar, is a physics expert and soon-to-turn biology wizard, a dancer, a free spirit, and my other favorite office companion. A quick-witted, open-minded intellectual and friend is Filippo, who certainly knows how to enjoy life and have a good time — cooking up a pasta dish for lunch in no time together with Mira, who became a brilliant teacher. Federica is the kindest soul, smart

and with a quiet grace that adds to her strength. João, a knight in shining armor, family man, and a splendid amigo who has returned to his home. Frederik is a genius in his own right, a wanderer and gatherer of the magical kind. TianTian is brilliant, resilient, and sweet; may she find her fortune among the dunes or fjords. Pradyumna is a persistent experimentalist, a master of spices, and sharp as a laser. Philipp is a recent deskmate and formidable Rubidium condenser who will always speak his mind. Camille, wielder of baguettes and cruncher of numbers, is a climbing partner of at least the seventh grade. Igor, the master of theories — from physics to theology and even catastrophe — strong-minded yet soft at the core, a companion and teacher over drinks. May the world never be as bleak as in this stoic pessimist's worst nightmares. Stephan, the kind, expert administrator and barbecue enthusiast, who I had the pleasure of sharing many beers with.

I also want to express my gratitude to all the people who work at the Atominstitut, my scientific colleagues, and the women and men who allow for its daily operation, especially the secretaries, porters, and professionals who run the mechanical workshop.

Finally, I thank my family: the woman and man who brought me into this world, shaped who I am, and gifted me with talents — some that have helped my work in physics and others beyond it. I'm grateful as well for my two brilliant and passionate sisters, my uncle, my cherished friends, and a special person who knows exactly who she is.